

Effect of Ship Motions on Propeller-Hull Interaction

by

©Md Ashim Ali

A thesis submitted to the School of Graduate Studies in partial fulfillment of the
requirements for the degree of

Doctor of Philosophy

**Department of Ocean and Naval Architectural Engineering
Faculty of Engineering and Applied Science**

Memorial University of Newfoundland

February 2020

St. John's

Newfoundland and Labrador, Canada

Abstract

It is important to consider the detailed hydrodynamics of the propeller, the associated flow conditions and the hull interaction with effective wake distribution for developing the best ship propulsion system design. Model experiments are conventionally used to assess propeller flow and performance but are subject to scale effect and difficulties in flow measurement. Computational Fluid Dynamics (CFD), using a viscous flow solver, provides an alternate way to simulate propeller flow conditions. Although simplified propeller flow models are currently available, this thesis extends the CFD approach to develop a more comprehensive model that includes detailed propeller geometry, ship motions and wave action.

Numerical self-propulsion simulations with propeller action and ship motions are performed using a newly developed dynamic motion class based on the sliding mesh method in OpenFOAM. Validation and verification are carried out in a step by step manner. As a first step, a model incorporating bare hull resistance, wave elevation on the hull surface, free surface wave contour, and axial velocity distribution at several transverse planes for a fixed ship condition and dynamic ship condition was developed and validated using available experimental data, and the comparison between the simulations and the experiments showed good agreement. Propeller open water simulations with detailed propeller geometry and using the body-force method were developed and validated with experimental data in the second step. Because of

the highly non-linear and rotational nature of the flow near to the propeller region, curvature correction was implemented to the standard $k - \omega$ SST turbulence model to improve the numerical predictions.

Prior to the third stage self-propulsion simulation, which combined the stage 1 and 2 simulations, a numerical wave tank was developed and validated. Numerical self-propulsion simulations were performed for a ship at an even keel condition with constant propeller rotational speed. The numerical calculation of the skin friction correction, thrust coefficient, torque coefficient, and axial velocity distribution downstream of the propeller, confirmed good accuracy against the available experimental data. Then the developed dynamic motion class was extended to models with ship sinkage and trim. Comparison with available data showed an excellent agreement for all self-propulsion parameters. An expected increase in total resistance and decrease in propeller thrust was observed due to ship motion.

As an alternative of detailed propeller geometry modelling, two body-force models were developed for self-propulsion simulation when detailed flow features are not required. The effective local velocity body-force model showed better numerical predictions than nominal average velocity body-force method. The self-propulsion simulation was performed in waves with forward speed using the developed dynamic motion class and it was able to incorporate the rotating propeller with large ship motions. The thrust generated by a propeller varied with encounter wave period and was reduced compared to the even keel condition.

Acknowledgements

Firstly, I would like to express my sincere gratitude to my supervisor, Dr. Heather Peng, for her continuous support throughout my PhD studies and research. I am very grateful for her patience and kindness. Not only her guidance consistently helped me throughout conducting my research, but also her encouragement has helped me through the difficult times I have encountered.

Besides my supervisor, I would like to thank the rest of my thesis committee, Dr. Wei Qiu and Dr. David Molyneux, for their insightful comments. They have helped me to better understand the field of marine hydrodynamics. Without their precious support, it would not have been possible to conduct this research. I would also like to show my gratitude to my colleagues and friends at Memorial University, for the helpful discussions and suggestions in all the stages of my research.

I am very grateful to the support by NSERC through its CREATE program. Without this support, I would have not been able to complete this research.

Last but not the least, I would like to thank my parents and my family. I would like to thank my wife, my son and my daughter, who sacrifices their time throughout my PhD studies. I also owe my deepest gratitude to my parents for their support and understanding all the time.

Table of Contents

| | |
|--|-----------|
| Abstract | ii |
| Acknowledgments | iv |
| Table of Contents | xi |
| List of Tables | xiv |
| List of Figures | xxiii |
| 1 Introduction | 1 |
| 1.1 Literature Review | 3 |
| 1.1.1 Experimental Studies | 4 |
| 1.1.2 Numerical Studies | 9 |
| 1.1.3 Problem Statement | 14 |
| 1.1.4 Research Aims and Objectives | 14 |
| 1.1.5 Thesis Outline | 17 |
| 2 Mathematical Formulation | 19 |
| 2.1 Governing Equation for Multiphase Flow | 19 |
| 2.1.1 Continuity and Momentum Equations | 20 |
| 2.1.1.1 Pressure Term | 21 |

| | | |
|---------|--|----|
| 2.1.1.2 | Viscous Term | 21 |
| 2.1.2 | Volume of Fluid | 22 |
| 2.1.3 | Interface Capturing Scheme | 24 |
| 2.1.3.1 | interfaceCompression Scheme | 25 |
| 2.1.3.2 | HRIC Scheme | 26 |
| 2.2 | Discretization of Governing Equations | 27 |
| 2.2.1 | Time Derivative | 28 |
| 2.2.2 | Convective Term | 29 |
| 2.2.3 | Diffusion Term | 29 |
| 2.2.4 | Source Term | 30 |
| 2.2.5 | Temporal Discretization | 30 |
| 2.3 | Pressure Velocity Coupling | 31 |
| 2.4 | Turbulence Modeling | 33 |
| 2.4.1 | $k - \omega$ SST Turbulence Model | 33 |
| 2.4.2 | LRR Turbulence Model | 36 |
| 2.5 | Near-Wall Treatment | 37 |
| 2.6 | Sliding Mesh | 40 |
| 2.7 | Dynamic Motion Solver | 41 |
| 2.8 | Body-Force Method | 44 |
| 2.8.1 | Fixed Velocity Body-Force Model (FV-BFM) | 45 |
| 2.8.2 | Local Velocity Body-Force Model (LV-BFM) | 46 |
| 2.9 | Convergence Criteria | 46 |
| 2.9.1 | Residual Convergence | 47 |
| 2.9.2 | Convergence Error | 48 |
| 2.10 | Numerical Solvers | 49 |
| 2.11 | Verification and Validation Methodology | 50 |

| | | |
|----------|--|-----------|
| 2.11.1 | Verification | 50 |
| 2.11.1.1 | Least Squares Root (LSR) Method | 50 |
| 2.11.2 | Validation | 52 |
| 2.12 | Numerical Wave Tank | 53 |
| 2.12.1 | Wave Generation | 54 |
| 2.12.2 | Wave Absorption | 55 |
| 2.13 | Vortex Identification Criteria | 56 |
| 2.13.1 | λ_2 -criterion | 57 |
| 2.13.2 | Q -criterion | 58 |
| 2.14 | Self-propulsion Modelling | 58 |
| 3 | Resistance and Flow Validation | 63 |
| 3.1 | Bare Hull | 64 |
| 3.1.1 | KCS Model | 65 |
| 3.1.1.1 | Geometry and Test Conditions | 66 |
| 3.1.1.2 | Computational Domain and Grid Generation | 66 |
| 3.1.1.3 | Resistance Validation | 70 |
| 3.1.1.4 | Free Surface Wave Contour | 74 |
| 3.1.1.5 | Flow Velocity | 75 |
| 3.1.1.6 | Effect of Turbulence Model | 80 |
| 3.1.2 | Japan Bulk Carrier | 86 |
| 3.1.2.1 | Geometry and Test Conditions | 86 |
| 3.1.2.2 | Computational Domain and Grid Generation | 86 |
| 3.1.2.3 | Resistance Validation | 88 |
| 3.1.2.4 | Free Surface Wave Contour | 89 |
| 3.1.2.5 | Flow Velocity | 96 |
| 3.1.3 | Fishing Vessel | 98 |

| | | |
|----------|--|------------|
| 3.1.3.1 | Geometry and Test Conditions | 98 |
| 3.1.3.2 | Computational Domain and Grid Generation | 99 |
| 3.1.3.3 | Resistance Validation | 101 |
| 3.1.3.4 | Free Surface Wave Contour | 105 |
| 3.1.3.5 | Flow Velocity | 106 |
| 3.2 | Hull with Appendages | 108 |
| 3.2.1 | KCS Model | 108 |
| 3.2.1.1 | Geometry and Test Conditions | 108 |
| 3.2.1.2 | Computational Domain and Grid Generation | 108 |
| 3.2.1.3 | Resistance, Sinkage, and Trim Validation | 111 |
| 3.3 | Scale Effect on Resistance, Sinkage and Trim | 115 |
| 3.3.1 | Computational Domain and Grid Generation | 115 |
| 3.3.2 | Resistance, Sinkage and Trim | 117 |
| 3.3.3 | Free Surface Wave Contour | 119 |
| 3.3.4 | Flow Velocity | 119 |
| 4 | Propeller Open Water Validation | 123 |
| 4.1 | KP505 Test Case | 124 |
| 4.1.1 | Geometry and Test Conditions | 124 |
| 4.1.2 | Actual Propeller Geometry | 124 |
| 4.1.2.1 | Computational Domain and Grid Generation | 125 |
| 4.1.2.2 | Numerical Results | 127 |
| 4.1.2.3 | Steady Simulation | 127 |
| 4.1.2.4 | Unsteady Simulation | 130 |
| 4.1.3 | Body-Force Method | 131 |
| 4.1.3.1 | Computational Domain and Grid Generation | 131 |
| 4.1.3.2 | Grid Dependency Study | 132 |

| | | |
|----------|---|------------|
| 4.1.3.3 | Sampling Plane Distance | 133 |
| 4.2 | MP687 Test Case | 136 |
| 4.2.1 | Propeller Geometry | 136 |
| 4.2.1.1 | Computational Domain and Grid Generation | 136 |
| 4.2.1.2 | Steady Simulation | 137 |
| 4.2.1.3 | Unsteady Simulation | 139 |
| 4.3 | NRC-IOT Propeller Test Case | 143 |
| 4.3.1 | Geometry | 143 |
| 4.3.2 | Numerical Results | 144 |
| 5 | Numerical Wave Tank Validation | 147 |
| 5.1 | Computational Domain | 148 |
| 5.2 | Grid Dependency | 149 |
| 5.3 | Time Step Size Dependency | 150 |
| 5.4 | Wave Validation | 152 |
| 6 | Self-Propulsion Simulation | 153 |
| 6.1 | KCS Test Case | 153 |
| 6.1.1 | Geometry | 155 |
| 6.1.2 | Computational Domain and Boundary Conditions | 155 |
| 6.1.3 | Self-Propulsion at Restrained Even Keel Condition | 156 |
| 6.1.3.1 | Pressure Distribution | 159 |
| 6.1.3.2 | Flow Velocity | 159 |
| 6.1.4 | Self-Propulsion with Sinkage and Trim | 161 |
| 6.1.4.1 | Pressure Distribution | 163 |
| 6.1.4.2 | Flow Velocity | 165 |
| 6.1.5 | Seakeeping Simulation | 169 |

| | | |
|----------|---|------------|
| 6.1.6 | Self-Propulsion in Waves | 171 |
| 6.1.6.1 | Ship Response | 174 |
| 6.1.6.2 | Free Surface Wave | 174 |
| 6.1.6.3 | Pressure Distribution | 177 |
| 6.2 | JBC Test Case | 179 |
| 6.2.1 | Geometry | 179 |
| 6.2.2 | Computational Domain and Grid Generation | 180 |
| 6.2.3 | Results Validation | 180 |
| 6.2.4 | Flow Velocity | 183 |
| 6.2.5 | Vortex Visualization | 190 |
| 6.3 | Fishing Vessel | 191 |
| 6.3.1 | Wave Elevations | 193 |
| 6.3.2 | Velocities on Propeller Plane | 194 |
| 6.3.3 | Thrust, Torque, Tow Force and Self-Propulsion Point | 197 |
| 6.3.4 | Self-Propulsion Results | 198 |
| 6.3.5 | Pressure Distribution | 199 |
| 6.4 | HPC and Computational Time | 202 |
| 7 | Conclusions and Recommendations | 203 |
| 7.1 | Conclusions | 203 |
| 7.2 | Best practice for propeller-hull interaction. | 209 |
| 7.2.1 | Selection of computational domain. | 209 |
| 7.2.2 | Mesh generation. | 210 |
| 7.2.3 | Selection of propeller modelling | 211 |
| 7.2.4 | Solver selection | 211 |
| 7.2.5 | Boundary conditions set-up | 211 |
| 7.2.6 | Selection of turbulence model | 212 |

| | | |
|-------|--|------------|
| 7.2.7 | Selection of numerical schemes | 212 |
| 7.2.8 | Time step size selection | 213 |
| 7.2.9 | Setting convergence criteria | 213 |
| 7.3 | Recommendations for Future Work | 213 |
| | Bibliography | 215 |
| | Appendices | 227 |
| | A Propeller Tip Vortex Simulation | 228 |
| A.1 | Geometry and Test Conditions | 228 |
| A.2 | Computational Domain and Grid generation | 229 |
| A.3 | Numerical Results Validation | 231 |
| | B Wave Run-up Simulation | 247 |
| B.1 | Model Experiment | 247 |
| B.2 | Computational Domain and Grid Generation | 248 |
| B.3 | Numerical Set-up | 250 |
| B.4 | Wave Generation Modules | 250 |
| B.5 | Grid Resolution Study | 252 |
| B.6 | Time Step Dependency | 252 |
| B.7 | Effect of Divergence Scheme | 253 |
| B.8 | Effect of Turbulence Model | 257 |
| B.9 | Wave Run-up Results | 257 |

List of Tables

| | | |
|------|---|-----|
| 3.1 | Principal particulars of the KCS bare hull. | 66 |
| 3.2 | Test case for bare hull resistance | 67 |
| 3.3 | Boundary conditions for RANS simulations | 69 |
| 3.4 | Computational grid for bare hull simulation. | 69 |
| 3.5 | Steady resistance and uncertainty of the KCS bare hull at $Fn = 0.26$ | 69 |
| 3.6 | Effect of turbulence model on total resistance for GRID-C | 80 |
| 3.7 | RMS error of the velocity components for different turbulence models for GRID-C. | 81 |
| 3.8 | Principal particulars of the JBC hull. | 87 |
| 3.9 | JBC test cases considered for validation of numerical results. | 87 |
| 3.10 | Computational grid for JBC bare hull simulation. | 88 |
| 3.11 | Grid dependency of C_T , sinkage and trim at $Fn = 0.142$ | 92 |
| 3.12 | Comparison of $ U_{SN}\%S $ for C_T , sinkage and trim at $Fn = 0.142$ | 92 |
| 3.13 | Principal particulars of the ship model and the propeller. | 99 |
| 3.14 | Test conditions for fishing vessel model. | 99 |
| 3.15 | Computational grids for simulations of fishing vessel. | 100 |
| 3.16 | Comparison of total resistance coefficient, C_T | 101 |
| 3.17 | Comparison of $ E\%D $ for C_T , sinkage and trim at $Fn = 0.34$ | 103 |
| 3.18 | Principal particulars of rudder for KCS hull. | 109 |

| | | |
|------|--|-----|
| 3.19 | Test conditions for appended KCS model. | 109 |
| 3.20 | Computational grid for KCS with rudder. | 111 |
| 3.21 | Grid dependency of C_T , sinkage and trim at $Fn = 0.26$ | 111 |
| 3.22 | Comparison of $ U_{SN}\%S $ for C_T , sinkage and trim at $Fn = 0.26$. . . | 111 |
| 3.23 | Results of unsteady simulation of KCS hull with rudder using GRID-C. | 112 |
| 3.24 | Computational grid for scale effect study. | 117 |
| 4.1 | Principal particulars of KP505 propeller. | 125 |
| 4.2 | Computational grid for KP505 propeller open water simulation | 127 |
| 4.3 | Grid dependency of open water performance at $J = 0.7$ using steady solver. | 129 |
| 4.4 | Grid dependency of open water performance at $J = 0.7$ using unsteady solver. | 130 |
| 4.5 | Principal particulars of MP687 propeller. | 137 |
| 4.6 | Computational grids for MP687 propeller open water simulation . . . | 138 |
| 4.7 | Grid dependency of open water performance at $J = 0.7$ using steady solver. | 138 |
| 4.8 | Grid dependency of open water performance at $J = 0.7$ using unsteady solver. | 140 |
| 4.9 | Principal particulars of the NRC-IOT propeller. | 143 |
| 5.1 | Wave conditions for numerical tank validation | 148 |
| 6.1 | Test cases for the validation of self-propulsion simulation of KCS model. | 154 |
| 6.2 | Numerical results of self-propulsion simulation. | 158 |
| 6.3 | Numerical results of self-propulsion test with ship motion. | 161 |
| 6.4 | Numerical results of self-propulsion test with ship motion in wave C3. | 171 |
| 6.5 | Test conditions for JBC self-propulsion simulation | 179 |

| | | |
|------|--|-----|
| 6.6 | Numerical results of self-propulsion of JBC model. | 181 |
| 6.7 | Comparison of $ E\%D $ for F_{Tow} , sinkage and trim at $Fn = 0.34$. . . | 195 |
| 6.8 | Self-propulsion simulation results using the load varying method by FV-BFM at $Fn = 0.34$ | 196 |
| 6.9 | Self-propulsion simulation results using the load varying method by LV-BFM at $Fn = 0.34$ | 196 |
| 6.10 | Self-propulsion parameters of fishing vessel at $Fn = 0.34$ | 198 |
| 6.11 | Computational time in skipper and openfoam server. | 202 |
| | | |
| A.1 | Propeller particulars | 228 |
| A.2 | Computational grids for DTM5168 propeller. | 232 |
| A.3 | Boundary conditions for tip vortex simulations. | 232 |
| A.4 | Comparison of K_T and $10K_Q$ | 233 |
| A.5 | RMS error of V_x , V_t and V_r at $x/R = 0.1756$ | 241 |
| A.6 | RMS error of V_x , V_t and V_r at $x/R = 0.2386$ | 241 |
| | | |
| B.1 | Wave probe locations. | 248 |
| B.2 | Wave matrix for wave run-up simulation. | 249 |
| B.3 | Boundary conditions for numerical wave generation. | 250 |

List of Figures

| | | |
|------|--|----|
| 1.1 | Contour of phase-averaged axial velocity in the longitudinal plane at the phase angle $\phi = 0^0$ | 5 |
| 1.2 | Axial velocity comparison in front of CP and CRP | 7 |
| 1.3 | The non-dimensional axial velocity at $x/R = -0.514$ | 8 |
| 1.4 | The non-dimensional axial velocity at $r/R = 0.7$ | 8 |
| 1.5 | Numerical wake contours behind the ship hull of a LPG carrier at $Fn = 0.242$ | 11 |
| 2.1 | Calculation of cell face volume fraction. | 25 |
| 2.2 | Parameters for finite control volume discretization (Rusche, 2002). . . | 27 |
| 2.3 | PIMPLE algorithm | 32 |
| 2.4 | Law of the wall | 38 |
| 2.5 | Illustration of the sliding mesh method. | 40 |
| 2.6 | Dynamic update of ship and propeller domains. | 42 |
| 2.7 | Calculation procedure using dynamic motion class. | 43 |
| 2.8 | Example of iterative convergence for variable x | 48 |
| 2.9 | Schematic of numerical wave tank | 55 |
| 2.10 | Variation of $\gamma_R (\chi_R)$ for damping zone | 56 |
| 3.1 | Body plan and profile elevation of KCS. | 65 |

| | | |
|------|---|----|
| 3.2 | KCS bare hull geometry. | 66 |
| 3.3 | Extent of the computational domain for bare hull simulation. | 67 |
| 3.4 | Grid distribution around the ship hull. | 68 |
| 3.5 | Grid refinement of Kelvin wedge on the free surface. | 68 |
| 3.6 | Convergence of total resistance coefficient, C_T for GRID-C. | 70 |
| 3.7 | Residual convergence for GRID-C. | 71 |
| 3.8 | Convergence error for total resistance coefficient for GRID-C at $Fn =$ 0.26. | 71 |
| 3.9 | Numerical uncertainty of C_T at $Fn = 0.26$ | 72 |
| 3.10 | Wave elevation along the ship hull at $Fn = 0.26$ | 72 |
| 3.11 | Free surface wave pattern comparison at $Fn = 0.26$ | 73 |
| 3.12 | Wave elevation at $y/L_{PP} = 0.1024$ | 74 |
| 3.13 | Wave elevation at $y/L_{PP} = 0.1509$ | 75 |
| 3.14 | Wave elevation at $y/L_{PP} = 0.30$ | 76 |
| 3.15 | Wave elevation at $y/L_{PP} = 0.40$ | 76 |
| 3.16 | Axial flow velocity contour on the propeller plane at $Fn = 0.26$ | 77 |
| 3.17 | Axial flow velocity on the propeller plane at $z/L_{PP} = -0.03$ | 78 |
| 3.18 | Transverse flow velocity on the propeller plane at $z/L_{PP} = -0.03$ | 78 |
| 3.19 | Vertical flow velocity on the propeller plane at $z/L_{PP} = -0.03$ | 79 |
| 3.20 | Effect of turbulence models on wave elevation along the hull surface for GRID-C. | 81 |
| 3.21 | Effect of turbulence models on free surface wave pattern for GRID-C. | 82 |
| 3.22 | Axial flow velocity contour on the propeller plane using different turbulence models for GRID-C. | 83 |
| 3.23 | Effect of turbulence model on axial flow velocity on the propeller plane at $z/L_{PP} = -0.03$ for GRID-C. | 84 |

| | | |
|------|---|-----|
| 3.24 | Effect of turbulence model on transverse flow velocity on the propeller plane at $z/L_{PP} = -0.03$ for GRID-C. | 84 |
| 3.25 | Effect of turbulence model on vertical flow velocity on the propeller plane at $z/L_{PP} = -0.03$ for GRID-C. | 85 |
| 3.26 | JBC bare hull geometry. | 86 |
| 3.27 | Computational domain of JBC hull. | 89 |
| 3.28 | Grid distribution around the JBC hull. | 89 |
| 3.29 | Convergence of C_T for GRID-C at $Fn = 0.142$ | 90 |
| 3.30 | Time history of residuals convergence for GRID-C. | 90 |
| 3.31 | Convergence error of C_T for GRID-C at $Fn = 0.142$ | 91 |
| 3.32 | Grid uncertainty for C_T at $Fn = 0.142$ | 91 |
| 3.33 | Wave elevation along the ship hull. | 92 |
| 3.34 | Free surface wave pattern comparison at $Fn = 0.142$ | 93 |
| 3.35 | Wave elevation at $y/L_{PP} = 0.1043$ at $Fn = 0.142$ | 94 |
| 3.36 | Wave elevation at $y/L_{PP} = 0.1900$ at $Fn = 0.142$ | 94 |
| 3.37 | Axial flow velocity contour on $x/L_{PP} = 0.9625$ for $Fn = 0.142$ | 95 |
| 3.38 | Axial flow velocity contour on $x/L_{PP} = 0.9843$ for $Fn = 0.142$ | 96 |
| 3.39 | Axial flow velocity contour on $x/L_{PP} = 1.0$ for $Fn = 0.142$ | 97 |
| 3.40 | Ship model of optimized fishing vessel. | 98 |
| 3.41 | Computational domain for Fishing vessel. | 100 |
| 3.42 | Grid distribution around the bulbous bow. | 101 |
| 3.43 | Total resistance coefficient for $Fn = 0.34$ | 102 |
| 3.44 | Total resistance coefficient of Model-H using GRID-C. | 103 |
| 3.45 | Free surface wave contours for Model-H at $Fn = 0.34$ | 104 |
| 3.46 | Bow waves of Model-H at $Fn = 0.34$ | 105 |
| 3.47 | Comparison of wave elevation along the hull of Model-H at $Fn = 0.34$ | 106 |

| | | |
|------|---|-----|
| 3.48 | Axial velocity contour on the propeller plane at $Fn = 0.34$ for GRID-C. | 107 |
| 3.49 | KCS model with rudder. | 108 |
| 3.50 | Semi-balanced horn rudder for KCS. | 110 |
| 3.51 | Grid distribution for sinkage and trim computation. | 110 |
| 3.52 | Comparison of total resistance coefficient using GRID-C. | 112 |
| 3.53 | Comparison of sinkage of KCS model using GRID-C. | 113 |
| 3.54 | Comparison of trim of KCS model GRID-C. | 113 |
| 3.55 | Computational domain for the study of scale effect. | 115 |
| 3.56 | Grid distribution at bow and stern of the model. | 116 |
| 3.57 | Effect of scale factor on frictional resistance. | 118 |
| 3.58 | Effect of scale factor on pressure resistance. | 118 |
| 3.59 | Effect of scale factor on sinkage. | 119 |
| 3.60 | Effect of scale factor on trim. | 120 |
| 3.61 | Effect of scale factor of free surface wave contour. | 121 |
| 3.62 | Effect of scale factor on axial velocity distribution on propeller plane. | 122 |
| 4.1 | Geometry of KP505 propeller. | 125 |
| 4.2 | Computational domain of KP505 propeller open water simulation. | 126 |
| 4.3 | Grid distribution on KP505 propeller blade. | 126 |
| 4.4 | Convergence of K_T , $10K_Q$ for $J = 0.7$ using steady solver for GRID-B. | 128 |
| 4.5 | Residual convergence using steady solver for GRID-B at $J = 0.7$. | 128 |
| 4.6 | KP505 propeller open water simulation using steady solver for GRID-B. | 129 |
| 4.7 | Convergence of K_T , $10K_Q$ for $J = 0.7$ using transient solver for GRID-B. | 130 |
| 4.8 | Residual convergence using transient solver for GRID-B at $J = 0.7$. | 131 |
| 4.9 | Open water simulation of KP505 using transient solver for GRID-B. | 132 |

| | | |
|------|--|-----|
| 4.10 | Computational domain for KP505 open water simulation using body-force method. | 133 |
| 4.11 | Effect of number of cells in radial direction. | 133 |
| 4.12 | Effect of velocity sampling plane distance. | 134 |
| 4.13 | Propeller open water characteristics of KP505 using body-force method. | 134 |
| 4.14 | MP687 propeller geometry. | 136 |
| 4.15 | Grid distribution on the propeller blade and hub of MP687. | 137 |
| 4.16 | Convergence history of K_T , K_Q and η_0 using steady solver for GRID-B at $J = 0.70$ | 138 |
| 4.17 | Residuals convergence for advance coefficient $J = 0.70$ for GRID-B. | 139 |
| 4.18 | Open water simulation of MP687 propeller using steady solver for GRID-B. | 140 |
| 4.19 | Convergence history of K_T , K_Q and η_0 using transient solver for GRID-B at $J = 0.70$ | 141 |
| 4.20 | Residuals convergence for GRID-B at advance coefficient $J = 0.70$ | 141 |
| 4.21 | Open water simulation of MP687 propeller using transient solver for GRID-B. | 142 |
| 4.22 | Effect of the cell numbers on propeller parameters at $J = 0.70$ using transient solver. | 143 |
| 4.23 | Effect of the velocity sampling plane distance on propeller parameters at $J = 0.70$ using transient solver. | 144 |
| 4.24 | Comparison of open water data of NRC-IOT propeller using transient solver. | 145 |
| 5.1 | Computational domain for numerical wave tank validation. | 148 |
| 5.2 | Grid distribution in the computational domain. | 149 |
| 5.3 | Comparison of wave elevation at WP-02 using TS03 of wave C1. | 150 |

| | | |
|------|--|-----|
| 5.4 | Comparison of wave elevation at WP-02 using GRID-C of wave C1. . . | 151 |
| 5.5 | Comparison of wave elevation at WP-02 using GRID-C of wave C3. . . | 151 |
| 6.1 | Geometry for KCS self-propulsion. | 155 |
| 6.2 | Computational grid for self-propulsion of KCS model. | 155 |
| 6.3 | Dynamic pressure distribution on the stern of KCS for self-propulsion. | 157 |
| 6.4 | Axial velocity distribution at $0.25D$ downstream of the propeller plane. | 158 |
| 6.5 | Velocity components comparison at $x/L_{PP} = 0.9910$ ($0.25D$ downstream of the propeller plane) and $z/L_{PP} = -0.0291$ | 160 |
| 6.6 | Residual convergence for self-propulsion with sinkage and trim. . . . | 162 |
| 6.7 | Total resistance convergence error for self-propulsion with sinkage and trim. | 162 |
| 6.8 | Propeller thrust convergence error for self-propulsion with sinkage and trim. | 163 |
| 6.9 | Pressure distribution on the hull and the propeller. | 164 |
| 6.10 | Virtual pressure gauge locations. | 165 |
| 6.11 | Numerical pressure measurement at the pressure gauges. | 166 |
| 6.12 | Axial velocity distribution on the centreplane. | 167 |
| 6.13 | Axial velocity distribution at $x/L_{PP} = 0.9910$ ($0.25D$ downstream of the propeller plane). | 168 |
| 6.14 | Comparison of total resistance coefficient in wave C3. | 169 |
| 6.15 | Motion response of KCS bare hull in wave C3. | 170 |
| 6.16 | Residual convergence for self-propulsion in wave C3. | 172 |
| 6.17 | Total resistance coefficient for self-propulsion in wave C3. | 172 |
| 6.18 | Thrust coefficient over one encounter wave period for self-propulsion in wave C3. | 173 |

| | | |
|------|--|-----|
| 6.19 | Torque coefficient over one encounter wave period for self-propulsion in wave C3. | 173 |
| 6.20 | Motion response of KCS hull during self-propulsion in wave C3. . . . | 175 |
| 6.21 | Free surface wave contour over one encounter wave period, T_e for self-propulsion in wave C3. | 176 |
| 6.22 | Pressure distribution on hull surface over one encounter wave period, T_e for self-propulsion in wave C3. | 177 |
| 6.23 | Geometry for JBC model for self-propulsion simulation. | 180 |
| 6.24 | Computational grid for self-propulsion of JBC model. | 181 |
| 6.25 | Residual convergence of self-propulsion simulation of JBC model. . . | 182 |
| 6.26 | Convergence of total resistance of JBC model. | 182 |
| 6.27 | Blade angle definition. | 183 |
| 6.28 | Axial velocity distribution at $x/L_{PP} = 0.9625$ | 185 |
| 6.29 | Axial velocity distribution at $x/L_{PP} = 0.9843$ for blade angle 0^0 . . . | 186 |
| 6.30 | Axial velocity distribution at $x/L_{PP} = 0.9843$ for blade angle 48^0 . . | 187 |
| 6.31 | Axial velocity distribution at $x/L_{PP} = 1.00$ for blade angle 0^0 | 188 |
| 6.32 | Axial velocity distribution at $x/L_{PP} = 1.00$ for blade angle 48^0 | 189 |
| 6.33 | Vortex structures based on $Q = 500$ for the self-propulsion simulation with sinage and trim at $Fn = 0.142$ | 190 |
| 6.34 | Computational grid for self-propulsion of Fishing vessel. | 191 |
| 6.35 | Comparison of free surface wave contour for GRID-C at $Fn = 0.34$ in calm water. | 192 |
| 6.36 | Comparison of wave elevation along the hull for GRID-C at $Fn = 0.34$. . . | 193 |
| 6.37 | Input velocity distribution on the propeller plane at $Fn = 0.34$ | 194 |
| 6.38 | Axial velocity distribution on the propeller plane at $Fn = 0.34$ | 195 |
| 6.39 | Effective wake distribution on the propeller plane at $Fn = 0.34$ | 196 |

| | | |
|------|---|-----|
| 6.40 | Propeller suction effect at $x/L_{pp} = 0.10D$ at $Fn = 0.34$ | 197 |
| 6.41 | Comparison of tow forces at $Fn = 0.34$ | 199 |
| 6.42 | Pressure distribution on the hull at $Fn = 0.34$ | 200 |
| 6.43 | Streamlines around the propeller plane for $Fn = 0.34$ | 201 |
| | | |
| A.1 | Geometry and computation domain for grid generation | 230 |
| A.2 | Type of refinement. | 230 |
| A.3 | Refinement level. | 231 |
| A.4 | Comparison of K_T and $10K_Q$ with experimental data (Chesnakas and Jessup (1998)) | 233 |
| A.5 | Axial velocity V_x contour at $x/R = 0.2386$ | 234 |
| A.6 | Tangential velocity V_t contour at $x/R = 0.2386$ | 235 |
| A.7 | Radial velocity V_r contour at $x/R = 0.2386$ | 236 |
| A.8 | V_x , V_t and V_r across vortex core at $x/R = 0.1756$ | 237 |
| A.9 | V_x , V_t and V_r across vortex core at $x/R = 0.1756$ | 238 |
| A.10 | V_x , V_t and V_r across vortex core at $x/R = 0.2386$ | 239 |
| A.11 | V_x , V_t and V_r across vortex core at $x/R = 0.2386$ | 240 |
| A.12 | V_x , V_t and V_r across vortex core at $x/R = 0.1756$ | 242 |
| A.13 | V_x , V_t and V_r across vortex core at $x/R = 0.2386$ | 243 |
| A.14 | Pressure coefficient on suction side. | 244 |
| A.15 | Pressure coefficient of pressure side. | 245 |
| A.16 | Vortex trajectory for GRID-C3. | 246 |
| | | |
| B.1 | Wave probes locations | 248 |
| B.2 | Schematic diagram of computational domain for wave tank validation. | 249 |
| B.3 | The computational grid for wave run-up simulation. | 249 |

| | | |
|------|---|-----|
| B.4 | Comparison of wave elevation at $x/\lambda = 0$ for T15S110 using $T_w/\Delta t = 2000$ | 251 |
| B.5 | Comparison of wave elevation at $x/\lambda = 0$ for T15S110 using $T_w/\Delta t = 2000$ | 251 |
| B.6 | Comparison of wave elevation at $x/\lambda = 0$ for T15S110 using $T_w/\Delta t = 2000$ | 253 |
| B.7 | Comparison of wave elevation $x/\lambda = 0$ for T15S116 using $T_w/\Delta t = 2000$. | 254 |
| B.8 | Comparison of wave elevation at $x/\lambda = 0$ for T15S110 using GR-03. | 254 |
| B.9 | Comparison of wave elevation at $x/\lambda = 0$ for T15S116 using GR-03. | 255 |
| B.10 | Comparison of wave elevation at $x/\lambda = 0$ for T12S110 using GR-03. | 255 |
| B.11 | Comparison of wave elevation at $x/\lambda = 0$ for T12S116 using GR-03. | 256 |
| B.12 | Effect of divergence scheme on wave generation. | 256 |
| B.13 | Effect of turbulence model on wave generation. | 257 |
| B.14 | Time history of wave force on the cylinder for wave T12S110. | 258 |
| B.15 | Time history of wave force on the cylinder for wave T15S110. | 259 |
| B.16 | Wave elevation comparison for wave T12S110 at $A2$ and $A4$ | 260 |
| B.17 | Wave elevation comparison for wave T12S110 at $B2$ and $B4$ | 260 |
| B.18 | Wave elevation comparison for wave T12S110 at $C2$ and $C4$ | 261 |
| B.19 | Instantaneous free surface for wave T12S110. | 262 |
| B.20 | Wave elevation comparison for wave T12S116 at $A2$ | 263 |
| B.21 | Wave elevation comparison for wave T12S116 at $A4$ | 263 |
| B.22 | Wave elevation comparison for wave T12S116 at $B2$ | 264 |
| B.23 | Wave elevation comparison for wave T12S116 at $B4$ | 264 |
| B.24 | Wave elevation comparison for wave T12S116 at $C2$ | 265 |
| B.25 | Wave elevation comparison for wave T12S116 at $C4$ | 265 |
| B.26 | Turbulence viscosity distribution on the centre plane. | 266 |

Chapter 1

Introduction

High propulsive efficiency, minimum noise, and low vibrations are desirable features in any ship design. All these features are associated with the propeller and the flow characteristics around the propeller. For merchant ships, the propulsive efficiency is most important, whereas, for naval vessels, minimum vibration and noise level are more important. It is essential to consider the detailed hydrodynamics of the propeller, the associated flow conditions, and the propeller-hull interaction for the best propulsion system design. Model experiments are conventionally used to assess propeller flow and performance but these are subject to scale effect. The flow pattern in front of the propeller also differs from the model scale to the full scale due to the different Reynolds Numbers. The current development of Computational Fluid Dynamics (CFD) enables researchers to simulate complex flow conditions in model scale as well as in full scale. The propeller-hull interaction can be predicted by numerical simulation using a viscous flow solver considering the free surface and detailed propeller geometry. Although a simplified propeller model can be used to model the propeller action, this neglects the flow alteration by the propeller itself. With the increasing computational power, it is becoming possible to use detailed

propeller geometry in numerical propeller-hull interaction studies to better model a very complex flow.

In the numerical simulation of ships moving in calm water or in waves, the propeller effect can be modelled using either detailed propeller geometry or a simplified propeller model. The most accurate method to simulate propeller-hull interaction in waves is to model the detailed propeller geometry and hull in viscous flow with the free surface. For a simplified propeller model, the propulsion effect can be simulated using the body-force method. The propeller effect can also be obtained using a potential flow solver. Although the wake distribution behind the ship hull can be modelled with a certain level of accuracy, the potential flow model is unable to predict the effective wake due to flow alteration by the propeller itself. Furthermore, when a ship experiences six degree of freedom motions, the interaction and flow between the propeller and hull is expected to be further influenced due to the load variation on the propeller caused by generated waves and ship motions. Also, for ships in waves, the effective wake varies depending on the position of the ship in the waves, which also influences the propeller performance. Research on the propeller-hull interaction in waves is essential to better ship design.

In realistic sea states, the motions of the hull create unfavourable wake and separated flow into the propeller, which reduces the propeller performance. The propeller loading conditions also change when the ship moves through waves due to the change of propeller submergence with respect to the free surface and the large motion of the vessel itself. In a propulsion system design, knowledge of the effects of these important factors would improve design for real-life operations. In the numerical simulation, the rotation of a propeller coupled to ship motions can be simulated using either the overset grid method or the sliding mesh method. In terms of accuracy and

computational time, the sliding mesh method is a good option for detailed propeller simulation coupled to ship motion.

This thesis details the development of a full numerical model of a working propeller on a ship undergoing forward motion in a wave field with the resultant six degree of freedom motions of the ship, using the open source viscous flow solver OpenFOAM. This development provides a full flow model of a working propeller on a moving ship and allows the realistic flow conditions of such a propeller to be modelled and assessed.

Due to the very complex nature of the final simulation, a step-wise development and validation process is followed where the model is built up in stages, starting with the model of a hull undergoing forward motion, and then adding in the propeller action, wave action, and finally ship with motions. Validation is performed at each stage using experimental data available in the open literature. According to the International Towing Tank Conference (ITTC) procedures (ITTC, 1978), three sets of model tests are required for power performance prediction behind the hull, including bare-hull resistance tests, propeller open water tests, and self-propulsion tests. In reality, it is very difficult to conduct the experimental flow measurements around a working propeller on a fully moving ship model. Whereas, CFD provides the opportunity for numerical simulation of self-propulsion tests covering the complex flow conditions of the full simulation.

1.1 Literature Review

The following review of the literature covers the current extent of available experimental and numerical works on propulsion systems and pays particular attention to the studies of propeller-hull interaction.

1.1.1 Experimental Studies

Extensive experimental results from benchmark ship models have been developed over the years for the validation of numerical methods for ship resistance, wave elevation on the hull surface, free surface wave contour, and wave elevation at different transverse and longitudinal positions. Self-propulsion data were also developed for different flow parameters to facilitate the validation of numerical self-propulsion simulations. The effect of propeller suction on the effective wake was studied by Nagamatsu (1975) using flow visualization by an air injection method. A considerable change was observed in the effective wake due to the propeller suction effect for a tanker model and a cargo liner model. Fujisawa et al. (2000) studied the resistance, wave elevation, and mean velocity for the KCS model, with and without a rotating propeller, at the even keel condition, in the towing tank of the National Maritime Research Institute in Japan (NMRI) following ITTC guidelines. A similar ship model was used by Kim et al. (2001) for the study of the bare hull resistance, mean flow velocity, and the free surface elevation of KRISO Container Ship (KCS) and two other vessels KVLCC and KVLCC2 experimentally in the towing tank of the Korea Research Institute for Ships and Ocean Engineering (KRISO). The unsteady wave pattern on the free surface behind the transom was reported at the design speed. A difference between the NMRI and KRISO results was reported due to a small difference in the ship model geometry.

Propeller-hull interaction was studied by Felli and Felice (2004) using LDV phase sampling techniques for a twin screw vessel. The wake was measured on the upstream section of the propeller disk and another section behind the rudder. From the experimental results, the propeller induced suction was found significant in the region of $x/R = 0.44$ to 0.68 . This interference led to the peak velocity at the entrance of the propeller. The effect of propeller induced suction was negligible in the downstream

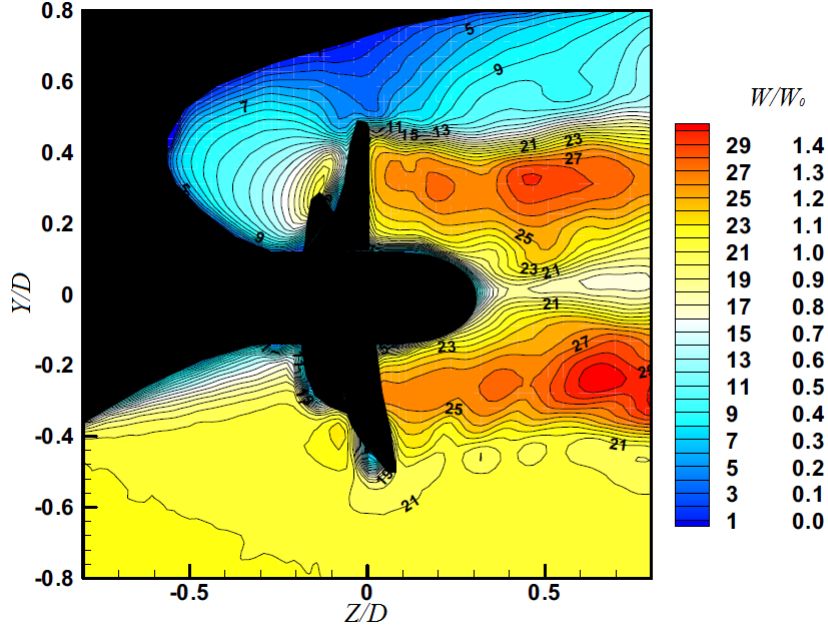


Figure 1.1: Contour of phase-averaged axial velocity in the longitudinal plane at the phase angle $\phi = 0^\circ$.

direction for distances over $x/R = 0.68$. The viscous wake generated by appendages such as shaft brackets also influences the incoming flow to the propeller. The asymmetric wake distribution was observed which leads to an unbalanced loading on the propeller, which causes vibrations, noise, and fatigue stress on the rotating shaft. Velocity reduction in the flow was also observed due to appendage vortices in the two stern sections. The deformation of the wake due to the combined effect of the propeller tip and vortices was observed on the downstream section. The vortices were found stretched on one surface of the rudder, which suffered vibration arising from interaction with the rudder tip vortex.

Paik et al. (2004, 2007) also investigated the effect of a rotating propeller behind the KCS model using a two-frame particle image velocimetry (PIV) technique. In the experiment, the origin was positioned at the center of the propeller boss. The Z -axis was set along the propeller shaft, pointing toward the stern of the ship; the X -axis was

set horizontally toward the starboard, and the Y -axis points upward. The difference between the incoming flow above the propeller axis and below the propeller axis is shown in Figure 1.1. The non-dimensionalized axial velocity component (W/W_0) is shown in the longitudinal plane for phase angle $\phi = 0^\circ$. The phase angle, (ϕ) is the angle (deg) measured from the vertical axis which is pointed in the upward direction. The distances are normalized by the propeller diameter D in this figure. It was found that the axial and tangential velocities in the propeller plane were modified by the hull wake and bilge vortices. The hull wake and free surface influenced the axial velocity distribution in the propeller plane, which also affected the tip vortex propagation in the downstream direction. The blade-to-blade interaction led to the trailing vortex rotating faster than the tip vortex in the longitudinal direction Z/D up to 0.5. An asymmetric inflow structure was observed due to the bilge vortex and hull wake interaction, which could be a source of cavitation, noise, and pressure fluctuations on the hull.

Inukai and Ochi (2009) studied the propeller suction effect on the effective wake for conventional propeller (CP) and contra-rotating propeller (CRP) on the different sections upstream of the propeller plane. Figure 1.2 shows a comparison of experimental results and calculated results using the infinite blade theory. There is a considerable deviation observed between the numerical results and experimental measurements.

Pecoraro et al. (2013) studied the inflow characteristics of a single-screw chemical tanker model due to the large flow separation in the stern region using LDV in the Large Circulating Water Channel of CNR-INSEAN. A 15% increase in flow rate was observed on the measurements plane, and non-uniform loading was observed on the propeller due to the propeller suction effect. The suction effect of the propeller on

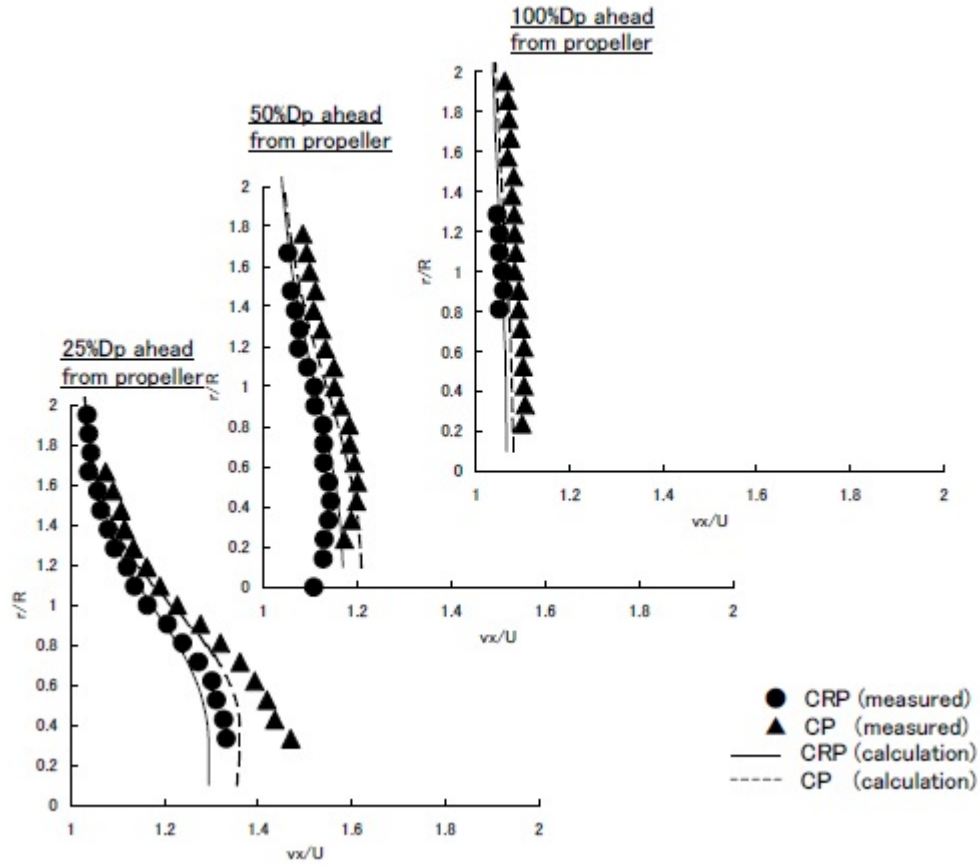


Figure 1.2: Axial velocity comparison in front of CP and CRP

incoming flow is shown in Figure 1.3 as a map for the change in axial velocity in the upstream plane at $x/R = -0.514$. The effect of propeller suction is more evident in Figure 1.4 which shows the same data as the change in axial velocity $r/R = 0.7$. The non-dimensional axial velocity is plotted against angular position (ϕ) from the vertical axis which is pointed in the upward direction. The curve of the non-dimensional velocity with propeller moves upward due to the propeller suction effect.

Most of the experimental studies have been carried out for the ship model at the even keel condition with a more or less incoming flow. Because of the cost, time, and difficulties involved in data acquisition for tests of the self-propulsion with ship motion

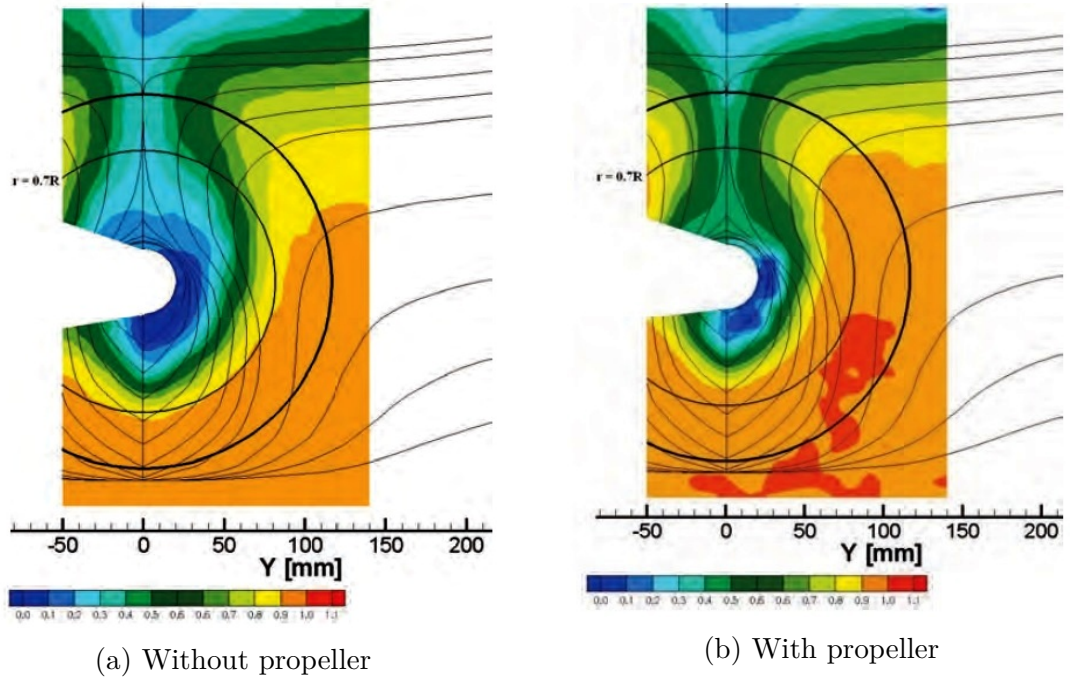


Figure 1.3: The non-dimensional axial velocity at $x/R = -0.514$

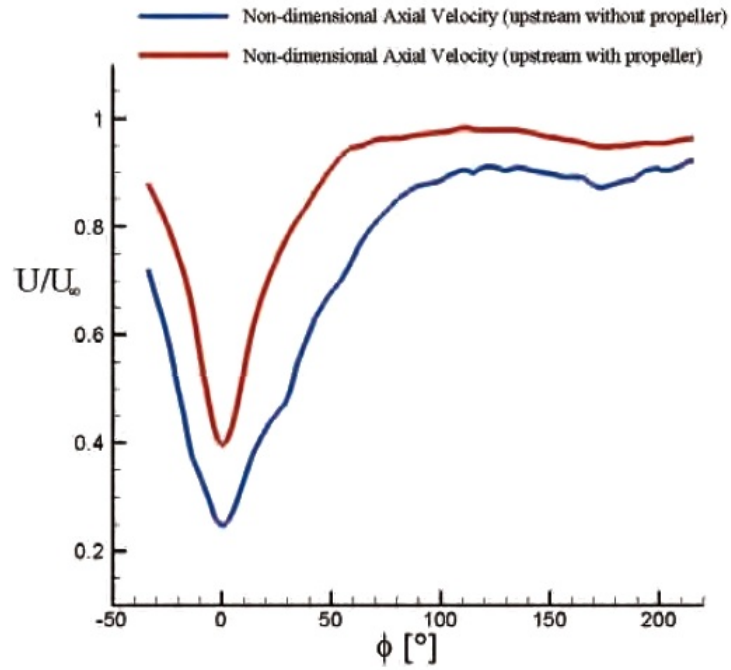


Figure 1.4: The non-dimensional axial velocity at $r/R = 0.7$.

and with incoming waves, limited information is available (Sigmund and el Moctar, 2017). A knowledge gap is still present in this research area. Recent advancements of computational fluid dynamics help to study the propeller-hull interaction involving different levels of complexities. The following review of numerical studies explains the current status of the propeller-hull interaction study.

1.1.2 Numerical Studies

Numerical studies of flow around ships are a more recent development. The use of numerical methods has grown with increasing computer power and the concurrent development of more capable software packages. The propeller-hull interaction was studied by Stern et al. (1988) using the RANS method. In the numerical simulation, the propeller was modelled using a body-force distribution model, which was calculated using the vortex-lattice lifting-surface method developed by Kerwin and Lee (1978). To consider the influence of the effective inflow velocity on the body-force distribution, the calculation was carried out iteratively. A similar approach was adopted by Zhang et al. (1992). An actuator disk with distributed body-force approach was used to model the propeller effect. The body forces were calculated using lifting-line propeller analysis program and incorporated in viscous flow solver. Watanabe et al. (1994) used a pressure jump condition to simulate the propeller effect. The value of uniform pressure jump was calculated from the measured thrust of self-propulsion experiment. The interaction between the propeller and stern flow was not considered in the calculation. Propeller-hull interaction was studied by Kawamura et al. (1997) using a finite volume viscous flow solver WISDAM-V combined with a potential flow solver developed by Nakatake (1989). The velocity distribution on the propeller disk was used from the converged RANS simulation (without propeller modelling) for body-force calculation based on the simplified propeller model. Then

the body-forces were introduced into the RANS simulation. The RANS simulation was performed repeatedly until the flow was converged for a specified thrust controlling the propeller rate of revolution. For the turbulence modelling, a hybrid turbulence model of Baldwin-Lomax model with an SGS sub-grid model was used to avoid an unrealistic velocity profile in the thin boundary layer region by sub-grid scale (SGS) model. An 11% deviation was observed in the thrust deduction factor between numerical and experimental results. In the numerical calculation, unsteady behaviour of the flow was neglected as an infinite number of blades were considered in the propeller model. Tocu and Amoraritei (2008) studied the propeller-hull interaction of an LPG carrier. The numerical computation was done using Shipflow, and an in-house code for propeller design. For turbulence modelling, the $k - \omega$ SST model was used, which acts as the $k - \omega$ model in the boundary layer region and $k - \epsilon$ outside the boundary layer region. The computations were carried out interactively with the propeller effect, which was obtained using an actuator disk or the lifting line method. The effective wake behind the ship hull was compared with experimental results and showed only a small deviation. The bilge vortices, which are usually generated by large block coefficient ships, can lead to wake hooks, as shown in Figure 1.5.

Banks et al. (2010) studied the resistance components of KCS using ANSYS CFX at model scale. The effect of the turbulence model on the numerical results was investigated using two turbulence models available in the software package, the $k - \omega$ SST and the BSL Reynolds stress turbulence models. The BSL Reynolds stress model performed better than the $k - \omega$ SST model. Dhinesh et al. (2010) studied the propeller-hull interaction at model scale using a RANS solver with the realizable $k - \epsilon$ turbulence model using STAR CCM+ for a self-propulsion condition. The propeller mesh motion was accounted for using rigid body motion. A sliding mesh interface was used to connect the rotating portion and the stationary portion of the mesh. The

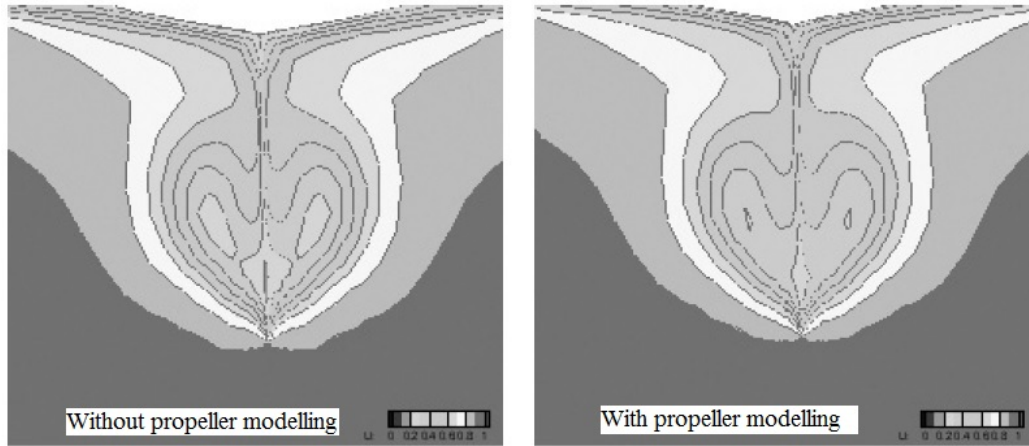


Figure 1.5: Numerical wake contours behind the ship hull of a LPG carrier at $Fn = 0.242$

numerical results for resistance and thrust were compared with experimental results. The flow developed by the propeller behind the ship was over-predicted, although the effect of propeller action was clearly observed on the pressure distribution on the ship hull and in the free surface elevation. Zhang (2010) used a sliding mesh method to study the propeller-hull interaction. Rotation of the propeller was modeled using rigid body motion and a sliding mesh interface. A simple body-force method was also used to model the propeller effect. The numerical simulations were carried out for the even keel condition only.

Win et al. (2013) studied the propeller-hull interaction for the Series 60 ship with $C_B=0.6$, using a combination of viscous flow solver and potential flow solver. The body-force distribution for the propeller was obtained using the quasi-steady blade element theory. The numerical results were validated with experimental results behind the ship model. The self-propulsion performance of a ship in waves was studied by Winden et al. (2013). In their simulation, the propeller was modelled using the Boundary Element Method with a RANS solver for the ship simulation. Body-force

modelling based on BEM was chosen over a dynamic mesh due to lower computational time.

The interaction between the hull and propeller was studied by Castro et al. (2011) at full scale and model scale for the KCS ship using an overset mesh technique. The overset interpolation was performed using SUGGAR. The numerical computation was done using CFDSHIP-IOWA, which is a RANS solver with a blended $k - \omega/k - \epsilon$ turbulence model. For the free surface simulation, single-phase level set method was adopted in the CFDSHIP-IOWA code. Differences in the torque coefficient K_Q and the nominal wake factor $1 - w_n$ for model scale and full scale simulations were observed. This was because the boundary layer thickness for the model is relatively thicker than the full scale, and the Reynolds number in each case is different. The incoming velocity to the propeller and outgoing velocity were found to be higher, and more uniform, for full scale than for model scale.

The overset grid method was also used by Shen et al. (2015), who studied the zigzag maneuvering of the KCS model in OpenFOAM. Actual propeller geometry was used for self-propulsion simulations. Carrica et al. (2016) studied the zigzag maneuvering of the KCS model in shallow water using CFDSHIP-IOWA with an overset method. The numerical results were compared with the experimental data.

Pereira et al. (2017) used an in-house code ReFRESH, for the KVLCC2 at model scale and full scale Reynolds numbers. The effect of turbulence models was investigated without a wall function using a double body method. The y^+ values were set to less than 1.0 for all computations. Results for ship resistance and flow field at

the propeller plane showed that the modelling error was strongly dependent on the turbulence model.

Hull pressure fluctuation due to the rotating propeller behind the hull is a significant source of hull vibration Hylarides (1978). The non-uniform wake flow into the propeller introduces unsteady propeller blade loading and pressure, which excites vibration due to the propeller rotation. The effective wake field due to propeller-hull interaction is key to the fluctuating pressure excitations. The wake is usually determined in model basin experiments. In practice, the unsteady propeller forces for the given wake are determined in numerical simulations Bertram (2012). It is essential to keep the excitation force within acceptable limits for sophisticated ships. Lee and Chen (2005) investigated the influence of the propeller-hull interaction effect on induced hull pressure for a cavitating propeller. The vortex lattice method was used for propeller simulation with RANS and Euler solvers. The propeller induced pressure was under-predicted using the Euler solver, which did not include propeller-hull interaction. Paik et al. (2013) used FLUENT to study the hull pressure fluctuation for a rotating propeller behind a ship. The importance of accurate wake prediction was identified for propeller-induced pressure fluctuation. Gaggero et al. (2016) studied propeller generated noise and hull pressure fluctuation for a single screw research vessel numerically and experimentally in model scale and full scale. The Boundary Element Method (BEM) method was used to model the propeller effect. Accurate prediction of the effective wake was emphasized for propeller radiated noise and pressure fluctuation on the ship hull. The shortcoming in the prediction of the propeller suction effect was mentioned. The BEM method tends to over-estimate the cavitation effect, which in turn influences the pressure prediction. Kim et al. (2018) used potential flow method to study the propeller-induced hull pressure fluctuation. The Boundary Element

Method (BEM) was coupled with the RANS method to predict the induced pressure. It was concluded that accurate effective wake prediction is crucial near the ship hull.

1.1.3 Problem Statement

From the literature review, it is found that very few attempts have been made to study the effective wake involving free surface using detailed propeller geometry. It is also well known that ship motions introduce unsteady flow patterns leading to load variation on the propeller and change the effective wake, which reduces the propulsive performance of a ship. The unsteady incoming flow and loading conditions lead to propeller vibration. The propeller generated vortices make the ship noisy and easily detectable. From an environmental point of view, propeller noise has a significant impact, particularly on marine mammals. A better understanding of the flow features can help to mitigate these unwanted effects.

This thesis uses CFD to get a better understanding of the detailed flow features in the interaction between the ship hull and the propeller under realistic operating conditions. This scenario presents considerable challenge for experimentation and thus CFD presents a viable option for design and evaluation.

1.1.4 Research Aims and Objectives

The aim of this research is to develop an efficient method to consider the propeller suction effect while considering the hull wake and ship motions using the open source Computational Fluid Dynamics (CFD) code OpenFOAM. The approach uses the sliding mesh interface method rather than the overset method for low computational cost. In addition to a model that uses the detailed propeller geometry, two body-force models are developed for faster self-propulsion simulation that still considers the

motion of the ship as well. The development of the full method requires the following intermediate objectives to be achieved in support of the full simulation. Five of these steps involve new software, or modifications of existing software, that were developed as part of this research.

1. In modelling the water surface, the volume fraction, which is discontinuous on the water surface, needs to be solved. To resolve the flow features, isotropic refinement of the grids in the free surface region is very costly due to the division of each cell in eight for a hexahedral cell. Thus, it becomes impossible to use isotropic meshing because of the large grids. However, the local flow features on the free surface can be solved by refining the cells in the normal direction of the free surface using anisotropic meshing, which greatly reduces the total number of cells required to solve the free surface accurately. In OpenFOAM, the native meshing module snappyHexMesh does not support anisotropic meshing. To overcome this limitation, an anisotropic meshing capability is developed based on snappyHexMesh for the numerical simulation involving the water surface. The developed anisotropic meshing method is used in the grid generation process for simulation of the propeller-hull interaction.
2. In recent versions of OpenFOAM, propeller rotation can be applied for a fixed condition of the ship. However, the motion of the ship changes the incoming flow to the propeller. A dynamic motion class is developed, which can be used for numerical simulation of ship motions combined with rotating propellers for the detailed study of propeller-hull interaction using actual propeller geometry.
3. The incoming flow to the propeller is highly non-linear due to the curved geometry of a ship hull and the propeller rotation itself. In the standard $k - \omega$ SST turbulence model, the effect of rotation is not considered. To

consider the effect of rotation and curvature of flow, a curvature correction is implemented in the standard $k - \omega$ SST turbulence model in OpenFOAM to improve the numerical prediction of propeller-hull interaction.

4. The wave generation and wave damping module in OpenFOAM is adapted for numerical wave simulation. The effect of ship motion in waves is simulated using the implemented wave module to investigate the effect of ship motion on propeller-hull interaction.
5. Two different velocity distribution based body-force methods are developed using propeller open water data for faster simulation of propeller effects in OpenFOAM. Although this body-force method is unable to predict flow features with the same accuracy as the detailed geometry simulation, the propulsion parameters can be predicted with reasonable accuracy in much shorter time. Depending on the time and resource availability, the implemented body-force method can be used for the numerical simulation of ships with or without ship motions.
6. There is no experimental data available in the open literature to validate a full CFD simulation that includes propeller action, ship forward motion and wave effects and wave induced motions. However, data is available for subsets of this total problem. Thus, the final simulation has been built up incrementally in stages consisting of:
 - (a) Ship resistance prediction, mean flow velocity, and pressure distribution on the hull surface with incoming current. Validation data available.
 - (b) Propeller open water performance, and upstream and downstream flow. Validation data available.

- (c) Water wave generation. Validated based on analytical solution.
- (d) A complete self-propulsion simulation that combines hull modelling, propeller modelling, wave modelling and wave induced motions. This simulation provides the final simulation objective of predicting the effective wave considering the viscous flow with free surface, and pressures around a working propeller under realistic ship operating conditions. No validation data are available.

1.1.5 Thesis Outline

The results of this research work are explained in this thesis. This thesis is organized in seven chapters as follows:

- Chapter 1 presents the current status of the propeller-hull interaction study using experimental and numerical approaches. The conclusions are summarized from the related research publications, and a knowledge gap is identified. The scope of this research is explained at the end of the chapter.
- In Chapter 2, the CFD methodologies, which are used in this thesis, are presented. Mathematical derivation of governing equations with the discretization procedures is described. The implemented curvature correction for the turbulence model, developed dynamic motion class, wave generation, and absorption modules are included in this chapter.
- The main focus of Chapter 3 is the validation and verification of numerical results. The detailed validation of the bare hull resistance, free surface wave contour, mean flow velocity, and pressure distribution on the hull surface of the KCS, JBC and Fishing vessel with and without ship motions using the experimental data are presented.

- The numerical propeller open water results using detailed propeller geometry and the body-force methods are validated against the experimental data and presented in Chapter 4. The objective of this chapter is to find the optimum settings for propeller modelling for self-propulsion simulation using a viscous flow solver. Three propeller models KP505, MP687 and a stock propeller, are used for this part of the study.
- Chapter 5 concentrates on the water wave validation. It explores different aspects of numerical wave generation, detailed grid dependency, and the time step size dependency for different wave steepness. The numerical wave generation for the self-propulsion is also validated.
- The objective of Chapter 6 is to demonstrate full implementation of this research. At first, the self-propulsion simulations are carried out for the fixed condition with detailed propeller geometry and body-force method. The predicted numerical results are validated with the experimental data. Then the self-propulsion simulations with the ship motions were performed, and numerical results are discussed. The seakeeping simulation is also validated with experimental data before the self-propulsion simulation in waves with forward speed. In the end, the previous simulation modules are integrated into a full self-propulsion in waves with ship motions.
- The main findings and conclusions are summarized in Chapter 7. The strengths and limitations of the current development with recommendations for further research are discussed.

Chapter 2

Mathematical Formulation

The following sections detail the mathematical basis for the general flow simulation and the developed simulation modules incorporated into OpenFOAM as part of this research.

2.1 Governing Equation for Multiphase Flow

A single-field formulation for two immiscible, incompressible fluids of constant viscosity is presented here. Neglecting heat and mass transfer only surface tension is considered in the formulation. In this representation, the fluids are identified by a step function α , which is 1 for one particular fluid and 0 for the other. Hence, the density and other material properties can be written in terms of their constant values for the two fluids as well as for interface.

$$\rho = \alpha\rho_1 + (1 - \alpha)\rho_2 \tag{2.1}$$

$$\mu = \alpha\mu_1 + (1 - \alpha)\mu_2 \quad (2.2)$$

where, ρ_1 is the density for fluid 1, and ρ_2 is the density for fluid 2.

2.1.1 Continuity and Momentum Equations

Assuming the fluid motion is governed by the Navier-Stokes equations, in the conservation equations for a single-field formulation (Tryggvason et al., 2001; Rusche, 2002), the differences of the material properties and the surface tension force acting at the interface are considered. The mass continuity and momentum equations are as follows:

$$\nabla \cdot \mathbf{U} = 0 \quad (2.3)$$

$$\frac{\partial}{\partial t}(\rho\mathbf{U}) + \nabla \cdot (\rho\mathbf{U}\mathbf{U}) = -\nabla p + \nabla \cdot \boldsymbol{\tau} + \rho\mathbf{f} + \int_{S(t)} \sigma\kappa'\mathbf{n}'\delta^\beta(\mathbf{x} - \mathbf{x}')dS \quad (2.4)$$

where \mathbf{U} is the velocity field, p is the pressure, $\boldsymbol{\tau}$ is the stress tensor, \mathbf{f} is the acceleration due to body-forces which is gravitational force, \mathbf{g} , δ^β is the three dimensional δ function, σ is the surface tension, and κ is twice the mean curvature for $3D$ flows.

Using the continuum surface force model, Brackbill et al. (1992) has shown that the last term of equation 2.4 is the continuous volumetric force acting within the transition region from one fluid to another fluid. The last term of equation 2.4 can be written as

$$\int_{S(t)} \sigma \kappa' \mathbf{n}' \delta^\beta (\mathbf{x} - \mathbf{x}') dS \approx \sigma \kappa \nabla \alpha \quad (2.5)$$

2.1.1.1 Pressure Term

The specification of the pressure boundary conditions is simplified if the modified pressure is used as a dependent variable. It is defined as:

$$p = p^* + \rho \mathbf{g} \cdot \mathbf{x} \quad (2.6)$$

where, p^* is the modified pressure and $\rho \mathbf{g} \cdot \mathbf{x}$ is the hydrostatic pressure. It helps to specify the pressure at the boundaries of the space domain. Taking the gradient of equation 2.6 gives

$$\begin{aligned} \nabla p &= \nabla p^* + \nabla(\rho \mathbf{g} \cdot \mathbf{x}) \\ &= \nabla p^* + \rho \mathbf{g} + \mathbf{g} \cdot \mathbf{x} \nabla \rho \end{aligned} \quad (2.7)$$

2.1.1.2 Viscous Term

For the Newtonian fluid the stress tensor can be written as.

$$\boldsymbol{\tau} = \mu (\nabla \mathbf{U} + (\nabla \mathbf{U})^T) \quad (2.8)$$

Using the equation 2.8, the viscous stress term can be simplified for numerical calculation as follows:

$$\begin{aligned}
\nabla \cdot \boldsymbol{\tau} &= \nabla \cdot \left(\mu \left(\nabla \mathbf{U} + (\nabla \mathbf{U})^T \right) \right) \\
&= \nabla \cdot (\mu \nabla \mathbf{U}) + \nabla \cdot \left(\mu (\nabla \mathbf{U})^T \right) \\
&= \nabla \cdot (\mu \nabla \mathbf{U}) + (\nabla \mathbf{U}) \cdot \nabla \mu + \mu \nabla (\nabla \cdot \mathbf{U}) \\
&= \nabla \cdot (\mu \nabla \mathbf{U}) + (\nabla \mathbf{U}) \cdot \nabla \mu
\end{aligned} \tag{2.9}$$

Substituting all the above derived terms in the momentum equation gives

$$\frac{\partial}{\partial t}(\rho \mathbf{U}) + \nabla \cdot (\rho \mathbf{U} \mathbf{U}) = -\nabla p^* + \nabla \cdot (\mu \nabla \mathbf{U}) + (\nabla \mathbf{U}) \cdot \nabla \mu - \mathbf{g} \cdot \mathbf{x} \nabla \rho + \sigma k \nabla \alpha \tag{2.10}$$

2.1.2 Volume of Fluid

The volume averaged flow equations are used to derive the governing equation for the volume of fluid method (Hirt and Nichols, 1981). The interface is tracked using the previously defined phase indicator function α (volume fraction) as follows:

$$\alpha = \begin{cases} 1, & \text{If the control volume is filled with phase 1} \\ 0, & \text{If the control volume is filled with phase 2} \\ 0 < \alpha < 1, & \text{If interface is present} \end{cases}$$

The volume fraction function α is further defined as

$$\alpha = \frac{\oint_{V_i} \alpha(x) dV_i}{|V_i|} \tag{2.11}$$

where, V_i is the volume i^{th} cell

Assuming the velocity is continuous across the interface, the governing equations can be written as

$$\frac{\partial \rho}{\partial t} + \nabla \cdot (\rho u) = 0 \quad (2.12)$$

$$\frac{\partial}{\partial t}(\rho u) + \nabla \cdot (\rho u u) = \nabla \cdot T - \rho g + F_s \quad (2.13)$$

where, F_s is the surface tension force and computed as

$$F_s = \sigma \kappa(x) \mathbf{n} \delta_\Gamma + (\nabla \sigma) \delta_\Gamma \quad (2.14)$$

For constant surface tension force,

$$F_s = \sigma \kappa(x) \mathbf{n} \delta_\Gamma \quad (2.15)$$

where, $\delta_\Gamma = |\nabla \alpha|$ and the unit vector $\mathbf{n} = \frac{\nabla \alpha}{|\nabla \alpha|}$ and $\kappa(x) = -\nabla \cdot \frac{\nabla \alpha}{|\nabla \alpha|}$ is the curvature at the interface. The surface tension force can be written as:

$$F_s = \sigma \kappa(x) \nabla \alpha \quad (2.16)$$

The volume fraction α can be computed from the general transport equation:

$$\frac{\partial \alpha}{\partial t} + \nabla \cdot (\alpha \mathbf{U}) = 0 \quad (2.17)$$

In OpenFOAM, an additional artificial compression term is introduced to achieve the necessary compression of the free surface, which is only active in the interface region. The transport equation for the VOF method can be given as follows:

$$\frac{\partial \alpha}{\partial t} + \nabla \cdot (\alpha \mathbf{U}) + \nabla \cdot (\alpha(1 - \alpha) \mathbf{U}_r) = 0 \quad (2.18)$$

where \mathbf{U}_r is a velocity field suitable to compress the interface, which is calculated using the following equation:

$$\mathbf{U}_r = \frac{\nabla \alpha}{|\nabla \alpha|} \min \left(C_\alpha \mathbf{n} \cdot \mathbf{u}, \max_f \left(\frac{\nabla \alpha}{|\nabla \alpha|} \cdot \mathbf{u} \right) \right) \quad (2.19)$$

with C_α the interface compression coefficient, which is typically set as one in numerical computations.

In the present study, *interfaceCompression* and High Resolution Interface Compression (HRIC) (Muzaferija and Peric, 1997) scheme are used to capture the free surface. As a single velocity \mathbf{U} is considered in the whole domain, \mathbf{U}_r or the cell face flux ϕ_f is approximated.

2.1.3 Interface Capturing Scheme

The interface capturing scheme discretizes the convective term of volume fraction to prevent the smearing of the free surface due to the numerical diffusion and maintain

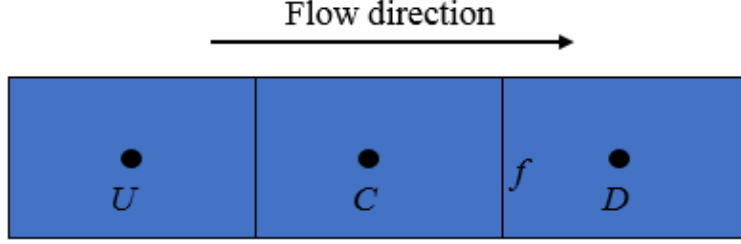


Figure 2.1: Calculation of cell face volume fraction.

the monotonic distribution of the volume fraction. The interface capturing scheme calculates the cell face value (ϕ_f) of the volume fraction using the neighbouring cell values (Figure 2.1). The *interfaceCompression* scheme and HRIC scheme is explained in this subsection.

2.1.3.1 interfaceCompression Scheme

In *interfaceCompression* scheme the cell face flux (ϕ_f) is obtained from the following formulation

$$\phi_f = \lambda(\phi_C - \phi_D) + \phi_D \quad (2.20)$$

where ϕ_C is the value of volume fraction at the current cell, and ϕ_D is the value of volume fraction in the neighbour cell. In *interfaceCompression* scheme the value of blending function is given by

$$\lambda = \min \left(\max \left[1 - \max \left\{ (1 - 4\phi_C(1 - \phi_C))^2, (1 - 4\phi_D(1 - \phi_D))^2 \right\}, 0 \right], 1 \right) \quad (2.21)$$

Although, this scheme is does not follow the Total Variation Diminishing (TVD) or Normalized Variable Diagram (NVD), it provides better boundedness and convergence (Weller, 2008).

2.1.3.2 HRIC Scheme

The High Resolution Interface Capturing (HRIC) scheme is based on the blending of the bounded downwind and upwind differencing schemes. This method is independent of the explicit Courant number. However, it depends on the local face Courant number (C_f). The cell face flux (ϕ_f) is calculated using the following formulations

$$\tilde{\phi}_C = \frac{\phi_C - \phi_U}{\phi_A - \phi_U} \quad (2.22)$$

$$\tilde{\phi}_f = \begin{cases} \tilde{\phi}_C & \text{if } \tilde{\phi}_C < 0 \text{ or } \tilde{\phi}_C > 1 \\ 2\tilde{\phi}_C & \text{if } 0 < \tilde{\phi}_C < 0.5 \\ 1 & \text{if } 0.5 \leq \tilde{\phi}_C \leq 1.0 \end{cases} \quad (2.23)$$

$$\tilde{\phi}_f^* = \begin{cases} \tilde{\phi}_f & \text{if } C_f < 0.3 \\ \tilde{\phi}_C + (\tilde{\phi}_f - \tilde{\phi}_C) \frac{0.7 - C_f}{0.7 - 0.3} & \text{if } 0.3 \leq C_f \leq 0.7 \\ \tilde{\phi}_C & \text{if } 0.7 \leq C_f \end{cases} \quad (2.24)$$

where, $\theta_f = \cos^{-1}(|\mathbf{d}\mathbf{n}|)$, $\mathbf{n} = \frac{\Delta\phi_C}{|\Delta\phi_C|}$ and $\mathbf{d} = \frac{\mathbf{CD}}{|\mathbf{CD}|}$.

$$\tilde{\phi}_f^{**} = \tilde{\phi}_f^* \sqrt{\cos\theta} + \tilde{\phi}_C(1 - \sqrt{\cos\theta}) \quad (2.25)$$

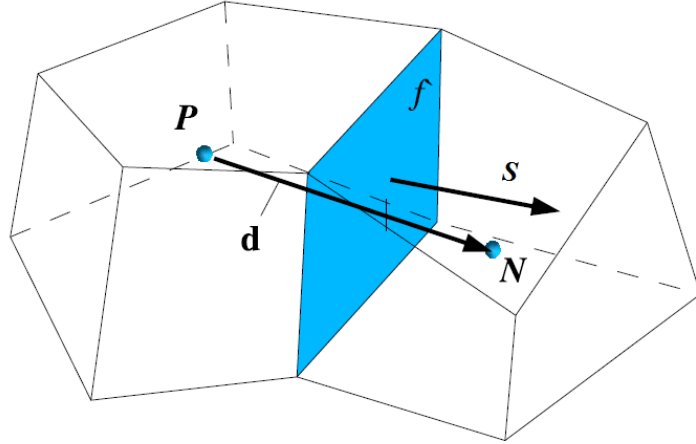


Figure 2.2: Parameters for finite control volume discretization (Rusche, 2002).

$$\phi_f = \widetilde{\phi}_f^{**} (\phi_D - \phi_U) + \phi_U \quad (2.26)$$

2.2 Discretization of Governing Equations

In Finite Volume Method, the RANS equations are solved in a fluid continuum, which is considered as the composition of discrete finite control volumes (CVs). The domain discretization can be divided into spatial discretization and temporal discretization. Many authors have described the discretization of the Finite Volume Method (Villiers, 2006; Rusche, 2002; Ferziger and Peric, 2012; Patankar, 1980; Versteeg and Malalasekera, 2007). The similar discretization approaches are used in this thesis. The spatial discretization represents the individual discrete control volume as shown in Figure 2.2. The face area vector \mathbf{S} is normal to the face and its magnitude is equal to the area of the face, and the normal vector on the face f is $\mathbf{n} = \frac{\mathbf{S}}{|\mathbf{S}|}$. It points out of the cell of interest P into the neighbouring cell N . The centres of cell P and N are connected with the vector \mathbf{d} . The standard transport

equation will be used to describe the discretization process. The general transport equation in integral form can be express as

$$\frac{\partial}{\partial t} \int_V \rho \phi dV + \int_V \nabla \cdot (\rho \mathbf{U} \phi) dV = \int_V \nabla \cdot (\Gamma \nabla \phi) dV + \int_V S_\phi(\phi) dV \quad (2.27)$$

Here, ϕ is the transport quantity such as velocity, \mathbf{U} is the velocity, Γ is the diffusivity and S_ϕ is the force term. The volume integrals are reduced to surface integrals by using Gauss's theorem. where S is the surface bounding the volume V and $d\mathbf{S}$ is an infinitesimal surface element with outward pointing normal on the surface S .

$$\int_V \nabla \phi dV = \int_S \phi d\mathbf{S} \quad (2.28)$$

2.2.1 Time Derivative

The time derivative $\frac{\partial}{\partial t} \int_V \rho \phi dV$ is discretized by integrating it over the control volume CV . For incompressible flow, assuming the linear variation of ϕ over the time step given by

$$\frac{\partial}{\partial t} \int_V \rho \phi dV \approx \rho \frac{\phi_P^n - \phi_P^o}{\Delta t} V_P \quad (2.29)$$

where $\phi^n \equiv \phi(t + \Delta t)$ is the new value at the current time step and $\phi^o \equiv \phi(t)$ the old values from previous time step.

2.2.2 Convective Term

The convective term $\nabla \cdot (\rho \mathbf{U} \phi)$ is discretized in the following form using Gauss's theorem

$$\int_V \nabla \cdot (\rho \mathbf{U} \phi) dV = \int_S (\rho \mathbf{U} \phi) \cdot d\mathbf{S} = \sum_f \mathbf{S} \cdot (\rho \mathbf{U})_f \phi_{f(F,S)} \quad (2.30)$$

Here $\mathbf{S} \cdot (\rho \mathbf{U})_f$ is the mass flux through the face f . The value of ϕ_f can be calculated using Central Differencing, Upwind Differencing and Blended Differencing schemes.

2.2.3 Diffusion Term

The diffusion term $\nabla \cdot (\Gamma \nabla \phi)$ is discretized using the similar procedure as the convective term. After applying Gauss's theorem, the diffusion term can be written as

$$\int_V \nabla \cdot (\Gamma \nabla \phi) dV = \int_S (\Gamma \nabla \phi) \cdot d\mathbf{S} \approx \sum_f \Gamma_f (\mathbf{S} \cdot \nabla_f \phi) \quad (2.31)$$

The face gradient of ϕ can be calculated as

$$\mathbf{S} \cdot (\nabla \phi)_f = |\mathbf{S}_d| \frac{\phi_N - \phi_P}{|\mathbf{d}|} + \mathbf{S}_\Delta \cdot (\nabla \phi)_f \quad (2.32)$$

Here the vector \mathbf{S}_d is the component parallel to the \mathbf{d} and \mathbf{S}_Δ is the remainder which needs to be calculated by the non-orthogonality treatment to preserve the second order accuracy. The over-relaxed approach proposed by Jasak (1996) is used in this study.

2.2.4 Source Term

The source term $S_\phi\phi$ can be expressed as

$$S_\phi\phi = S_c + S_p\phi \quad (2.33)$$

where S_c and S_p can also depend on ϕ . The volume integral of the source term can be written as

$$\int_V S_\phi(\phi)dV = S_cV_p + S_pV_p\phi_p \quad (2.34)$$

2.2.5 Temporal Discretization

The temporal discretization of equation 2.27 can be written as

$$\begin{aligned} & \int_t^{t+\Delta t} \left[\frac{\partial}{\partial t} \int_V \rho\phi dV + \int_V \nabla \cdot (\rho\mathbf{U}\phi) dV \right] dt \\ &= \int_t^{t+\Delta t} \left[\int_V \nabla \cdot (\Gamma\nabla\phi) dV + \int_V S_\phi(\phi) dV \right] dt \end{aligned} \quad (2.35)$$

Using the derived discretized term of the transport equation the above equation can be rewritten as follows

$$\begin{aligned}
& \int_t^{t+\Delta t} \left[\rho \frac{\phi_P^n - \phi_P^o}{\Delta} V_P + \sum_f \mathbf{S} \cdot (\rho \mathbf{U})_f \phi_{f(F,S)} \right] dt \\
&= \int_t^{t+\Delta t} \left[\sum_f \Gamma_f (\mathbf{S} \cdot \nabla_f \phi) + S_c V_p + S_p V_p \phi_p \right] dt
\end{aligned} \tag{2.36}$$

2.3 Pressure Velocity Coupling

Since there is no explicit equation for pressure calculation, an equation is derived from the continuity equation for pressure calculation using momentum conservation equation. There are several pressure-velocity coupling algorithms, such as SIMPLE, SIMPLEC, PISO, and PIMPLE available in OpenFOAM. The PIMPLE algorithm is the combination of SIMPLE and PISO algorithm. The PIMPLE algorithm provides the advantages of both SIMPLE and PISO algorithm.

SIMPLE (Semi-Implicit Method for Pressure-Linked Equations) was originally developed by Patankar and Spalding (1972). In the SIMPLE algorithm, a initial guess pressure field is set to solve the momentum equation for velocities. Since the velocities are calculated using the guessed pressure, the calculated velocities do not satisfy the continuity equation. Then the pressure and velocities are modified using pressure correction equations in order for modified velocities to satisfy the continuity equation. The difference between the SIMPLEC (SIMPLE Consistent) (Doormaal and Raithby, 1984) and SIMPLE is the how the pressure is corrected. SIMPLEC shows better performance over the SIMPLE algorithm.

The PISO (Pressure Implicit with Splitting Operator) was developed by Issa (1986) for pressure velocity calculation procedure. Oliveira and Issa (2001) presented the

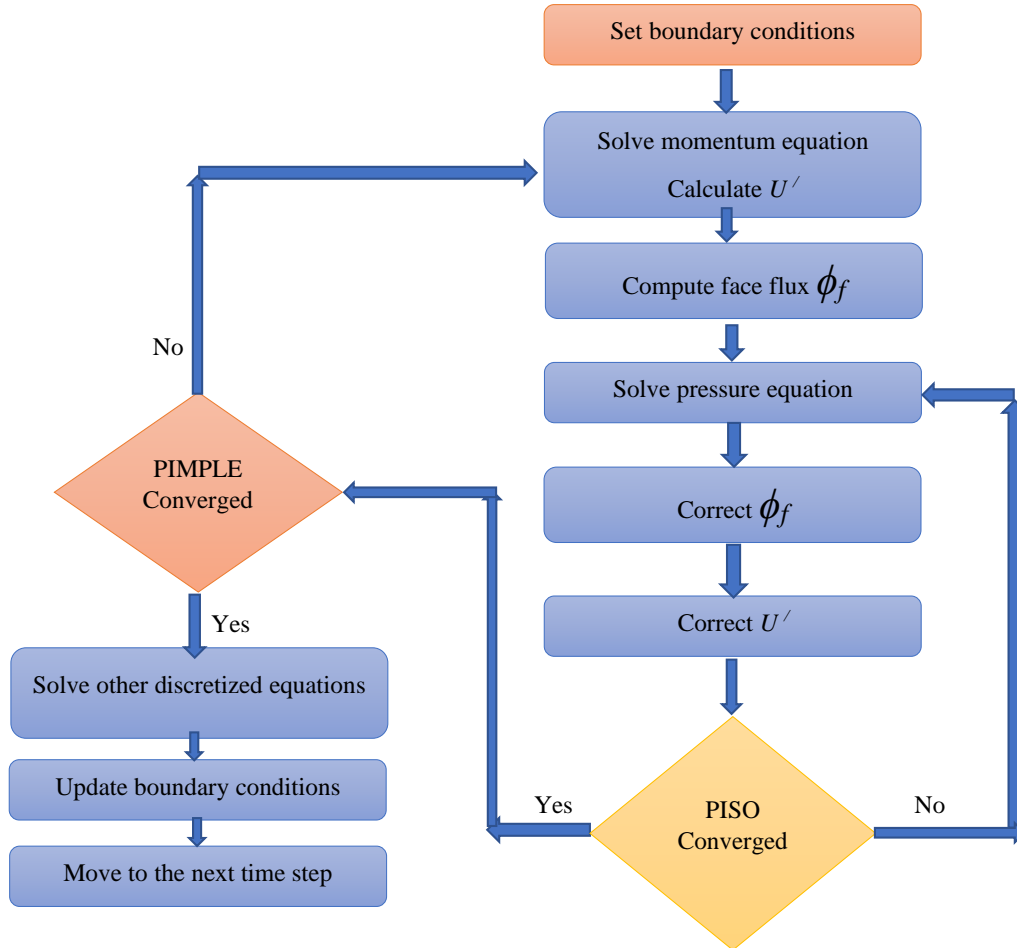


Figure 2.3: PIMPLE algorithm

improved version of PISO algorithm. In contrast to the SIMPLE algorithm where pressure correction is employed once for each time step, PISO algorithm involves two pressure correction steps. A small time step size and Courant number less than 1.0 are the major drawback of PISO algorithm. In PIMPLE algorithm, the whole solution procedure is repeated for a number of times until the convergence achieved. This allows it to use for a larger Courant number. The flow chart of PIMPLE algorithm is shown in Figure 2.3.

2.4 Turbulence Modeling

2.4.1 $k - \omega$ SST Turbulence Model

The standard $k - \omega$ SST model is a blended turbulence model that uses the $k - \omega$ model for near wall flow and transitions to $k - \epsilon$ model away from the wall as suggested by Menter et al. (2003) to overcome the individual weaknesses of the $k - \omega$ and $k - \epsilon$ models. The governing equations of the standard model are defined as follows:

$$\frac{\partial(\rho k)}{\partial t} + \frac{\partial(\rho u_j k)}{\partial x_j} = P + \beta^* \rho \omega k + \frac{\partial}{\partial x_j} \left[(\mu + \sigma_k \mu_t) \frac{\partial k}{\partial x_j} \right] \quad (2.37)$$

$$\frac{\partial(\rho \omega)}{\partial t} + \frac{\partial(\rho u_j \omega)}{\partial x_j} = \frac{\gamma}{\nu_t} P - \beta \rho \omega^2 + \frac{\partial}{\partial x_j} \left[(\mu + \sigma_\omega \mu_t) \frac{\partial \omega}{\partial x_j} \right] + 2(1 - F_1) \frac{\rho \sigma_\omega^2}{\omega} \frac{\partial k}{\partial x_j} \frac{\partial \omega}{\partial x_j} \quad (2.38)$$

The coefficients are blended forms of the two baseline models. The blending function F_1 is defined as

$$F_1 = \tanh \left(arg_1^4 \right) \quad (2.39)$$

where

$$arg_1 = \min \left[\max \left(\frac{\sqrt{k}}{C_\mu \omega y}, \frac{500\nu}{y^2 \omega} \right), \frac{4\rho \sigma_\omega^2 k}{CD_{k\omega} y^2} \right] \quad (2.40)$$

Here y is the normal distance to the wall and $CD_{k\omega}$ is the positive portion of the cross-diffusion term

$$CD_{k\omega} = \max \left(2\rho \sigma_\omega^2 \frac{1}{\omega} \frac{\partial k}{\partial x_i} \frac{\partial \omega}{\partial x_i}, 10^{-20} \right) \quad (2.41)$$

The coefficients $\sigma_k, \sigma_\omega, \gamma$ and β in above equation are computed with the general form

$$\phi = F_1 \phi_1 + (1 - F_1) \phi_2 \quad (2.42)$$

where ϕ_1 and ϕ_2 are the coefficients of the $k - \omega$ and $k - \epsilon$ turbulence models. The eddy viscosity is calculated from

$$\nu_t = \frac{a_1 k}{\max(a_1 \omega, \Omega F_2)} \quad (2.43)$$

where F_2 is given by

$$F_2 = \tanh\left(\text{arg}_2^2\right) \quad (2.44)$$

and

$$\text{arg}_2 = \max\left(\frac{2\sqrt{k}}{C_\mu \omega}, \frac{500\nu}{y^2 \omega}\right) \quad (2.45)$$

The flow system rotation and streamline curvature influence the turbulence generation on convex and concave surfaces. The standard $k - \omega$ SST turbulence model is unable to capture this effect. Smirnov and Menter (2009) proposed a rotation and curvature correction term, f_{r1} for the turbulence production term of the standard model. The production term P is defined as:

$$P = f_{r1} \tau_{ij} \frac{\partial u_i}{\partial x_j} \quad (2.46)$$

$$\tau_{ij} = \mu_t \left(2S_{ij} - \frac{2}{3} \frac{\partial u_k}{\partial x_k} \delta_{ij} \right) - \frac{2}{3} \rho k \delta_{ij} \quad (2.47)$$

where

$$f_{r1} = \max[\min(f_{rotation}, 1.25), 0.0] \quad (2.48)$$

$$f_{rotation} = (1 + c_{r1}) \frac{2r^*}{1 + r^*} \left[1 - c_{r3} \tan^{-1}(c_{r2} \hat{r}) \right] - c_{r1} \quad (2.49)$$

where c_{r1} , c_{r2} and c_{r3} are set as 1.0, 2.0 and 1.0. Einstein notation is adopted in the equations. The other terms are defined as:

$$r^* = S/\Omega \quad (2.50)$$

$$\hat{r} = \frac{2\Omega_{ik}S_{jk}}{\Omega D^3} \left(\frac{DS_{ij}}{Dt} + (\varepsilon_{imn}S_{jn} + \varepsilon_{jmn}S_{in})\Omega_m^{rot} \right) \quad (2.51)$$

$$S_{ij} = \frac{1}{2} \left(\frac{\partial u_i}{\partial x_j} + \frac{\partial u_j}{\partial x_i} \right) \quad (2.52)$$

$$\Omega_{ij} = \frac{1}{2} \left[\left(\frac{\partial u_i}{\partial x_j} - \frac{\partial u_j}{\partial x_i} \right) + 2\varepsilon_{mji}\Omega_m^{rot} \right] \quad (2.53)$$

$$S^2 = 2S_{ij}S_{ij} \quad (2.54)$$

$$\Omega^2 = 2\Omega_{ij}\Omega_{ij} \quad (2.55)$$

$$D^2 = \max(S^2, 0.09\omega^2) \quad (2.56)$$

where Ω^{rot} is the rotation of the reference frame and the term DS_{ij}/Dt represents the Lagrangian derivative of the strain rate tensor. S_{ij} is the strain rate tensor and Ω_{ij} is the rotation rate tensor. The anisotropic effects were considered in the numerical simulation by solving the turbulence equation.

2.4.2 LRR Turbulence Model

The effects of streamline curvature, changes in pressure strain and secondary flow are considered in a Reynolds Stress Turbulence model developed by Launder et al. (1975). The components of Reynolds stress and the resulting dissipation are calculated by solving the transport equations. The equations of the LRR model are:

$$\begin{aligned} \frac{D\overline{u'_i u'_j}}{Dt} = & - \left[\overline{u'_j u'_k} \frac{\partial \bar{u}_i}{\partial x_k} + \overline{u'_i u'_k} \frac{\partial \bar{u}_j}{\partial x_k} \right] - \frac{2}{3} \delta_{ij} \epsilon \\ & - C_1 \frac{\epsilon}{k} \left(\overline{u'_i u'_j} - \frac{2}{3} \delta_{ij} k \right) + (\phi_{ij} + \phi_{ji})_2 + (\phi_{ij} + \phi_{ji})_w \\ & - C_s \frac{\partial}{\partial x_k} \left[\frac{k}{\epsilon} \left(\overline{u'_i u'_l} \frac{\partial \overline{u'_j u'_k}}{\partial x_l} + \overline{u'_j u'_l} \frac{\partial \overline{u'_k u'_i}}{\partial x_l} + \overline{u'_k u'_l} \frac{\partial \overline{u'_j u'_i}}{\partial x_l} \right) \right] \end{aligned} \quad (2.57)$$

The influence of the mean velocity gradient on the pressure strain correlation is expressed by

$$\begin{aligned}
(\phi_{ij} + \phi_{ji})_2 = & -\frac{(C_2 + 8)}{11} \left(P_{ij} - \frac{2}{3} P \delta_{ij} \right) - \frac{(30C_2 - 2)}{55} k \left(\frac{\partial \bar{u}_i}{\partial x_j} + \frac{\partial \bar{u}_j}{\partial x_i} \right) \\
& - \frac{(8C_2 - 2)}{11} \left(D_{ij} - \frac{2}{3} P \delta_{ij} \right)
\end{aligned} \tag{2.58}$$

where

$$P_{ij} \equiv - \left(\overline{u'_i u'_k} \frac{\partial \bar{u}'_j}{\partial x_k} + \overline{u'_j u'_k} \frac{\partial \bar{u}'_i}{\partial x_k} \right) \tag{2.59}$$

$$D_{ij} \equiv - \left(\overline{u'_i u'_k} \frac{\partial \bar{u}'_k}{\partial x_j} + \overline{u'_j u'_k} \frac{\partial \bar{u}'_k}{\partial x_i} \right) \tag{2.60}$$

The transport equation for ϵ is given by

$$\frac{D\epsilon}{Dt} = C_\epsilon \frac{\partial}{\partial x_k} \left(\frac{k}{\epsilon} \overline{u'_k u'_l} \frac{\partial \epsilon}{\partial x_l} \right) - C_{\epsilon 1} \frac{\overline{\epsilon u'_i u'_k}}{k} \frac{\partial \bar{u}_i}{\partial x_k} - C_{\epsilon 2} \frac{\epsilon^2}{k} \tag{2.61}$$

The constants for LRR model are $C_1 = 1.8$, $C_2 = 0.6$, $C_S = 0.25$, $C_{\epsilon 1} = 1.44$, $C_{\epsilon 2} = 1.92$, and $C_\epsilon = 0.15$

2.5 Near-Wall Treatment

To resolve the boundary layer, it is very important to know the near-wall grid resolutions. A non-dimensional parameter, is used to introduce the near-wall region, y^+ is defined as

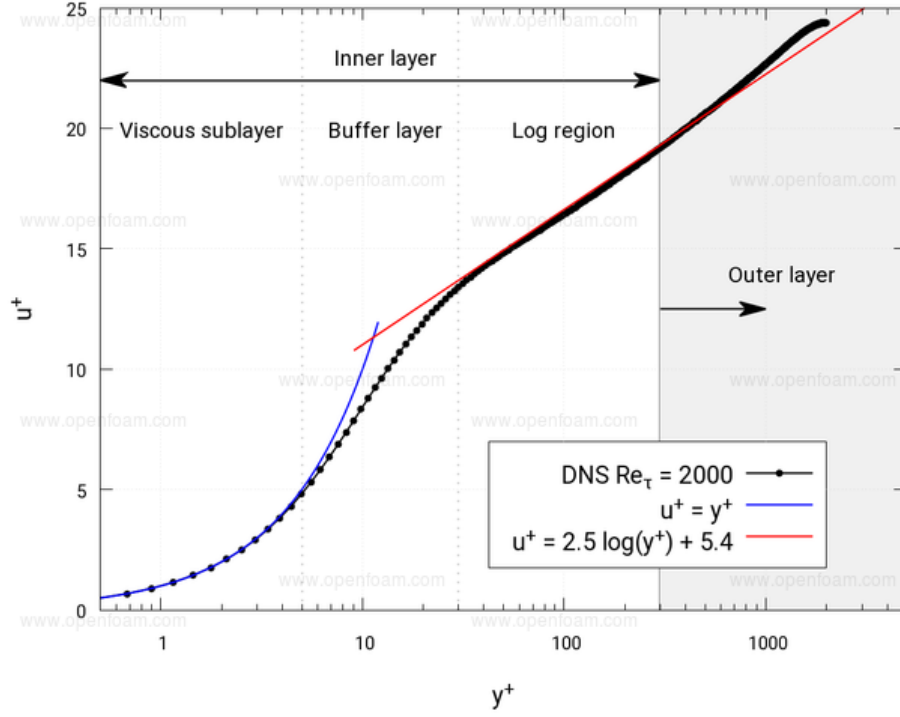


Figure 2.4: Law of the wall

$$y^+ = \frac{u_\tau y}{\nu} \quad (2.62)$$

$$u_\tau = \sqrt{\frac{\tau_w}{\rho}} \quad (2.63)$$

where u_τ is the friction velocity, τ_w is the wall shear stress, y is the distance to the wall, ν is the kinematic viscosity, and ρ is the density. The non-dimensional velocity is given by

$$u^+ = \frac{u}{u_\tau} \quad (2.64)$$

Experimental measurement shows that near-wall region consists of three layers, viscous sub-layer, buffer layer and log-law layer as shown in Figure 2.4 (OpenFOAM, 2019)

- The viscous sub-layer exist approximately upto $y^+ = 5$. In the viscous sub-layer viscous stress is dominant. The shear stress can be assumed the wall shear stress and the velocity profile is linear, which is given by

$$u^+ = y^+ \quad (2.65)$$

- The logarithmic layer exist between $y^+ = 5$ to $y^+ = 200$. In logarithmic layer, the turbulence stress dominate and control the flow. The velocity profile follows the logarithmic function given by

$$u^+ = \frac{1}{\kappa} \times \log(Ey^+) \quad (2.66)$$

where κ is the von Karman constant which is equal to 0.41, and $E = 9.8$

- In the buffer layer, Reynolds stress and viscous stress are both important, this layer lies between $y^+ = 5$ to $y^+ = 30$. The velocity profile does not follow any specific function.

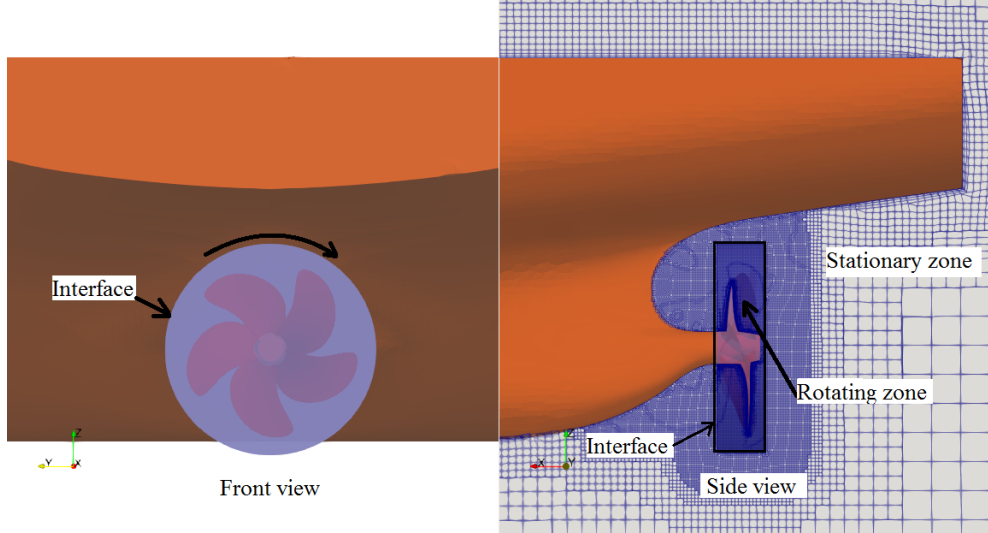


Figure 2.5: Illustration of the sliding mesh method.

In OpenFOAM, viscous shear stress can be calculated either by solving the viscous sub-layer directly or using the empirical wall functions. The approach depends on the non-dimensional parameters y^+ . A number of wall functions are available in OpenFOAM for modelling the shear stress. The blended wall functions are also available in OpenFOAM, which switches from viscous sub-layer to fully developed turbulent formulation depending on the local y^+ . In this thesis both approaches are used. Several turbulence models are also available for high Reynolds number turbulence modelling and low Reynolds number turbulence modelling.

2.6 Sliding Mesh

The Arbitrary Mesh Interface (AMI) is a sliding mesh technique which is implemented using the local Galerkin projection as described in Farrell and Maddison (2011) for unsteady flow simulation in turbo-machinery applications. In sliding mesh method two or more cell zones are used. At each time step, the mesh of the rotating/translating zones move relative to each other along the mesh interface. An

illustration of a rotating mesh zone is shown in Figure 2.5. At every time step, the cells of rotating zone updated using a sliding mesh method, and the values lying on the interface are interpolated to the updated mesh. This enables simulation across disconnected, non-conformal patches but adjacent mesh domains. In OpenFOAM, the implementation is fully parallelized, using constrained decomposition. Bensow (2013) studied propeller performance including the transient wake field and cavitation behaviour using the sliding mesh interface in OpenFOAM for a 7000 DWT chemical tanker in model scale. The simulations were performed using a double body model with a rotating propeller. The vorticity components in planes across the propeller disc were well predicted using the AMI method without any dissipation or generation of spurious solution. Chandar and Gopalan (2016) studied the comparative performance of the AMI, the Generalized Grid Interface (GGI) and the overset method, in terms of predicted force coefficients, mass conservative properties and parallel scalability for flow past a spinning cylinder. The global mass conservation for the AMI and overset were 5.83×10^{-11} and 5.04×10^{-10} respectively. The AMI method has an order of magnitude lower error than the overset method. Less computational time for the AMI method is also reported relative to the overset method using parallel computation.

2.7 Dynamic Motion Solver

A new dynamic motion class is implemented in OpenFOAM as part of this research to study propeller-hull interaction with both the motion of the ship and the rotating propeller. In the motion class, the propeller rotation is accomplished using the solid body motion and the cell zone approach. The propeller domain is updated with respect to the rotation center of the ship. Then the ship motions are calculated using a six degree of freedom motion solver. The rotating propeller domain is connected to

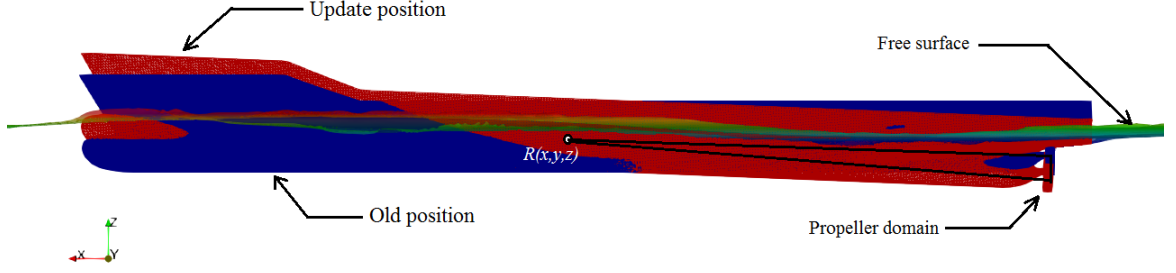


Figure 2.6: Dynamic update of ship and propeller domains.

the moving ship domain using the Arbitrary Mesh Interface (AMI) to transfer data from the ship domain to the propeller domain. In the motion solver, the propeller first rotates at the given rotational speed and the mesh points of the propeller domain are updated. The resultant forces and moments acting on the whole system are then calculated by integrating the fluid pressure, p over entire surface area S .

$$F_p = \iint_S p \hat{\mathbf{n}} dS \quad (2.67)$$

$$M_p = \iint_S r_{CS} \times \hat{\mathbf{n}} dS \quad (2.68)$$

where r_{CS} is the position vector of each surface relative to the center of rotation of the body. The velocity and acceleration of the ship are calculated by solving the equation of motion using the motion solver. Then the mesh is moved to the new position using the mesh morphing based on spherical linear interpolation method. Figure 2.6 shows

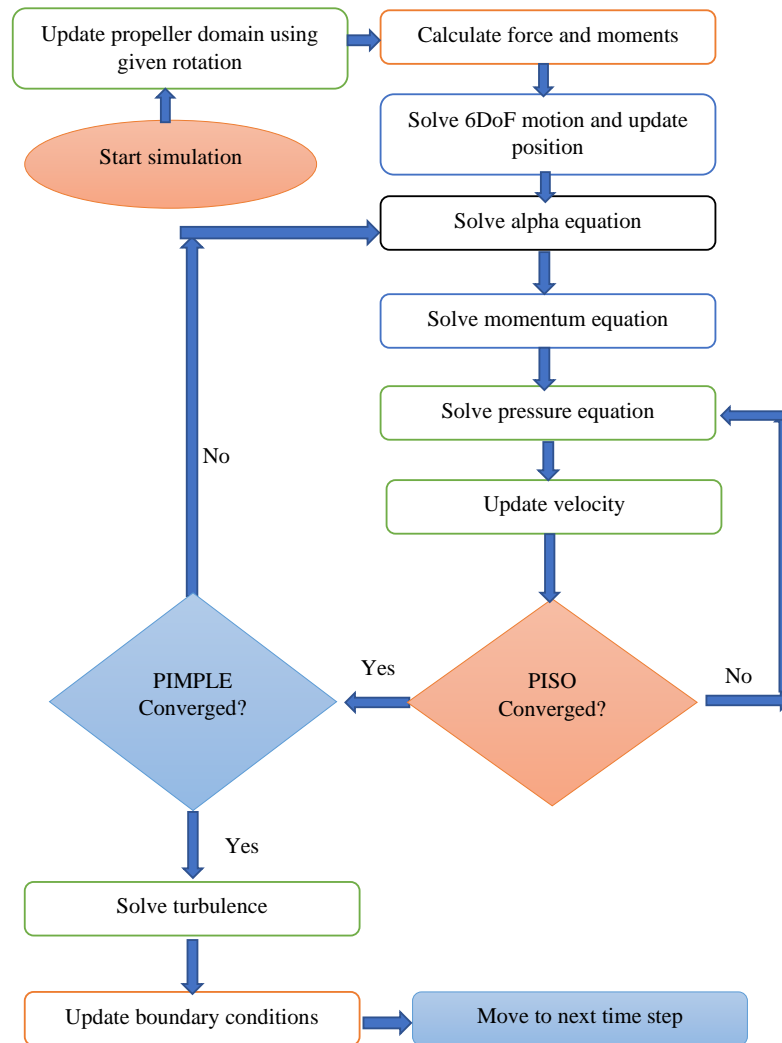


Figure 2.7: Calculation procedure using dynamic motion class.

a schematic diagram of the domain update considering the propeller rotation. The calculation steps are presented in Figure 2.7.

2.8 Body-Force Method

As an alternative approach to the previous one, which is relatively computationally intensive, the effect of the propeller was also modelled using the actuator disk based on the load distribution proposed by Hough and Ordway (1964). The momentum due to the propeller action is added as a body-force in the RANS solver. The body-force varies in the radial direction and the resulting total thrust and torque imposed on the fluid is the same as the prescribed thrust and torque. The body-force is computed in such a way that the force distribution approximately follows Goldstein's optimum (Goldstein, 1929) distribution. The non-dimensional body-forces in the axial and tangential directions are calculated using the following equations:

$$f_{bx} = A_x r^* \sqrt{1 - r^*} \quad (2.69)$$

$$f_{b\theta} = A_\theta \frac{r^* \sqrt{1 - r^*}}{r^* (1 - r'_h) + r'_h} \quad (2.70)$$

where $r^* = \frac{r' - r'_h}{1 - r'_h}$, $r' = \frac{r}{R_P}$, $r'_h = \frac{R_H}{R_P}$, r is the radius of a propeller section, R_H is the radius of propeller hub and R_P is the radius of propeller tip. Since the body-forces must result in the prescribed thrust, T , and the torque, Q , coefficients, A_x and A_θ , can be computed from:

$$A_x = \frac{C_T}{\Delta} \frac{105}{16 (4 + 3r'_h) (1 - r'_h)} \quad (2.71)$$

$$A_\theta = \frac{K_Q}{\Delta J^2} \frac{105}{16(4 + 3r'_h)(1 - r'_h)} \quad (2.72)$$

$$C_T = \frac{T}{\frac{1}{2}\rho V_a^2 \pi R_P^2} = \frac{8K_T}{\pi J^2} \quad (2.73)$$

$$J = \frac{V_a}{nD} \quad (2.74)$$

where Δ is the mean chord length projected into the xz plane.

The advance coefficient, J is calculated based on the advance velocity which can be obtained depending on the the body-force model. Then thrust coefficient K_T and torque coefficient K_Q are calculated for the respective J from the open-water propeller curve. The body-force for each cell in the actuator disk is calculated using the propeller geometric information and open-water data.

Two different body-force models were developed based on the above formulation. One is the fixed velocity body-force model (FV-BFM) and the other one is the local velocity body-force model (LV-BFM). These two models are explained in more detail in the following subsections.

2.8.1 Fixed Velocity Body-Force Model (FV-BFM)

In the FV-BFM, the average velocity, calculated based on the computed axial velocity distribution on the propeller plane without involving propeller modelling, is applied

on the propeller disk as input. The major drawback of this approach is, the average velocity does not change with time and the local velocity effect is not considered in this model. This is important for the ship hull interaction case where the flow differs across the propeller plane due to the presence of the hull surface as well as the presence of hull appendages. The self-propulsion simulation was carried out using this method to provide a comparison with the numerical predictions with the detailed propeller geometry model.

2.8.2 Local Velocity Body-Force Model (LV-BFM)

As for LV-BFM, the input velocity for each cell is obtained from the velocity sampling plane upstream of the propeller disk and updated at every time step. Note that correction is made to the input velocity based on the distance of the velocity sampling plane from the propeller plane, rotational speed of the propeller, and the propeller diameter.

2.9 Convergence Criteria

In computational fluid dynamics, a continuous problem domain is replaced with a discrete domain using a grid. In the continuous domain, each flow variable is defined at every point in the domain. This discrete system is a large set of coupled, algebraic equations in the discrete variables. These large systems of linear equations are solved using an iterative procedure and it is important to monitor the convergence of the numerical solution. Overall convergence of numerical results is based on the residual convergence and the convergence error.

2.9.1 Residual Convergence

The discretized governing equations are solved as large system of linear equations in iterative way. The problem can be expressed in matrix form

$$\mathbf{Ax} = \mathbf{b} \quad (2.75)$$

and the residual is defined as:

$$\mathbf{r} = \mathbf{b} - \mathbf{Ax} \quad (2.76)$$

The residuals are then normalized using a normalizing factor:

$$n = \sum (|\mathbf{Ax} - \mathbf{Ax}| + |\mathbf{b} - \mathbf{Ax}|) \quad (2.77)$$

where x is the solution vector and \bar{x} is the average of solution vector.

Then the normalized residuals are expressed as:

$$r = \frac{1}{n} \sum |\mathbf{b} - \mathbf{Ax}| \quad (2.78)$$

Since the CFD solution is iterative, it is not possible to achieve exactly zero residuals. However, the lower the residual value is, the more numerically accurate the solution. The solution is considered converged when the residuals do not change significantly over the simulation time. In most of the cases, pressure residuals were obtained at 10^{-2} or less, and for other parameters the initial residuals were 10^{-6} .

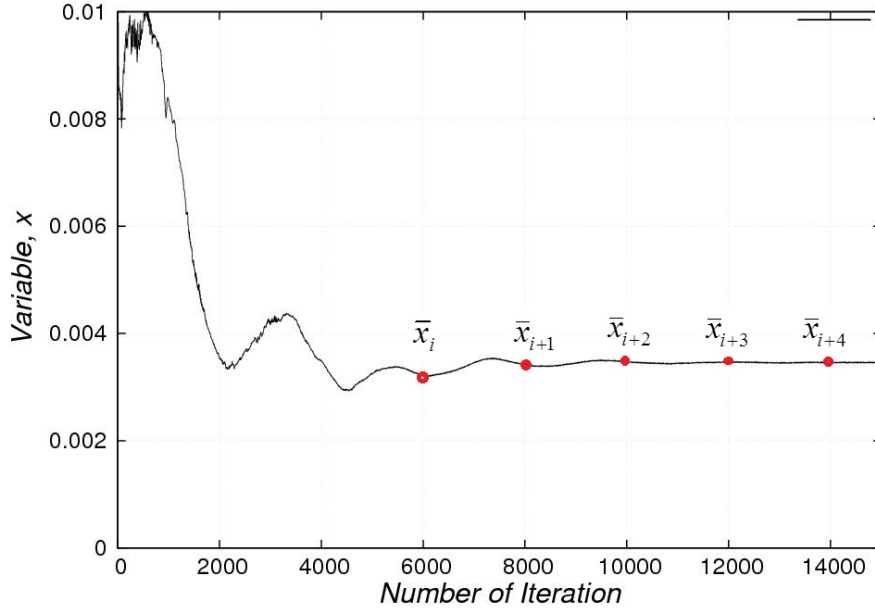


Figure 2.8: Example of iterative convergence for variable x .

2.9.2 Convergence Error

The convergence error, $E\%C$ is monitored for integrated quantities such as resistance, and propeller thrust is used to judge the convergence of the numerical simulation. The convergence error $E\%C$ for the quantity of interest x is illustrated in Figure 2.8

$$\bar{x}_i = \frac{1}{Ndata} \sum_{j=1}^{Ndata} x_j \quad (2.79)$$

$$E\%C = \frac{\bar{x}_{i+1} - \bar{x}_i}{\bar{x}_{i+1}} \times 100 \quad (2.80)$$

The numerical simulation can be considered converged when it meets both of the residual convergence and the convergence error criteria.

2.10 Numerical Solvers

In OpenFOAM, a large numbers of solvers are available for steady and unsteady simulation. In this thesis *simpleFoam*, *pimpleDyMFoam*, *interFoam*, and *interDyMFoam* solvers were used for steady and unsteady simulations. A short description of the mentioned solvers are given below.

simpleFoam is a steady-state solver for incompressible, turbulent flow, single phase flow. The pressure-velocity coupling is obtained using the SIMPLE (Semi-Implicit Method for Pressure Linked Equations) algorithm. In the newer releases, it also includes an option to use the SIMPLEC (Semi-Implicit Method for Pressure Linked Equations Consistent) algorithm. The multiple reference frames (MRF) models can be used for the steady-state simulation of turbo-machinery problems.

pimpleDyMFoam- is a transient solver for incompressible, turbulent flow of Newtonian fluids on a moving mesh for single phase flow. The pressure-velocity coupling is obtained using PISO and PIMPLE algorithm in OpenFOAM. The time step size in PISO algorithm is restricted to the Courant number 1.0 for stability reason, whereas the PIMPLE algorithm allows to use higher time step size.

interFoam and *interDyMFoam* - are solvers for two incompressible, isothermal immiscible fluids using a VOF (volume of fluid) phase-fraction based interface capturing approach, with optional mesh motion and mesh topology changes including adaptive re-meshing. Both the PISO and PIMPLE algorithm can be used for pressure-velocity coupling. For the steady-state simulation, Local Time Stepping (*LTS*) method is used for time scheme.

2.11 Verification and Validation Methodology

2.11.1 Verification

Several methods are available for verification of numerical results. The first one is the grid-triplet method, which only considers the first term of the Richardson extrapolation and assumes that the solutions are in the asymptotic range. The Grid Convergence Index (GCI) derived by Roache (1998) can be used to estimate the uncertainties due to spatial and temporal discretizations and is widely used and recommended by ASME and AIAA. The other two common verification methods in ship hydrodynamics are the Factor of Safety methods (FS) developed by Xing and Stern (2010) and the Least Squares Root (LSR) method introduced by Eça and Hoekstra (2014). The LSR method is explained in the following subsections

2.11.1.1 Least Squares Root (LSR) Method

In ship hydrodynamics applications, it is challenging to keep the variation of the grid exactly systematic (Zou and Larsson, 2014). Since the LSR method considers the scatter of numerical solutions, it was used in this work to assess the uncertainties in the numerical solutions due to spatial discretization. The discretization error was obtained by the Richardson extrapolation as below:

$$\delta_{RE} = \phi_i - \phi_0 = \beta h_i^P \quad (2.81)$$

$$h = \left[\frac{1}{N} \sum_{i=1}^N (\Delta V_i) \right]^{\frac{1}{3}} \quad (2.82)$$

where ϕ_i is the numerical solution of any parameter on a given grid, ϕ_0 is the estimated exact solution, β is a constant, h is the cell size, P is the observed order of accuracy, ΔV_i is the volume of the i^{th} cell, and N is the numbers of cells. If the numerical solutions are available on more than three grids, the parameters, ϕ_0 , β and P , can be obtained in the least square sense with or without weight by minimizing the following function (Eça and Hoekstra, 2006):

$$S(\phi_0, \beta, P) = \sqrt{\sum_{i=1}^{n_g} w_i (\phi_i - (\phi_0 + \beta h_i^P))^2} \quad (2.83)$$

where n_g is the number of grid sets. For the non-weighted approach, $w_i = 1$, and for the weighted approach, $w_i = \frac{1/h_i}{\sum_{i=1}^{n_g} (1/h_i)}$.

The convergence condition is then decided based on the P , following the rules below:

1. Monotonic divergence: $P < 0$
2. Monotonic convergence: $P > 0$
3. Oscillator convergence: $n_{ch} \geq INT(n_g/3)$, where n_{ch} is the number of triplets with $(\phi_{i+1} - \phi_i)(\phi_i - \phi_{i-1}) < 0$
4. Otherwise, anomalous behavior

The following three additional error estimator are introduced including the general RE error estimator to consider the scatter in the numerical solutions (Eça et al., 2010; Larsson et al., 2014):

$$\delta_{RE}^{02} = \phi_i - \phi_0 = \beta_{02} h^2 \quad (2.84)$$

$$\delta_{RE}^{12} = \phi_i - \phi_0 = \beta_{11} h + \beta_{12} h^2 \quad (2.85)$$

$$\delta_{\Delta M} = \frac{\max(|\phi_i - \phi_j|)}{\left(\frac{h_{n_g}}{h_1}\right) - 1} \quad (2.86)$$

where, $1 \leq i, j \leq n_g$

Based on the convergence condition, the numerical uncertainty is defined as follows:

1. Monotonic convergence:

$$(a) \quad 0.95 \leq P \leq 2.05 : U_{SN} = 1.25\delta_{RE} + \sigma_{SD}$$

$$(b) \quad P \leq 0.95 : U_{SN} = \min(1.25\delta_{RE} + \sigma_{SD}, 3\delta_{RE}^{12} + \sigma_{SD}^{12})$$

$$(c) \quad P \geq 2.05 : U_{SN} = \max(1.25\delta_{RE} + \sigma_{SD}, 3\delta_{RE}^{02} + \sigma_{SD}^{02})$$

2. Oscillatory convergence: $U_{SN} = 3\delta_{\Delta M}$

3. Anomalous behavior: $U_{SN} = \min(3\delta_{\Delta M}, 3\delta_{RE}^{12} + \sigma_{SD}^{12})$

where $\sigma_{SD}, \sigma_{SD}^{02}, \sigma_{SD}^{12}$ are the standard deviations of the curve fit. The standard deviation of the least square fit is given by

$$\sigma_{SD} = \sqrt{\frac{\sum_{i=1}^{n_g} n_g w_i (\phi_i - (\phi_0 + \beta h_i^P))^2}{n_g - 3}} \quad (2.87)$$

2.11.2 Validation

The validation of the numerical results was carried out using the simplified version of the ASME V&V 20 Committee Standard (ASME, 2009) for modelling deficiencies.

The validation error is defined as follows

$$E = S - D \quad (2.88)$$

$$|E\%D| = \left| \frac{S - D}{D} \right| \times 100 \quad (2.89)$$

where S is the numerical solution and D is experimental data. The uncertainty of validation error E is given by

$$U_E^2 = U_D^2 + U_{SN}^2 + U_{SM}^2 \quad (2.90)$$

where U_D is the experimental uncertainty, U_{SN} is the numerical uncertainty and U_{SM} is the simulation modelling uncertainty. According to Stern et al. (1999), it is impossible to calculate U_{SM} . So the validation uncertainty U_V is introduced instead of U_E . The validation error U_V is given by

$$U_V^2 = U_D^2 + U_{SN}^2 \quad (2.91)$$

If $|E| \leq U_V$, it is assumed that the validation is achieved at U_V level, and if $|E| \geq U_V$, the simulation modelling needs to be improved.

2.12 Numerical Wave Tank

Numerical wave generation is an important step in the study of wave structure interaction, propeller-hull interaction in waves, seakeeping problems etc. For wave generation in the present work, the wave generation and absorption modules are studied from IHFOAM (Higuera et al., 2013) and waves2Foam (Jacobsen et al.,

2012). In IHFOAM, waves are generated at the inlet boundary, and absorbed right on the outlet boundary. The wave generation right on the boundary reduces the computational grid by one wave length at least. The wave absorption formulation in IHFOAM is based on the shallow water wave absorption. The wave reflection occurs from the outlet boundary, particularly when the waves are generated for deep water cases and have high wave steepness (Higuera, 2020). In waves2Foam, relaxation zone techniques are used for wave generation and wave absorption. The waves are generated using an analytical expression. The wave velocity, and wave height are imposed using a blending function in the inlet relaxation zone. Then the generated waves are propagated through the computational domain. This wave generation technique increases the computational domain by one wave length which is computationally expensive for most of the cases. For wave absorption, the wave damping functions are introduced in the wave absorption zone. Wave reflection is minimal from the outlet boundary due to the wave damping zone.

In this study, the wave generation approaches are adopted from both modules but for wave absorption, only the relaxation zone approach is used. For the study of wave generation effectiveness, the wave generation on the boundary is named Module-01 and wave generation using inlet relaxation is named Module-02. A schematic of a numerical wave tank is shown in Figure 2.9.

2.12.1 Wave Generation

The wave generation module from IHFOAM will be discussed in this section. Several waves theories are available for wave generation. Details can be found in IHFOAM user guide (Higuera et al., 2013). The wave height is calculated based on the wave theory based on the input wave type in wave dictionary. This boundary condition

includes wet, dry and partially wet cells depending on the calculated wave elevation. Then the wave velocity and volume fraction are calculated and imposed on the inlet boundary face by face approach. The pressure at the inlet boundary is calculated using fixed flux pressure boundary condition, which works as a zero gradient boundary condition.

2.12.2 Wave Absorption

The wave damping method is implemented same as in waves2Foam for wave damping at the outlet boundary of the computational domain. The damping technique is applied from the work of Mayer et al. (1998). A damping function:

$$\gamma_R(\chi_R) = 1 - \frac{\exp(\chi_R^{3.5}) - 1}{\exp(1) - 1} \quad (2.92)$$

for $\chi_R \in [0; 1]$

is applied inside the damping zone in the following way:

$$\phi = \gamma_R \phi_{computed} + (1 - \gamma_R) \phi_{target} \quad (2.93)$$

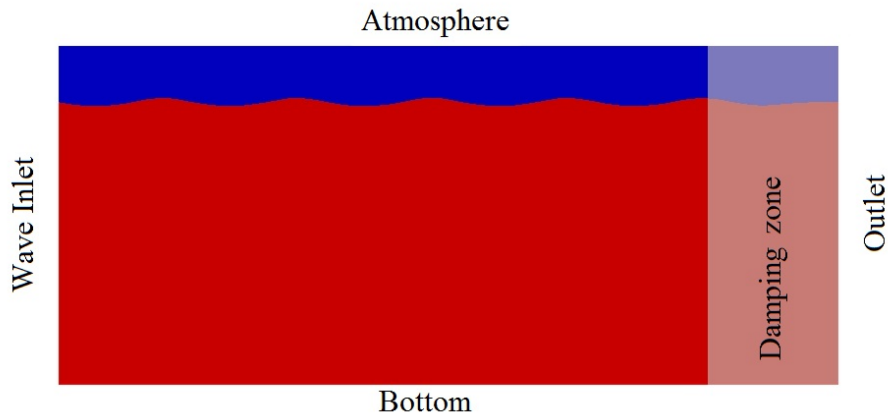


Figure 2.9: Schematic of numerical wave tank

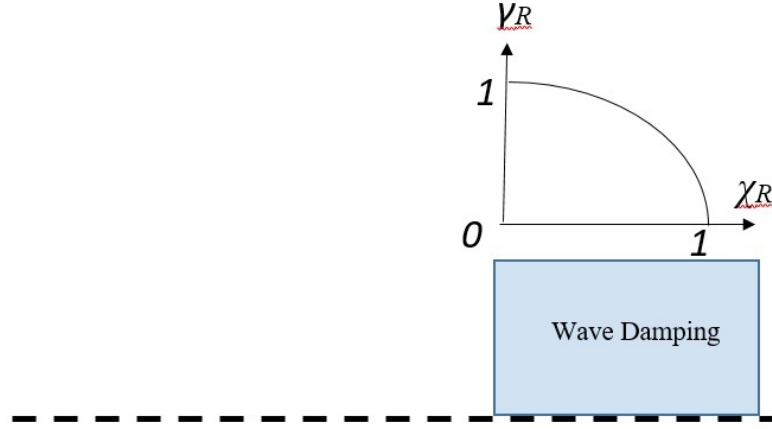


Figure 2.10: Variation of $\gamma_R(\chi_R)$ for damping zone

where ϕ is either \mathbf{U} or γ . The variation of γ_R is the same as in Figure. 2.10. The definition of χ_R is such that γ_R is always 1.0 at the interface between the non-damping part of the computational domain and the damping zone is shown in Figure. 2.9.

2.13 Vortex Identification Criteria

In OpenFOAM, two vortex identification criteria are available based on the velocity gradient. The velocity gradient \bar{D} can be decomposed into symmetric tensor and skew-symmetric components which are strain rate tensor and vorticity tensor.

$$\bar{D} = S_{ij} - \Omega_{ij} \quad (2.94)$$

where $S_{ij} = \frac{1}{2} \left(\frac{\partial u_i}{\partial x_j} + \frac{\partial u_j}{\partial x_i} \right)$ and $\Omega_{ij} = \frac{1}{2} \left(\frac{\partial u_i}{\partial x_j} - \frac{\partial u_j}{\partial x_i} \right)$. The characteristic of velocity gradient is given by

$$\lambda^3 + P\lambda^2 + Q\lambda + R = 0 \quad (2.95)$$

where, P , Q and R are the three invariants of the velocity gradient tensor. The invariants can be decomposed into symmetric and anti-symmetric parts

$$P = -tr(\overline{D}) \quad (2.96)$$

$$Q = \frac{1}{2} [tr(\overline{D})^2 - tr(\overline{D}^2)] = \frac{1}{2} \|\overline{\Omega}\|^2 - \|\overline{S}\|^2 \quad (2.97)$$

$$R = -det(\overline{D}) \quad (2.98)$$

2.13.1 λ_2 -criterion

According to Holmen (2012), λ_2 criterion is based on the local minimum pressure criteria which entails the vortex. The gradient of the acceleration a_{ij} can be obtained from the gradient of the Navier-stokes equations as

$$a_{ij} = -\frac{1}{\rho} p_{ij} + \nu u_{i,jkk} \quad (2.99)$$

The transport equation of vorticity can be obtained using the symmetric and anti-symmetric parts of the acceleration gradient

$$\frac{DS_{ij}}{Dt} - \nu S_{ij,kk} + \Omega_{ik}\Omega_{kj} + S_{ik}S_{kj} = -\frac{1}{\rho}p_{ij} \quad (2.100)$$

The negative eigenvalues of $S^2 + \Omega^2$ defines the vortex core (Chong et al., 1990). The $-\lambda_2$ iso-surfaces present the vortex.

2.13.2 Q -criterion

The fluid region connected with the positive second invariant of the velocity gradient presents the vortex. This vortex criterion imposes a lower pressure requirement in the vortex core from ambient pressure. The positive Q value presents the region where the rotation rate tensor is higher than the strain rate tensor.

2.14 Self-propulsion Modelling

The self-propulsion point for a ship model can be obtained by the load varying method, the constant loading method, or the mixed loading method (ITTC, 2008). In the load varying (constant speed) method, the model speed remains constant and the propeller load is changed by adjusting the revolution rate of the propeller. A set of numerical simulations are carried out for different propeller revolutions, and the thrust T , the torque Q , and the tow force F_{Tow} are calculated. The propeller revolution rate at the model self-propulsion point is then determined by interpolation of the tow force curve versus the propeller revolution rate. Note that the tow force is referred to the force on the tow post in physical model tests, which is determined from $F_{Tow} = R_{T(SP)} - T$, where $R_{T(SP)}$ is the total resistance of the vessel including the propeller. The tow

force at the ship self-propulsion point, also known as the skin friction correction SFC is calculated using

$$SFC = \frac{1}{2}\rho S_{W_m} V_m (C_{T_s} - C_{T_m}) \quad (2.101)$$

Here, m subscript refers to the model scale and s refers to the full scale data. S_W is wetted surface, V is the velocity, and C_T is the total resistance coefficient.

After running the self-propulsion simulation for different rates of propeller revolution, the tow force is plotted against the rate of revolutions. The ship self-propulsion point can be found using the calculated SFC . The rate of revolution n_m , thrust T_m and torque Q_m are all calculated at model scale. The calculated data at model scale is converted to full scale using the thrust identity method. The self-propulsion parameters at full scale are calculated following procedures in Lewis (1988)

The propeller rotational speed at full scale

$$n_s = \frac{n_m}{\sqrt{\lambda}} \quad (2.102)$$

The thrust and Torque is given by

$$T_s = T_m \lambda^3 \quad (2.103)$$

$$Q_s = Q_m \lambda^4 \quad (2.104)$$

The thrust deduction factor at self-propulsion is calculated

$$t = t_s = t_m = 1.0 + (FD - R_{T_m})/T_m \quad (2.105)$$

The open water propeller efficiency η_0 , and advance coefficient, J_0 are calculated using the propeller open water curve. The wake fraction at model scale is given by

$$w_m = 1.0 - \frac{J_0}{J_{SP}} \quad (2.106)$$

The wake fraction from model scale to full scale is calculated using Lewis (1988),

$$w_s = w_m \cdot \frac{C_{F_s}}{C_{F_m}} + (t + 0.04) \left(1.0 - \frac{C_{F_s}}{C_{F_m}} \right) \quad (2.107)$$

The relative rotative efficiency is given by

$$\eta_R = \frac{Q_0}{Q_{SP}} \quad (2.108)$$

The hull efficiency is given by

$$\eta_H = \frac{1 - t_s}{1 - w_s} \quad (2.109)$$

The Quasi Propulsive Efficiency(QPC)

$$QPC = \frac{P_E}{P_D} \tag{2.110}$$

where, effective power, $P_E = R_{T_s} V_s$ and delivered power, $P_D = 2\pi Q_s n_s$.

This page intentionally left blank.

Chapter 3

Resistance and Flow Validation

A comprehensive flow simulation that included ship resistance, sinkage, trim, wave elevation along the hull surface and the wave elevation at different longitudinal cuts was conducted using the steady and unsteady solvers in OpenFOAM and validated using experimental data available from the CFD workshops T2005 (2005); G2010 (2010); T2015 (2015). The following sections present the numerical results for the KRISO Container Ship (KCS), Japan Bulk Carrier (JBC), and a multi-species Fishing vessel.

The pressure resistance, frictional resistance, and total resistance coefficients were validated against the experimental data. The resistance coefficients are defined as:

$$C_T = \frac{R_T}{\frac{1}{2}\rho S_W U^2} \quad (3.1)$$

$$C_F = \frac{R_F}{\frac{1}{2}\rho S_W U^2} \quad (3.2)$$

$$C_P = \frac{R_P}{\frac{1}{2}\rho S_W U^2} \quad (3.3)$$

where R_T is the total resistance, R_F is the frictional resistance, R_P is the pressure resistance, ρ is the water density, S_W is the wetted surface and U is the ship velocity, C_T is the total resistance coefficient, C_F is the frictional resistance coefficient, and C_P is the pressure resistance coefficient. For transient simulation, the time step size is calculated based on the Courant number. The Courant number is defined as:

$$Co = \frac{U\Delta t}{\Delta x} \quad (3.4)$$

where U is the ship velocity, Δt is the time step size and Δx is the grid size. The average cell size for the computational grid is calculated

$$h = \left[\frac{1}{N} \sum_{i=1}^N (\Delta V_i) \right]^{\frac{1}{3}} \quad (3.5)$$

where N is the number of cells, and ΔV_i is the volume of the i^{th} cell

3.1 Bare Hull

For verification and validation of the numerical results, the bare hull numerical results from the KCS test case 2.1 of the Gothenburg 2010 CFD workshop are considered. The test conditions are listed in Table 3.2. The bare hull resistances of the KCS hull at model scale were computed using the Local Time Stepping (*LTS*) method in

OpenFOAM. The *LTS* method reduces the computational time to obtain a steady simulation significantly. Steady simulation results can also be used as the initial conditions for an unsteady simulation, which helps to get a steady start-up of the unsteady simulation and speed up the convergence. Since the JBC hull was free to heave and pitch in the model tests, the bare hull resistance was computed using the unsteady solver. At first the steady simulations were carried out using the *LTS* method, then the steady solution was used as the initial condition of the unsteady simulation.

3.1.1 KCS Model

A well-known KRISO Container Ship (KCS) model, which was built at a scale 1:31.5994, was tested at the Maritime and Ocean Engineering Research Institute (MOERI), Korea, and National Maritime Research Institute (NMRI) in Japan at different Froude numbers. Resistance, sinkage, trim, and local flow measurement on the propeller plane were recorded. This data is in public domain (T2005; G2010; T2015) were used for the validation of the current numerical results.

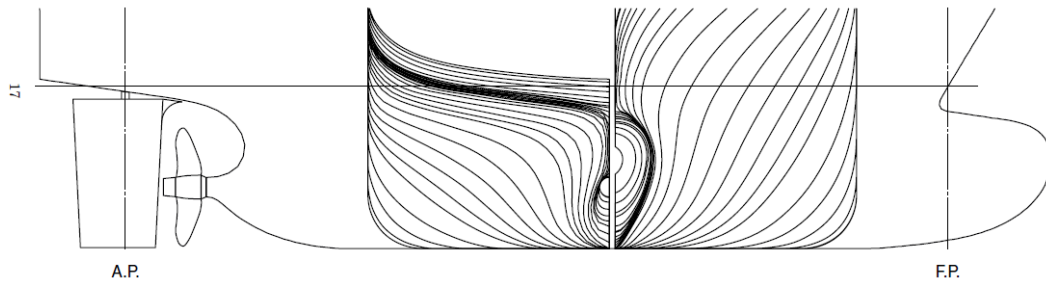


Figure 3.1: Body plan and profile elevation of KCS.



Figure 3.2: KCS bare hull geometry.

Table 3.1: Principal particulars of the KCS bare hull.

| Parameters | Full scale | Model Scale | Unit |
|------------------------|------------|-------------|----------------|
| Length, L_{PP} | 230.00 | 7.2786 | m |
| Breadth, B | 32.20 | 1.0190 | m |
| Depth, H | 19.00 | 0.6013 | m |
| Draft, T | 10.80 | 0.3418 | m |
| Displacement, ∇ | 52030.00 | 1.6489 | m ³ |
| Wetted surface, S | 9530.00 | 9.5437 | m ² |
| Design speed, V | 12.35 | 2.1960 | m/s |

3.1.1.1 Geometry and Test Conditions

The body plan and profile of the KCS model are shown in Figure 3.1 and Figure 3.2. The surface file for the geometry of the KCS model was obtained from the T2015 CFD workshop website. The principal particulars of the KCS model are summarized in Table 3.1. The bare hull test conditions are listed in Table 3.2.

3.1.1.2 Computational Domain and Grid Generation

The computational domain for the numerical simulation of the KCS bare hull was created following the ITTC guidelines (ITTC, 2011) for CFD applications. A schematic diagram of the computational domain is shown in Figure 3.3. The inlet boundary was set $1.0L_{PP}$ in front of the model, and the outlet boundary was $3.0L_{PP}$

Table 3.2: Test case for bare hull resistance

| | |
|----------------------|--|
| Case | 1.1 |
| Model | Model 1 |
| Wave | Calm |
| Condition | Towing |
| L_{PP} | 7.2786 |
| Fn | 0.26 |
| $Rn \times 10^7$ | 1.26 |
| Rudder | without |
| Propeller | without |
| Attitude | No sinkage & trim |
| Validation variables | Resistance wave elevation Mean Flow velocity |
| EFD provider | NMRI* |

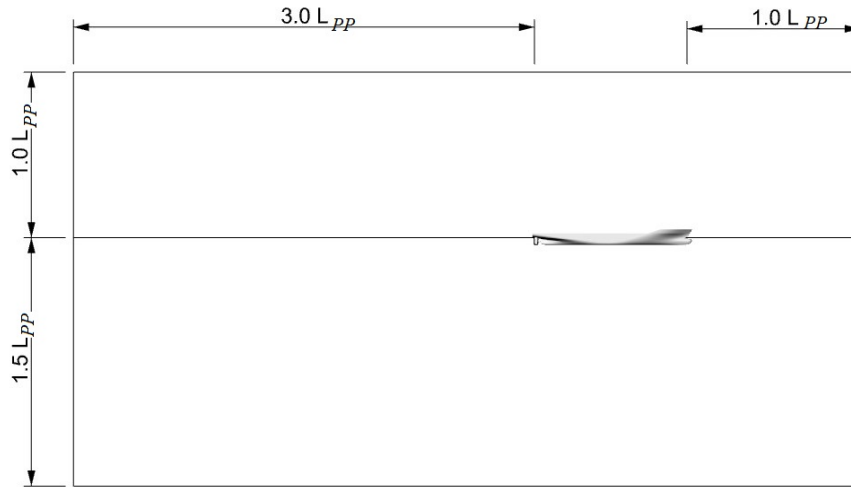


Figure 3.3: Extent of the computational domain for bare hull simulation.

behind the model. The side boundaries were set $1.5L_{PP}$ from the central plane to avoid the wall effect on the numerical simulation. The bottom boundary was set $1.5L_{PP}$ from the free surface, and the top boundary was set $1.0L_{PP}$ from the free surface. For

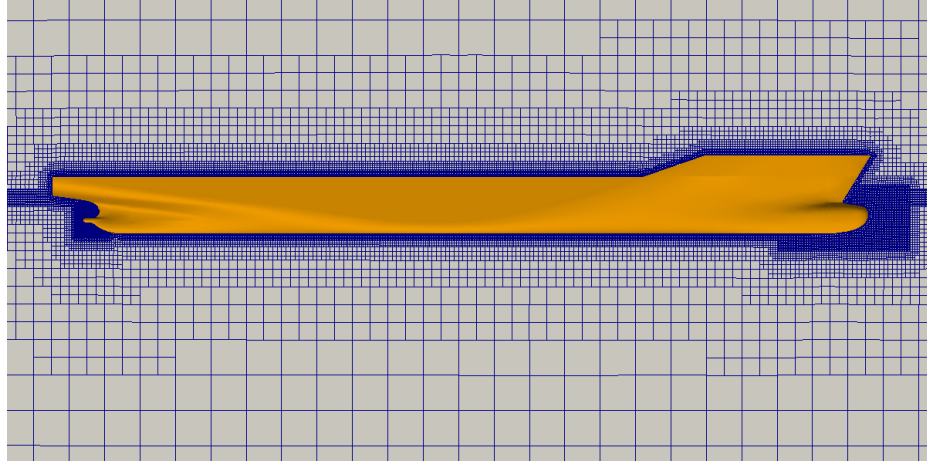


Figure 3.4: Grid distribution around the ship hull.

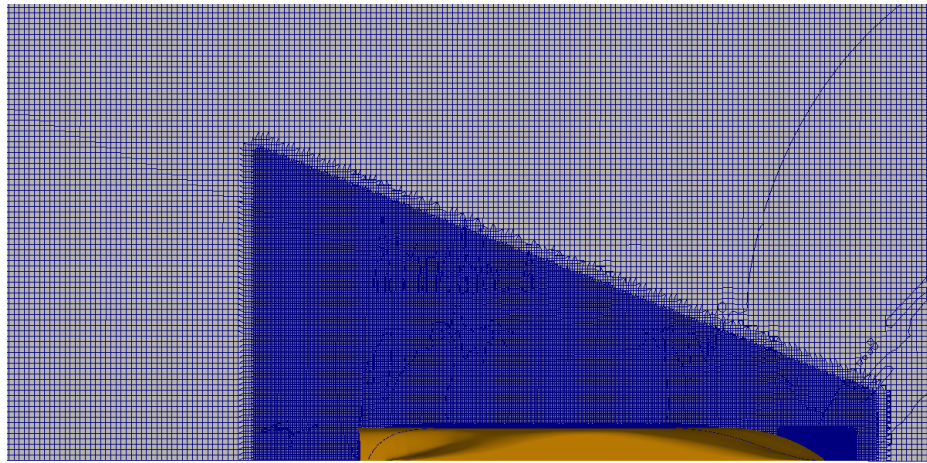


Figure 3.5: Grid refinement of Kelvin wedge on the free surface.

the numerical simulation, four computational grids were generated using the mesh generation module `navalSnappyHexMesh` in OpenFOAM. The `navalSnappyHexMesh` mesh generation module was developed for this research, based on `snappyHexMesh`, in order to generate the anisotropic cells in the free surface region. The generation of the anisotropic cells in the free surface region greatly reduces the number of cells in the computational domain. The grid distribution around the hull is shown in Figure 3.4. Local grid refinements were employed in the bow and stern region of the model to capture the flow changes. A cylindrical refinement domain is used to capture the

Table 3.3: Boundary conditions for RANS simulations

| Parameters | Inlet | Outlet | top | bottom/sides | hull |
|------------|-------------------|-------------------------|-----------------------------|---------------|--------------------------|
| U | fixedValue | outletPhaseMeanVelocity | pressureinletOutletVelocity | symmetry/slip | noSlip |
| p_rgh | fixedFluxPressure | zeroGradient | totalPressure | symmetry/slip | fixedFluxPressure |
| alpha | fixedvalue | variableHeightFlowRate | inletOutlet | symmetry/slip | zeroGradient |
| k | fixedValue | inletOutlet | inletOutlet | symmetry/slip | kLowReWallFunction |
| ω | fixedValue | inletOutlet | inletOutlet | symmetry/slip | omegaWallFunction |
| ν_t | fixedValue | zeroGradient | zeroGradient | symmetry/slip | nutUSpaldingWallFunction |

Table 3.4: Computational grid for bare hull simulation.

| GRID | Base cell size (m) | h | h_i/h_1 | No. of cells | Average, y^+ |
|--------|--------------------|--------|-----------|--------------|----------------|
| GRID-A | 1.00 | 0.1768 | 1.84 | 1649858 | 52.01 |
| GRID-B | 0.80 | 0.1458 | 1.52 | 2943851 | 53.27 |
| GRID-C | 0.67 | 0.1293 | 1.35 | 4219043 | 52.64 |
| GRID-D | 0.50 | 0.0960 | 1.00 | 10315239 | 46.59 |

Table 3.5: Steady resistance and uncertainty of the KCS bare hull at $Fn = 0.26$.

| GRID | C_P | C_F | C_T | $ E\%D $ | $ U_{SN}\%S $ |
|--------------|----------|----------|----------|----------|---------------|
| GRID-A | 0.000807 | 0.002700 | 0.003507 | 0.76 | 8.05 |
| GRID-B | 0.000824 | 0.002730 | 0.003554 | 0.57 | 5.74 |
| GRID-C | 0.000788 | 0.002723 | 0.003511 | 0.66 | 4.80 |
| GRID-D | 0.000758 | 0.002707 | 0.003464 | 1.97 | 3.16 |
| Experimental | | | 0.003534 | | |

wake in the propeller plane as well as behind the propeller plane. A Kelvin wedge grid refinement was used near to the ship hull to capture the generated wave systems more accurately. The Kelvin wedge refinement for the KCS bare hull simulation is shown in Figure 3.5. For the bare hull simulation, a symmetry plane boundary condition was used on the center plane to reduce the computational cost and time. The boundary conditions used in the numerical simulation are listed in Table 3.3. The summary of the computational grids for the bare hull resistance validation are presented in Table 3.4.

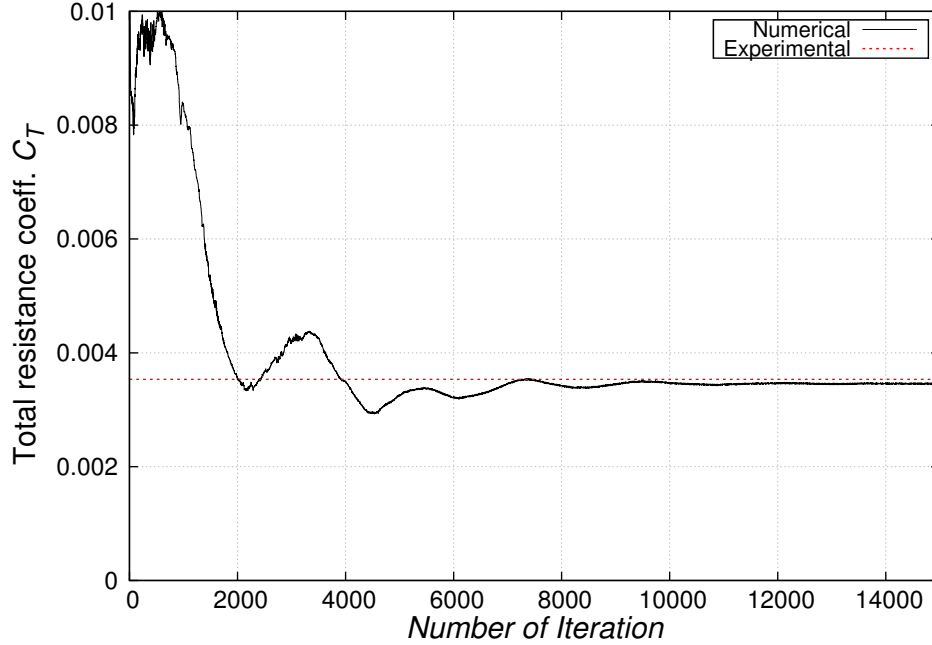


Figure 3.6: Convergence of total resistance coefficient, C_T for GRID-C.

3.1.1.3 Resistance Validation

The resistance coefficients for the bare hull were calculated for the design Froude number, $Fn = 0.26$ using the four generated sets of grid and steady solver. The model was restrained from any motion. The numerical results of the force calculation are shown in Table 3.5. The convergence history of the total resistance coefficient for GRID-C is shown in Figure 3.6. The simulation was considered converged when the residual did not change with the number of iterations and the physical quantity (such as resistance) was stable or followed the same pattern of oscillation. The convergence of residuals for GRID-C at $Fn = 0.26$ are presented in Figure 3.7. The convergence error $E\%C$ was calculated from averages of 500 iterations for the total resistance coefficient. The convergence error for GRID-C is shown in Figure 3.8. It is seen that the convergence error for C_T is less than 0.01% after 12000 iterations.

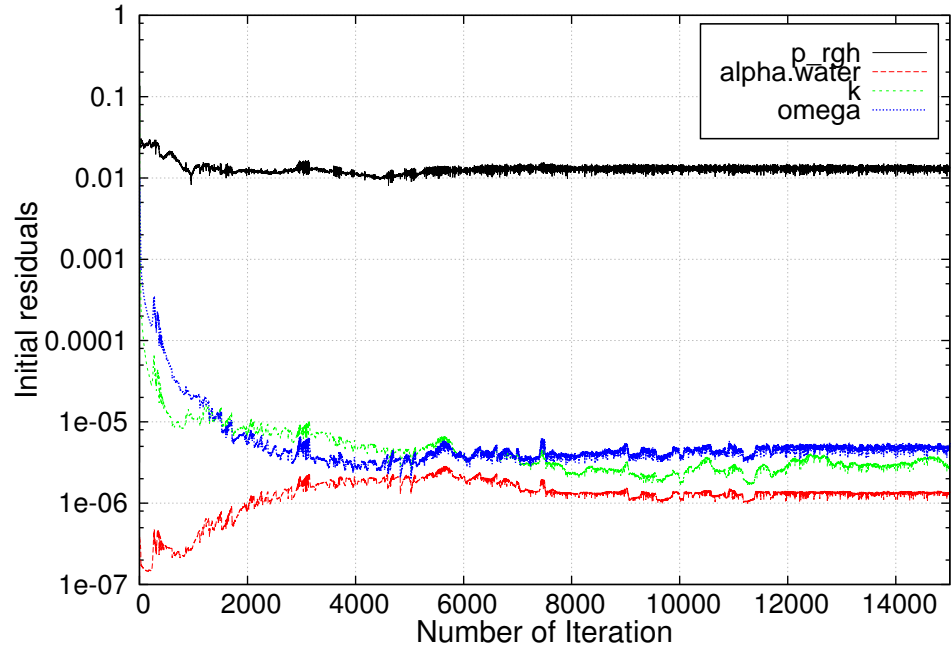


Figure 3.7: Residual convergence for GRID-C.

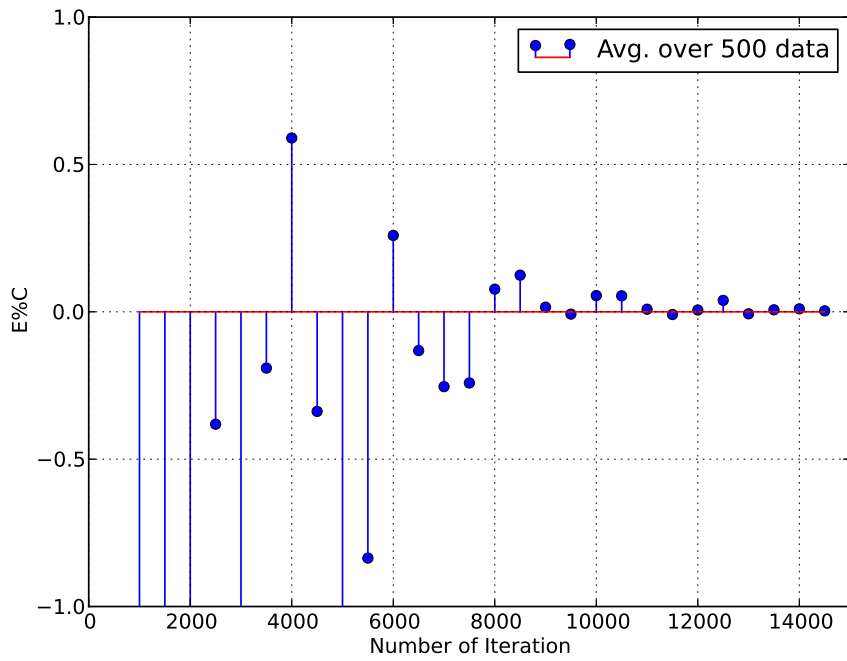


Figure 3.8: Convergence error for total resistance coefficient for GRID-C at $Fn = 0.26$.

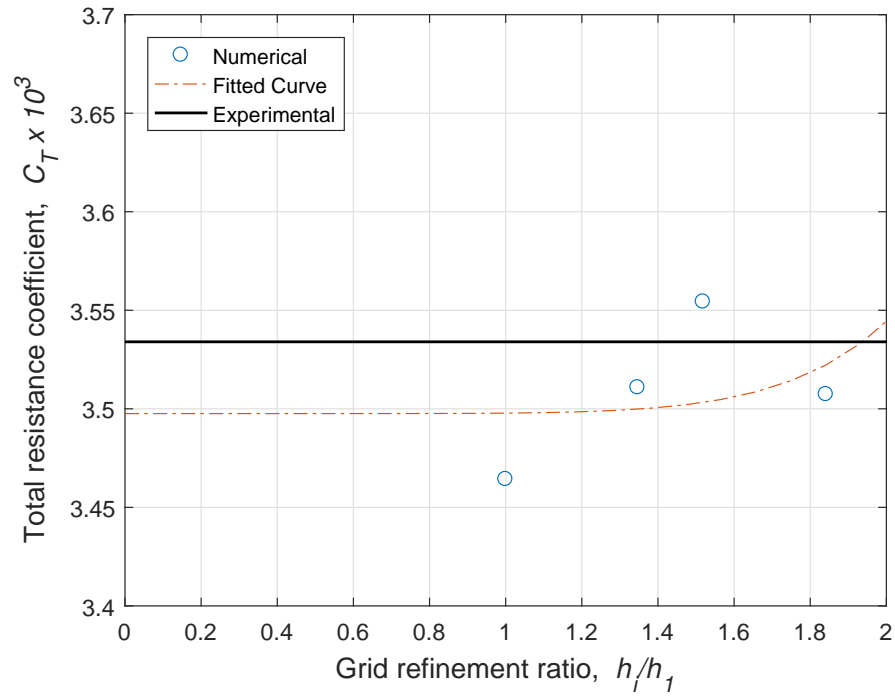


Figure 3.9: Numerical uncertainty of C_T at $F_n = 0.26$.

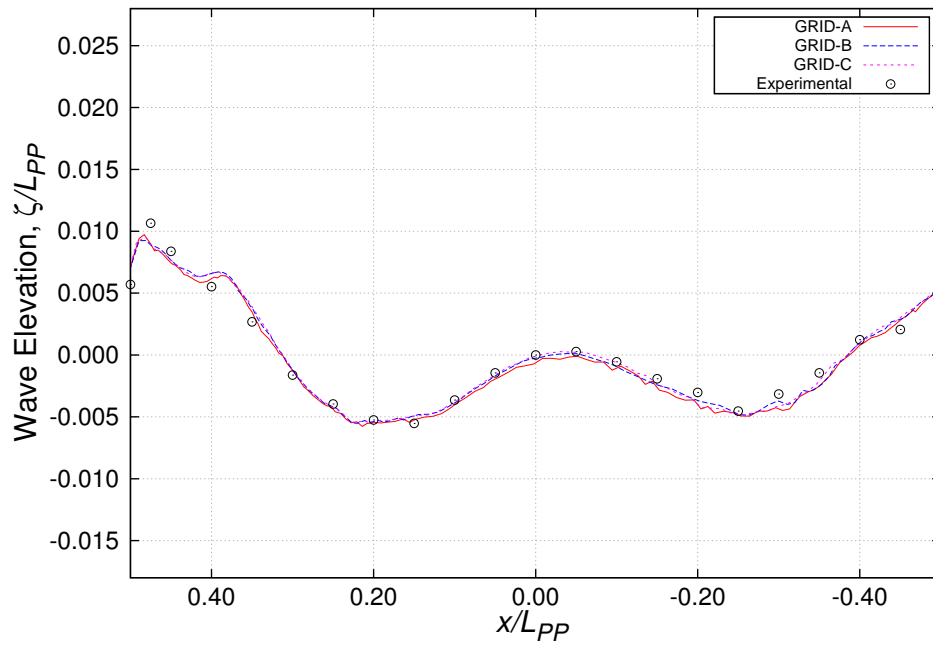
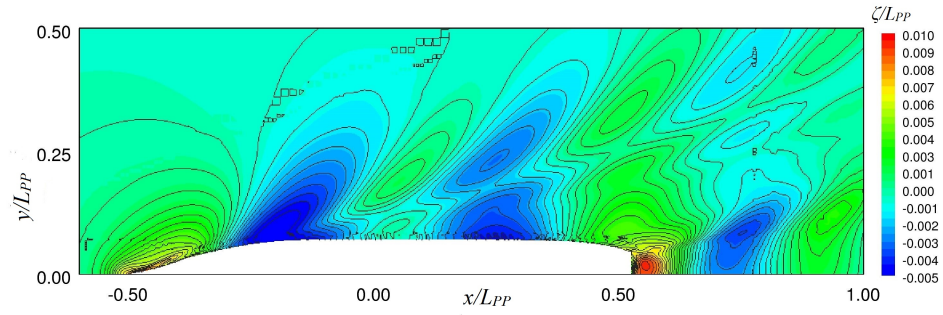
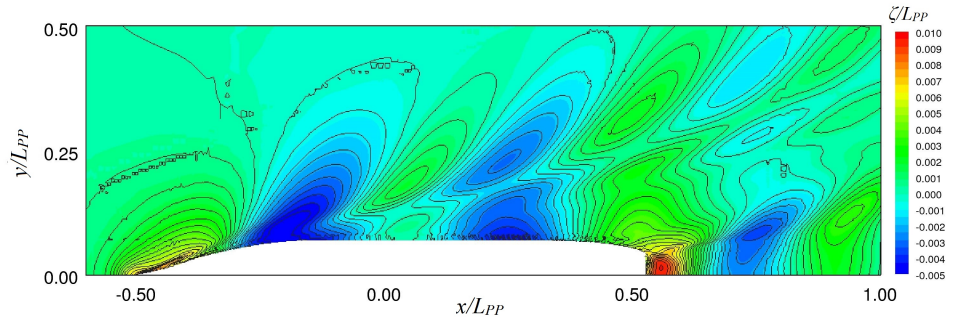


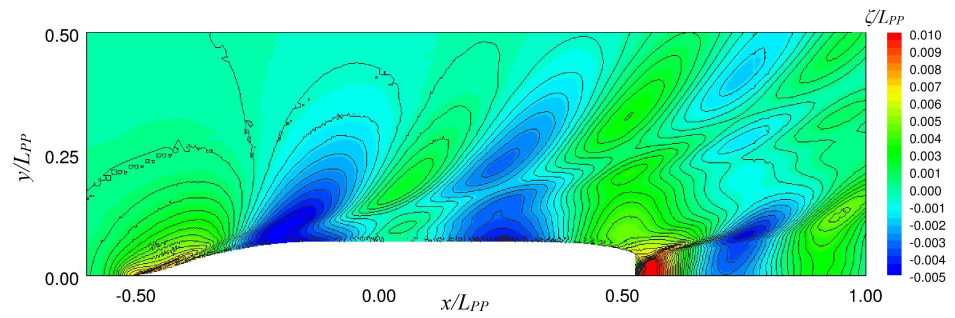
Figure 3.10: Wave elevation along the ship hull at $F_n = 0.26$.



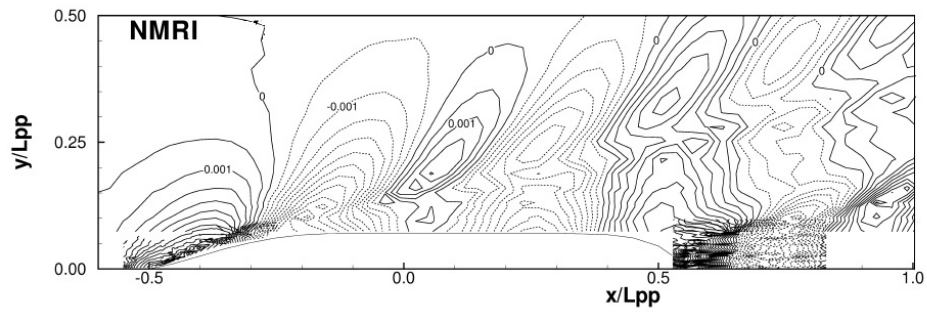
(a) GRID-A



(b) GRID-B



(c) GRID-C



(d) Experimental (NMRI)

Figure 3.11: Free surface wave pattern comparison at $Fn = 0.26$.

The validation error for resistance coefficients from the steady simulation are presented in Table 3.5. The validation error against the experimental data for the total resistance coefficient C_T is less than 2.0%. The uncertainty of the numerical results for the bare hull resistance is calculated using Least Squares Root (LSR) method. The fitted curve using LSR method is shown in Figure 3.9. The numerical uncertainties of the resistance components are also shown in Table 3.5. The numerical result obtained using GRID-C shows only 5% numerical uncertainty.

3.1.1.4 Free Surface Wave Contour

The numerically predicted wave elevations along the hull surface using three grids are compared with the experimental data for $Fn = 0.26$ in Figure 3.10. Although there is a small difference in the prediction for different grids, the overall numerical wave

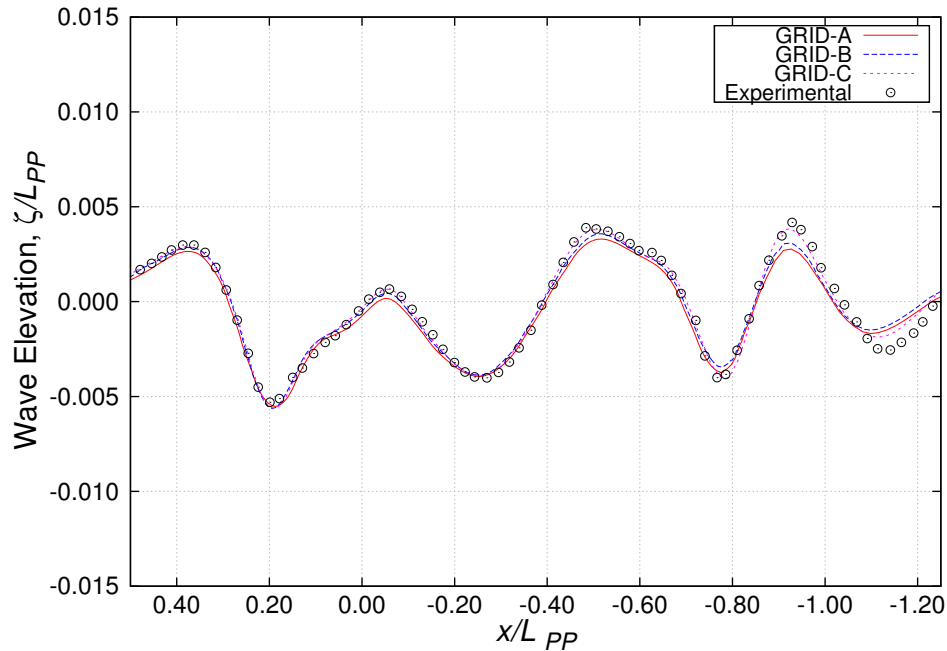


Figure 3.12: Wave elevation at $y/L_{PP} = 0.1024$

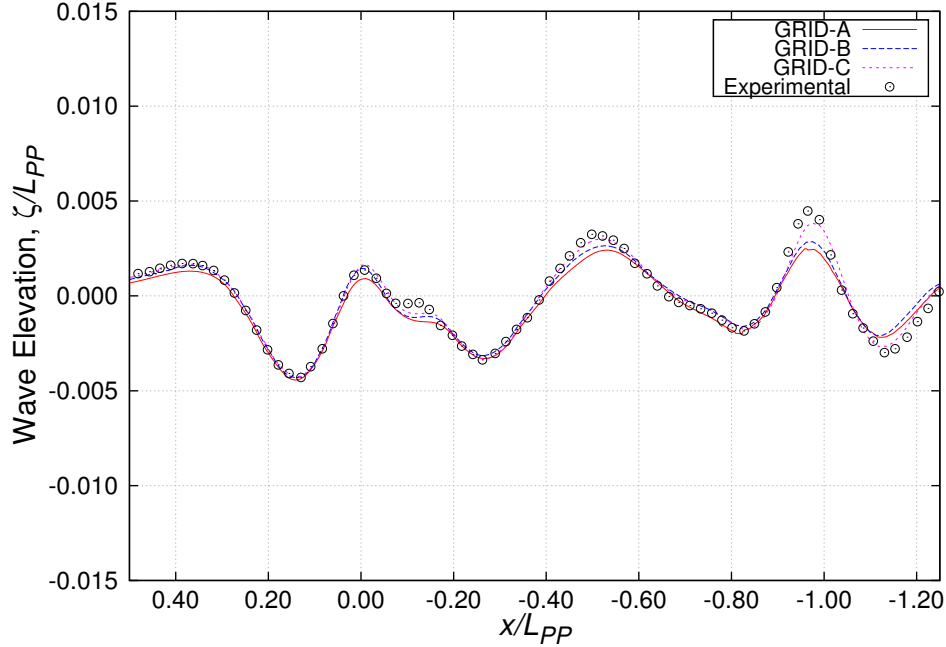


Figure 3.13: Wave elevation at $y/L_{PP} = 0.1509$

elevation agrees very well with the experimental data. The generated wave pattern on the free surface is also computed for different grids and is compared with the experimental results in Figure 3.11. From the figure, it is seen that small cell size, same as the minimum cell size on the hull surface is necessary to capture the free surface deformation behind the stern. The wave elevations at the four different transverse positions $y/L_{PP} = 0.10, 0.15, 0.30,$ and 0.40 are compared with the experimental data in Figures 3.12 to 3.15. The numerical wave prediction using GRID-C shows good agreement with the experimental results.

3.1.1.5 Flow Velocity

The axial flow velocity at the propeller plane is compared for the three grids with the experimental results in Figure 3.16. The wake fraction on the propeller plane is also compared with the experimental results. From the wake fraction comparison, it

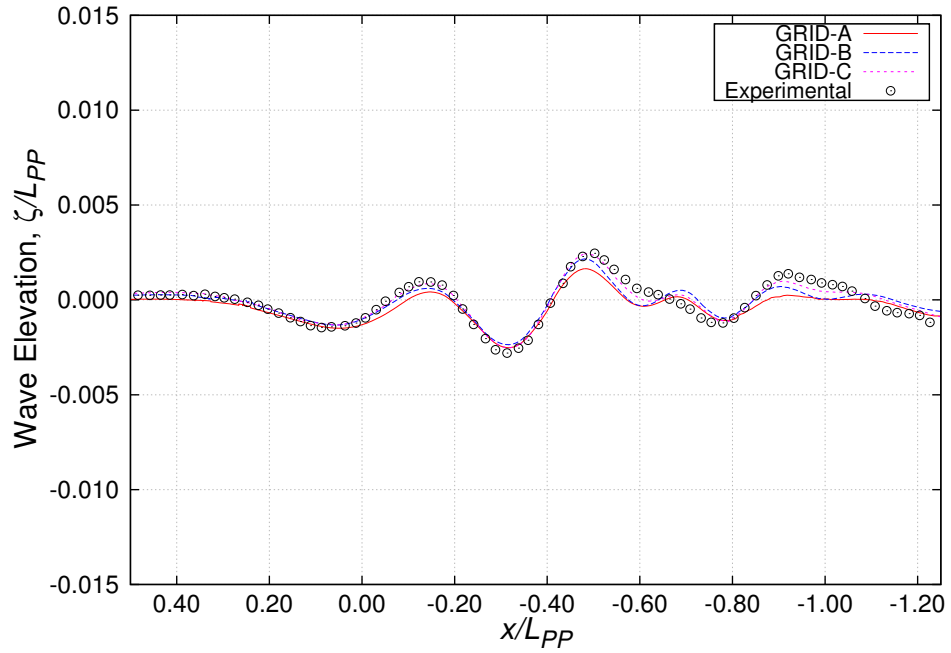


Figure 3.14: Wave elevation at $y/L_{PP} = 0.30$

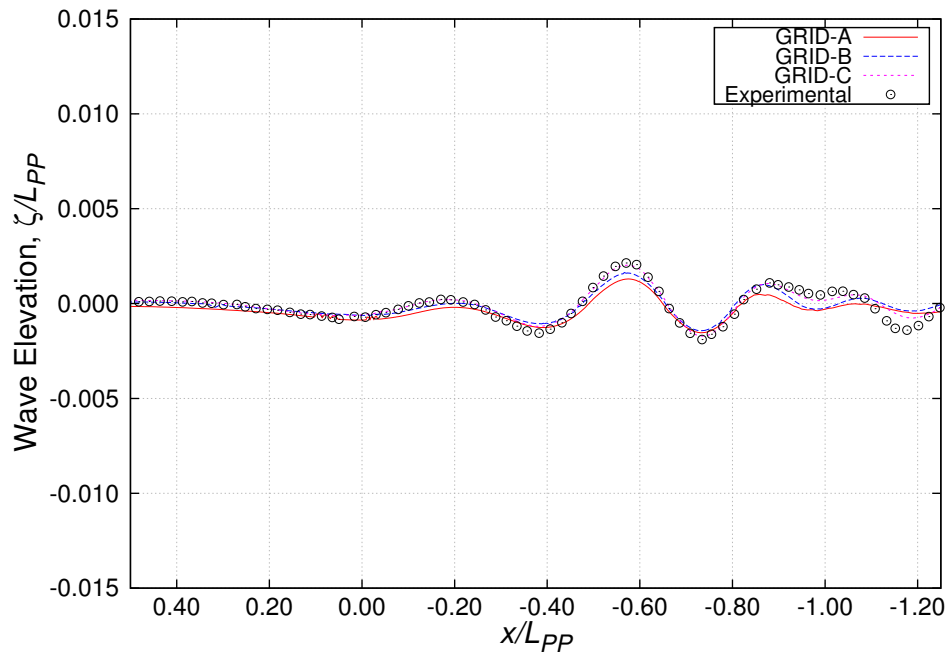


Figure 3.15: Wave elevation at $y/L_{PP} = 0.40$

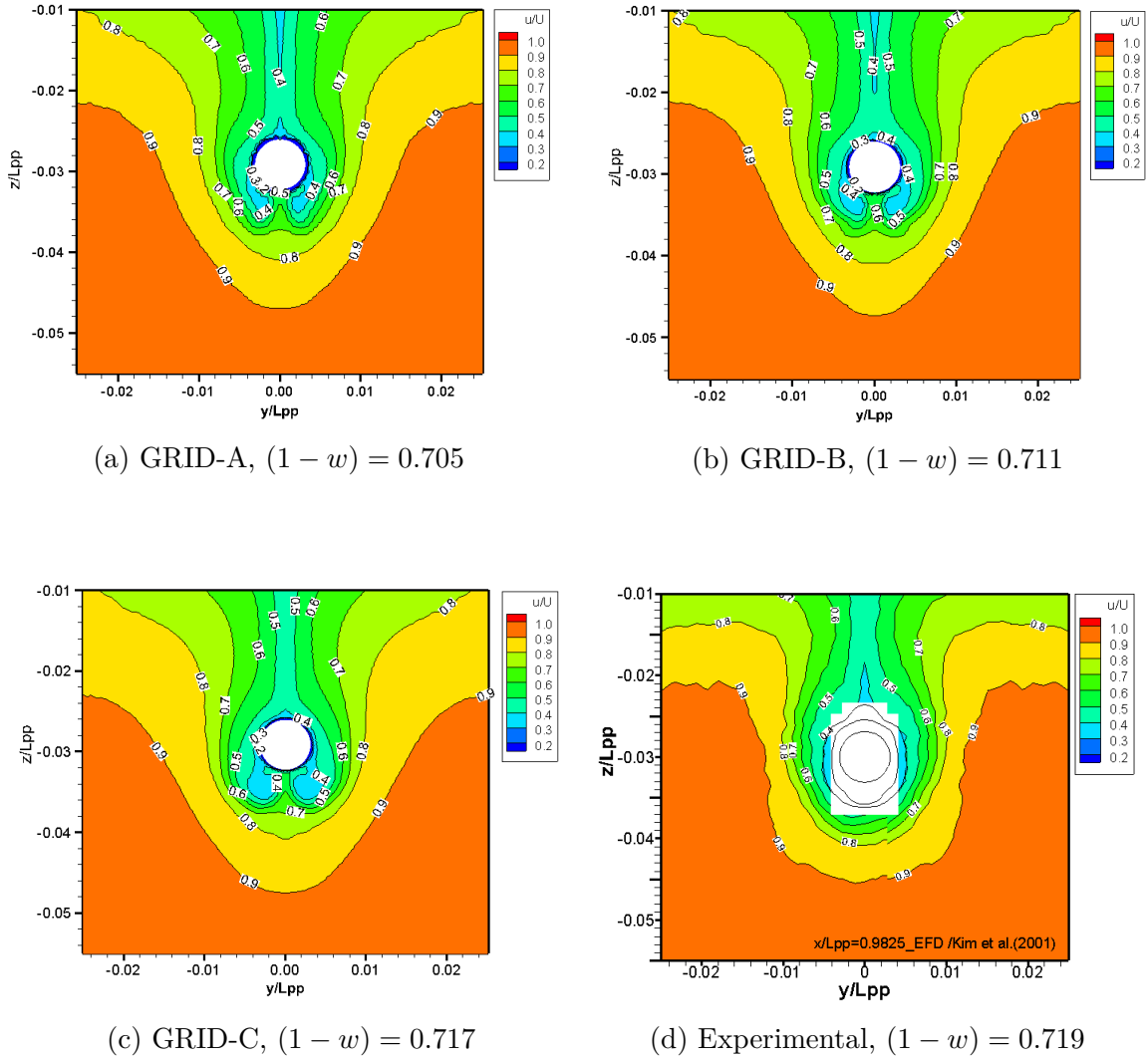


Figure 3.16: Axial flow velocity contour on the propeller plane at $F_n = 0.26$.

is seen that GRID-C predicts the wake fraction with more accuracy than the other grids. The numerical simulation shows two strong opposite vortices just below the stern bulb, which can not be confirmed because experimental data near the bulb are not available. The velocity components (u, v, w) are also compared on the propeller plane at $z/L_{PP} = -0.030$ in Figures 3.17, 3.18, and 3.19 respectively using all three computational grids. The velocity components predicted by GRID-C show best agreement with the experimental data.

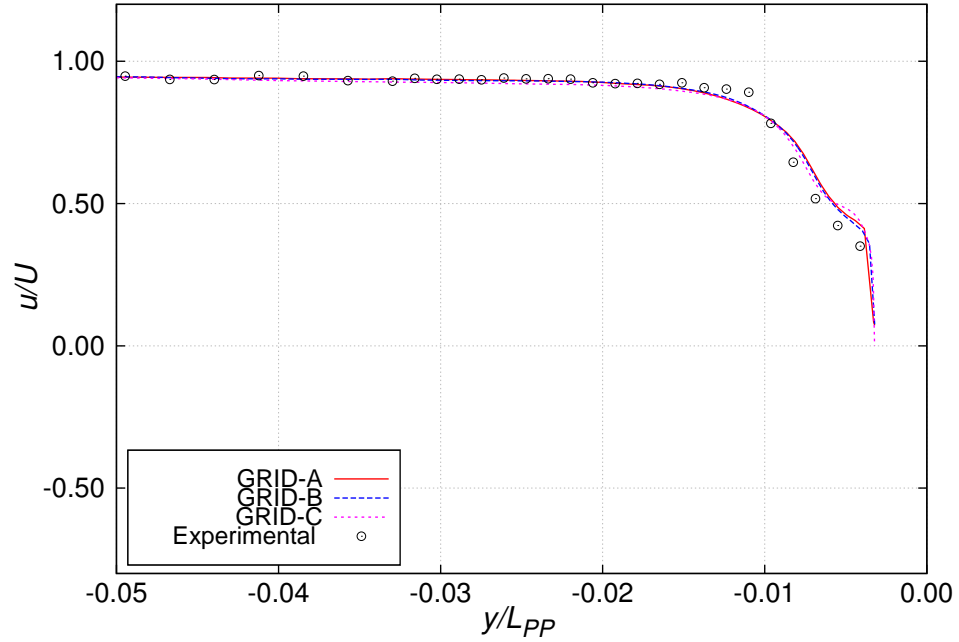


Figure 3.17: Axial flow velocity on the propeller plane at $z/L_{PP} = -0.03$.

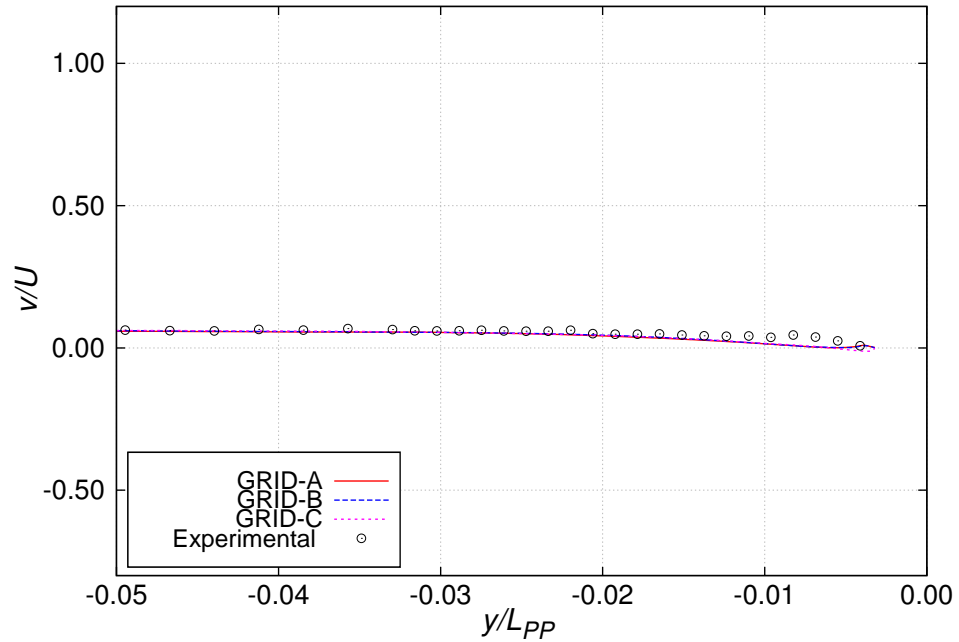


Figure 3.18: Transverse flow velocity on the propeller plane at $z/L_{PP} = -0.03$.

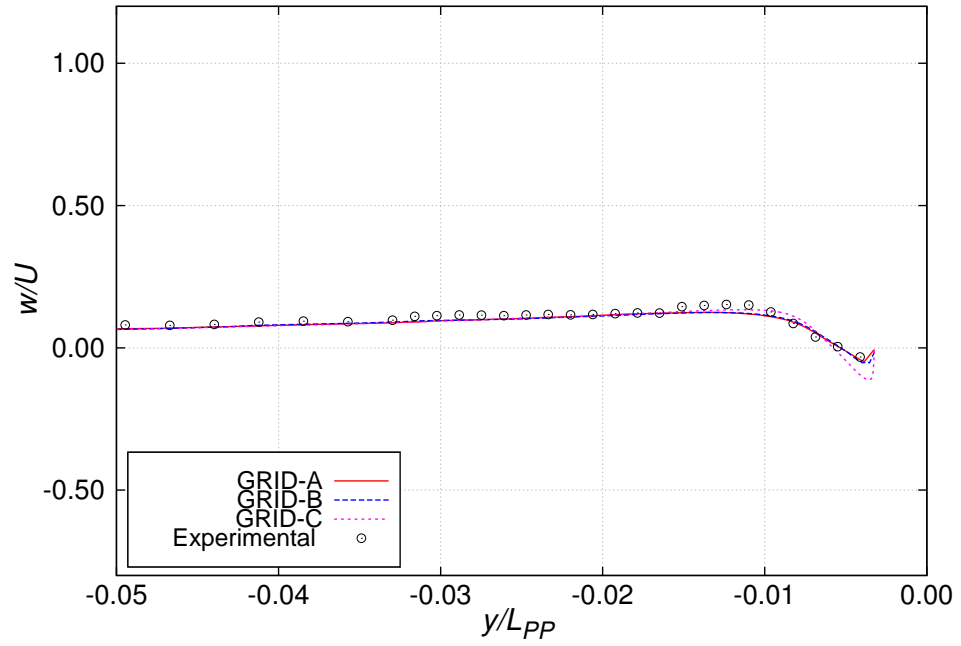


Figure 3.19: Vertical flow velocity on the propeller plane at $z/L_{PP} = -0.03$.

3.1.1.6 Effect of Turbulence Model

The effect of turbulence model on the resistance computation was investigated using $k-\omega$ SST, $k-\omega$ SST with curvature correction ($k-\omega$ SSTCC), and the Reynolds Stress Turbulence model LRR for GRID-C. The total resistance coefficient, free surface wave contour, wave elevation along the hull surface, and nominal wake were computed using GRID-C with different turbulence models. The numerical results were compared with the experimental results.

The comparison of total resistance coefficient for different turbulence models is shown in Table 3.6. The LRR turbulence model shows a larger deviation from the experimental results than $k-\omega$ SSTCC and $k-\omega$ SST turbulence models because the frictional resistance is over-predicted using RSM model. The effect of turbulence models on the wave elevation along the hull surface is compared in Figure 3.20. Different turbulence models predict the wave elevation with similar level of accuracy. The free surface wave contours are also compared with the experimental measurements in Figure 3.21. No significant difference in wave contours is observed for different turbulence models.

The axial velocity distribution for the different turbulence models is compared in Figure 3.22. From the comparison, it seems that the Reynolds Stress Turbulence model predicts the vortex more accurately, but without experimental data, it is

Table 3.6: Effect of turbulence model on total resistance for GRID-C

| GRID | C_P | C_F | C_T | $ E\%D $ |
|------------------|----------|----------|----------|----------|
| $k-\omega$ SST | 0.000788 | 0.002723 | 0.003511 | 0.66 |
| $k-\omega$ SSTCC | 0.000822 | 0.002823 | 0.003644 | 3.12 |
| LRR | 0.000779 | 0.003009 | 0.003788 | 7.19 |
| Experimental | | | 0.003534 | |

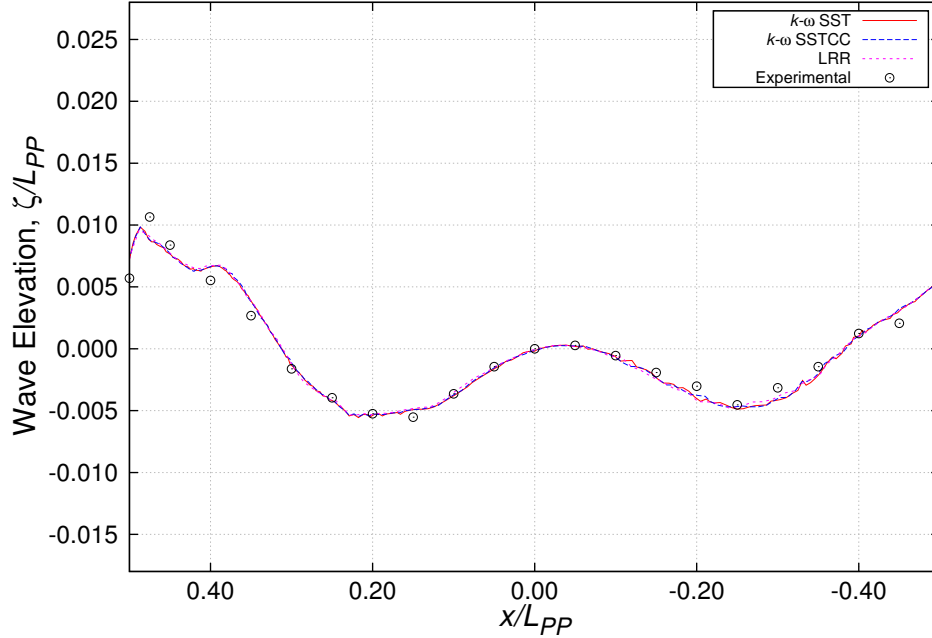
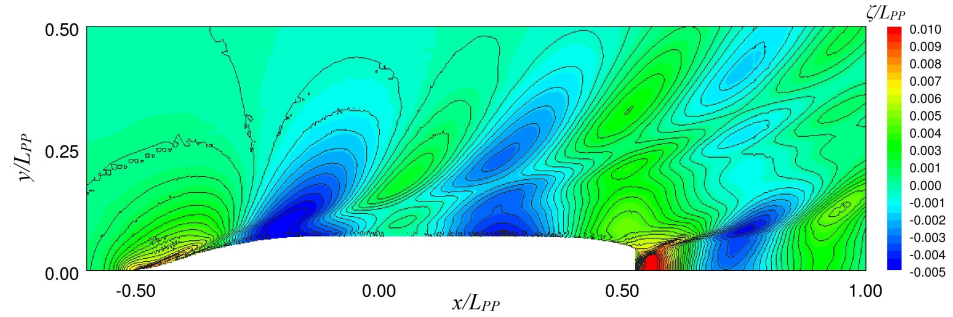


Figure 3.20: Effect of turbulence models on wave elevation along the hull surface for GRID-C.

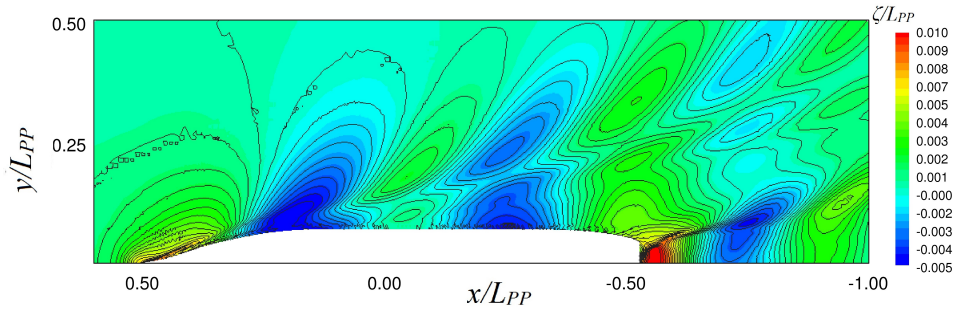
Table 3.7: RMS error of the velocity components for different turbulence models for GRID-C.

| Turbulence Model | u/U | v/U | w/U |
|--------------------|--------|--------|--------|
| $k - \omega$ SST | 0.0386 | 0.0108 | 0.0160 |
| $k - \omega$ SSTCC | 0.0311 | 0.0147 | 0.0184 |
| LRR | 0.0357 | 0.0190 | 0.0183 |

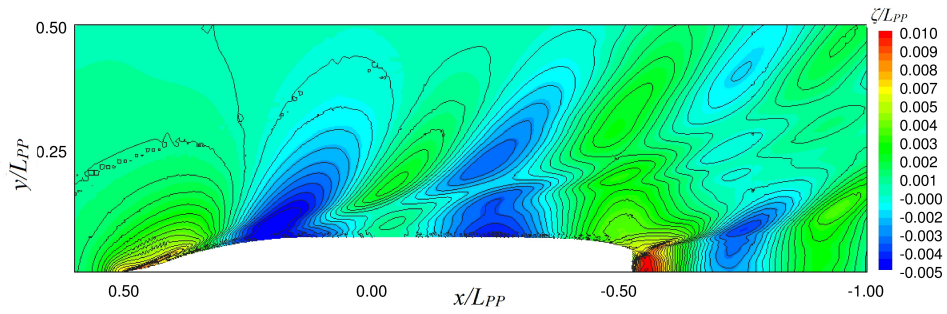
difficult to draw specific conclusions because the Reynolds Stress model under predicts the nominal wake fraction relative to the $k - \omega$ SSTCC model. Figures 3.23, 3.24 and 3.25 show the comparison of the velocity components (u, v, w) on the propeller plane at $z/L_{PP} = -0.030$. The *RMS* errors are compared for predicted velocity components using different turbulence models in Table 3.7. The $k - \omega$ SSTCC turbulence model shows minimum error for axial velocity component, whereas $k - \omega$ SST turbulence model presents minimum error for both transverse and vertical velocity components.



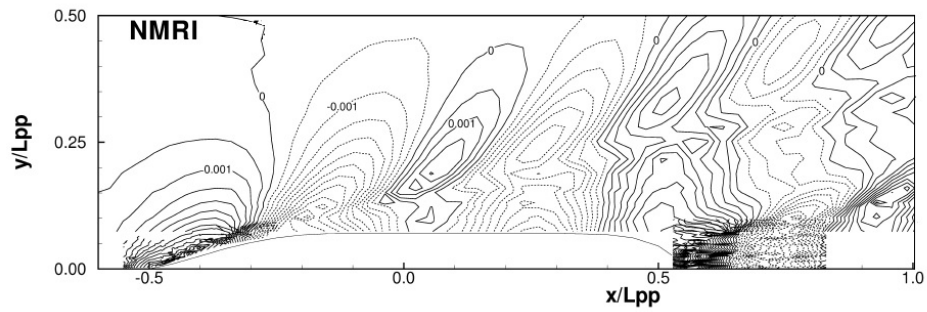
(a) $k - \omega$ SST Model.



(b) $k - \omega$ SSTCC Model.

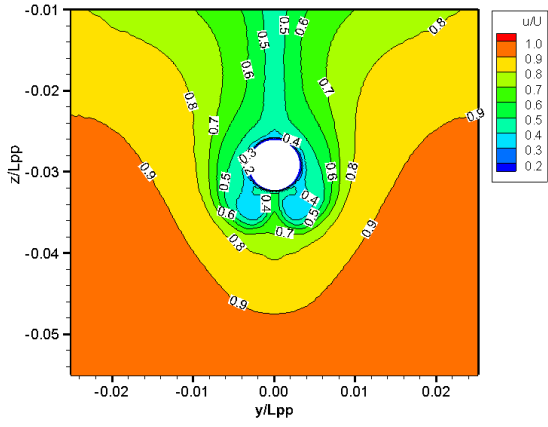


(c) LRR Model.

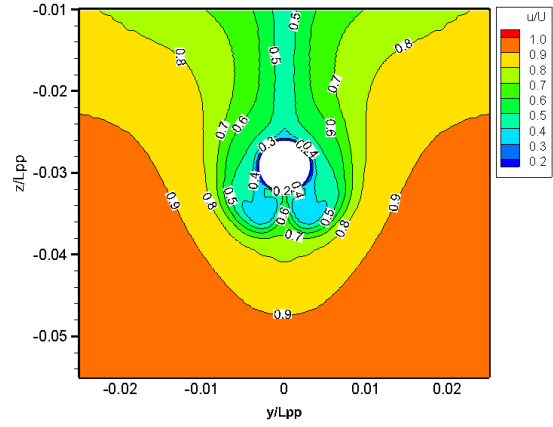


(d) Experimental (NMRI).

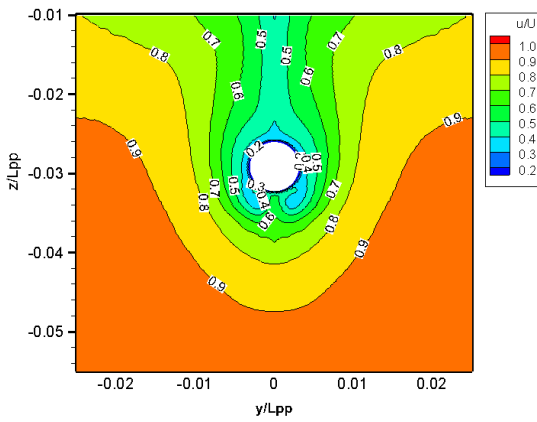
Figure 3.21: Effect of turbulence models on free surface wave pattern for GRID-C.



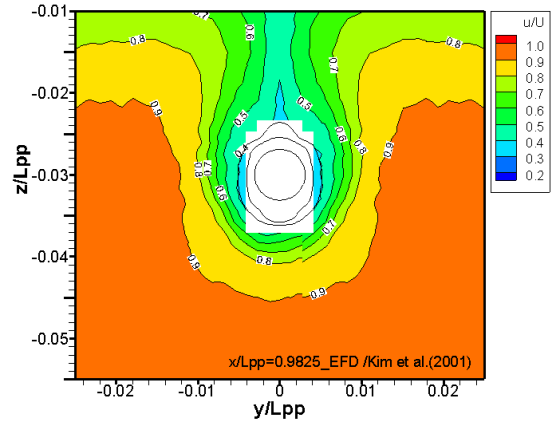
(a) $k - \omega$ SST, $(1 - w) = 0.720$.



(b) $k - \omega$ SSTCC, $(1 - w) = 0.717$.



(c) LRR, $(1 - w) = 0.711$.



(d) Experimental, $(1 - w) = 0.719$.

Figure 3.22: Axial flow velocity contour on the propeller plane using different turbulence models for GRID-C.

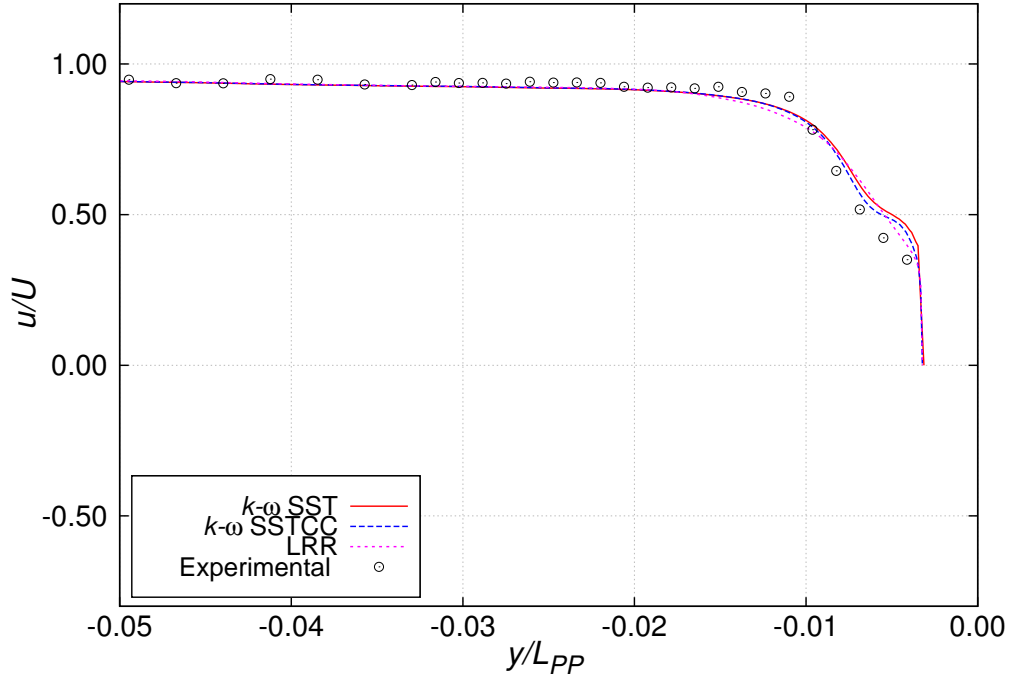


Figure 3.23: Effect of turbulence model on axial flow velocity on the propeller plane at $z/L_{PP} = -0.03$ for GRID-C.

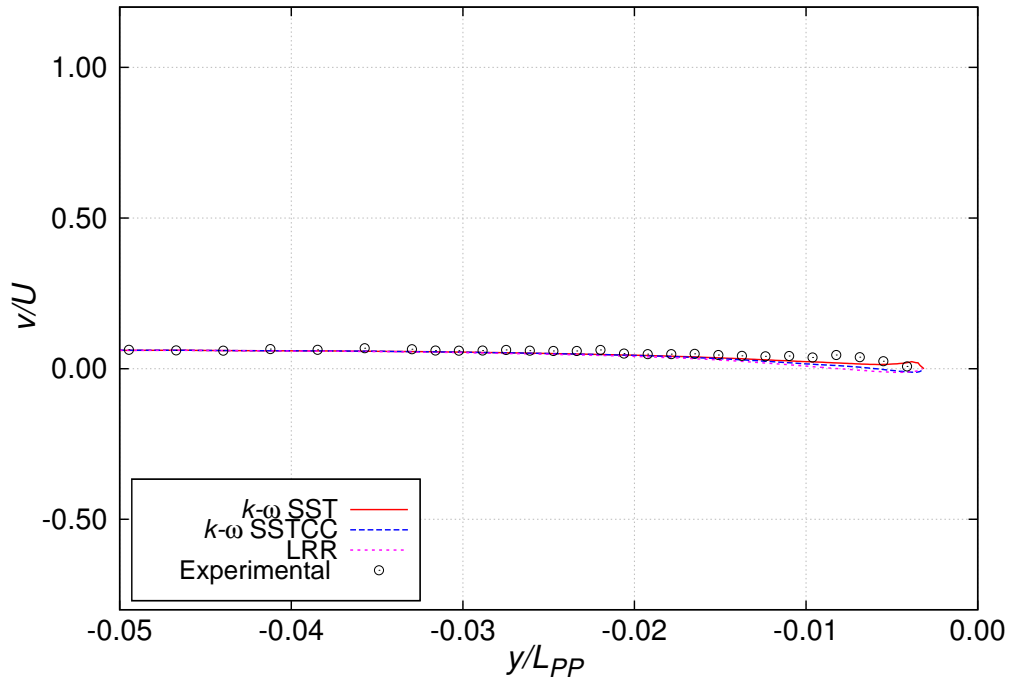


Figure 3.24: Effect of turbulence model on transverse flow velocity on the propeller plane at $z/L_{PP} = -0.03$ for GRID-C.

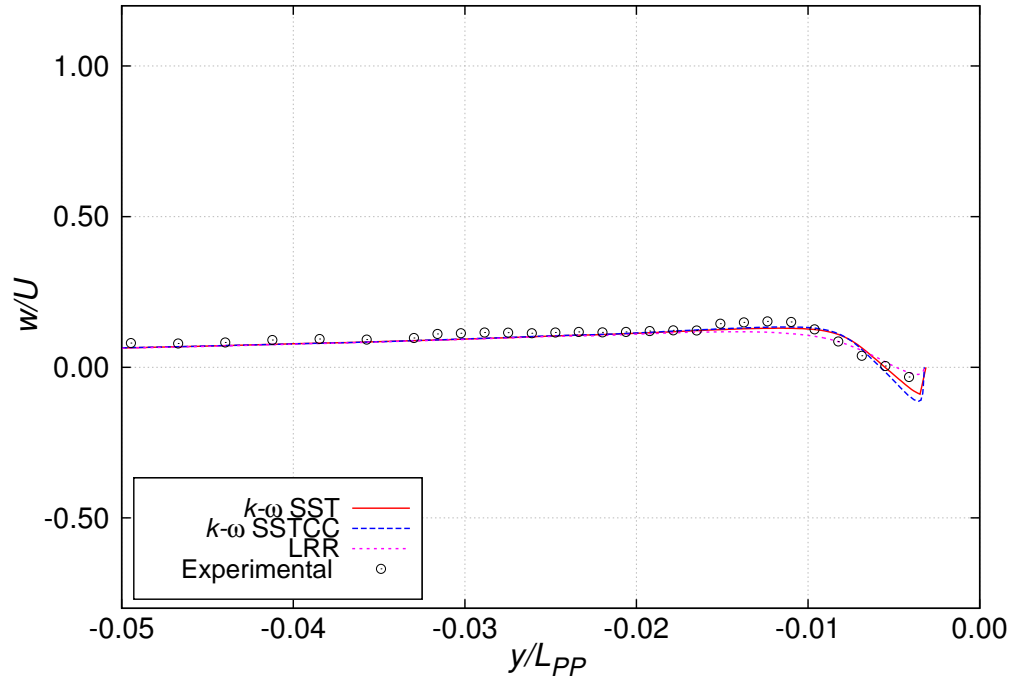


Figure 3.25: Effect of turbulence model on vertical flow velocity on the propeller plane at $z/L_{PP} = -0.03$ for GRID-C.

3.1.2 Japan Bulk Carrier

3.1.2.1 Geometry and Test Conditions

The geometry file for the JBC hull was obtained from the T2015 workshop website as an IGES file. Figure 3.26 shows the hull surface for the resistance validation of the JBC. The principal particulars of the JBC hull at full scale and model scale are shown in Table 3.8.

The CFD simulation conditions were set to be the same as the test conditions determined by the T2015 organizing committee. The model tests were carried out for resistance, sinkage and trim for the JBC hull at Froude number, $Fn = 0.142$. All tests were carried out without rudder. Since the propeller has an overlapping area with the Energy Saving Device (ESD), the test cases without ESD were considered for this comparison. The test conditions for resistance, sinkage, trim, and mean flow are listed in Table 3.9.

3.1.2.2 Computational Domain and Grid Generation

The computational domain for the numerical simulation of the JBC hull was also created using the ITTC guidelines (ITTC, 2011) for CFD simulation of bare hull



Figure 3.26: JBC bare hull geometry.

Table 3.8: Principal particulars of the JBC hull.

| Parameters | Full scale | Model Scale | Unit |
|------------------------------------|------------|-------------|----------------|
| Length, L_{PP} | 280.00 | 7.000 | m |
| Length, L_{WL} | 285.00 | 7.125 | m |
| Breadth, B | 45.00 | 1.125 | m |
| Depth, D | 25.00 | 0.625 | m |
| Draft, T | 16.50 | 0.4125 | m |
| Displacement, ∇ | 178369.90 | 2.787 | m ³ |
| Wetted surface w/o ESD, S_W | 19556.10 | 12.223 | m ² |
| Wetted surface of ESD, S_{ESD} | 745.20 | 0.466 | m ² |
| Block coefficient, C_B | 0.8580 | 0.8580 | |
| Midship section coefficient, C_M | 0.9981 | 0.9981 | |
| $L_{CB}(\%L_{PP}).fwd+$ | 2.5475 | 2.5475 | |
| VCG | 13.29 | 0.3323 | m |
| Design speed, Fn | 0.142 | 0.142 | |

Table 3.9: JBC test cases considered for validation of numerical results.

| | |
|----------------------|---|
| Case | 2.1 |
| Loading condition | Design full |
| Wave | Calm |
| Condition | Towing |
| ESD | W/O |
| Rudder | without |
| Propeller | without |
| Attitude | sinkage & trim |
| Validation variables | Resistance, Mean velocity sinkage and trim wave pattern, turbulence |
| EFD provider | NMRI |

Table 3.10: Computational grid for JBC bare hull simulation.

| GRID | Base cell size (m) | h | h_i/h_1 | No. of cells | Average, y^+ |
|--------|--------------------|--------|-----------|--------------|----------------|
| GRID-A | 1.00 | 0.1511 | 2.50 | 648657 | 42.53 |
| GRID-B | 0.67 | 0.1094 | 1.81 | 1707903 | 43.13 |
| GRID-C | 0.50 | 0.0811 | 1.34 | 4203020 | 54.77 |
| GRID-D | 0.33 | 0.0604 | 1.00 | 10132950 | 57.71 |

resistance. A schematic diagram of the computational domain is shown in Figure 3.27. The boundaries were placed in the same way as the KCS model computational domain. The grids were also generated using `navalSnappyHexMesh` in OpenFOAM with local grid refinement. The grid distribution around the JBC hull is shown in Figure 3.28. Four sets of grids were generated to study the bare hull resistance of the JBC hull using the unsteady solver. The grid parameters are listed in Table 3.10.

3.1.2.3 Resistance Validation

The bare hull resistance, sinkage and trim of the JBC hull were calculated using the unsteady multiphase solver *interDyMFoam*. The model was allowed for sinkage and trim only. The calculated resistance coefficients, sinkage and trim are compared with the experimental data in Table 3.11 for Froude number, $Fn = 0.142$. The validation error for total resistance coefficient, and sinkage for GRID-C is smaller than the other grids. For trim, the validation error for GRID-C is higher than the other grids. The overall prediction using GRID-C shows good agreement. The numerical uncertainty for C_T , sinkage and trim is presented in Table 3.12. The uncertainty for C_T and trim obtained using GRID-C is around 10%. Whereas, for trim the uncertainty is just less than 3% of the numerical results. The uncertainty calculation shows good convergence for C_T and trim. In the following subsection the numerical results for the first three grids are presented.

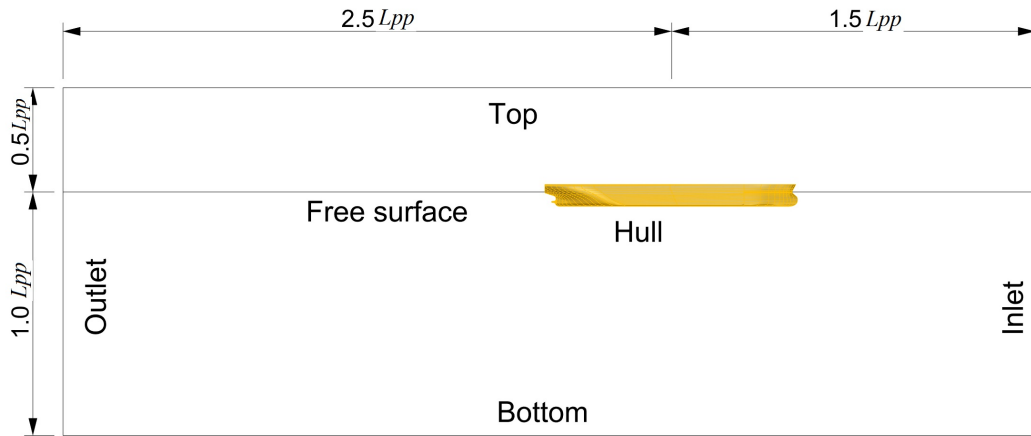


Figure 3.27: Computational domain of JBC hull.

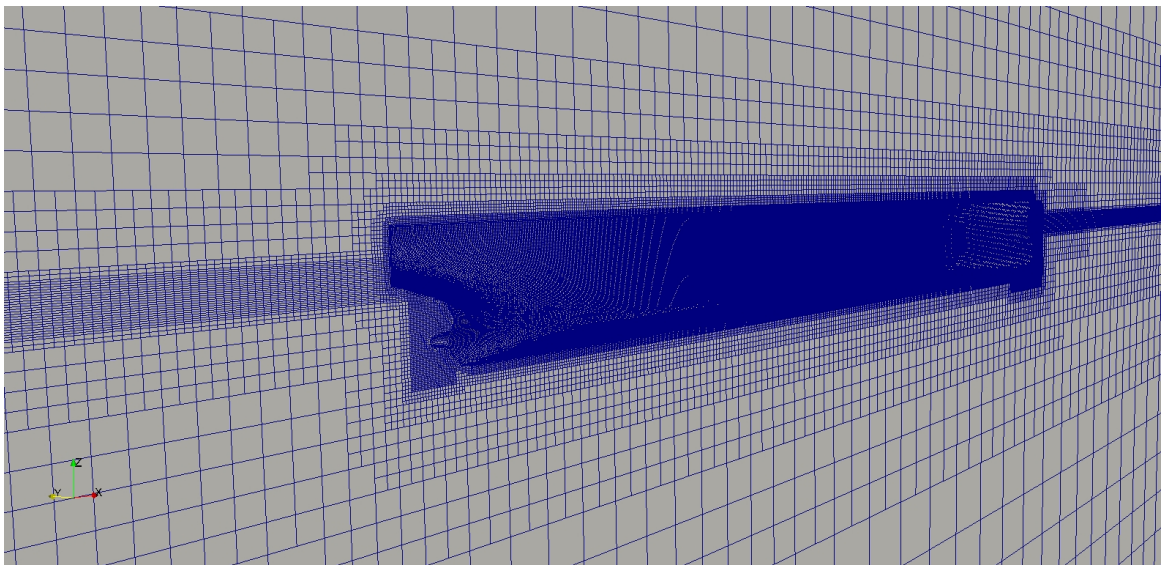


Figure 3.28: Grid distribution around the JBC hull.

3.1.2.4 Free Surface Wave Contour

The wave elevation along the hull surface was computed using three grids at $Fn = 0.142$. The numerical results are compared with the experimental values in Figure 3.33. The numerical results show good agreement with the experimental data. The free surface wave contours for the three grids are also compared with the experimental

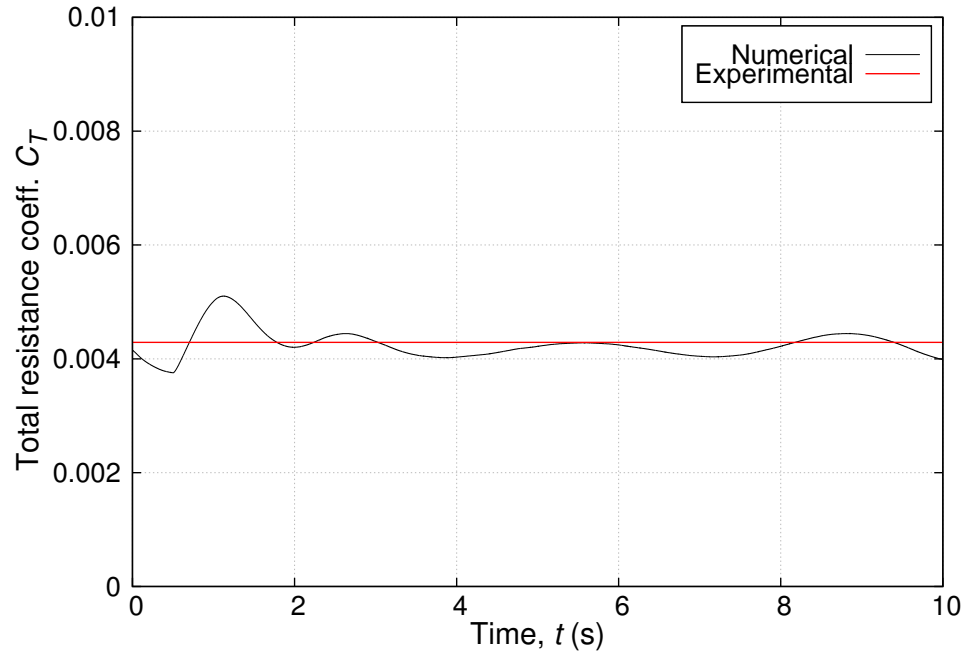


Figure 3.29: Convergence of C_T for GRID-C at $Fn = 0.142$.

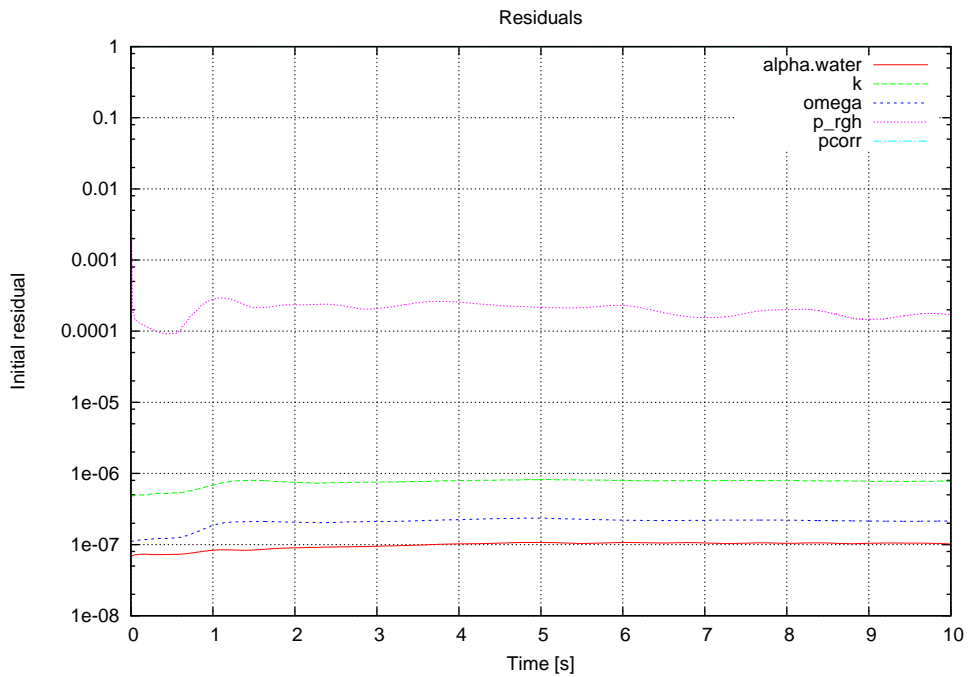


Figure 3.30: Time history of residuals convergence for GRID-C.

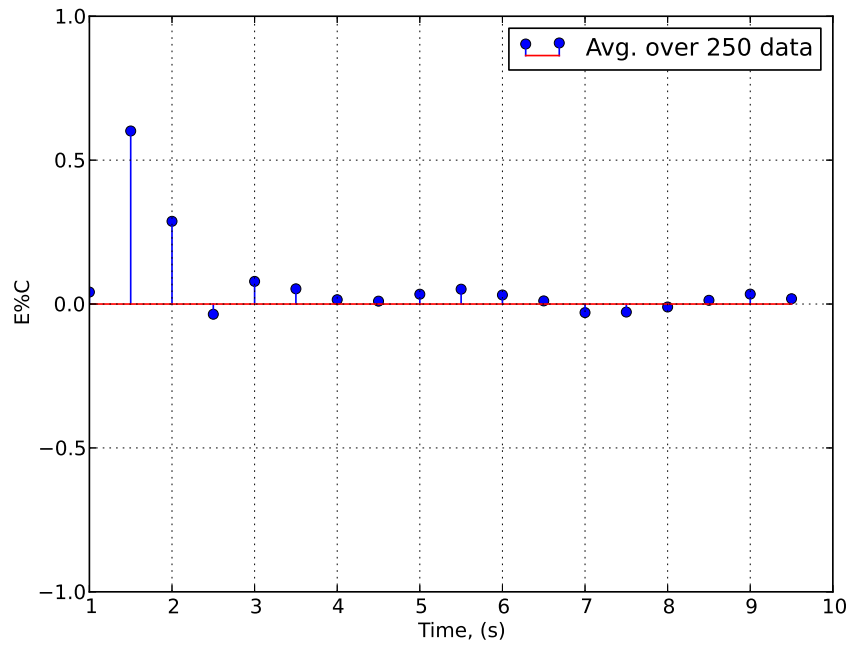


Figure 3.31: Convergence error of C_T for GRID-C at $Fn = 0.142$.

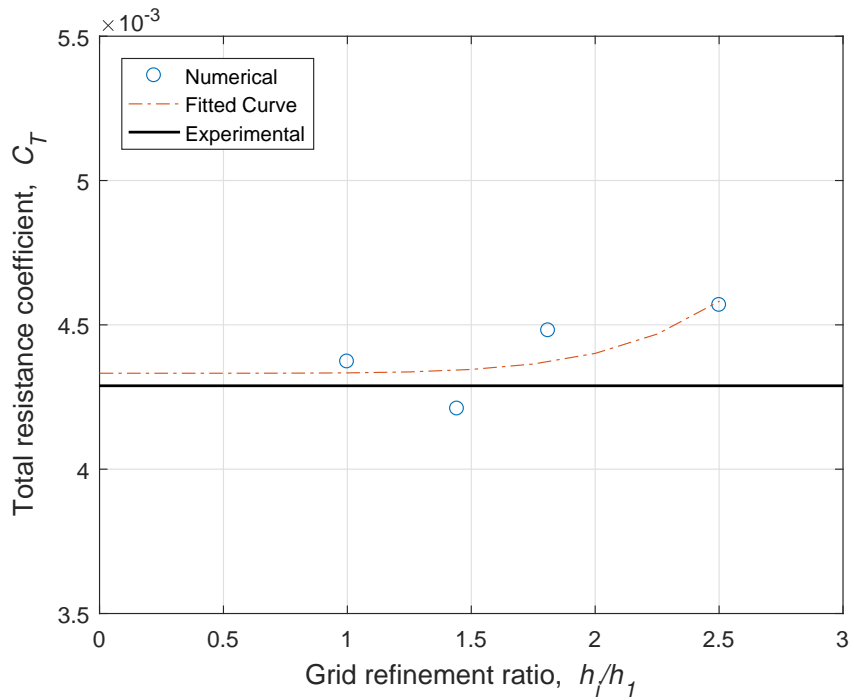


Figure 3.32: Grid uncertainty for C_T at $Fn = 0.142$.

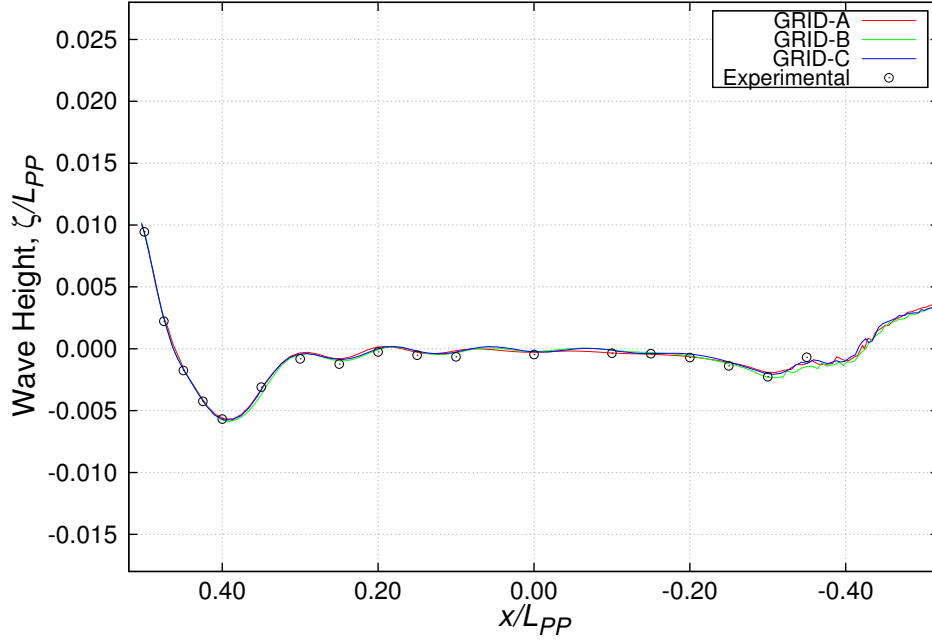


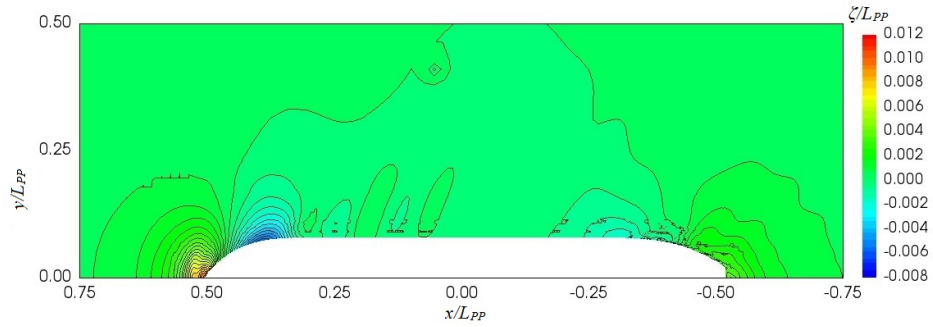
Figure 3.33: Wave elevation along the ship hull.

Table 3.11: Grid dependency of C_T , sinkage and trim at $Fn = 0.142$.

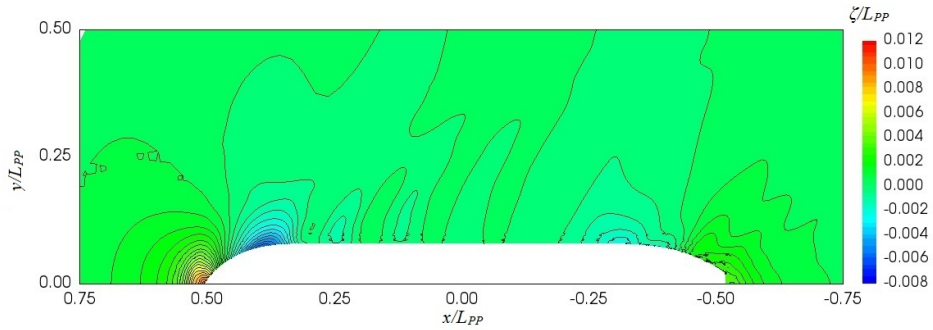
| GRID | C_T | $ E\%D $ | Sinkage (m) | $ E\%D $ | Trim (deg) | $ E\%D $ |
|--------|---------|----------|-------------|----------|------------|----------|
| GRID-A | 0.00457 | 6.50 | -0.00548 | 8.98 | 0.10807 | 4.78 |
| GRID-B | 0.00448 | 4.45 | -0.00563 | 6.53 | 0.10742 | 6.66 |
| GRID-C | 0.00421 | 1.86 | -0.00651 | 7.97 | 0.11130 | 7.92 |
| GRID-D | 0.00437 | 1.93 | -0.00586 | 2.65 | 0.10907 | 5.75 |
| Exp. | 0.00429 | | -0.00602 | | 0.10313 | |

Table 3.12: Comparison of $|U_{SN}\%S|$ for C_T , sinkage and trim at $Fn = 0.142$.

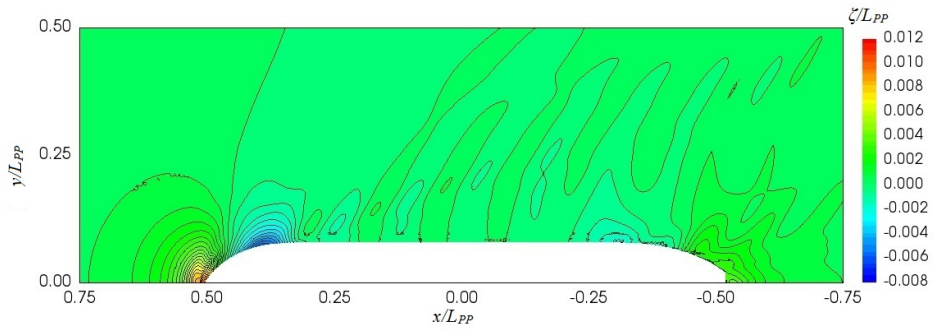
| GRID | h_i/h_1 | C_T | Sinkage | Trim |
|--------|-----------|-------|---------|------|
| GRID-A | 2.50 | 23.32 | 3.09 | 0.14 |
| GRID-B | 1.81 | 13.76 | 8.47 | 1.87 |
| GRID-C | 1.34 | 9.34 | 9.10 | 2.17 |
| GRID-D | 1.00 | 6.24 | 10.51 | 2.32 |



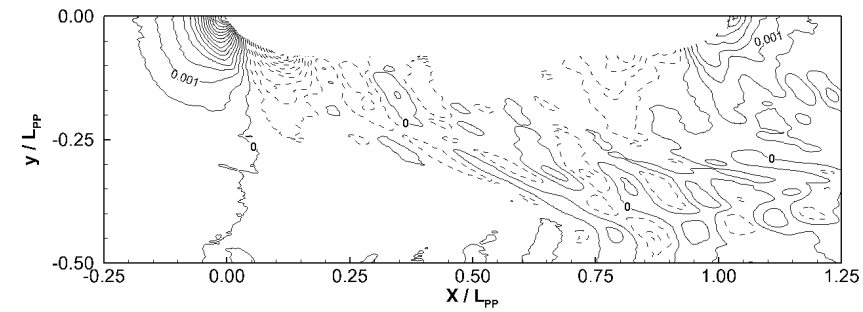
(a) GRID-A



(b) GRID-B



(c) GRID-C



(d) Experimental (NMRI)

Figure 3.34: Free surface wave pattern comparison at $Fn = 0.142$.

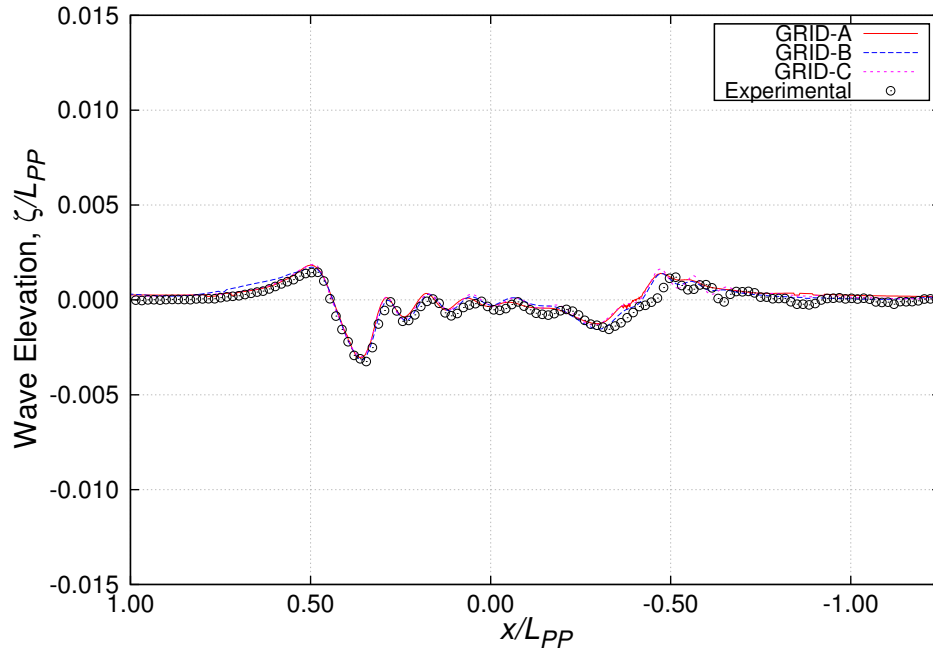


Figure 3.35: Wave elevation at $y/L_{PP} = 0.1043$ at $Fn = 0.142$.

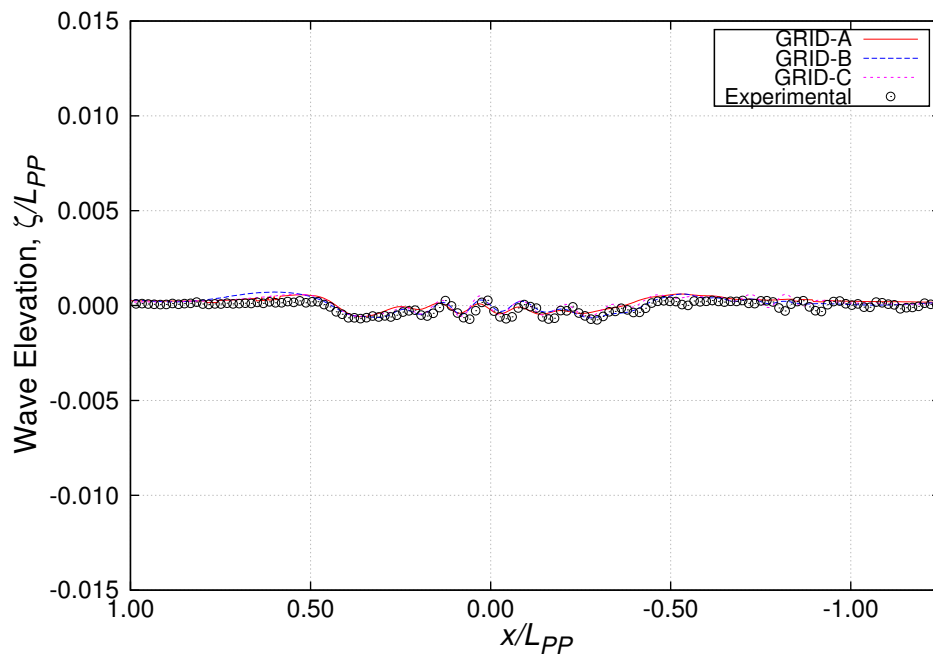


Figure 3.36: Wave elevation at $y/L_{PP} = 0.1900$ at $Fn = 0.142$.

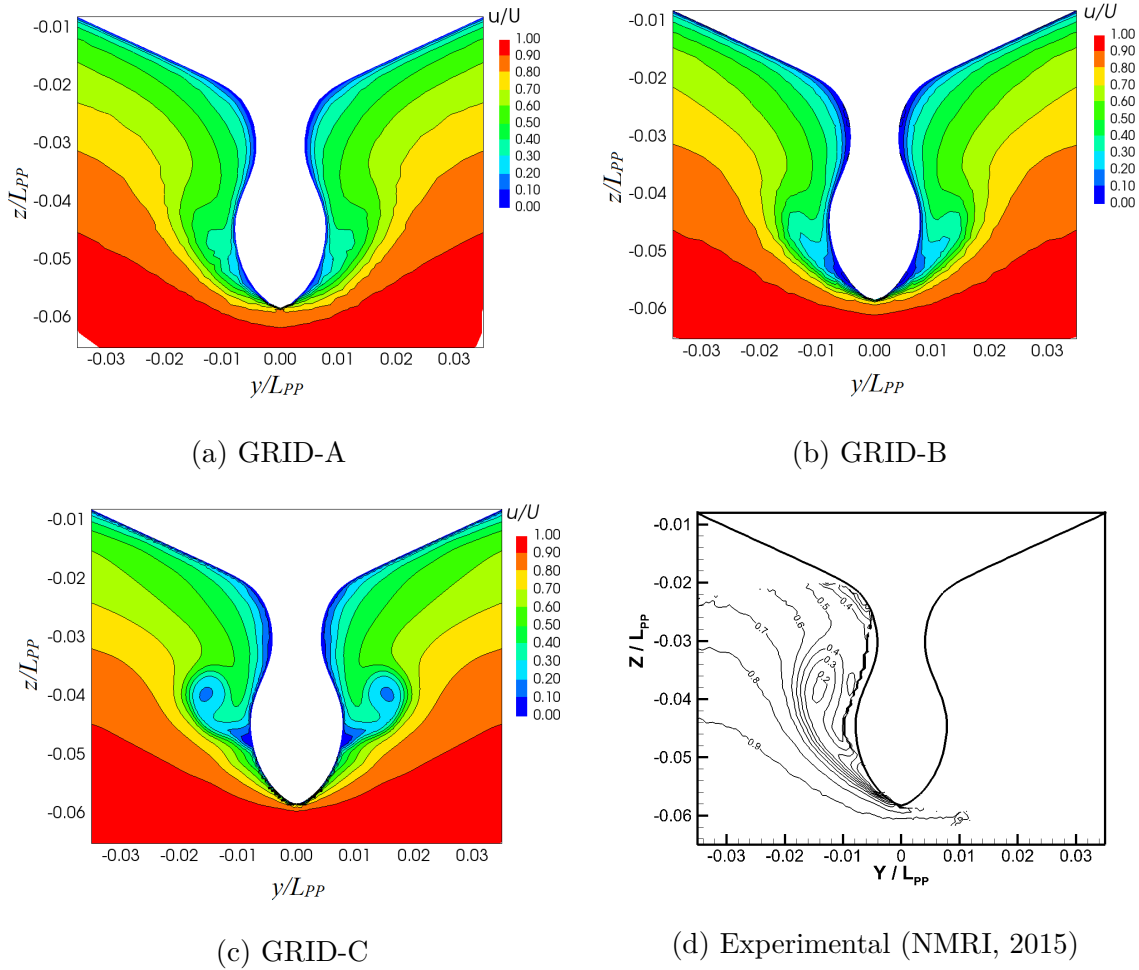


Figure 3.37: Axial flow velocity contour on $x/L_{PP} = 0.9625$ for $Fn = 0.142$.

data in Figure 3.34. It is observed that GRID-C predicts the wave contour with more accuracy than the other two grids.

The numerical wave elevations at two longitudinal wave cut locations $y/L_{PP} = 0.1043$ and $y/L_{PP} = 0.19$ are compared in Figure 3.35 and 3.36 for different grid densities. Although the overall comparison shows good agreement for GRID-C, a small difference is observed at $y/L_{PP} = 0.1043$ near $x/L_{PP} = 0.5$. However a better prediction is observed at $y/L_{PP} = 0.19$.

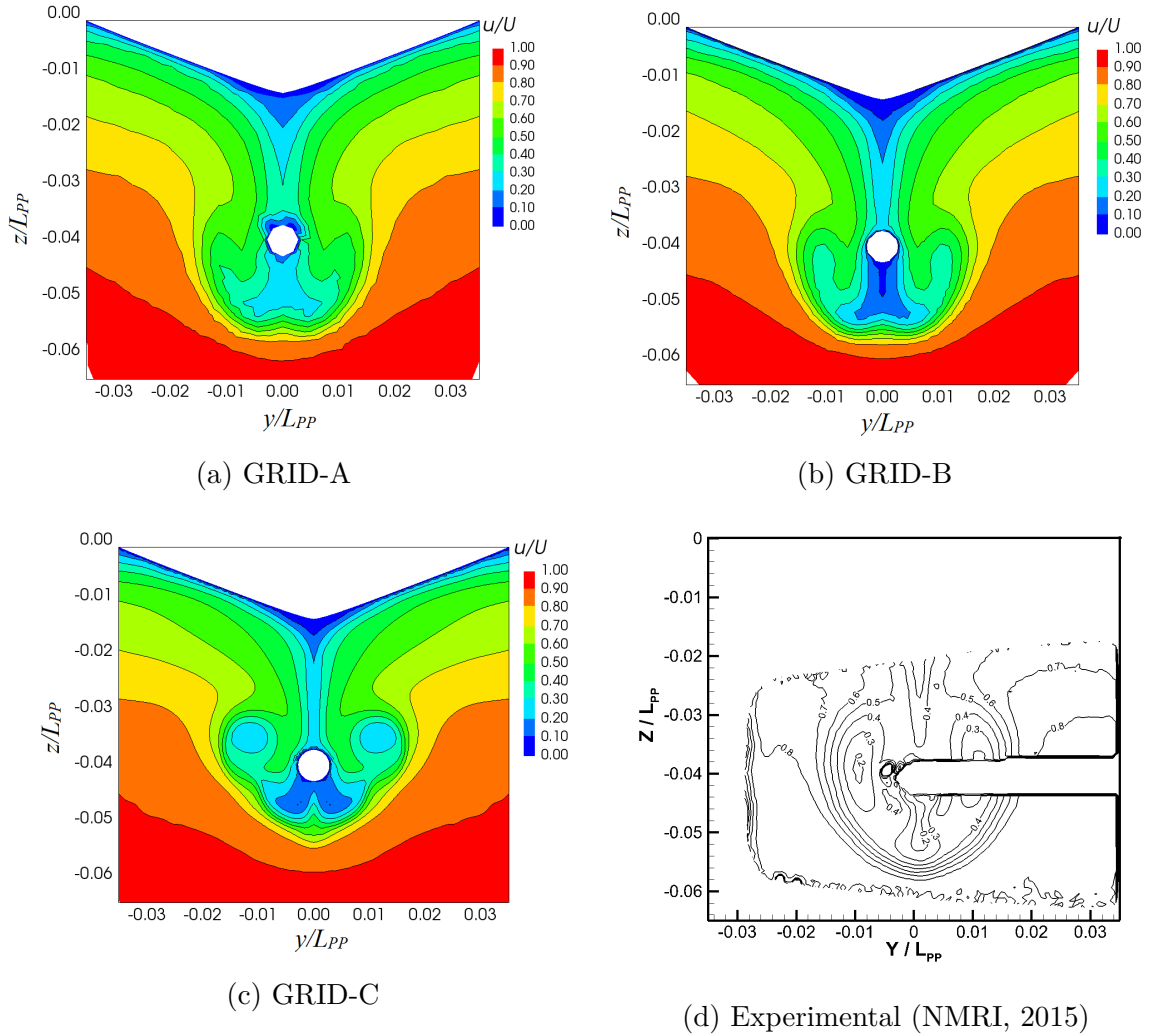


Figure 3.38: Axial flow velocity contour on $x/L_{PP} = 0.9843$ for $Fn = 0.142$.

3.1.2.5 Flow Velocity

The normalized axial velocity at three different longitudinal positions $x/L_{PP} = 0.9625$, 0.9843 and 1.00 were computed using $k-\omega$ SSTCC turbulence model for $Fn = 0.142$. Comparison is made with the experimental data from NMRI. Figure 3.37 shows the comparison at $x/L_{PP} = 0.9625$ for the different grid resolutions. The hull vortex is captured quite well with GRID-C, but the vortex is stretched-out from the center plane. A similar phenomenon is observed for the axial velocity contour at $x/L_{PP} =$

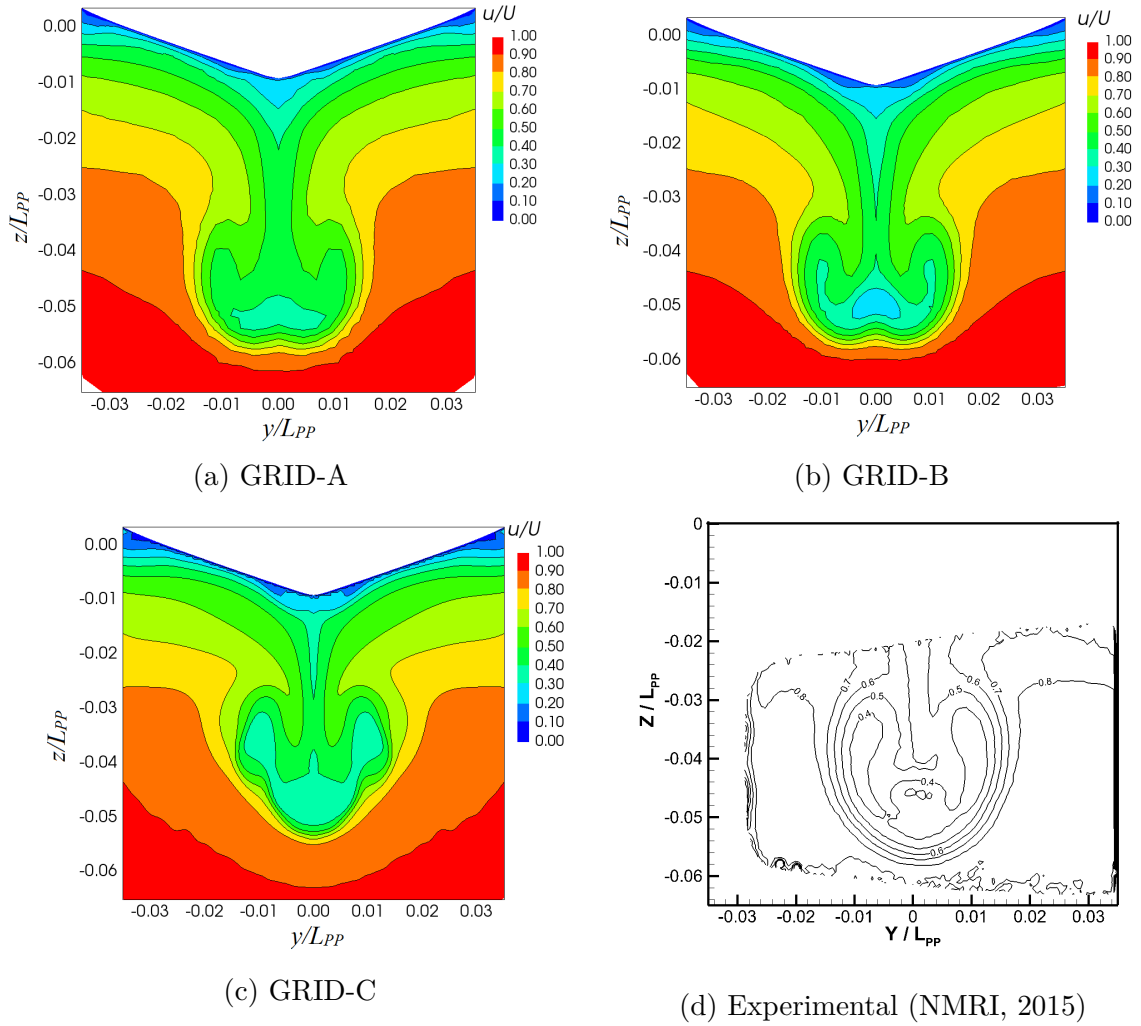


Figure 3.39: Axial flow velocity contour on $x/L_{PP} = 1.0$ for $Fn = 0.142$.

0.9843 and $x/L_{PP} = 1.00$ using GRID-C. It can be concluded that GRID-C has sufficient grid density to capture the local features of the flow.

3.1.3 Fishing Vessel

A multi-species fishing vessel model with an optimized bulbous bow was also used for validation of the resistance calculation and numerical self-propulsion using the body-force method. The detailed grid dependency study can be found in (Ali et al., 2018) and (Ali et al., 2019a).

3.1.3.1 Geometry and Test Conditions

The hull form of the fishing vessel with bulbous bow is shown in Figure 3.40. The vessel has a small length-beam ratio of 3.67. The principal particulars of the ship model and the NRC-IOT stock propeller are given in Table 3.13.

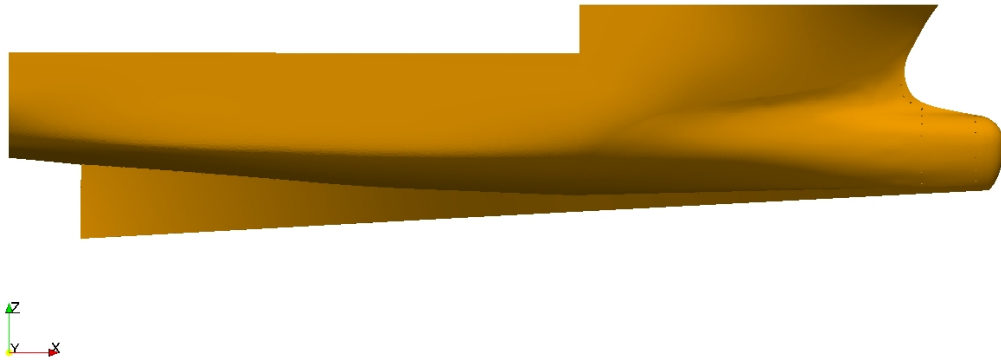


Figure 3.40: Ship model of optimized fishing vessel.

The bare-hull resistance model tests were carried out for the fishing vessel in calm water and in head seas at the Memorial University towing tank at various speeds, including the full scale design speed of 12 knots (Friis et al., 2007). The vessel was free to heave and pitch during the model tests. The test conditions for the fishing vessel are listed in Table 3.14.

Table 3.13: Principal particulars of the ship model and the propeller.

| Parameters | Model scale | Full scale | Units |
|----------------------------------|-------------|------------|----------------|
| Length, L_{pp} | 1.833 | 33.603 | m |
| Breadth, B | 0.499 | 9.148 | m |
| L_{pp}/B | 3.67 | 3.67 | |
| Draft, d | 0.224 | 4.106 | m |
| Wetted Surface Area, S_w | 1.110 | 372.90 | m ² |
| Volume of Displacement, ∇ | 0.072 | 442.30 | m ³ |
| LCG | 0.878 | 16.096 | m |
| VCG | 0.259 | 4.748 | m |
| Propeller Diameter, D | 0.1205 | 2.209 | m |
| P/D | 1.27 | 1.27 | |
| A_E/A_0 | 0.906 | 0.906 | |
| Number of Blades, Z | 4 | 4 | |

Table 3.14: Test conditions for fishing vessel model.

| | |
|----------------------|----------------|
| Case | 3.1 |
| Loading condition | Design full |
| Wave | Calm |
| Condition | Towing |
| Rudder | without |
| Propeller | without |
| Attitude | sinakge & trim |
| Validation variables | Resistance, |

3.1.3.2 Computational Domain and Grid Generation

The computational domain for the numerical simulation of the fishing vessel is shown in Figure 3.41. The origin o , of the coordinate system, $oxyz$, was set at the intersection point of the calm water surface, the midship section, and the ship's centreplane. The positive oz points up vertically, and the positive ox points from the stern to the bow.

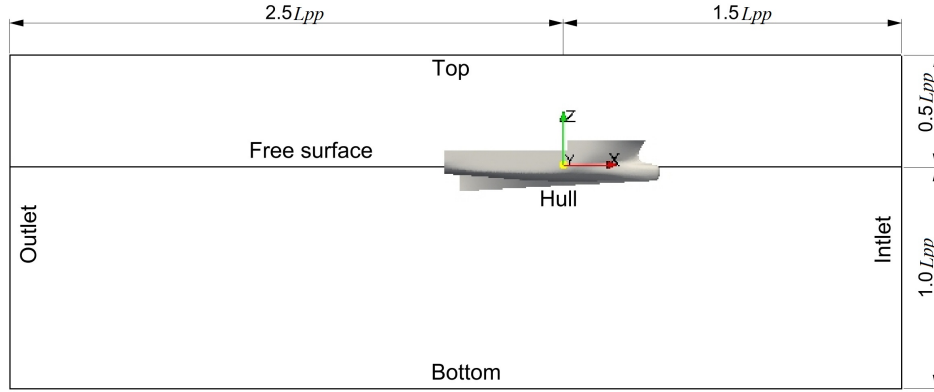


Figure 3.41: Computational domain for Fishing vessel.

In the computational domain, the inlet and outlet boundaries are $1.5 L_{PP}$ and $2.5 L_{PP}$ from the midship section, respectively. The side boundaries are $1.0 L_{PP}$ from the centreplane. The bottom is $1.0 L_{PP}$ below the free surface, and the top boundary is placed $0.5 L_{PP}$ above the free surface. The symmetry boundary condition is imposed on the centreplane to reduce the number of grids and computational time.

Grids were generated using blockMesh and navalSnappyHexMesh in OpenFOAM. Using the STL surface of the vessel model, isotropic cells were generated near the ship hull. To reduce the number of cells in the free surface region, anisotropic cells were generated. Fine cells were also generated in the propeller domain so that a sufficient number of cells can be distributed inside the actuator disk region. Different grid refinement ratios were used in the grid generation process because of difficulties

Table 3.15: Computational grids for simulations of fishing vessel.

| | $L_{PP}/\Delta x$ | No. of cells (million) | h_i/h_1 |
|--------|-------------------|------------------------|-----------|
| GRID-A | 470 | 0.70 | 2.36 |
| GRID-B | 700 | 1.48 | 1.84 |
| GRID-C | 940 | 4.16 | 1.31 |
| GRID-D | 1400 | 9.24 | 1.00 |

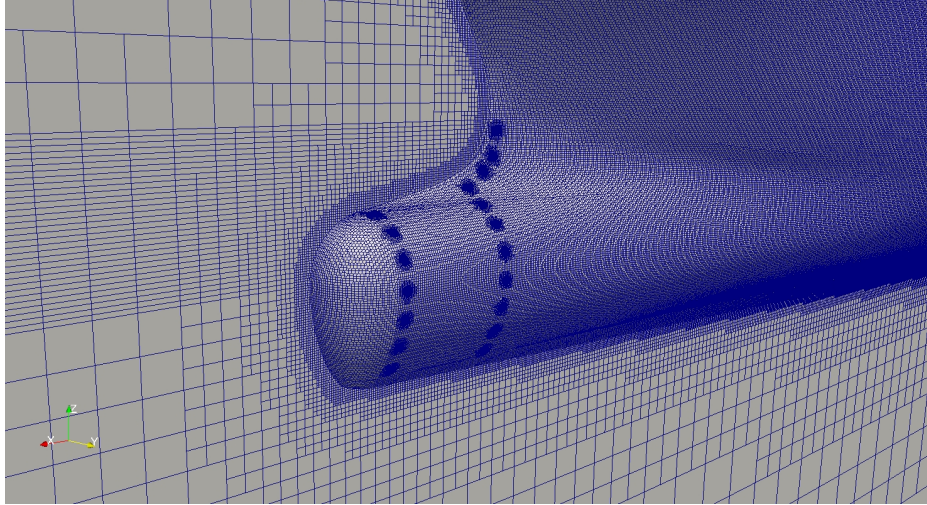


Figure 3.42: Grid distribution around the bulbous bow.

Table 3.16: Comparison of total resistance coefficient, C_T .

| Grid | C_p | C_F | C_T | $ E\%D $ | $ U_{SN}\%S $ |
|--------------|----------|----------|----------|----------|---------------|
| GRID-A | 0.006431 | 0.002885 | 0.010424 | 8.82 | 31.30 |
| GRID-B | 0.006166 | 0.002779 | 0.010011 | 4.51 | 19.64 |
| GRID-C | 0.005874 | 0.002732 | 0.009655 | 0.79 | 10.46 |
| GRID-D | 0.005914 | 0.002626 | 0.009547 | 0.33 | 6.28 |
| Experimental | | | 0.009578 | | |

in maintaining a constant grid refinement ratio using `navalSnappyHexMesh`. The generated grids for bare hull resistance simulation are summarized in Table 3.15.

3.1.3.3 Resistance Validation

The bare hull resistance of the fishing vessel was calculated using the steady solver in OpenFOAM. The model was fixed at the experimental sinkage and trim condition. Table 3.16 presents $|E\%D|$ of total resistance coefficient for different grids. It can be seen that $|E\%D|$ gradually decreases with the increased number of cells in the computational domain. The $|E\%D|$ values for the predicted total resistance coefficient for both models are less than 1.0 % using GRID-C and GRID-D.

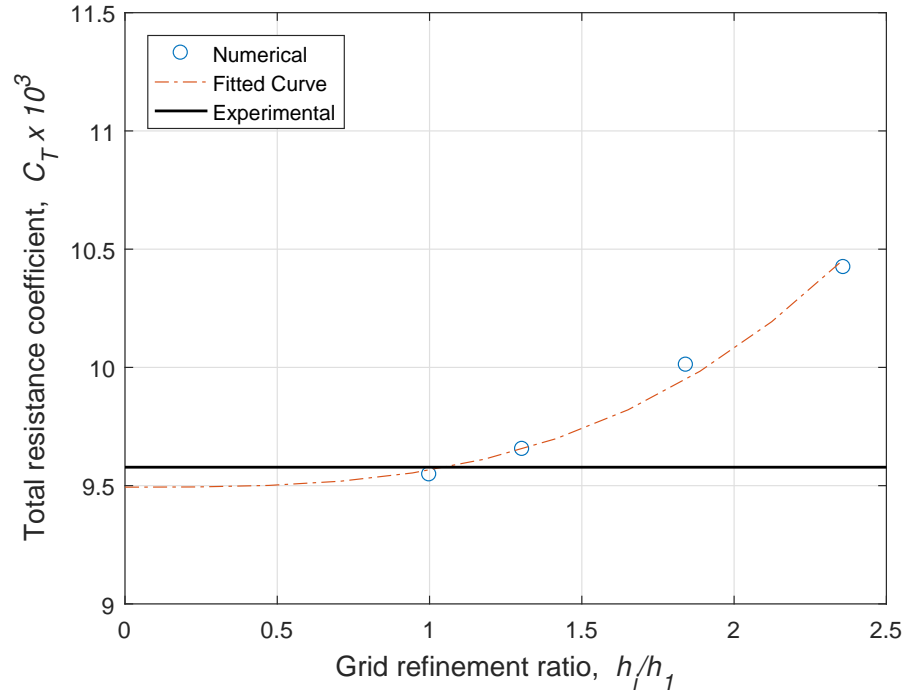


Figure 3.43: Total resistance coefficient for $Fn = 0.34$.

The convergence of the numerical solution to the grid was assessed using the LSR method for the total resistance coefficients. As shown in Table 3.16, the uncertainty for each grid is given in percentage term $|U_{SN}\%S|$, where U_{SN} is the uncertainty of the solution, S . GRID-C and GRID-D have uncertainties around 10.0% and 5.0%. The fitted curve using the weighted LSR method for the total resistance coefficient is plotted in Figure 3.43 with the experimental data. A satisfactory grid convergence was achieved with an order of accuracy $P = 3.09$ for the model.

GRID-C was then used to predict the total resistance coefficients of the model for another five Froude numbers (Fn). Figure 3.44 shows comparison of the numerical results and experimental data. The numerical results show a good agreement for all Froude numbers.

Table 3.17: Comparison of $|E\%D|$ for C_T , sinkage and trim at $Fn = 0.34$

| GRID | C_T | $ E\%D $ | Sinkage (m) | $ E\%D $ | Trim (deg) | $ E\%D $ |
|--------------|--------|----------|-------------|----------|------------|----------|
| GRID-A | 0.0106 | 12.80 | 0.0143 | 6.26 | 0.5103 | 6.99 |
| GRID-B | 0.0104 | 10.70 | 0.0142 | 5.69 | 0.5194 | 5.34 |
| GRID-C | 0.0096 | 1.79 | 0.0137 | 1.82 | 0.5265 | 4.04 |
| Experimental | 0.0094 | - | 0.0135 | - | 0.5487 | - |

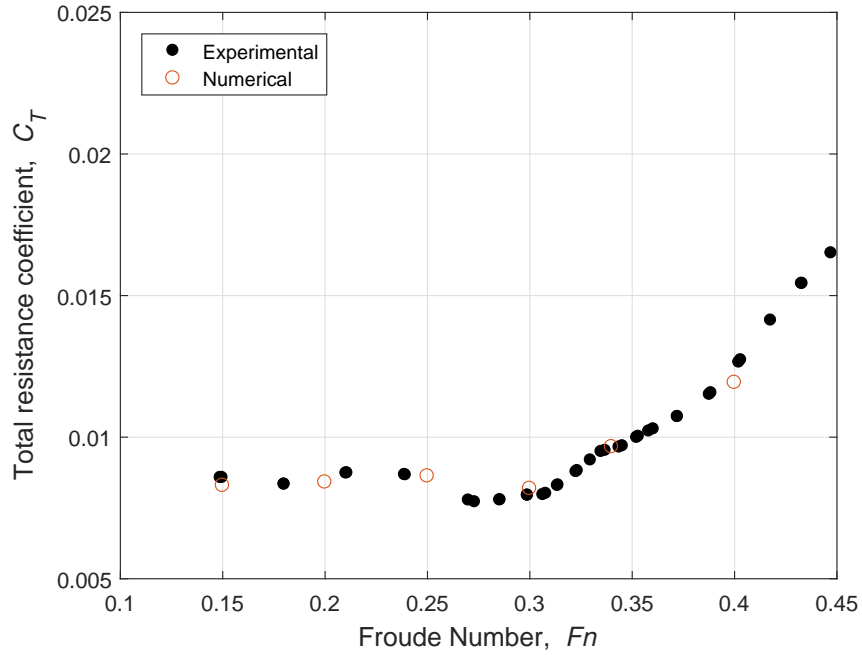
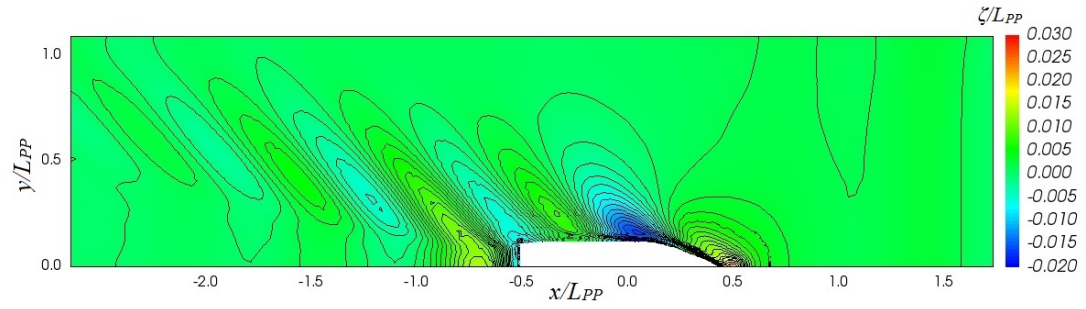
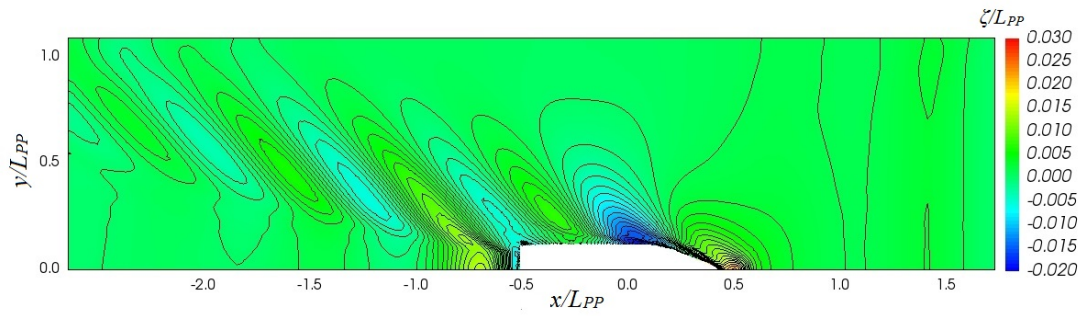


Figure 3.44: Total resistance coefficient of Model-H using GRID-C.

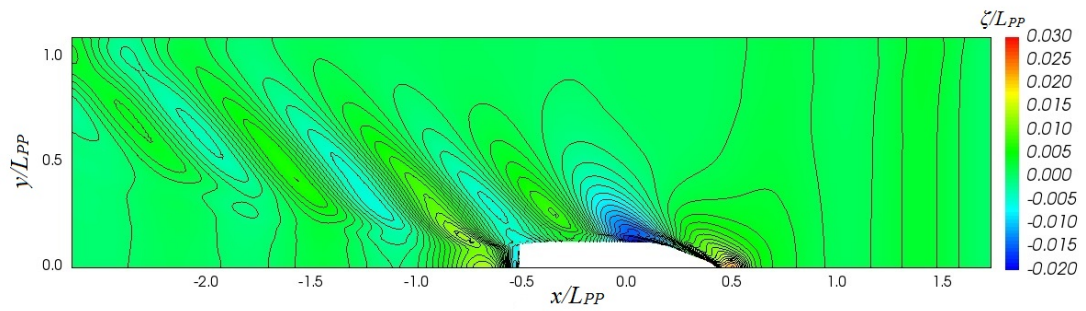
The bare-hull resistance, sinkage, and trim were computed using the unsteady solver, *interDyMFoam* at the design Froude number, $Fn = 0.34$. The predicted total resistance coefficient, sinkage, and trim with the three grids are compared with the experimental data in Table 3.17. The relative errors of predicted total resistance, sinkage and trim are less than 5.0 % when GRID-C is used.



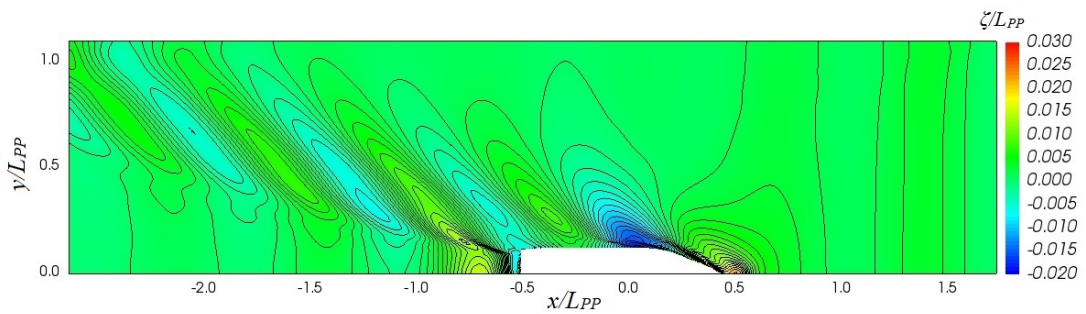
(a) GRID-A



(b) GRID-B

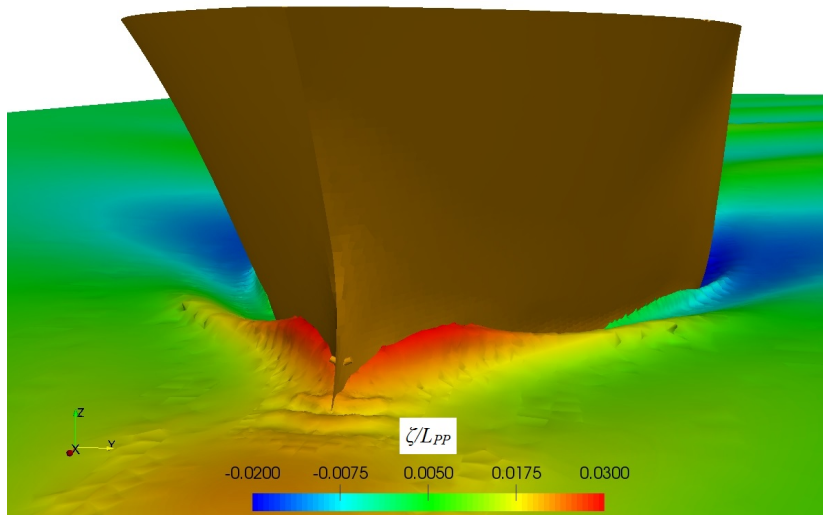


(c) GRID-C

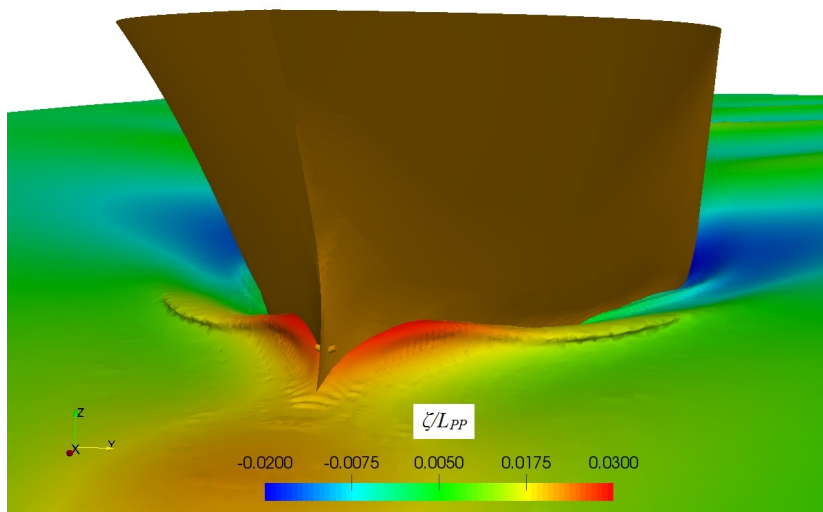


(d) GRID-D

Figure 3.45: Free surface wave contours for Model-H at $Fn = 0.34$



(a) GRID-A



(b) GRID-D

Figure 3.46: Bow waves of Model-H at $Fn = 0.34$

3.1.3.4 Free Surface Wave Contour

The non-dimensional wave patterns generated by the fishing vessel model are compared in Figure 3.45 for the four computational grids. The simulated wave contours show differences in the bow region. Wave elevations in the bow region by

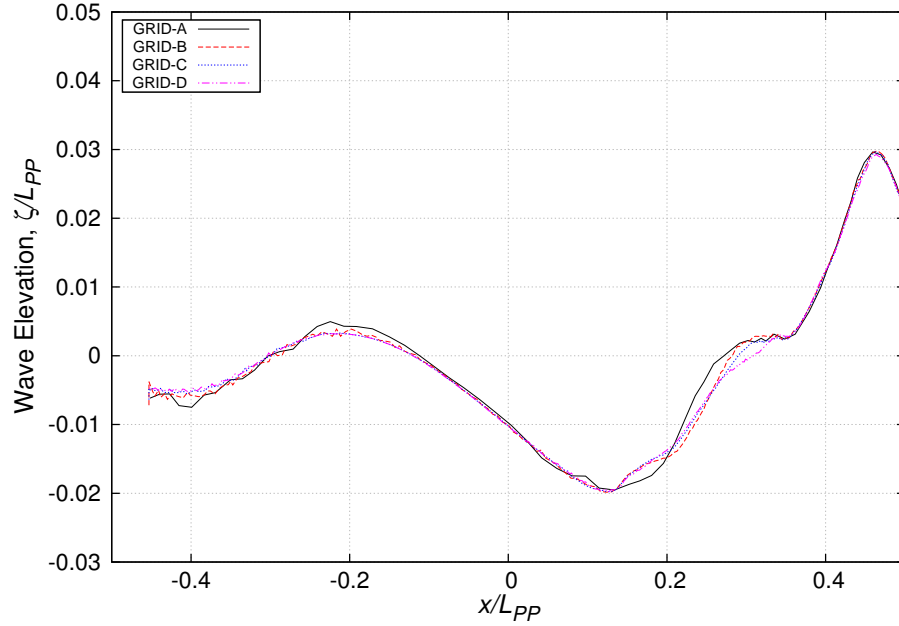


Figure 3.47: Comparison of wave elevation along the hull of Model-H at $F_n = 0.34$

GRID-A are less than those by GRID-D. To investigate the generated wave in the bow region, snapshots of the bow wave using two grids are compared in Figure 3.46. From the comparison, it is seen that GRID-D was able to capture the overturning of the bow wave better than GRID-A. It is evident that fine cells are required to capture the highly non-linear waves in the bow region.

Figure 3.47 presents the predicted wave elevations along the hull using different grid resolutions. Some differences in the bow shoulder waves ($x/L_{PP} = 0.15 \sim 0.4$) can be observed.

3.1.3.5 Flow Velocity

The axial flow velocity for the bare hull was computed on the propeller plane using the unsteady solver and is shown in Figure 3.48 for $F_n = 0.34$. A strong boundary layer effect due to the skag is visible.

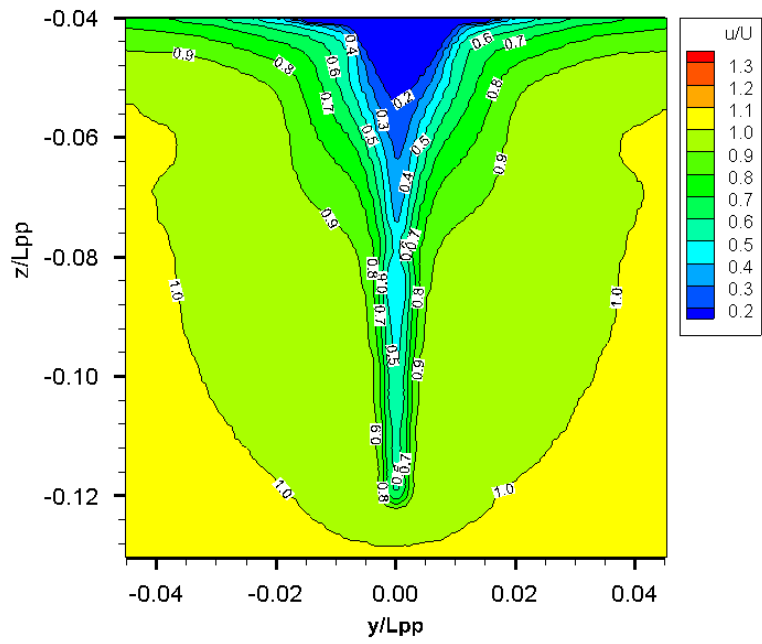


Figure 3.48: Axial velocity contour on the propeller plane at $F_n = 0.34$ for GRID-C.

3.2 Hull with Appendages

3.2.1 KCS Model

The resistance, sinkage, and trim of the KCS model with rudder were numerically computed using the unsteady multiphase solver in OpenFOAM. The geometry of the KCS model and rudder is shown in Figure 3.49.



Figure 3.49: KCS model with rudder.

3.2.1.1 Geometry and Test Conditions

For the test case 2.1 from Tokyo 2015 CFD workshop, the KCS model was equipped with a semi-balanced horn rudder. The geometry of the rudder is shown in Figure 3.50. Table 3.18 gives the particulars of the KCS rudder at full scale and model scale. The test conditions for the appended KCS model are shown in Table 3.19

3.2.1.2 Computational Domain and Grid Generation

A right-handed Cartesian coordinate system was used for numerical simulation set-up. The origin O was set at the intersection of midship section, transverse plane, and calm water surface. The x -axis is positive pointing to the bow from the stern, the positive y is in the starboard direction, and the positive z is in the upward direction. The same computational domain from the bare hull resistance computation was used for transient simulation. The same grid resolution was also used for the dynamic

Table 3.18: Principal particulars of rudder for KCS hull.

| Parameters | Full scale | Model Scale | Unit |
|-------------------------------------|------------|-------------|----------------|
| Profile type | NACA 0018 | NACA 0018 | |
| Rudder area A_R | 54.45 | 1.7232 | m ² |
| Percentage of lateral area A_R/LT | 2.21 | 2.21 | % |
| Movable rudder area A_M | 45.3 | 1.4336 | m ² |
| Percentage of lateral area A_M/LT | 1.83 | 1.83 | % |
| Balancing rudder area A_B | 13.62 | 0.4310 | m ² |
| Rudder height b | 9.9 | 0.3133 | m |
| Mean chord length c_m | 5.5 | 0.1741 | m |
| Mean thickness t_m | 0.99 | 0.0313 | m |
| Aspect ratio, geometric | 1.8 | 1.8 | |
| Thickness ratio t_m/c_m | 0.18 | 0.18 | |
| Degree of twist | 0 | 0 | deg |

Table 3.19: Test conditions for appended KCS model.

| | |
|----------------------|--|
| Case | 1.2 |
| Model | Model 1 |
| Wave | Calm |
| Condition | Towing |
| L_{PP} | 7.2786 |
| Fn | 0.108, 0.152, 0.195, 0.227, 0.26, 0.282 |
| $Rn \times 10^6$ | 5.23, 7.33, 9.42 11.0, 12.6, 13.6 |
| Rudder | with |
| Propeller | without |
| Attitude | sinkage & trim |
| Validation variables | Resistance sinkage and trim |
| EFD provider | NMRI* |

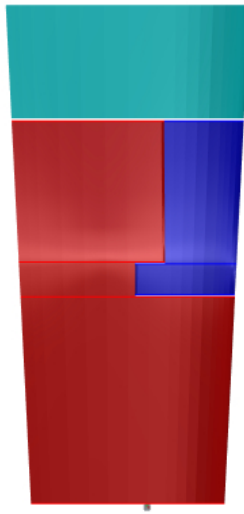


Figure 3.50: Semi-balanced horn rudder for KCS.

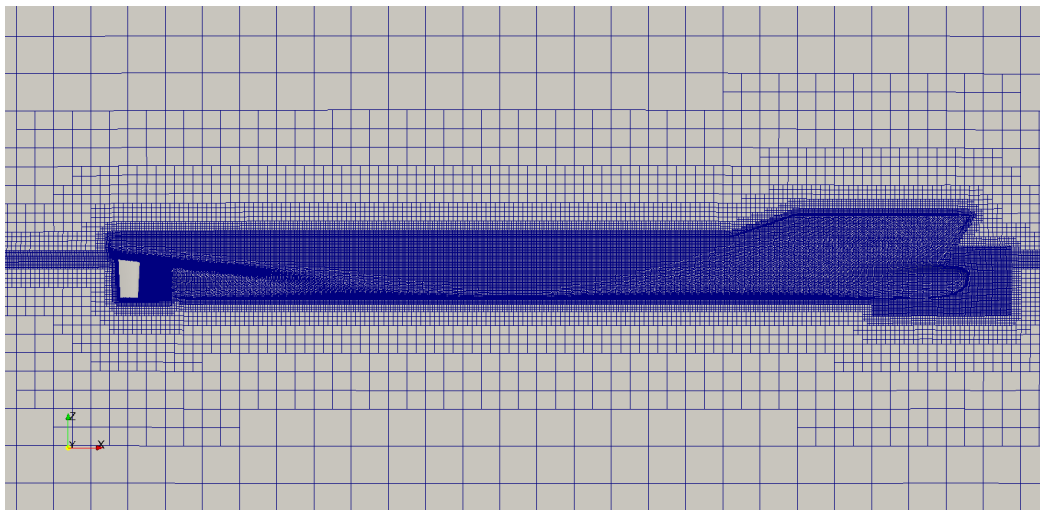


Figure 3.51: Grid distribution for sinkage and trim computation.

simulation case. The computational grids for resistance, sinkage, and trim calculation are summarized in Table 3.20. The grid distribution along the ship hull with local refinement is shown in Figure 3.51.

Table 3.20: Computational grid for KCS with rudder.

| GRID | Base cell size (m) | h | h_i/h_1 | No. of cells | Average, y^+ |
|--------|--------------------|--------|-----------|--------------|----------------|
| GRID-A | 1.00 | 0.1716 | 1.79 | 1804097 | 52.01 |
| GRID-B | 0.80 | 0.1409 | 1.47 | 3257069 | 53.27 |
| GRID-C | 0.67 | 0.1269 | 1.32 | 4461541 | 52.64 |
| GRID-D | 0.50 | 0.0960 | 1.00 | 10344597 | 41.58 |

Table 3.21: Grid dependency of C_T , sinkage and trim at $Fn = 0.26$

| GRID | $C_T \times 10^3$ | $ E\%D $ | Sinkage (m) | $ E\%D $ | Trim (deg) | $ E\%D $ |
|--------------|-------------------|----------|-------------|----------|------------|----------|
| GRID-A | 3.577 | 3.6014 | -0.01440 | 3.2999 | 0.1616 | 4.3787 |
| GRID-B | 3.568 | 3.8520 | -0.01459 | 4.6628 | 0.1605 | 5.0296 |
| GRID-C | 3.594 | 3.1449 | -0.01441 | 3.3716 | 0.1650 | 2.3669 |
| GRID-D | 3.600 | 2.9957 | -0.01501 | 7.6758 | 0.1638 | 3.0769 |
| Experimental | 3.711 | | -0.01394 | | 0.1690 | |

Table 3.22: Comparison of $|U_{SN}\%S|$ for C_T , sinkage and trim at $Fn = 0.26$.

| GRID | h_i/h_1 | C_T | Sinkage | Trim |
|--------|-----------|-------|---------|------|
| GRID-A | 1.79 | 0.09 | 0.90 | 0.55 |
| GRID-B | 1.47 | 0.45 | 1.91 | 0.85 |
| GRID-C | 1.32 | 0.52 | 2.45 | 1.18 |
| GRID-D | 1.00 | 0.59 | 2.77 | 1.59 |

3.2.1.3 Resistance, Sinkage, and Trim Validation

The total resistance coefficient (C_T), sinkage, and trim for the three grids were computed for $Fn = 0.26$. The model was allowed only heave and pitch. The numerical results are validated against the experimental data in Table 3.21. The numerical uncertainty for resistance, sinkage and trim are calculated using LSR method and summarized in Table 3.22 for the four computational grids. The numerical uncertainty for total resistance coefficient of GRID-C and GRID-D is less than 1%. For sinkage and trim, the numerical uncertainty of GRID-C and GRID-D are also less than 3%.

Table 3.23: Results of unsteady simulation of KCS hull with rudder using GRID-C.

| | | Experimental | | Numerical | | |
|-------|-------------------|--------------------------|-------------|-------------------|--------------------------|-------------|
| F_n | $C_T \times 10^3$ | Sinkage, σ/L_{pp} | Trim τ | $C_T \times 10^3$ | Sinkage, σ/L_{pp} | Trim τ |
| 0.108 | 3.796 | -0.00012 | -0.017 | 3.626 | -0.00027 | -0.021 |
| 0.152 | 3.641 | -0.00038 | -0.053 | 3.461 | -0.00056 | -0.047 |
| 0.195 | 3.475 | -0.00082 | -0.097 | 3.350 | -0.00105 | -0.089 |
| 0.227 | 3.467 | -0.00130 | -0.127 | 3.390 | -0.00141 | -0.123 |
| 0.260 | 3.711 | -0.00192 | -0.169 | 3.594 | -0.00198 | -0.165 |
| 0.282 | 4.501 | -0.00234 | -0.159 | 4.410 | -0.00255 | -0.143 |

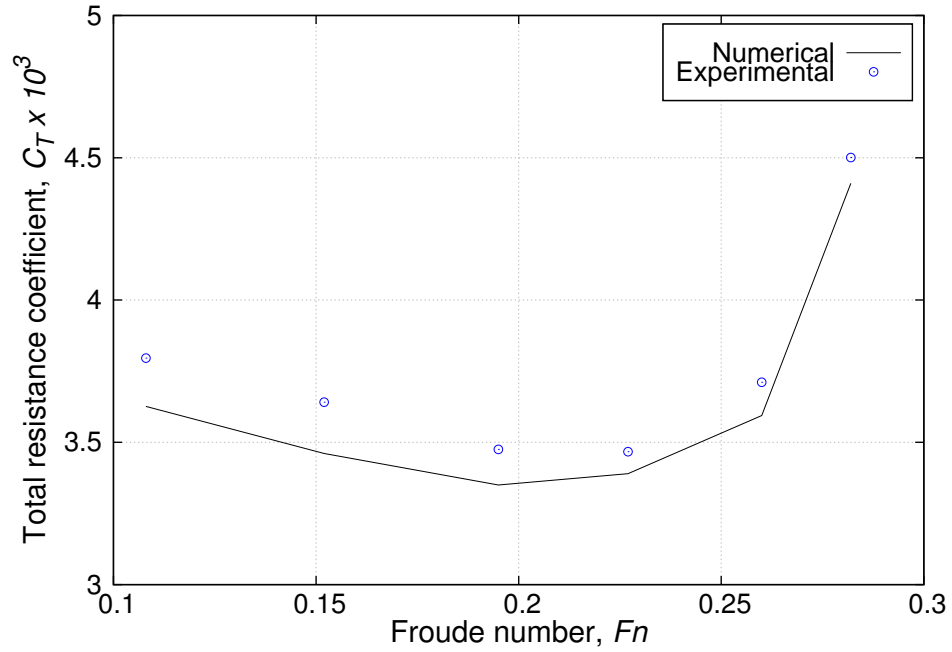


Figure 3.52: Comparison of total resistance coefficient using GRID-C.

GRID-C was used for the computation of total resistance coefficient, sinkage and trim for five other Froude numbers. The results are summarized in Table 3.23. For the low-speed case, it is found that the error in numerical prediction is quite large. The total resistance coefficient, C_T is compared with the experimental data in Figure 3.52. A large deviation from the experimental data is observed for low speeds. The discrepancy is reduced with increasing Froude numbers. A similar trend is also observed in sinkage results in Figure 3.53. However, numerical results for trim show

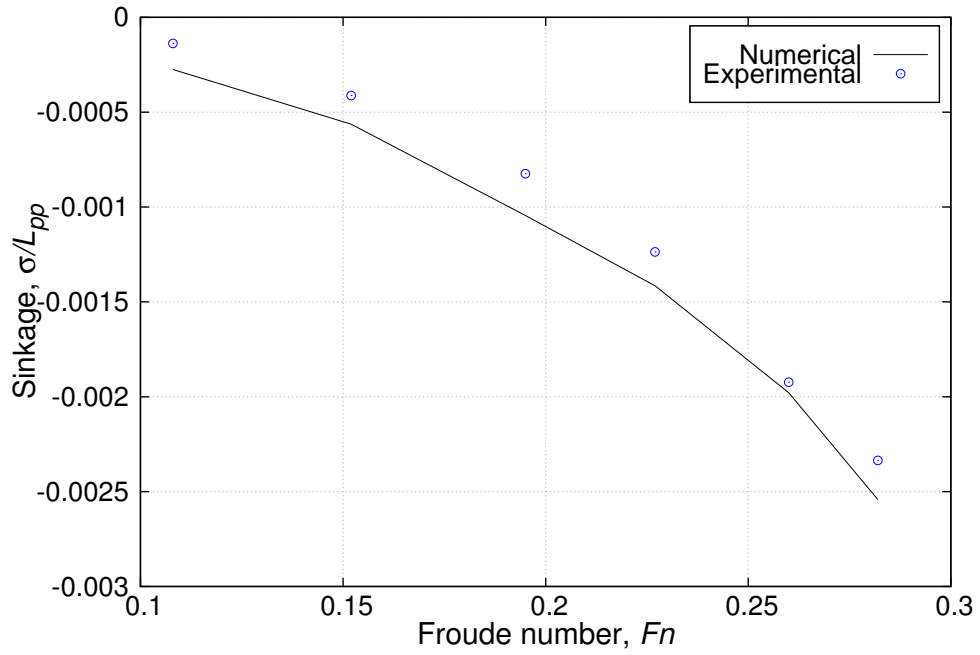


Figure 3.53: Comparison of sinkage of KCS model using GRID-C.

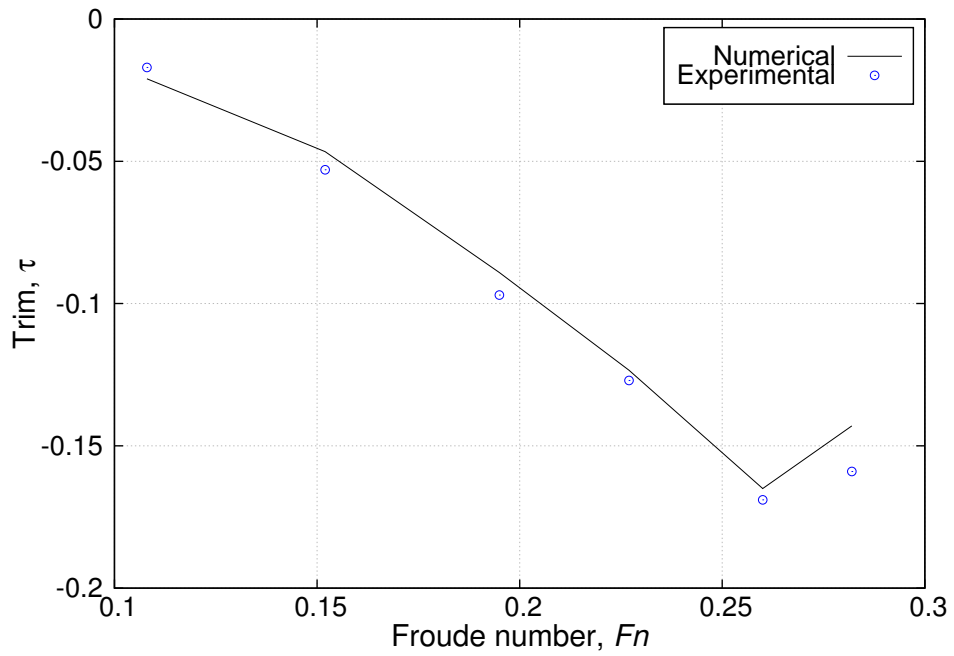


Figure 3.54: Comparison of trim of KCS model GRID-C.

good agreement with the experimental data at low speed in Figure 3.54. At the low speed, the Reynolds number is lower than the higher speed. It increases the laminar boundary layer and turbulent boundary layer thickness. To keep the same y^+ for low speed simulation, the near-wall thickness should be adjusted for similar level of accuracy as for high speed. The grids were designed for Froude number $Fn = 0.26$ and it was necessary to modify the grids according to the Froude number.

3.3 Scale Effect on Resistance, Sinkage and Trim

The scale effect on resistance coefficient, sinkage, trim, free surface wave contour, axial flow velocity was studied for the design speed ($Fn = 0.26$) using the similar set-up for the computational domain as for bare hull resistance. Four different scales of the KCS model were used for this study.

3.3.1 Computational Domain and Grid Generation

The computational domain for grid generation to study the scale effect is shown in Figure 3.55. The domain shape and size with respect to the ship length was same for four scale factors. The grid density along the ship length, in the free surface region, and the in Kelvin wedge refine was similar. To reduce the number of computational grids for the different scale, the near-wall cell height was increased and the number of prism layer also was changed. It is quite impractical to generate grids with the same y^+ for different model scale. In this case, the total number of

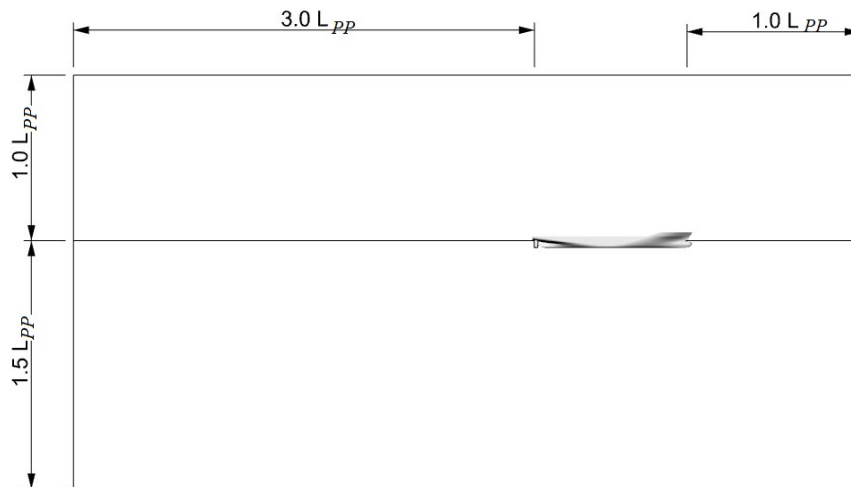
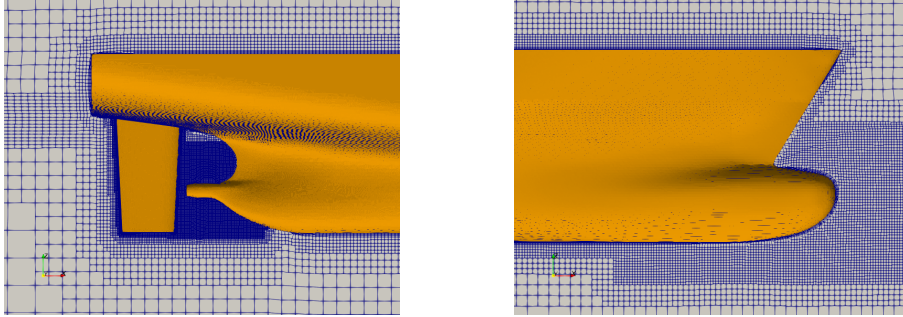
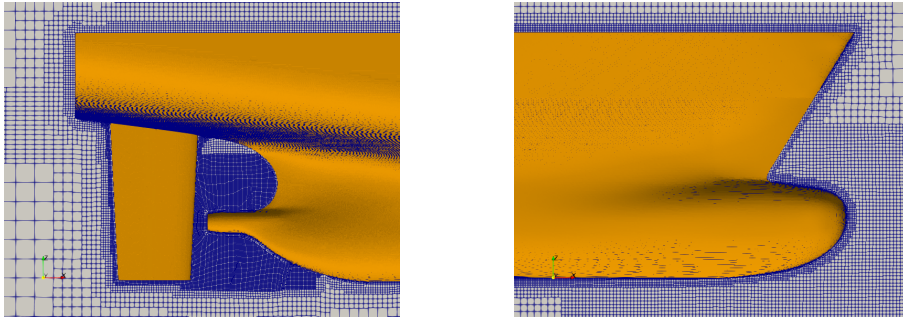


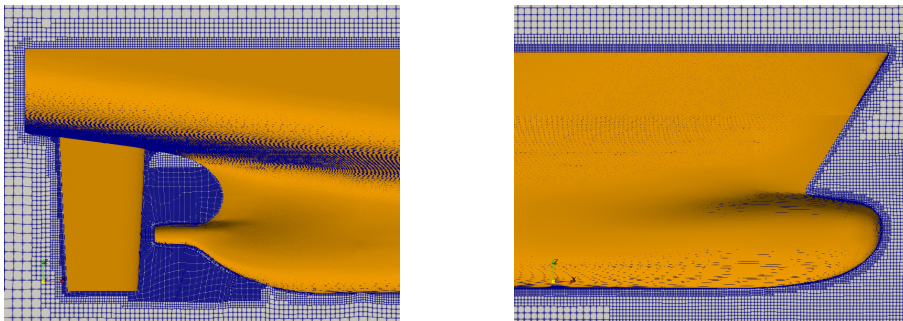
Figure 3.55: Computational domain for the study of scale effect.



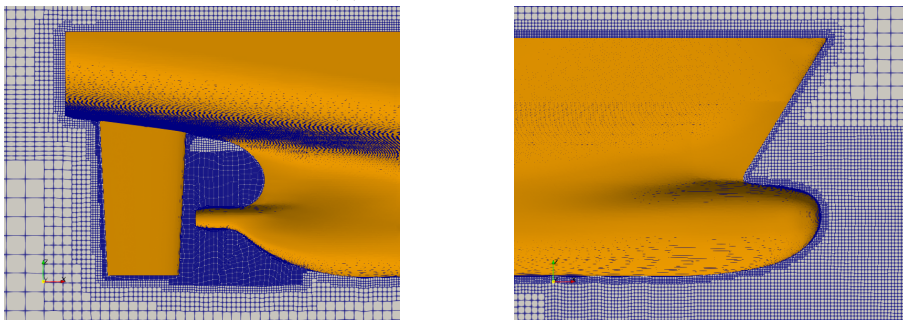
(a) Scale factor = 31.599



(b) Scale factor = 16.



(c) Scale factor = 8.



(d) Full scale.

Figure 3.56: Grid distribution at bow and stern of the model.

Table 3.24: Computational grid for scale effect study.

| Scale factor | No. of cells | Average, y^+ |
|--------------|--------------|----------------|
| 1 | 7437954 | 715.42 |
| 8 | 6430654 | 293.48 |
| 16 | 6430654 | 109.71 |
| 31.599 | 4461541 | 44.21 |

grids was very high. In multiphase simulations, high aspect cells on the hull surface leads to the numerical ventilation. This unwanted phenomenon lead to the wrong numerical results and eventually the simulation crash. Special attention was paid during the mesh generation step to maintain the cell aspect ratio as low as possible. The comparison of the distribution on the bow for four scale factor is shown in Figure 3.56. The grid information is summarized in Table 3.24.

3.3.2 Resistance, Sinkage and Trim

The frictional resistance and pressure resistance were computed using the multiphase dynamic motion solver *interDyMFoam*. The ship was appended with semi-balanced rudder. The numerical frictional resistance coefficients are compared with ITTC-57 for different scale factors in Figure 3.57. The difference between the numerical results and ITTC data is higher for the full scale ship than at model scale. The higher Reynolds number reduces the relative boundary layer thickness for the full scale case which increases the frictional resistance. The pressure resistance coefficients are also compared for the different scale factors in Figure 3.58. A large deviation is observed for the full scale simulation.

The scale effect on sinkage and trim was investigated, and the comparisons are presented in Figures 3.59 and 3.60 for sinkage and trim respectively. The

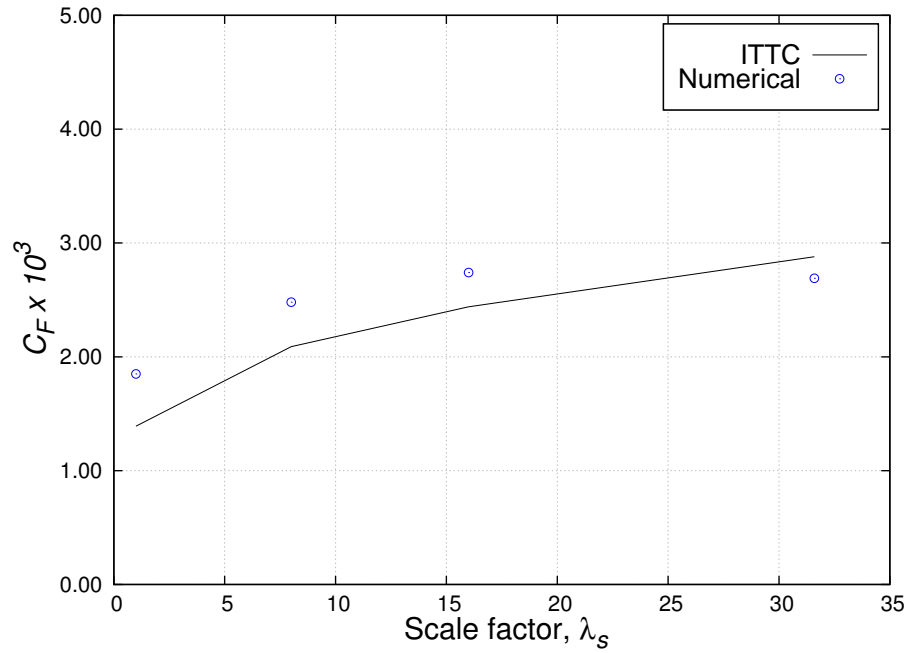


Figure 3.57: Effect of scale factor on frictional resistance.

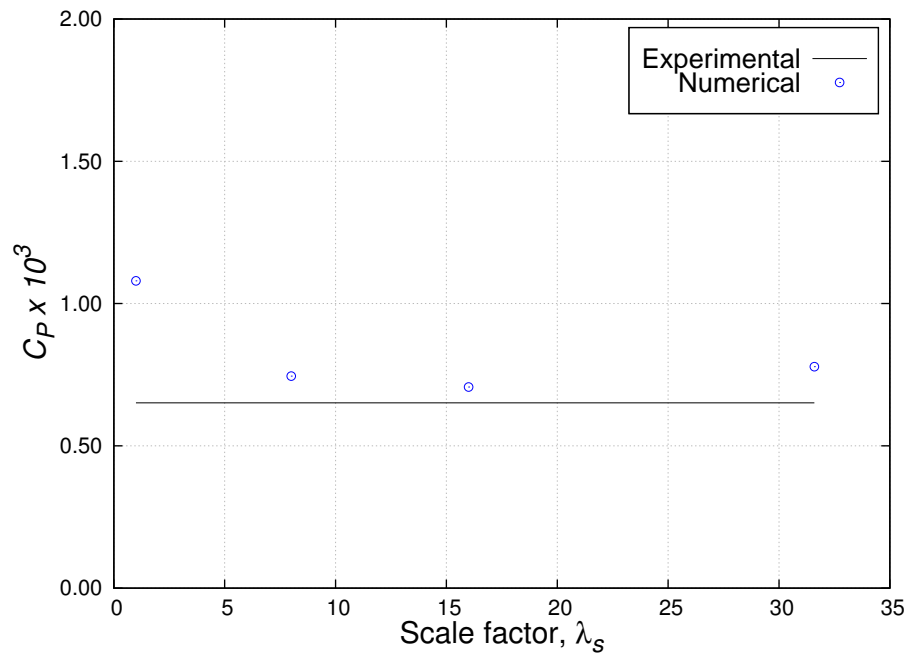


Figure 3.58: Effect of scale factor on pressure resistance.

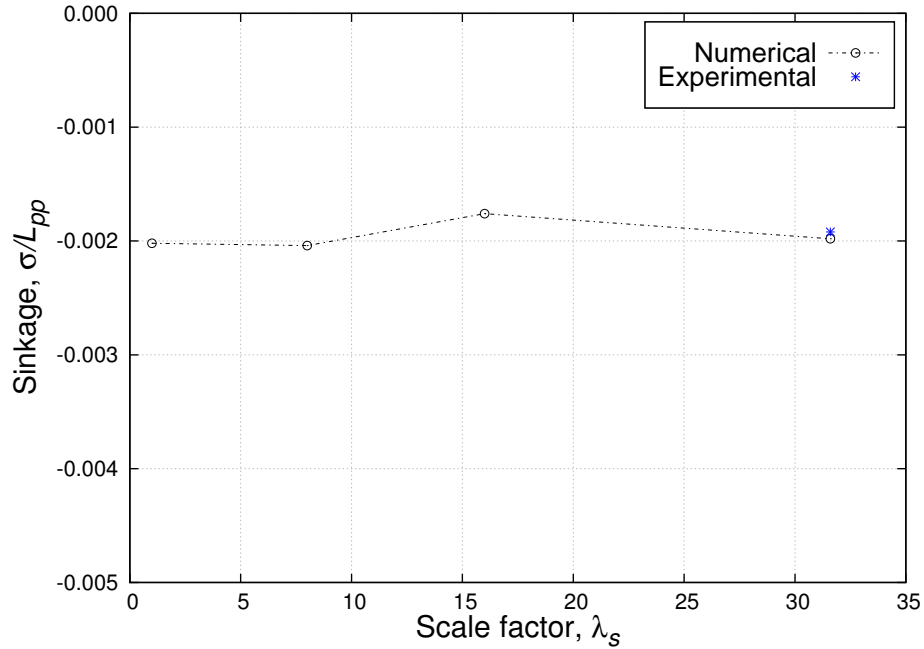


Figure 3.59: Effect of scale factor on sinkage.

non-dimensional sinkage shows similar values for all scale factors except 16. The comparison for trim shows that trim is higher at model scale.

3.3.3 Free Surface Wave Contour

The effect of scale factor on the free surface was examined for the cases given in Table 3.24. Figure 3.61 shows the comparison for four scale factors. The difference in the bow region is not significant. However, the difference at the stern is significant. Higher wave height is observed for full scale simulation than model scale behind the stern of the vessel.

3.3.4 Flow Velocity

The axial velocity distribution in the propeller plane is compared in Figure 3.62 for different scale factors. The vortex around the stern bulb is stronger in model scale than

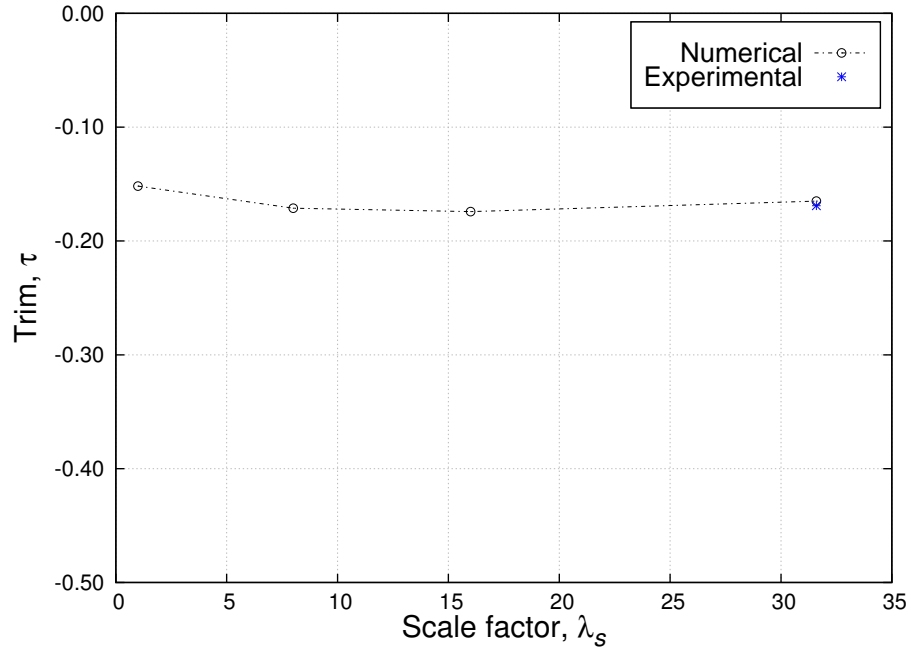
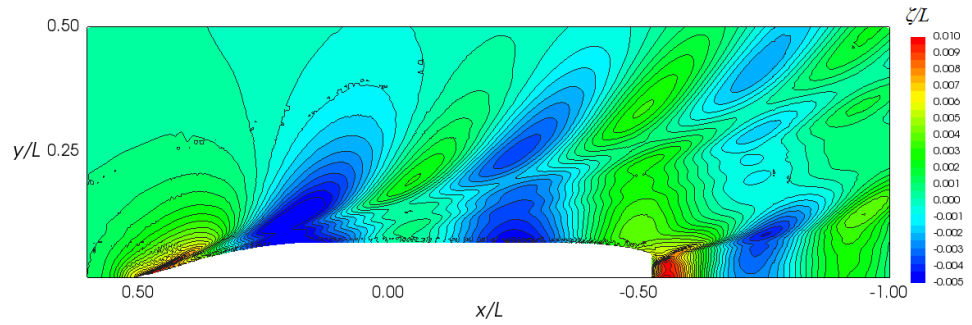
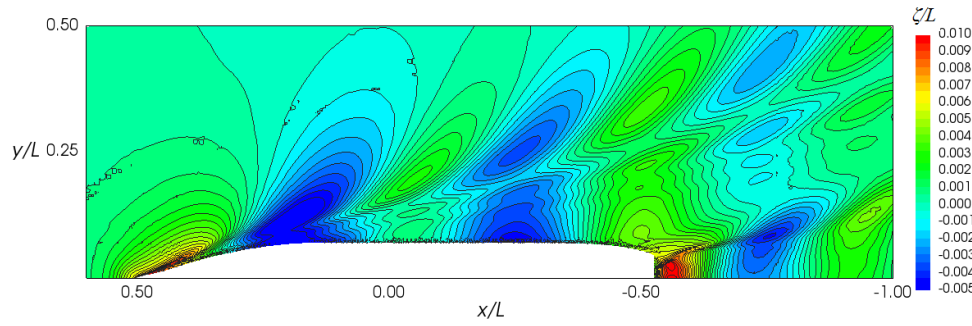


Figure 3.60: Effect of scale factor on trim.

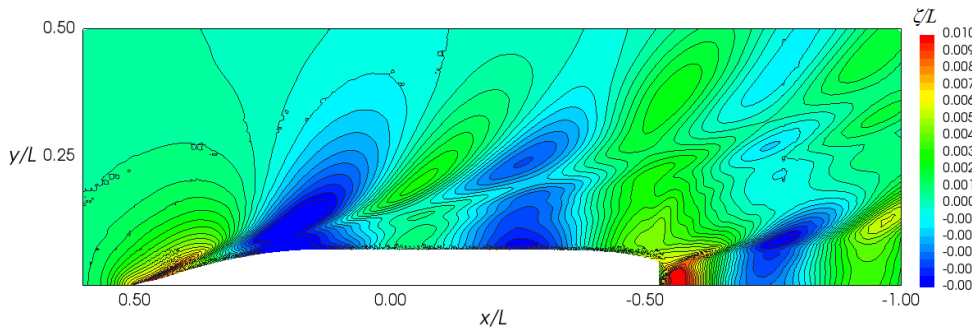
in full scale. The boundary layer is also smaller in the full scale than at model scale which causes higher incoming velocity to the propeller. This difference in incoming velocity leads to a difference in propulsive performance from model scale to full scale. The challenges involve in the full scale numerical simulation is the grid generation. The wall function approach predicts the pressure force on the hull surface when y^+ is less than 300. The insufficient number of grid points near to the wall lead to the large deviation in pressure force prediction. From the comparison of force coefficients, it is recommended to increase the grid resolution in the log law region. Items for summary covers the first stage of the simulation development and shows that the ship resistance, flow and pressures can be reasonably predicted.



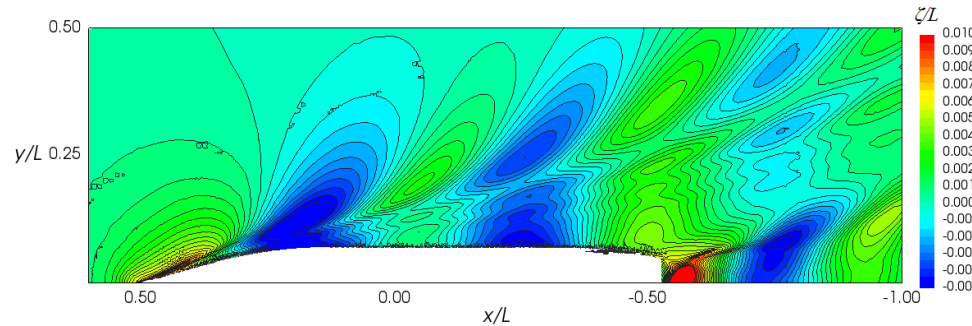
(a) Scale Factor 31.599



(b) Scale Factor 16



(c) Scale Factor 8



(d) Scale Factor 1

Figure 3.61: Effect of scale factor of free surface wave contour.

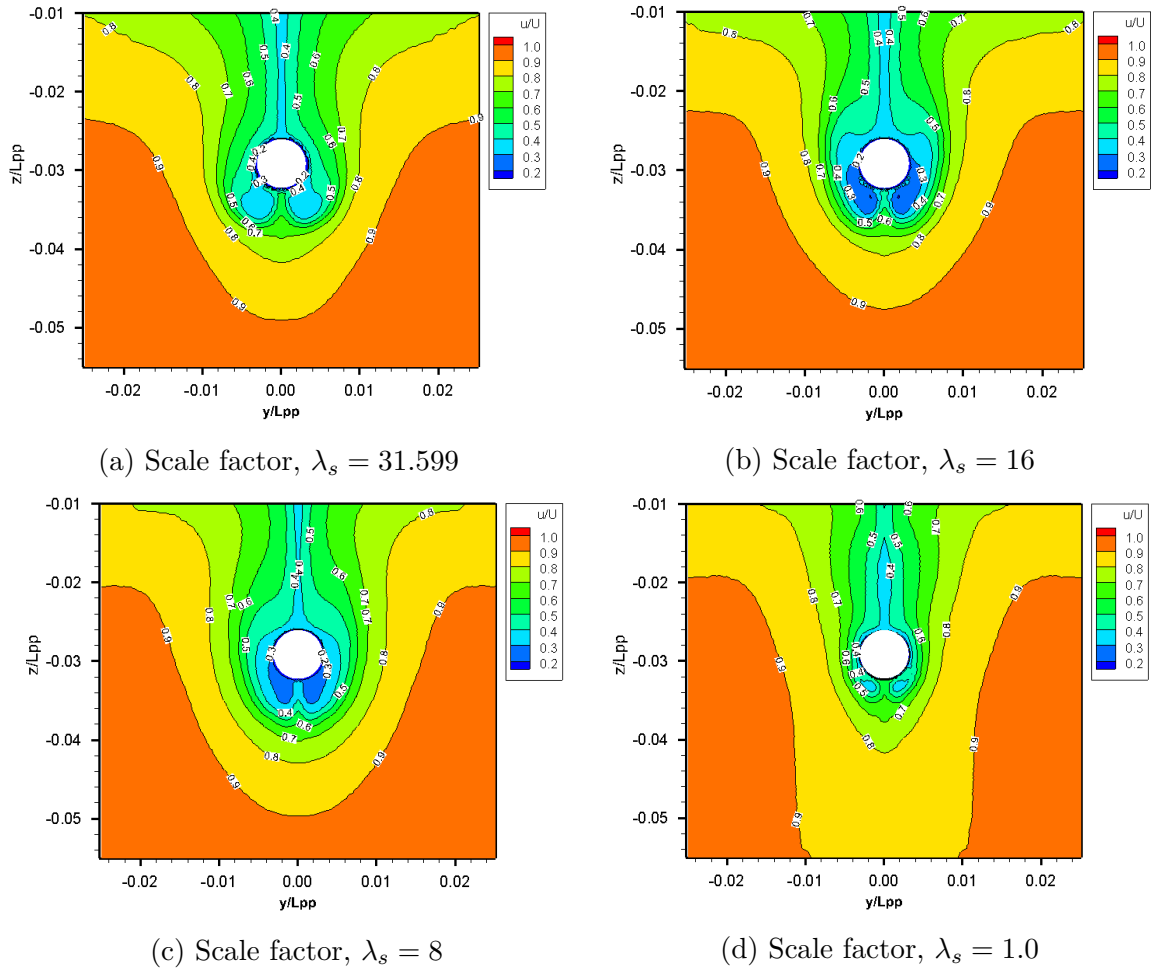


Figure 3.62: Effect of scale factor on axial velocity distribution on propeller plane.

Chapter 4

Propeller Open Water Validation

This chapter presents the validation of propeller open water simulations of three different propellers KP505, MP687, and NRC IOT stock propeller using the detailed propeller geometry or/and body-force method. Detailed propeller geometry was used for the KP505, and MP687 propellers and the body-force method, described in section 2.8, was used for the KP505 and NRC IOT stock propeller. The open water hydrodynamic characteristics of the propellers are compared with the experimental data using thrust coefficient K_T , torque coefficient K_Q , and efficiency η_o as defined by the following equations:

$$K_T = \frac{T}{\rho n^2 D^4} \quad (4.1)$$

$$K_Q = \frac{Q}{\rho n^2 D^5} \quad (4.2)$$

$$\eta_o = \frac{J K_T}{2\pi K_Q} \quad (4.3)$$

where T is the thrust, Q is the torque, ρ is the fluid density, n is the rate of revolution, D is the propeller diameter, and J is the advance coefficient which is defined as:

$$J = \frac{V_a}{nD} \quad (4.4)$$

where V_a is the advance velocity. Ali et al. (2017b) carried out a detailed investigation of tip vortex prediction of the DTMB5168 propeller can be found in Appendix-A. Based on the experience of tip vortex study, propeller open water data validation were performed for the KP505, MP687 and NRC-IOT propellers.

4.1 KP505 Test Case

4.1.1 Geometry and Test Conditions

4.1.2 Actual Propeller Geometry

The self-propulsion test case 2.7 from the T2015 workshop was performed using a five bladed right-hand fixed pitch propeller designated KP505. The open water experiments were carried out at NMRI, Japan using a propeller provided by KRISO. The surface file for the KP505 propeller was obtained from the T2015 workshop website. The geometry of the KP505 propeller is shown in Figure 4.1. The main particulars of the KP505 propeller are listed in Table 4.1.

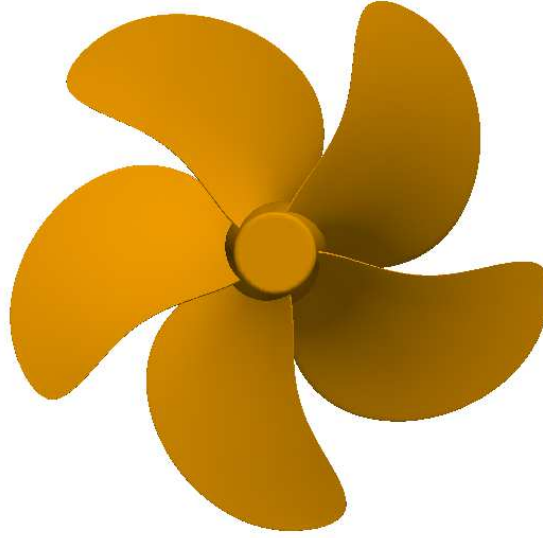


Figure 4.1: Geometry of KP505 propeller.

Table 4.1: Principal particulars of KP505 propeller.

| Item | Full scale | Model scale |
|---------------|------------|-------------|
| Type | FP | FP |
| No. of blades | 5 | 5 |
| D (m) | 7.9 | 0.25 |
| $P/D(0.7R)$ | 0.997 | 0.997 |
| $Ae/A0$ | 0.8 | 0.8 |
| Rotation | Right hand | Right hand |
| Hub ratio | 0.18 | 0.18 |

4.1.2.1 Computational Domain and Grid Generation

Cylindrical computational grids were generated for the propeller open water simulation of KP505. The inlet boundary was placed $2.0D$ from the propeller center, the outlet boundary was set at $4.0D$ behind the propeller plane, and the outer boundary was set $2.0D$ from the propeller axis of rotation as shown in Figure 4.2. The computational domain consists of two regions, one is stator which is stationary about the global coordinate system and the other one is the rotor which rotates

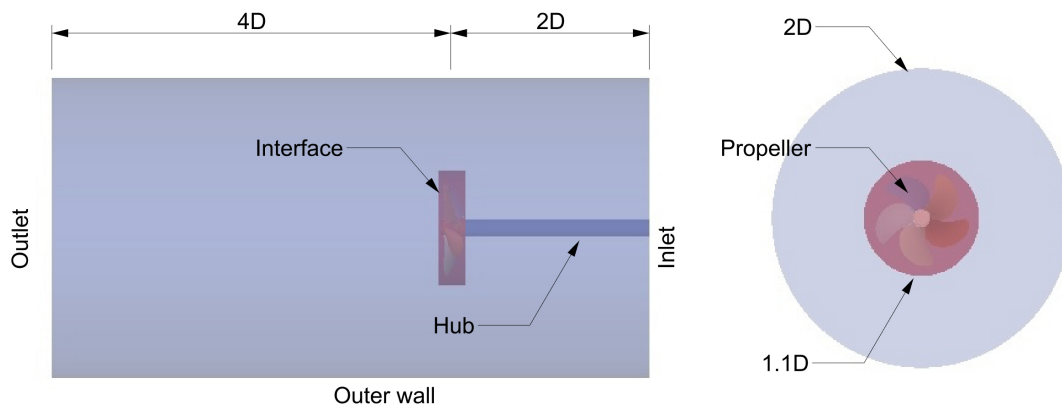


Figure 4.2: Computational domain of KP505 propeller open water simulation.

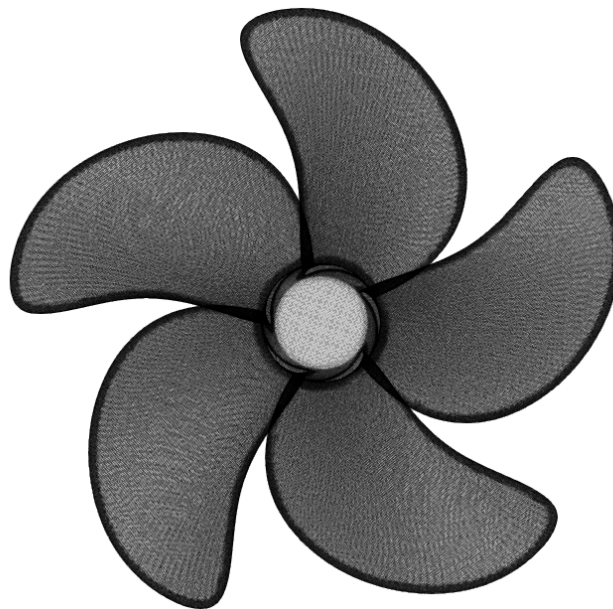


Figure 4.3: Grid distribution on KP505 propeller blade.

about the propeller axis of rotation in a transient simulation. The rotating region covers the propeller diameter, which is connected with the static region using the sliding mesh interface. Three computational grids were generated using NUMECA Hexpress, cfMesh (Juretic, 2017) and navalSnappyHexMesh in OpenFOAM. The grid distribution on the propeller blade is shown in Figure 4.3. The computational grids for propeller open water simulations are summarized in Table 4.2.

Table 4.2: Computational grid for KP505 propeller open water simulation

| Grid | Stator | Rotor | Average y^+ |
|--------|---------|---------|---------------|
| GRID-A | 2182803 | 1347576 | 45.51 |
| GRID-B | 2182803 | 2905635 | 22.72 |
| GRID-C | 2182803 | 4250712 | 15.23 |
| GRID-D | 2182803 | 5868703 | 4.23 |

4.1.2.2 Numerical Results

The propeller open water simulations of the KP505 propeller were performed using the steady and unsteady solvers for a wide range of advance coefficients. For steady simulations, the *simpleFoam* solver was used, and for transient simulations the *pimpleDyMFoam* solver was used.

4.1.2.3 Steady Simulation

The steady simulations were performed using a moving reference frame (MRF) method. In the MRF method, a Coriolis force was applied to the cells inside the rotating region to mimic the rotational effect of the propeller. Physically the rotational part of the domain stays fixed. In OpenFOAM, *SIMPLE* algorithm was used for pressure-velocity coupling. The grid uncertainty is studied using the above mentioned grids using LSR method for $J = 0.7$. Table 4.3 presents the validation error with the grid uncertainty for each grid for steady solution. The order of accuracy, P for K_T is 1.09 and for $10K_Q$ is 2.01. The numerical uncertainty for K_T varies from 25% to 30% and for K_Q the numerical uncertainty varies from 0.5% to 1.0%. The validation error for both K_T and K_Q is less than 10%. The convergence of K_T , $10K_Q$ and η_o for $J = 0.7$ is shown in Figure 4.4. The parameters converged after 50 iterations, whereas the residuals did not converge until 1200 iterations as shown in Figure 4.5. Simulations were stopped after the residuals converged.

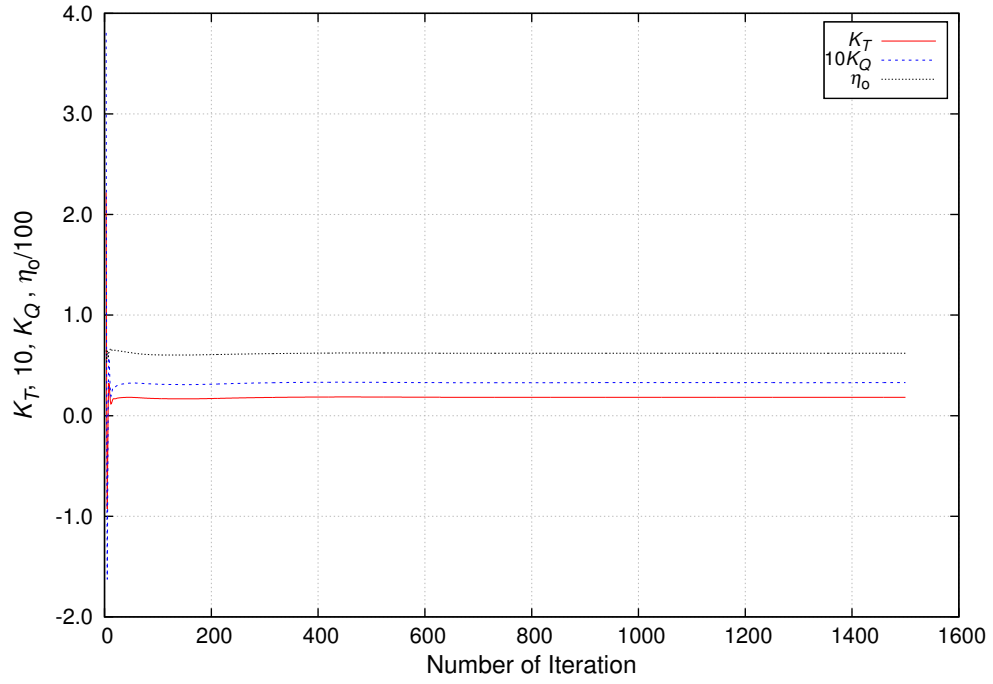


Figure 4.4: Convergence of K_T , $10K_Q$ for $J = 0.7$ using steady solver for GRID-B.

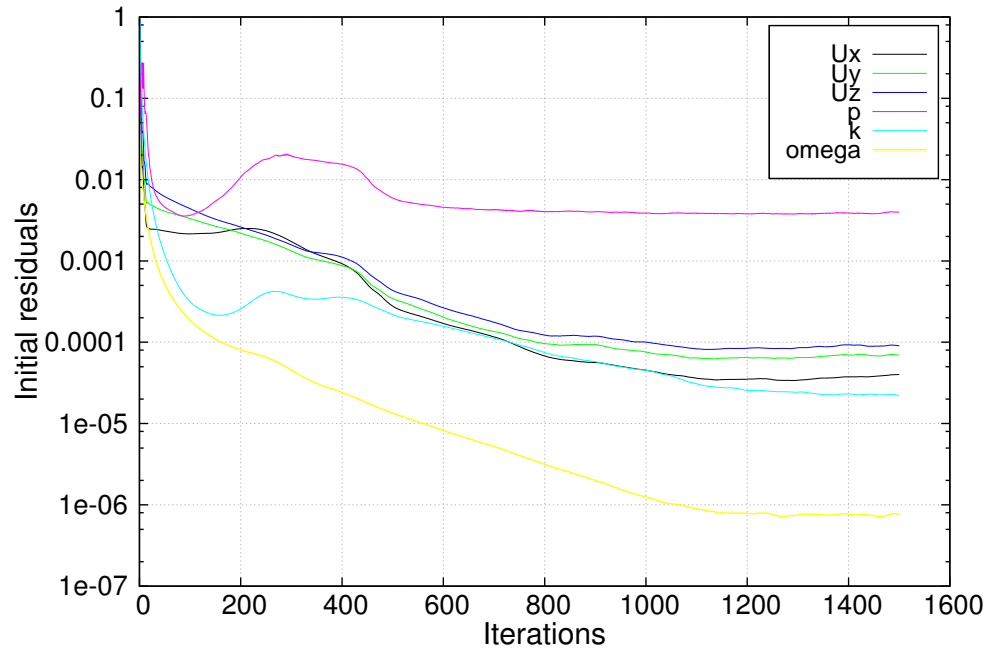


Figure 4.5: Residual convergence using steady solver for GRID-B at $J = 0.7$.

Table 4.3: Grid dependency of open water performance at $J = 0.7$ using steady solver.

| GRID | h_i/h_1 | K_T | $ E\%D $ | $ U_{SN}\%S $ | $10K_Q$ | $ E\%D $ | $ U_{SN}\%S $ |
|--------|-----------|--------|----------|---------------|---------|----------|---------------|
| | | | $P=1.09$ | | | $P=2.01$ | |
| GRID-A | 1.32 | 0.1915 | 3.50 | 31.12 | 0.3204 | 3.03 | 0.32 |
| GRID-B | 1.17 | 0.1832 | 1.00 | 28.61 | 0.3286 | 5.66 | 0.67 |
| GRID-C | 1.08 | 0.1814 | 1.93 | 26.62 | 0.3206 | 3.07 | 0.87 |
| GRID-D | 1.00 | 0.1793 | 3.07 | 24.90 | 0.3243 | 4.27 | 1.02 |

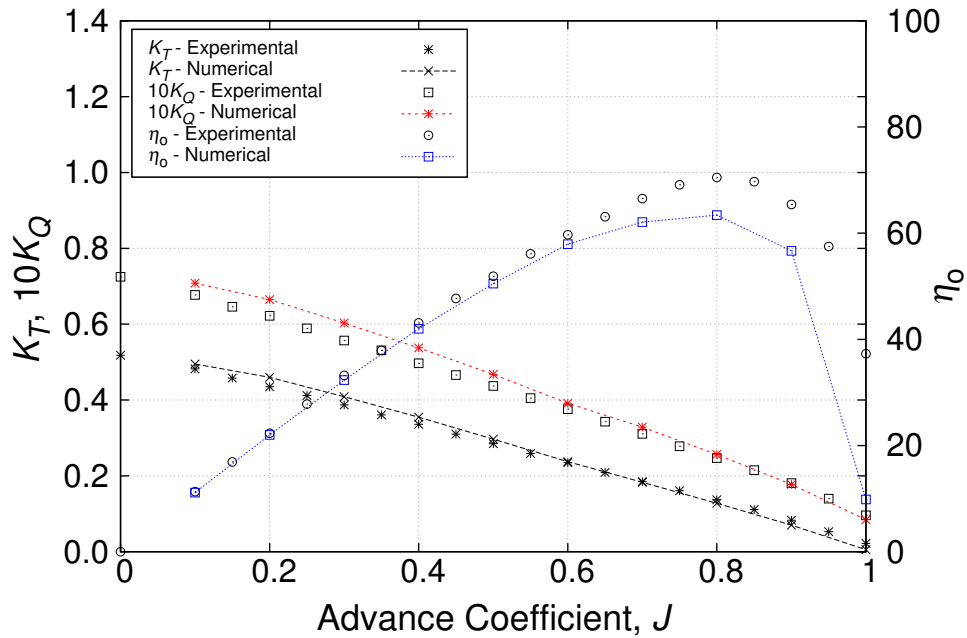


Figure 4.6: KP505 propeller open water simulation using steady solver for GRID-B.

The results obtained using the MRF method using GRID-B are compared with the experimental results from Fujisawa et al. (2000) in Figure 4.6. The predicted K_T and $10K_Q$ showed good agreement with the experimental measurements. However, the open water efficiency was under predicted for $J = 0.7$ and higher values.

Table 4.4: Grid dependency of open water performance at $J = 0.7$ using unsteady solver.

| GRID | h_i/h_1 | K_T | $ E\%D $ | $ U_{SN}\%S $ | $10K_Q$ | $ E\%D $ | $ U_{SN}\%S $ |
|--------|-----------|--------|----------|---------------|----------|----------|---------------|
| | | | | $P= 2.35$ | | | |
| | | | | | $P=2.86$ | | |
| GRID-A | 1.32 | 0.1868 | 0.99 | 4.13 | 0.3118 | 0.24 | 2.54 |
| GRID-B | 1.17 | 0.1789 | 3.32 | 4.29 | 0.3187 | 2.47 | 2.37 |
| GRID-C | 1.08 | 0.1808 | 2.29 | 4.22 | 0.3181 | 2.30 | 2.37 |
| GRID-D | 1.00 | 0.1876 | 1.41 | 4.06 | 0.3103 | 0.22 | 2.43 |

4.1.2.4 Unsteady Simulation

Unsteady numerical simulations of propeller open water tests were also carried out for the same advance coefficients as the steady simulations. In the transient simulations, the rotating part of the computational grid rotates at a given rotational speed. The data from the static part are transferred to the rotating part using the sliding mesh method. The grid uncertainty was also calculated for $J = 0.7$ for four grids. The

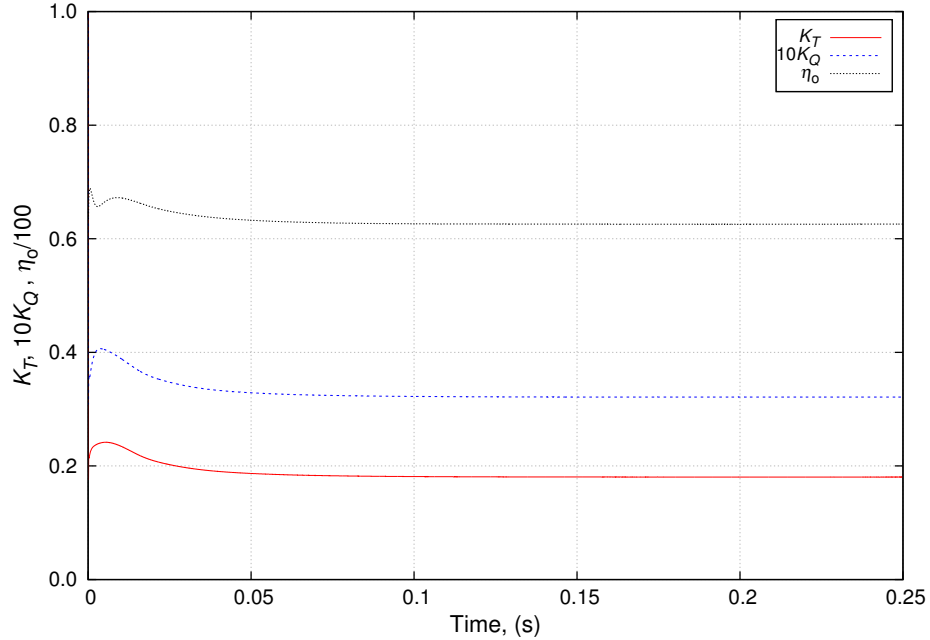


Figure 4.7: Convergence of K_T , $10K_Q$ for $J = 0.7$ using transient solver for GRID-B.

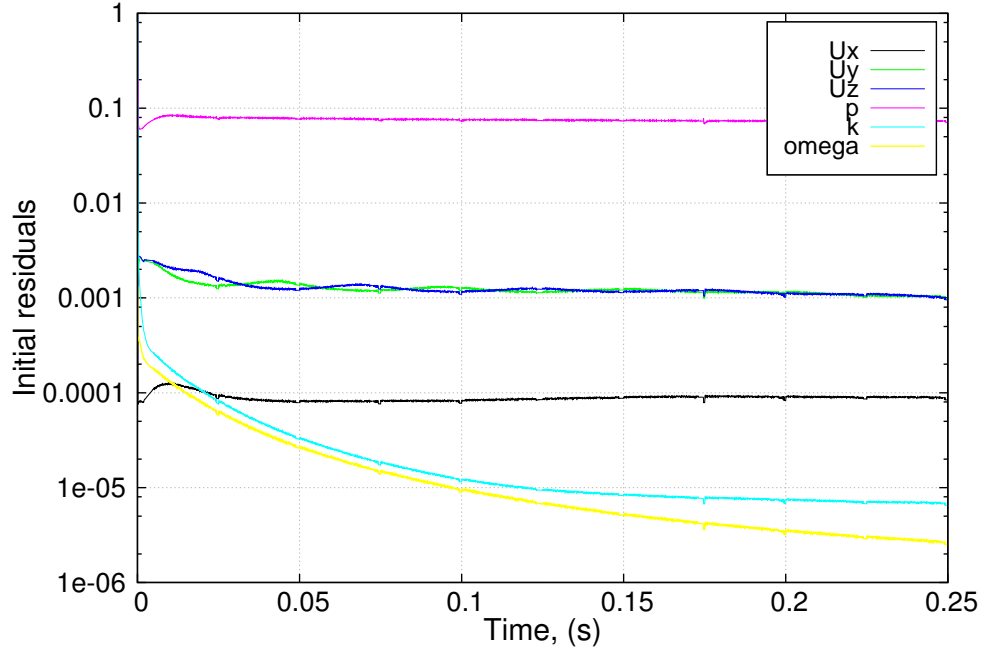


Figure 4.8: Residual convergence using transient solver for GRID-B at $J = 0.7$.

validation error and the numerical uncertainty are presented in Table 4.4. It is observed that the numerical uncertainties for K_T are less than 5%, and for K_Q are less than 3%. Even for the fine grid resolution, the grid uncertainty is close to the other grid resolutions. The validation error for K_T and K_Q is less than 4.0%. The convergences of K_T , $10K_Q$ and η_o for $J = 0.7$ are shown in Figure 4.7. The residual convergences are shown in Figure 4.8. The comparison of open water prediction with the measured data performance is shown in Figure 4.9. Good agreement was found for K_T , $10K_Q$, whereas the efficiency η_0 shows deviation for higher advance coefficients.

4.1.3 Body-Force Method

4.1.3.1 Computational Domain and Grid Generation

For the body-force modelling of the KP505 propeller, a rectangular computational domain was created for open water simulation. The grid is shown in Figure 4.10. The

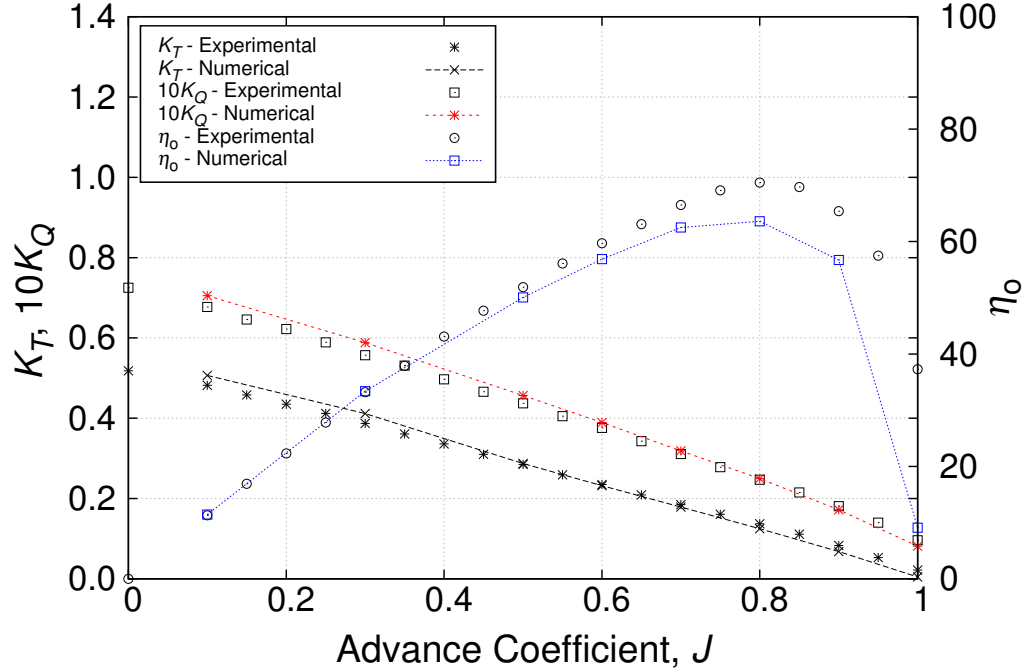


Figure 4.9: Open water simulation of KP505 using transient solver for GRID-B.

inlet boundary was set at $4D$ and the outlet boundary was set at $8D$ from the propeller plane. The side boundaries were set at $2D$ from the centre plane. A cylindrical cell zone was defined for the propeller disk where the body-force was applied to the cells.

4.1.3.2 Grid Dependency Study

The effect of the number of cells (M_R) along the radial direction of the propeller disk was studied using the transient solver with local velocity body-force model, LV-BFM for advance coefficient $J = 0.70$. The sampling was set $d = 0.3D$ upstream from the propeller plane. In numerical simulation, $M_R = 8, 16, 32,$ and 64 were used for the grid dependency study. Figure 4.11 shows the effect of the number of cells on numerical prediction accuracy with respect to the experimental data. It is found that $M_R = 16$ and higher shows good convergence with the experimental results.

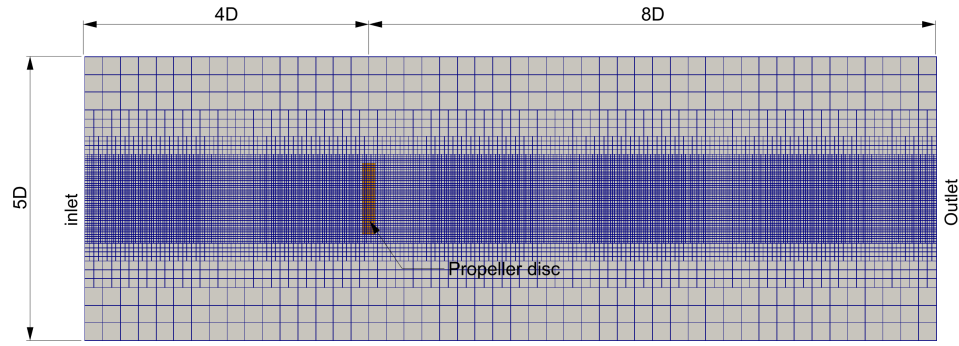


Figure 4.10: Computational domain for KP505 open water simulation using body-force method.

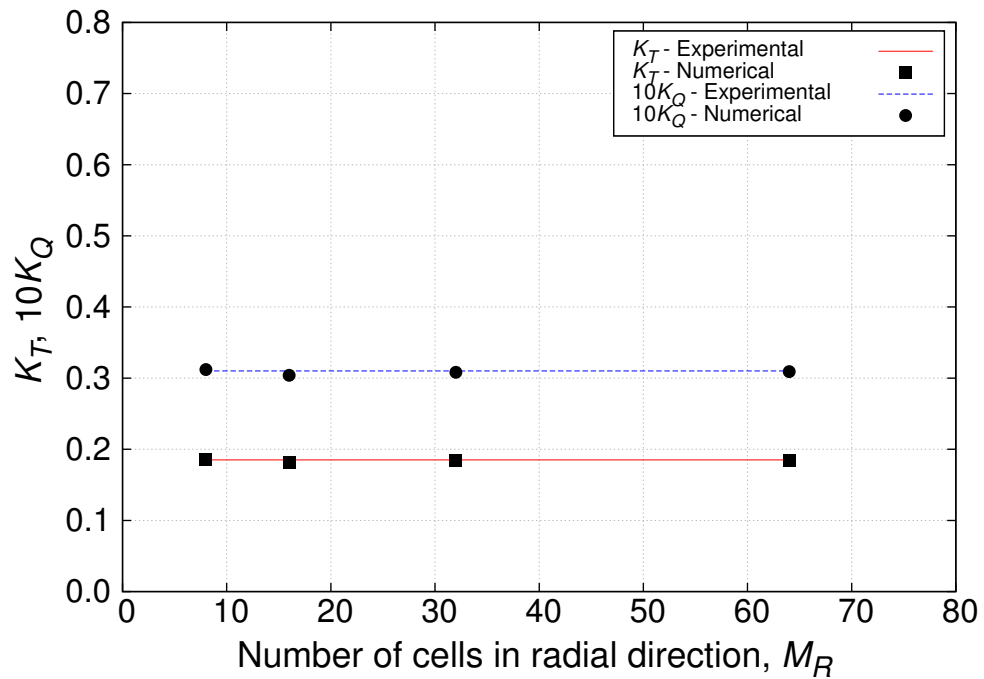


Figure 4.11: Effect of number of cells in radial direction.

4.1.3.3 Sampling Plane Distance

The effect of the velocity sampling plane distance on the propeller performance predicted by the body-force method was studied from $d/D = 0.10$ to $d/D = 0.40$,

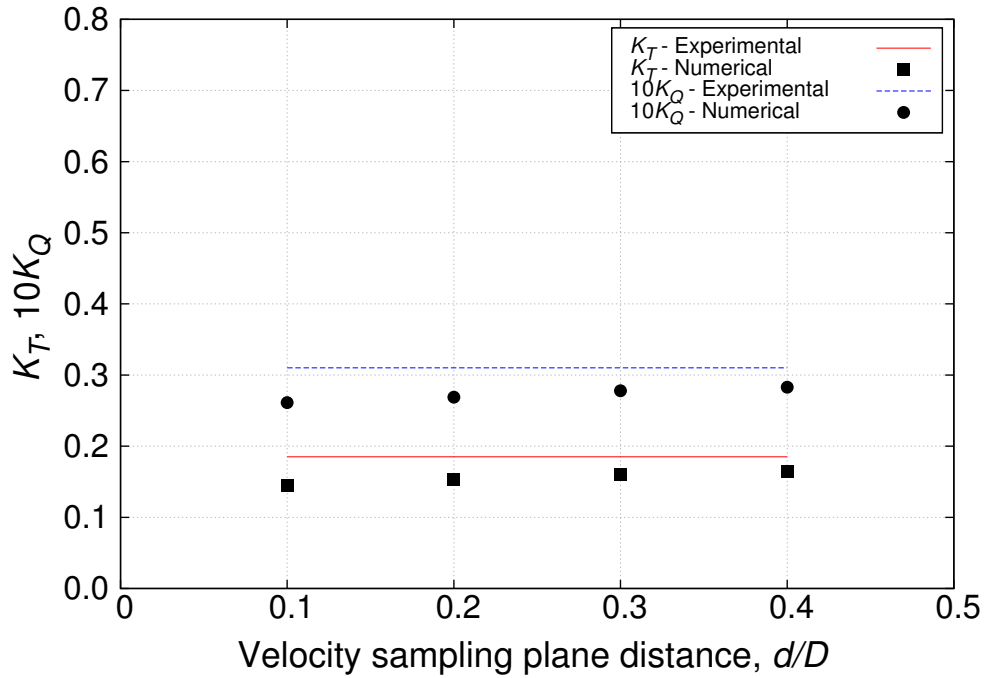


Figure 4.12: Effect of velocity sampling plane distance.

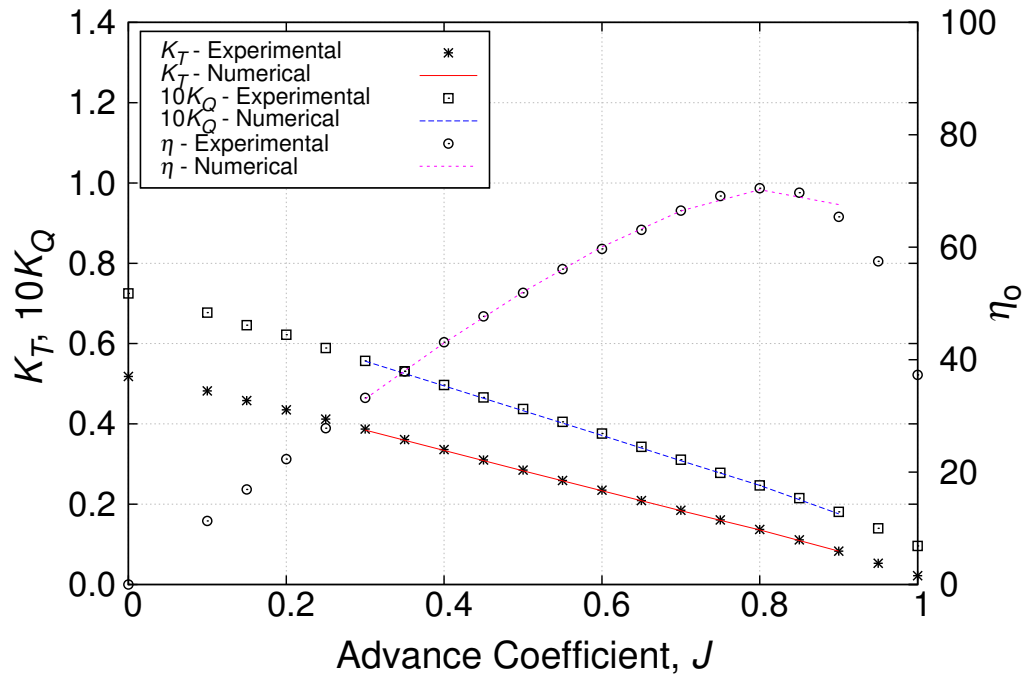


Figure 4.13: Propeller open water characteristics of KP505 using body-force method.

where d is the offset distance of the sampling plane from the propeller plane, and D is the diameter of the propeller. The LV-BFM was used for body-force modelling without induced velocity correction. Comparison between the numerical data and experimental values is shown in Figure 4.12 for $J = 0.70$. The influence of the propeller disk position on the incoming velocity is higher for lower offset distances. The influence effect is not significant for $d/D = 0.30$ and higher.

Then $M_R = 32$ was used for different advance coefficients for the validation of the open water data. Comparison between the numerical results and experimental data shows good agreement in Figure 4.13.

4.2 MP687 Test Case

4.2.1 Propeller Geometry

The propeller geometry for the self-propulsion simulation of the JBC hull is shown in Figure 4.14. The propeller is designated MP687. The principal particulars of the MP687 propeller are listed in Table 4.5. The surface file for the propeller geometry and open water data were obtained from the T2015 workshop website. The open water performance tests were carried out at NMRI, Japan.

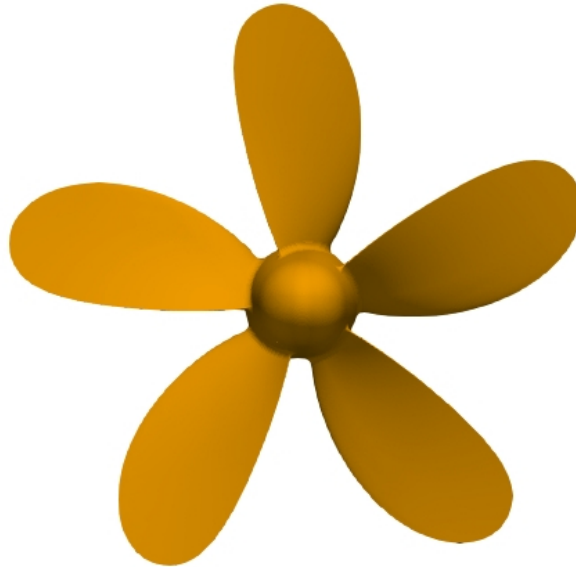


Figure 4.14: MP687 propeller geometry.

4.2.1.1 Computational Domain and Grid Generation

A similar cylindrical computational domain to that used for the KP505 propeller was also used for the grid generation of MP687 propeller for open water simulation. The

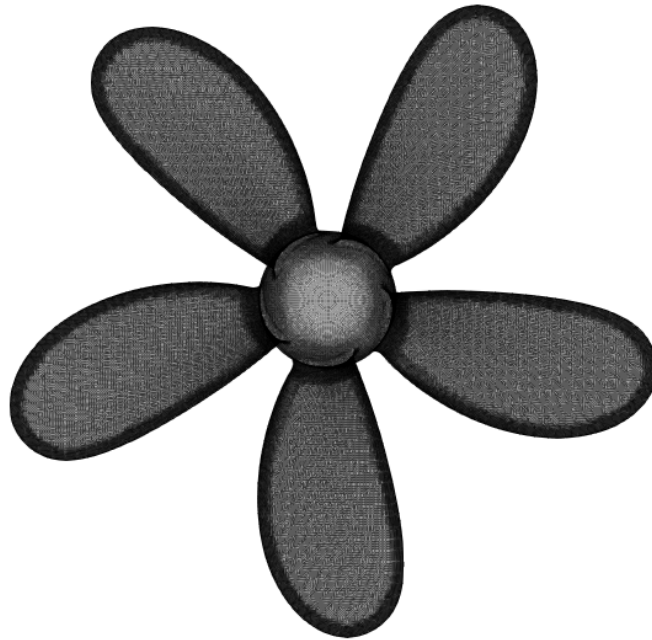


Figure 4.15: Grid distribution on the propeller blade and hub of MP687.

grid distribution on the propeller blade is shown in Figure 4.15. The computational grids for open water simulations of the MP687 propeller are summarized in Table 4.6.

4.2.1.2 Steady Simulation

The MRF method was used to perform the steady simulation of the MP687 propeller using the steady solver. The grid uncertainty for the numerical results was studied

Table 4.5: Principal particulars of MP687 propeller.

| Item | Full scale | Model scale |
|---------------|------------|-------------|
| Type | FP | FP |
| No. of blades | 5 | 5 |
| D (m) | 8.12 | 0.203 |
| $P/D(0.7R)$ | 0.75 | 0.75 |
| $Ae/A0$ | 0.5 | 0.5 |
| Rotation | Right hand | Right hand |
| Hub ratio | 0.18 | 0.18 |

Table 4.6: Computational grids for MP687 propeller open water simulation

| Grid | Stator | Rotor | Average y^+ |
|--------|--------|---------|---------------|
| GRID-A | 797083 | 547454 | 20.03 |
| GRID-B | 797083 | 1632402 | 20.57 |
| GRID-C | 797083 | 2736403 | 20.71 |
| GRID-D | 797083 | 3113553 | 15.20 |

Table 4.7: Grid dependency of open water performance at $J = 0.7$ using steady solver.

| GRID | h_i/h_1 | K_T | $ E\%D $ | $ U_{SN}\%S $ | $P = 1.79$ | | $ U_{SN}\%S $ |
|--------|-----------|--------|----------|---------------|------------|----------|---------------|
| | | | | | $10K_Q$ | $ E\%D $ | |
| GRID-A | 1.43 | 0.0864 | 0.29 | 0.63 | 0.1669 | 10.62 | 6.72 |
| GRID-B | 1.17 | 0.0870 | 0.38 | 0.08 | 0.1640 | 8.70 | 4.97 |
| GRID-C | 1.03 | 0.0862 | 0.55 | 0.18 | 0.1623 | 7.54 | 4.13 |
| GRID-D | 1.00 | 0.0876 | 1.01 | 0.23 | 0.1637 | 8.50 | 3.90 |

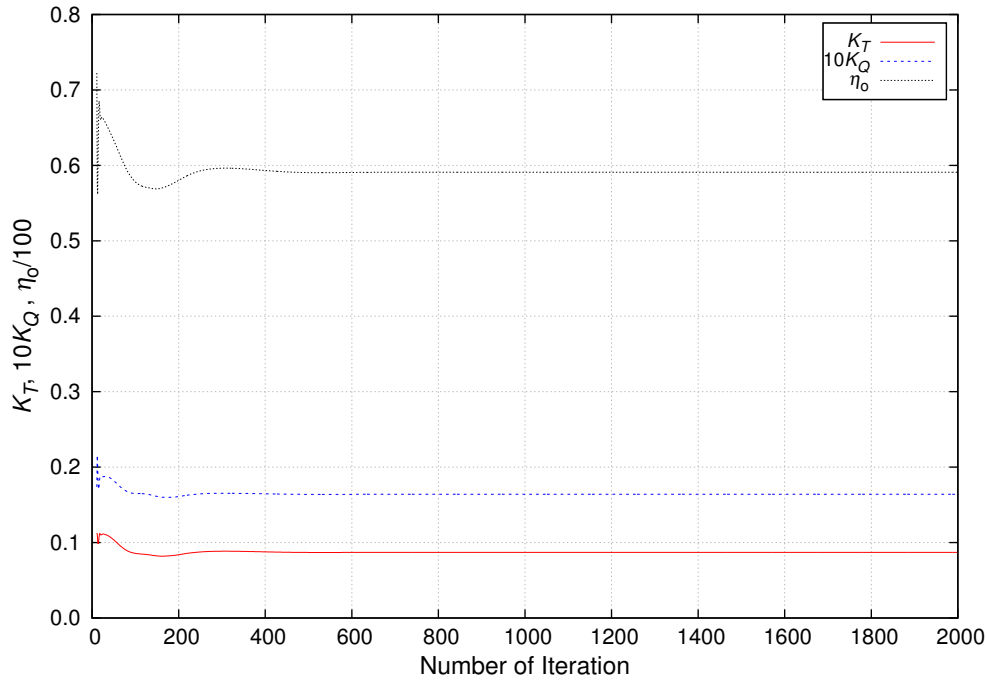


Figure 4.16: Convergence history of K_T , K_Q and η_0 using steady solver for GRID-B at $J = 0.70$.

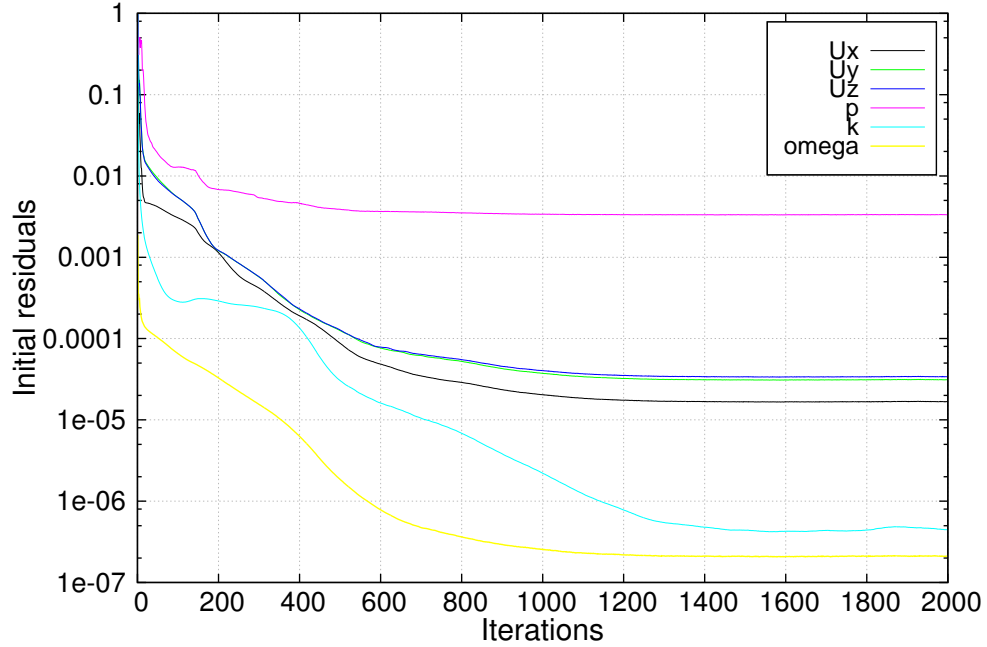


Figure 4.17: Residuals convergence for advance coefficient $J = 0.70$ for GRID-B.

using the four grids in Table 4.6 for $J = 0.70$. The validation error and the uncertainty of the numerical results is shown in Table 4.7. The validation error of K_T for the four grids is around 1% and for K_Q is around 8% except for the coarse grid. The numerical uncertainty for the fine grids are similar. The convergences of K_T , K_Q and η_0 for GRID-B are shown in Figure 4.16. The residuals are also plotted in Figure 4.17. The open water performance was simulated using the steady solver for different advance coefficients and the results are compared with experimental data in Figure 4.18.

4.2.1.3 Unsteady Simulation

The unsteady numerical open water simulations for the MP687 propeller were also carried out using transient solver *pimpleDyMFoam* for the four grids at $J = 0.70$. The validation error and numerical uncertainty are presented in Table 4.8. The convergences of force coefficients are shown in Figure 4.19. The residuals are also

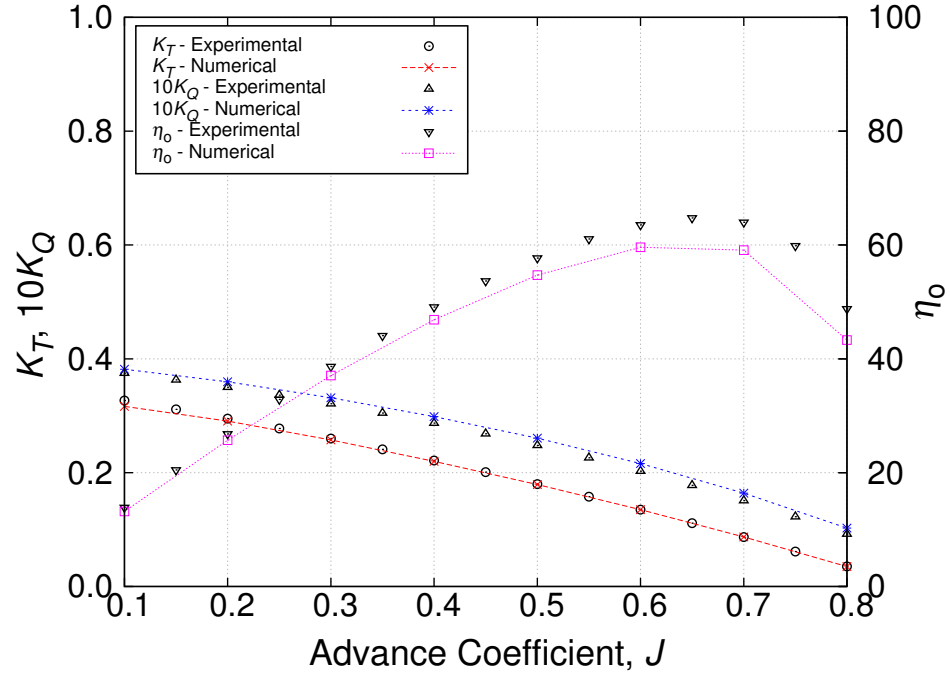


Figure 4.18: Open water simulation of MP687 propeller using steady solver for GRID-B.

shown in Figure 4.20. The change in residuals after 0.2 is not significant and the solution can be considered converged. Figure 4.21 shows the comparison of K_T , $10K_Q$ and η with the experimental data for a range of advance coefficients for GRID-B, and the comparison shows better agreement than steady simulation.

Table 4.8: Grid dependency of open water performance at $J = 0.7$ using unsteady solver.

| GRID | h_i/h_1 | K_T | $ E\%D $ | $ U_{SN}\%S $ | $10K_Q$ | $ E\%D $ | $ U_{SN}\%S $ |
|--------|-----------|--------|------------|---------------|---------|------------|---------------|
| | | | $P = 1.38$ | | | $P = 1.92$ | |
| GRID-A | 1.43 | 0.0863 | 0.41 | 7.92 | 0.1654 | 9.64 | 3.96 |
| GRID-B | 1.17 | 0.0889 | 2.56 | 5.51 | 0.1648 | 9.21 | 2.88 |
| GRID-C | 1.03 | 0.0880 | 1.45 | 4.45 | 0.1630 | 8.00 | 2.41 |
| GRID-D | 1.00 | 0.0895 | 3.20 | 4.11 | 0.1635 | 8.33 | 2.28 |

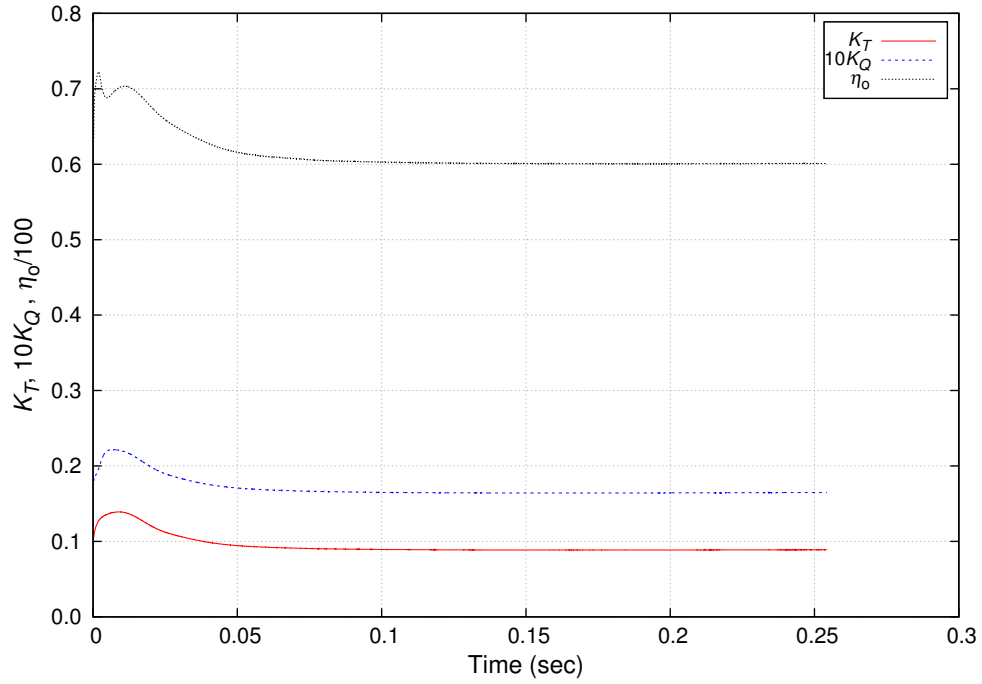


Figure 4.19: Convergence history of K_T , K_Q and η_0 using transient solver for GRID-B at $J = 0.70$.

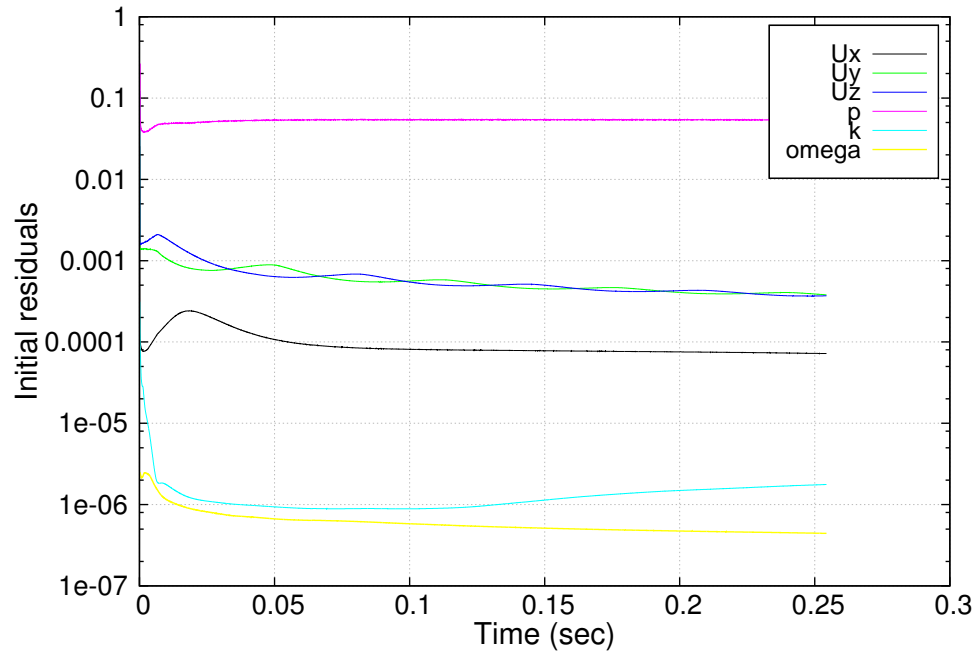


Figure 4.20: Residuals convergence for GRID-B at advance coefficient $J = 0.70$.

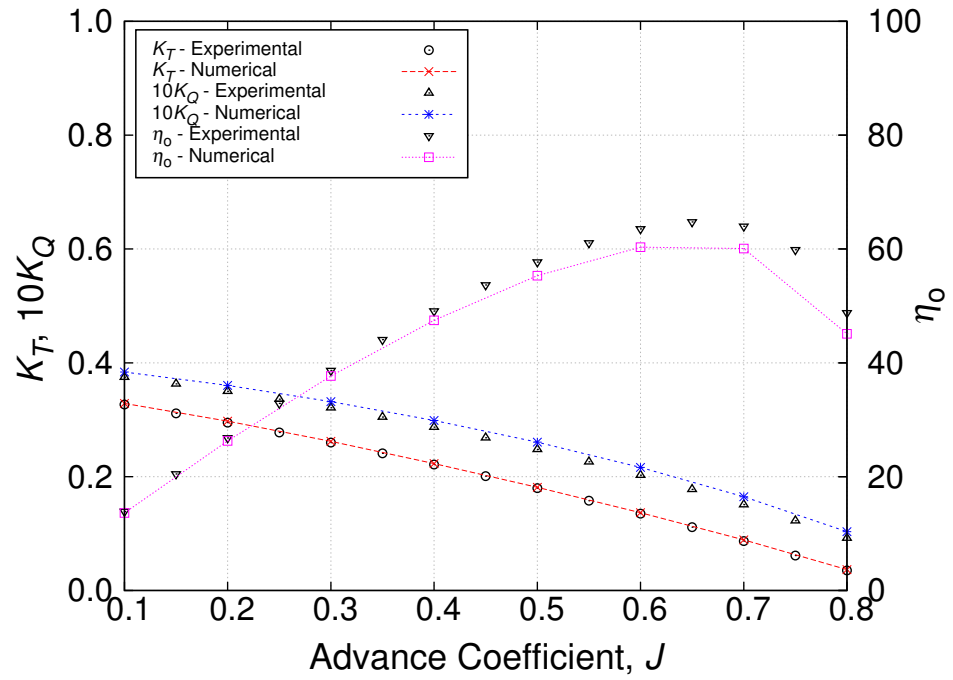


Figure 4.21: Open water simulation of MP687 propeller using transient solver for GRID-B.

4.3 NRC-IOT Propeller Test Case

4.3.1 Geometry

A rectangular computational domain was created similar to the KP505 propeller domain to study the open water test of the NRC-IOT propeller using the body-force method. The principal particulars are listed in Table 4.9. A sampling plane for the velocity inlet was set $1.0D$ upstream from the propeller plane.

Table 4.9: Principal particulars of the NRC-IOT propeller.

| Item | Model scale |
|---------------|-------------|
| Type | FP |
| No. of blades | 4 |
| D (m) | 0.1205 |
| $P/D(0.7R)$ | 1.27 |
| $Ae/A0$ | 0.906 |

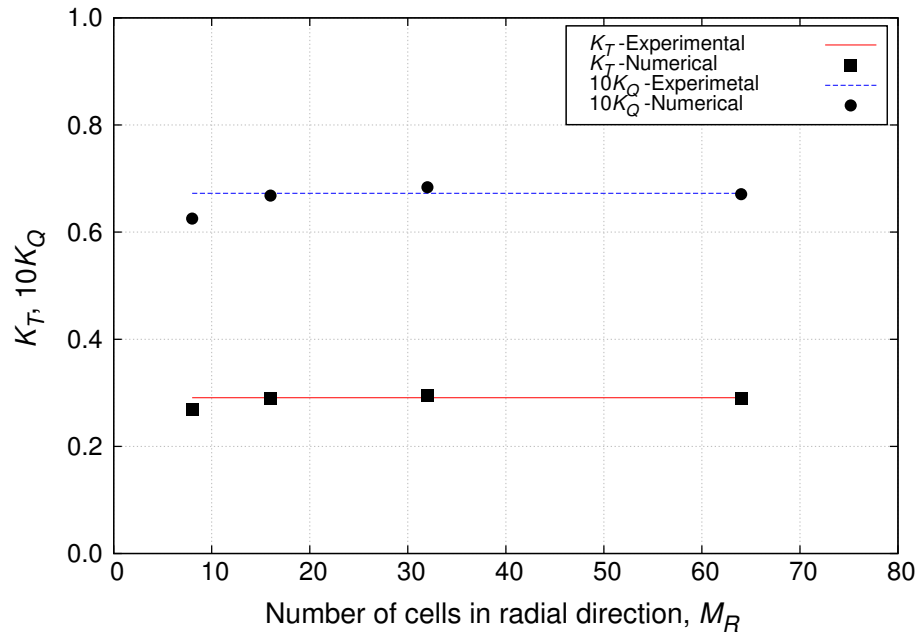


Figure 4.22: Effect of the cell numbers on propeller parameters at $J = 0.70$ using transient solver.

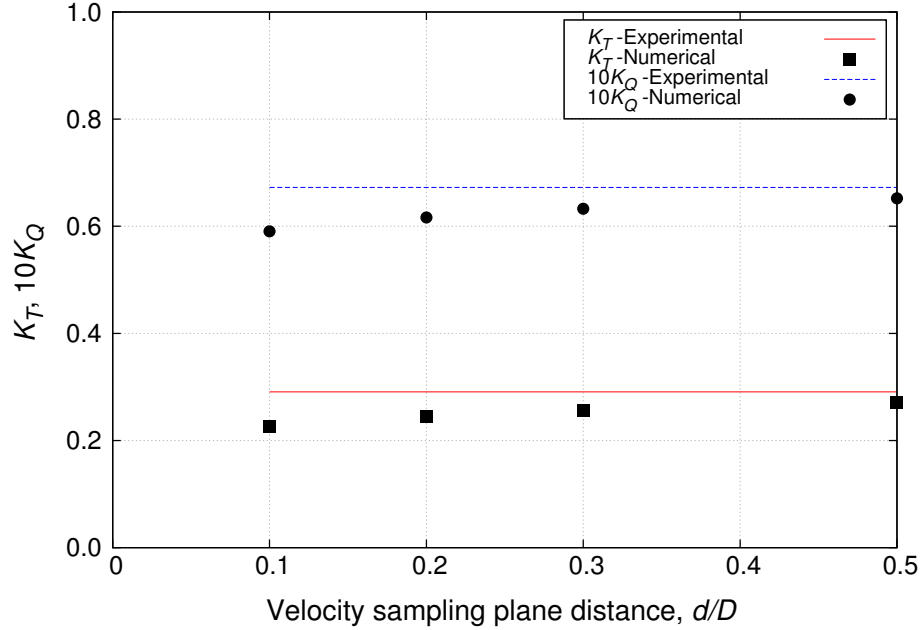


Figure 4.23: Effect of the velocity sampling plane distance on propeller parameters at $J = 0.70$ using transient solver.

4.3.2 Numerical Results

The effect of number of cells in the radial direction of the propeller disk was studied for four resolutions, $M_R = 8, 16, 32$ and 64 . In these cases, the velocity sampling plane was set at $1.0D$ upstream from the propeller plane. The simulations were performed for advance coefficient, $J = 0.70$. For grid resolution 16 and more along the radial direction, the numerical results show good agreement with the experimental data as seen in Figure 4.22. The effect of velocity sampling plane distance from the propeller plane was also investigated. The open water performance was calculated for $d/D = 0.1, 0.2, 0.3$ and 0.5 using the LV-BFM without induced velocity correction. The numerical results are compared with the experimental data in Figure 4.23. The effect of sampling plane distance greatly influences the numerical prediction when it is close to the propeller disk due to the higher input velocity to the propeller disk. Then the open water simulations for the other advance coefficients were carried out using $d/D =$

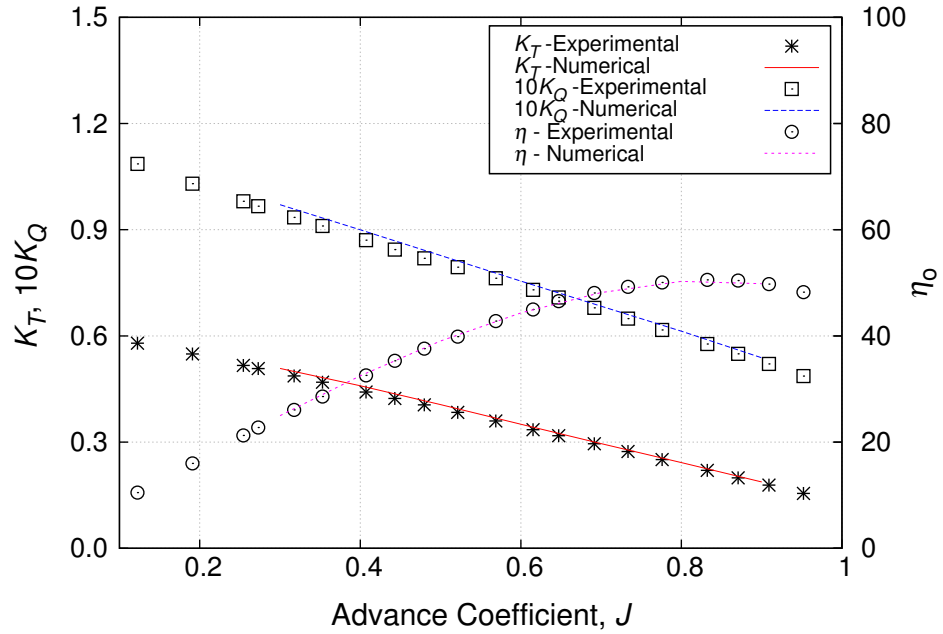


Figure 4.24: Comparison of open water data of NRC-IOT propeller using transient solver.

1.0 and $M_R = 32$. The comparison of numerical results and experimental results is shown in Figure 4.24. The numerical results agreed well with the experimental data.

This page intentionally left blank.

Chapter 5

Numerical Wave Tank Validation

The numerical wave tank validation is an important step before application in wave-body interaction simulations. In this chapter, the available generation modules are studied for a steep wave. Depending on the numerical results obtained by different modules the most efficient module is adopted for the grid dependency and time dependency studies. The effect of turbulence model on numerical wave generation was also studied. Based on the findings of the grid dependency and time step size dependency analysis, the optimum settings are used for wave run-up study of a truncated square cylinder (Ali et al., 2017a). The detailed numerical results validation can be found in Appendix-B. Since the grid resolution and time step size depends on the wave steepness and wave length, the wave validation also was studied for the waves prior to the self-propulsion simulation in waves.

To study the effect of ship motion on propeller-hull interaction in waves, the numerical wave tank without ship model was validated for the waves listed in Table 5.1 for the KCS model. The numerical wave elevations at the three different locations as shown in Figure 5.1 were compared with the analytical wave elevation. The details of the validation process are described in the following subsections.

5.1 Computational Domain

The schematic diagram of the numerical wave tank is shown in Figure 5.1. The computational domain with grid distribution for the wave validation with the virtual ship model is shown in Figure 5.2. The inlet boundary was set $1.0L_{pp}$ in front of the ship model. The outlet boundary was set $3.0L_{pp}$ behind the ship model, and the side boundaries were set $1.5L_{pp}$ from the center plane. The wave was generated at the inlet boundary and the numerical wave damping zone was used for wave damping in front of the outlet. The bottom boundary was set $1.5L_{pp}$ from the calm water surface.

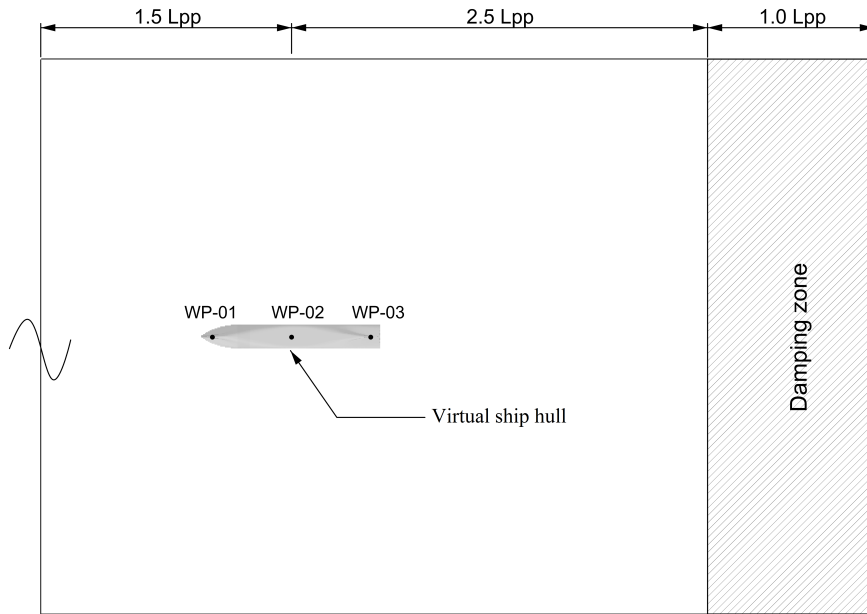


Figure 5.1: Computational domain for numerical wave tank validation.

Table 5.1: Wave conditions for numerical tank validation

| No | C1 | C3 |
|----------------------------|--------|--------|
| Wave length, λ (m) | 4.7351 | 8.3683 |
| Wave height, H (m) | 0.0743 | 0.1475 |

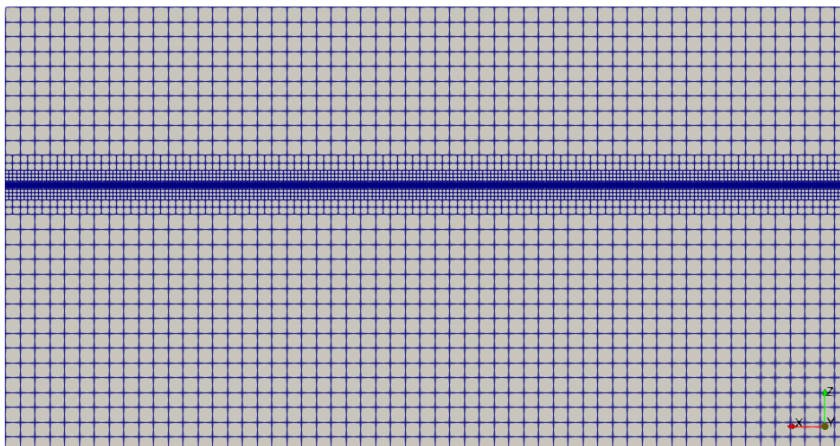


Figure 5.2: Grid distribution in the computational domain.

The same grid resolutions as the grid for the bare hull resistance study were used for wave validation. The computational grids were generated using blockMesh and navalSnappyHexMesh. For incoming wave simulation, a computational domain with a symmetry plane was generated to reduce the computational cost. The symmetry plane was set at the centreplane.

5.2 Grid Dependency

The sensitivity of grid resolution on the numerical wave elevation was studied for the wave C1 with three grids resolutions having $\lambda/\Delta x = 40, 50$ and 60 and $H/\Delta z = 5, 6,$ and 7 , where is H is the wave height. The normalized wave elevation with respect to the wave amplitude $A_1 = H/2.0$ are compared at longitudinal position of the forward perpendicular (WP-01), midship section (WP-02), and at the aft perpendicular (WP-03). The numerical simulations for grid dependency were carried out using time step size TS-03 ($T_w/\Delta t = 500$). Figure 5.3 shows the comparison

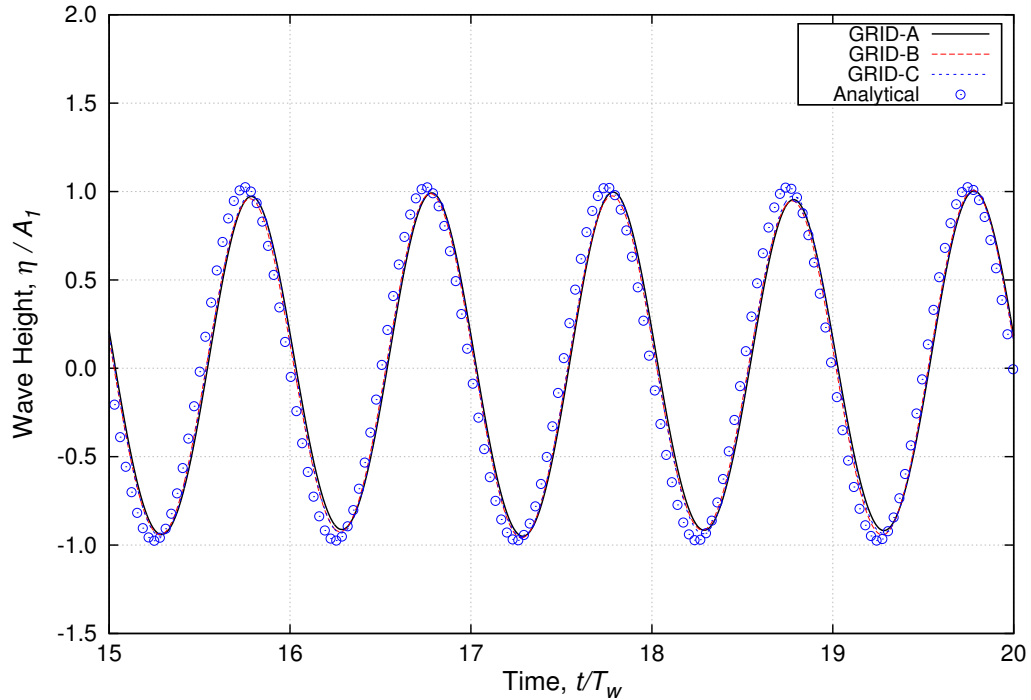


Figure 5.3: Comparison of wave elevation at WP-02 using TS03 of wave C1.

between the analytical and numerical prediction. It is observed that the GRID-C prediction shows good agreement with the analytical values.

5.3 Time Step Size Dependency

For the study of the influence of time step size on the numerical wave generation three time step sizes, TS01($T_w/\Delta t = 125$), TS02($T_w/\Delta t = 250$), TS03($T_w/\Delta t = 500$), for GRID-C were used in numerical simulations. The comparison is shown in Figure 5.4 for wave probe WP-02. It is seen that TS-03 predicts the wave elevation accurately. From the comparison, it was found that both TS-01 and TS-02 under predict the wave elevation.

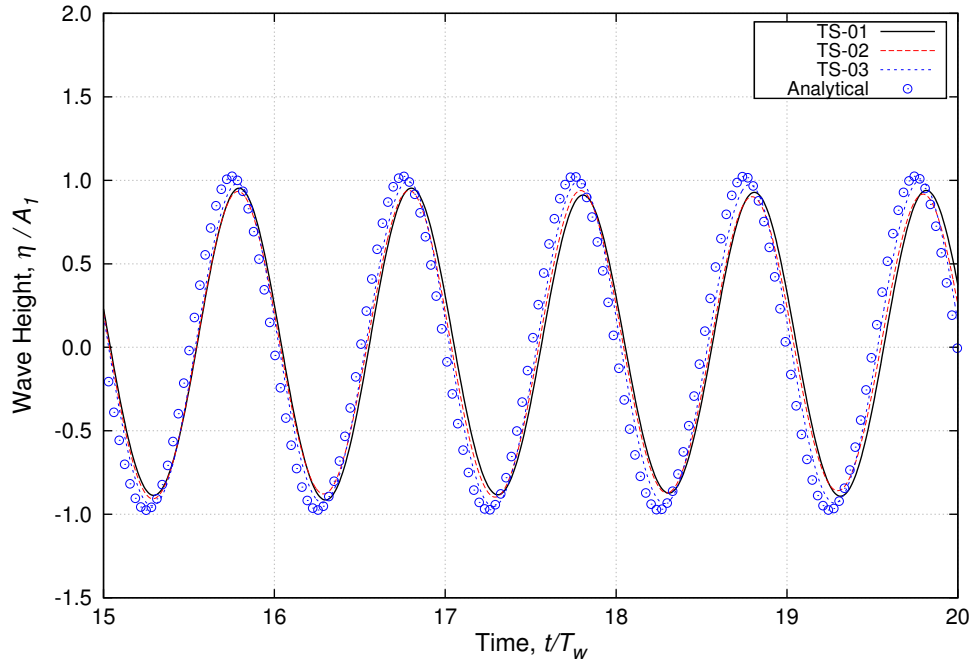


Figure 5.4: Comparison of wave elevation at WP-02 using GRID-C of wave C1.

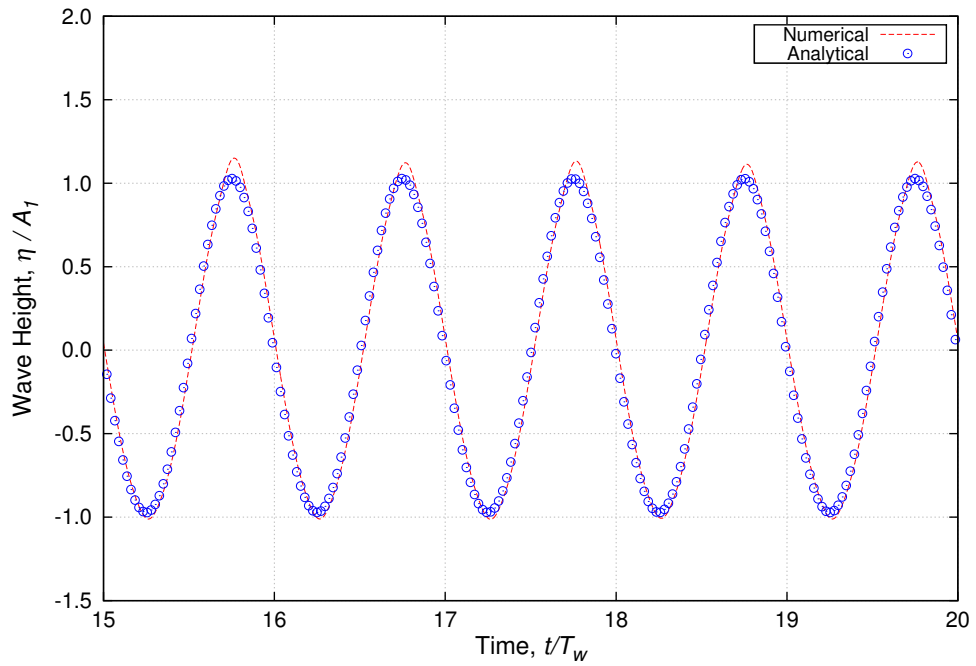


Figure 5.5: Comparison of wave elevation at WP-02 using GRID-C of wave C3.

5.4 Wave Validation

For the self-propulsion simulation in waves, the C3 wave was validated against the analytical wave elevation. The grid resolution for C3 is $\lambda/\Delta x = 100$ and $H/\Delta z = 14$ with the time step size $T_w/\Delta t = 500$ for the numerical wave simulation. The numerical wave elevation at the midship section is compared with the analytical wave elevation in Figure 5.5. The wave crests are slightly over predicted compared with analytical wave elevation.

Chapter 6

Self-Propulsion Simulation

This chapter presents the validation of numerical self-propulsion simulation of the selected ship models. The numerical self-propulsion simulations for the KCS and JBC model were carried out using detailed propeller geometry. The developed body-force models were also used for self-propulsion simulations for the KCS model and the Fishing vessel. For the self-propulsion simulation with detailed propeller geometry, the developed dynamic motion class was used. Since the code was developed for the constant rotational speed of the propeller, fixed rpm was used for propeller rotation.

6.1 KCS Test Case

The self-propulsion simulations for the KCS model were performed for the even keel condition, with sinkage and trim, and in head wave conditions. The test conditions for the self-propulsion simulations are presented in Table 6.1.

Table 6.1: Test cases for the validation of self-propulsion simulation of KCS model.

| Case | 6.1 | 6.2 | 6.3 |
|----------------------|---|------------------|------------------|
| Model | KCS | KCS | KCS |
| Wave | Calm | Calm | Head sea |
| Condition | Self-prop (ship) | Self-prop (ship) | Self-prop (ship) |
| L_{PP} | 7.2786 | 7.2786 | 7.2786 |
| Fn | 0.26 | 0.26 | 0.26 |
| $Rn \times 10^7$ | 1.26 | 1.26 | 1.26 |
| Rudder | without | without | without |
| Propeller | with | with | with |
| Attitude* | FR_0 | $FR_{z\theta}$ | $FR_{z\theta}$ |
| Validation variables | Thrust, resistance, wave elevation, prop factor, mean flow velocity | | |
| EFD provider | NMRI | | |

*Hull Attitude Definitions:

FR_0 = Zero sinkage and zero trim at the design speed.

$FR_{z\theta}$ = Free to heave and pitch.

6.1.1 Geometry

The self-propulsion for the KCS ship model was carried out for fixed rpm of the propeller. The ship model was equipped with the KP505 propeller as shown in Figure 6.1. The rudder was not included with the ship model during the model test.

6.1.2 Computational Domain and Boundary Conditions

From the bare hull resistance validation and propeller open water test validation, the computation grid for numerical self-propulsion simulation, the optimum bare hull grid was combined with the propeller grid. For the self-propulsion simulation of the KCS model, the bare hull grid GRID-C was combined with propeller grid GRID-B.



Figure 6.1: Geometry for KCS self-propulsion.

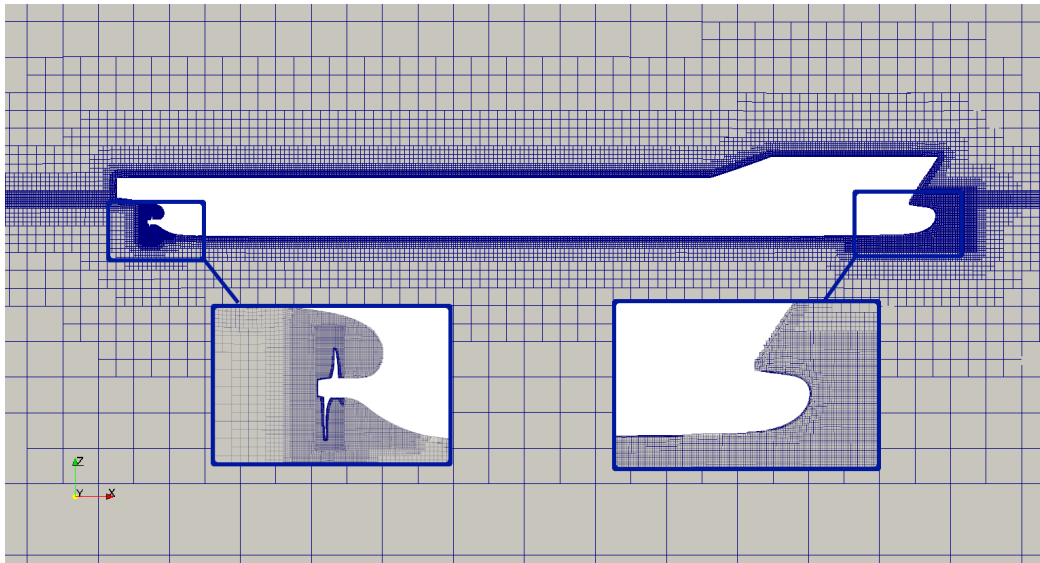


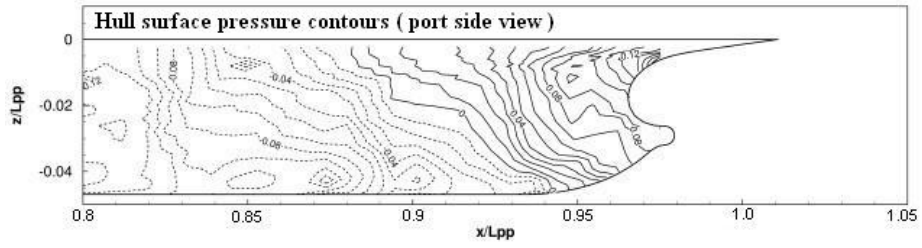
Figure 6.2: Computational grid for self-propulsion of KCS model.

Due to the non-symmetric condition of the propeller wake, the whole computational domain was used in this numerical simulation. The same coordinate system as the bare hull case was used for the self-propulsion simulation. The grid distribution using the actual propeller geometry is shown in Figure 6.2. For the self-propulsion simulation using the body-force method, the bare hull grid GRID-C was used. To reduce the computational time, a steady simulation was carried out initially, and then the steady solution was used as the initial condition for the unsteady simulation.

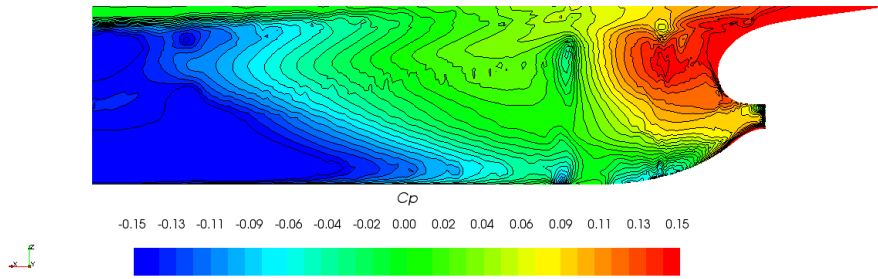
The self-propulsion simulation using the body-force model, as described in section 2.8 was carried out for $n = 9.5$ at the design speed $Fn = 0.26$. The incoming velocity to the propeller domain was the average of the local velocity on the sampling plane which was set in the upstream of the propeller domain. The local velocity on the sampling plane was also used as input velocity in the propeller body-force calculation to improve the velocity distribution and the propulsion factor prediction. The diameter of the actuator disk was set equal to the diameter of the propeller and the longitudinal extent is the width of the projected chord length on the propeller plane.

6.1.3 Self-Propulsion at Restrained Even Keel Condition

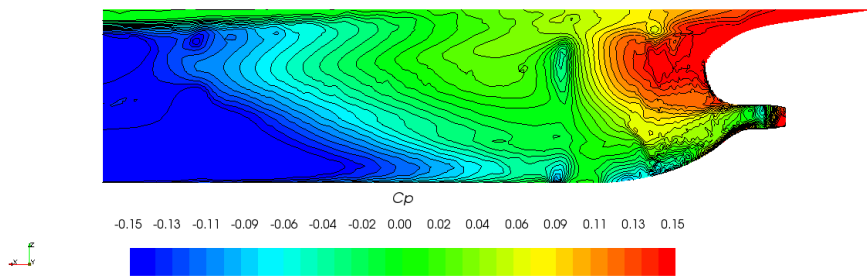
The self-propulsion simulations were performed using the detailed propeller geometry, the body-force model based on fixed input velocity, and the body-force model using local velocity. The numerical results from the self-propulsion simulation are compared in Table 6.2. For turbulence modelling, $k - \omega$ SSTCC and $k - \omega$ SST were used for detailed propeller cases. The Skin Friction Correction ($SFC = R_{T(SP)} - T$) using $k - \omega$ SSTCC turbulence model with detailed propeller geometry shows less than 1.0 % error against the experimental values. However, the thrust and torque were over predicted by a small amount. From the comparison it can be concluded



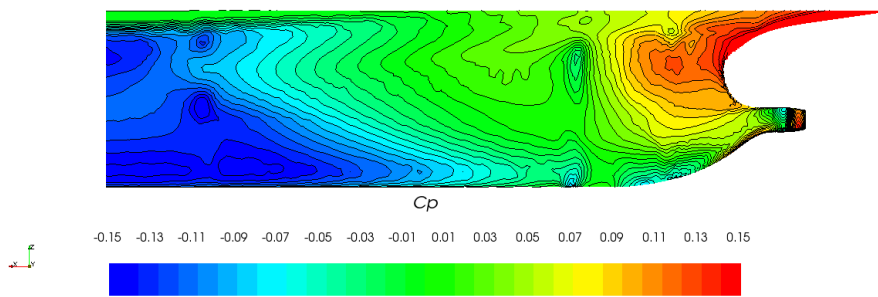
(a) Experimental



(b) Detailed propeller geometry



(c) FV-BFM



(d) LV-BFM

Figure 6.3: Dynamic pressure distribution on the stern of KCS for self-propulsion.

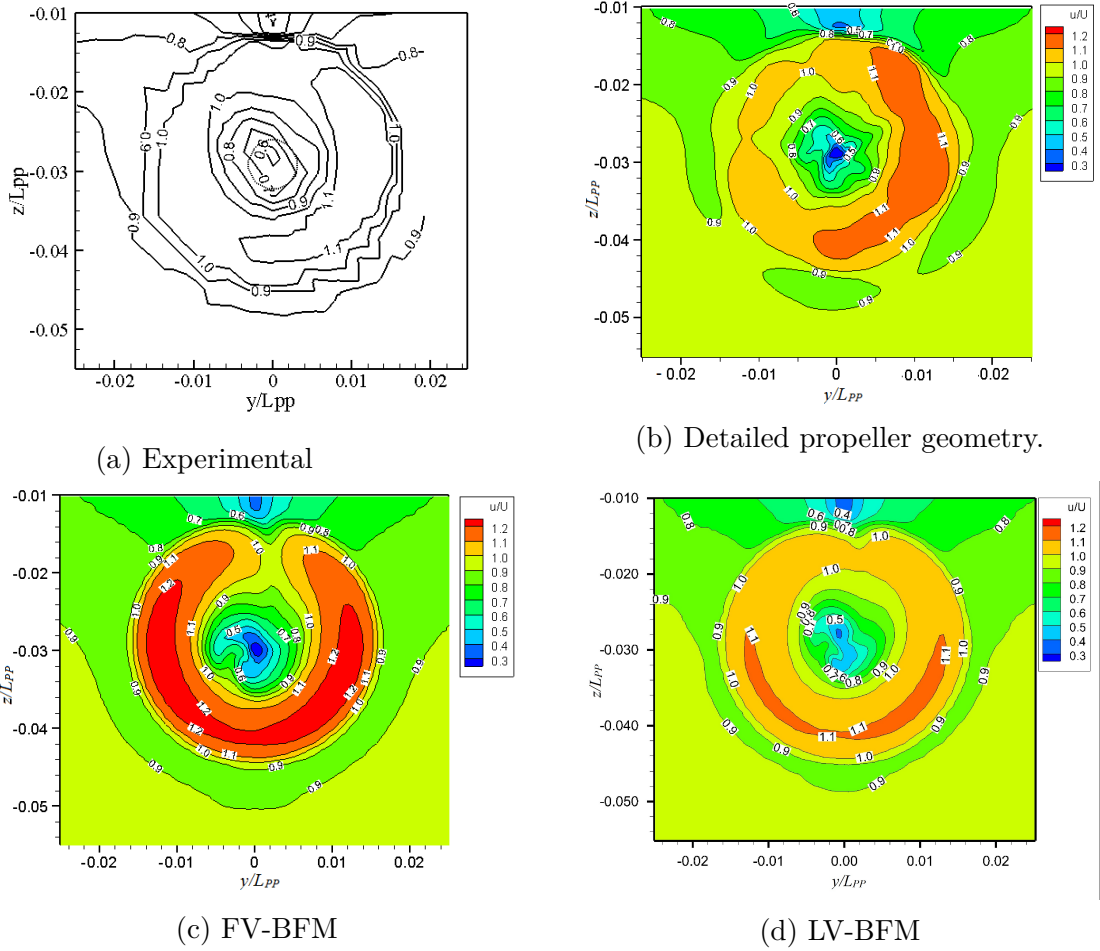


Figure 6.4: Axial velocity distribution at $0.25D$ downstream of the propeller plane.

Table 6.2: Numerical results of self-propulsion simulation.

| Method | $R_{T(SP)}$ (N) | C_T | Thrust, T (N) | Torque, Q (N-m) | $R_{T(SP)} - T$ (N) | $ E\%D $ | K_T | K_Q | V_A (m/s) | w |
|--------------------|-----------------|----------|-----------------|-------------------|---------------------|----------|--------|--------|-------------|--------|
| $k - \omega$ SST | 91.05 | 4.00E-03 | 62.79 | 2.7314 | 28.26 | 1.990 | 0.1781 | 0.0310 | 1.695 | 0.2281 |
| $k - \omega$ SSTCC | 92.88 | 4.08E-03 | 63.49 | 2.7503 | 29.39 | 0.852 | 0.1801 | 0.0312 | 1.689 | 0.2309 |
| LV-BFM | 89.00 | 3.91E-03 | 57.04 | 2.4880 | 31.96 | 1.712 | 0.1620 | 0.0280 | 1.776 | 0.1910 |
| FV-BFM | 88.55 | 3.89E-03 | 71.66 | 2.9391 | 17.09 | 13.359 | 0.2033 | 0.0334 | 1.570 | 0.2851 |
| Experimental | | 3.97E-03 | | | | | 0.1700 | 0.0288 | | |

that self-propulsion with detailed propeller geometry and $k - \omega$ SSTCC shows better accuracy than the other approaches although the computation time is longer than that for the simple body-force method. The simulation time can be reduced considerably by using the steady solution as the initial condition for the unsteady simulation.

6.1.3.1 Pressure Distribution

Figure 6.3 illustrates the pressure distribution on the stern region of the KCS model using the detailed propeller geometry and two body-force models. A difference is observed on the lower region of the stern bulb due to the incoming flow alteration by the propeller action itself. The overall pressure distribution on the hull surface shows a good agreement with experimental results.

6.1.3.2 Flow Velocity

The axial velocity distribution at $0.25D$ downstream of the propeller plane ($x/L_{PP} = 0.9910$ from the forward perpendicular) with the working propeller is compared in Figure 6.4 with the experimental data. The comparison shows that, although the body-force method can predict the K_T , K_Q , and effective wake fraction w with reasonable accuracy, it failed to predict the velocity distribution.

The velocity components obtained for self-propulsion simulation using $k - \omega$ SSTCC with working propeller are compared at $0.25D$ behind the propeller plane and $z/L_{PP} = -0.0291$ with the experimental data in Figure 6.5. The comparison shows higher deviation near the hub center. The results indicate the hub vortex strength is under predicted.

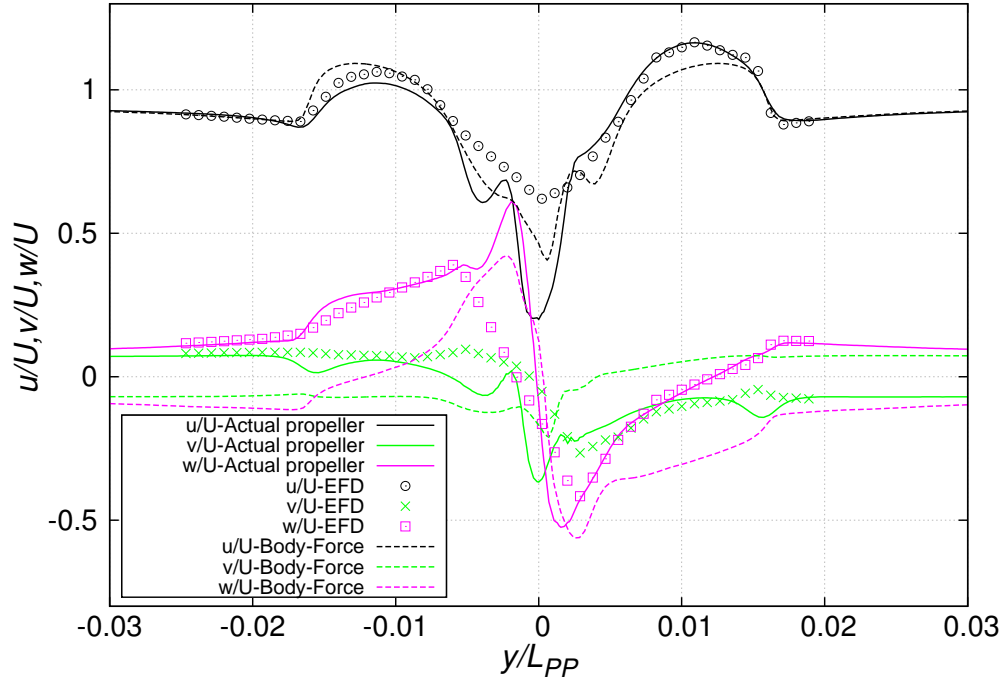


Figure 6.5: Velocity components comparison at $x/L_{PP} = 0.9910$ ($0.25D$ downstream of the propeller plane) and $z/L_{PP} = -0.0291$.

6.1.4 Self-Propulsion with Sinkage and Trim

The effect of ship motion on self-propulsion parameters was investigated for the KCS hull with the KP505 propeller. The computational grid used for self-propulsion for the even keel condition was used for numerical simulation of self-propulsion with ship motions. The ship model was free to heave and pitch only. Mesh morphing method was adopted to consider the ship motion in numerical simulations. The simulation was carried out using the $k - \omega$ SSTCC turbulence model. The results from the numerical simulation are presented in Table 6.3. For the dynamic case, the skin friction correction SFC is about 21% higher than the even keel condition. The wake fraction w , for the dynamic condition is also reduced at the same ship speed and propeller rotational speed. In the case of propeller design, these changes should be included in the optimum propulsive system design considering the ship motion.

Figure 6.6 presents the time history of residual convergence for the numerical simulation when the ship model is allowed heave and pitch motions. The sudden change in residual parameters is due to the restart of the case from the previous saved data or changes in time step size. The residuals for $alpha.water$, k and $omega$ converged to 10^{-6} . For pressure the residual obtained was 10^{-4} . The convergence error, $E\%C$, for total resistance, $R_{T(SP)}$ is shown in Figure 6.7. The error was calculated based on the average of 250 data points, is less than 1.0%. Figure 6.8 shows the convergence error for propeller thrust, which is much lower than 1.0% for the average of 250 data points.

Table 6.3: Numerical results of self-propulsion test with ship motion.

| Condition | $R_{T(SP)}$ (N) | C_T | Thrust, T (N) | Torque, Q (N-m) | $R_{T(SP)} - T$ (N) | V_A (m/s) | w |
|-----------|-----------------|----------|-----------------|-------------------|---------------------|-------------|--------|
| Even keel | 92.88 | 4.08E-03 | 63.4847 | 2.7503 | 28.8331 | 1.689 | 0.2309 |
| Dynamic | 96.83 | 4.26E-03 | 61.8382 | 2.2684 | 34.9949 | 1.711 | 0.2209 |

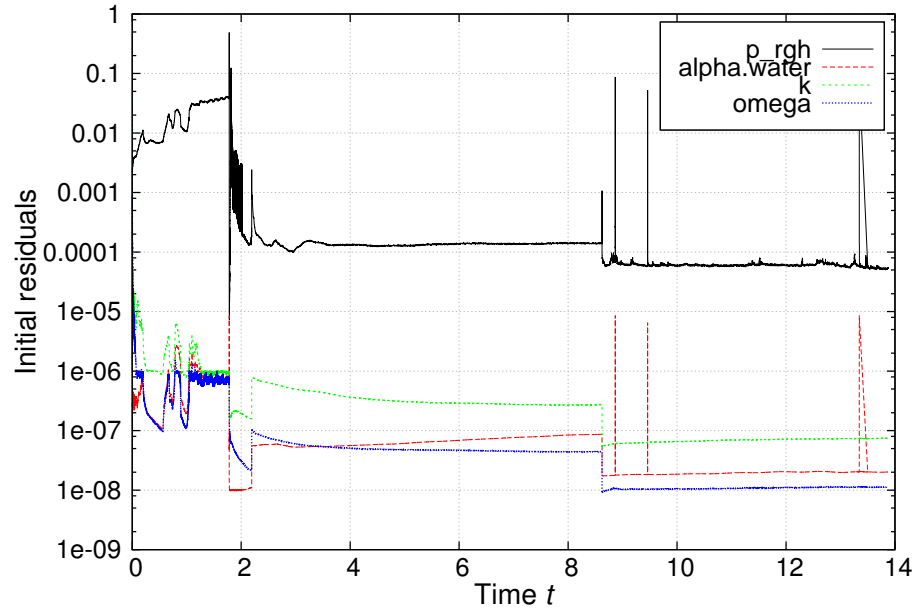


Figure 6.6: Residual convergence for self-propulsion with sinkage and trim.

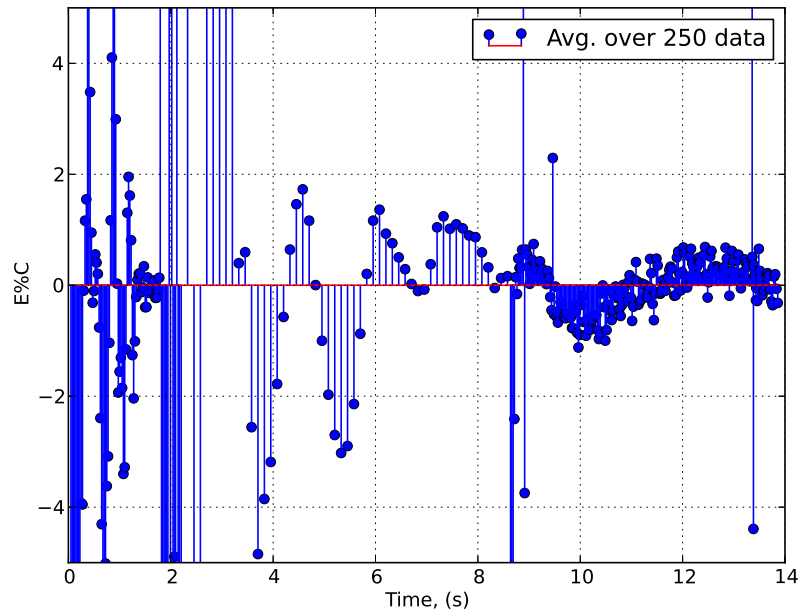


Figure 6.7: Total resistance convergence error for self-propulsion with sinkage and trim.

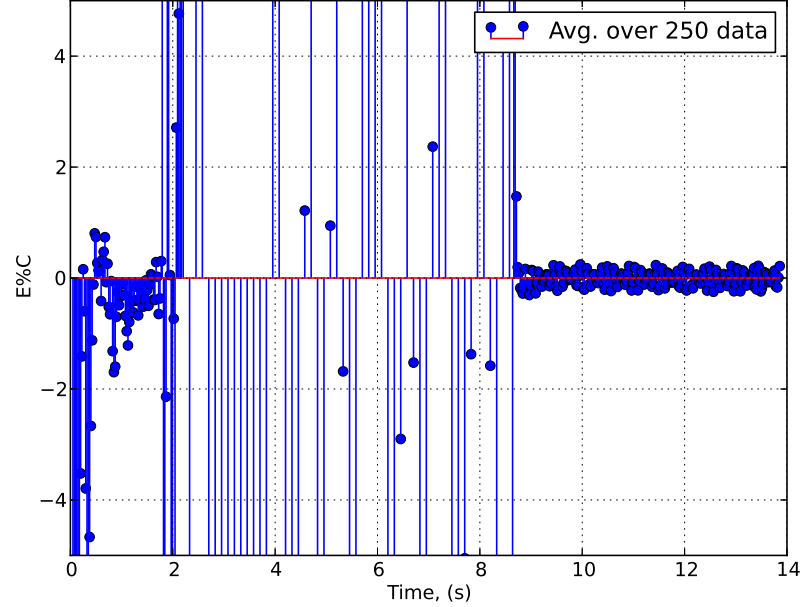
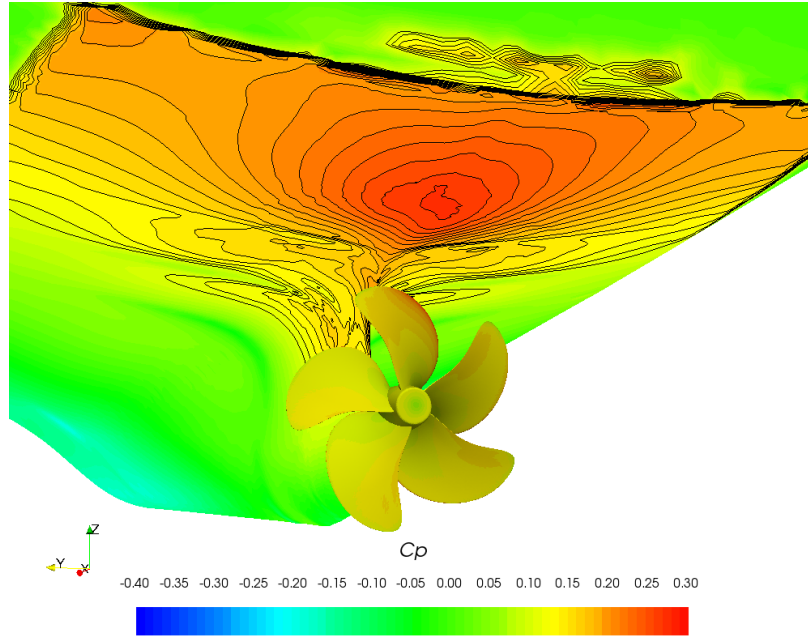


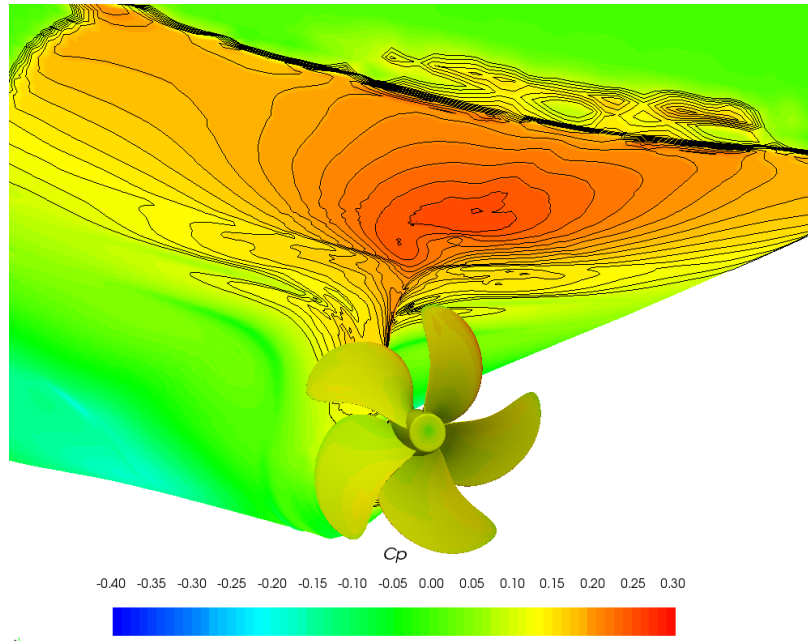
Figure 6.8: Propeller thrust convergence error for self-propulsion with sinkage and trim.

6.1.4.1 Pressure Distribution

The effect of ship motion on pressure distribution on the hull was investigated for the self-propulsion simulation with ship motion. The comparison of dynamic pressure coefficient (C_p) is shown in Figure 6.9. For the dynamic condition, the pressure distribution is found more asymmetric than even keel condition on the hull surface above the propeller, which will lead to vibration in the hull. The detailed hull pressure fluctuation due to the propeller rotation for the even keel condition and the dynamic condition was investigated by measuring the pressure on the hull surface using pressure probes as shown in Figure 6.10. The pressure gauges $P1$, $P2$, $P3$ were placed on the center line, $P4$ on starboard, and $P5$ on the port side. Pressure gauge $P2$ was placed at the intersection of the propeller plane and the ship center plane. The pressure fluctuations due to the propeller rotation are compared in Figure 6.11 for all the



(a) Sinkage and trim constrained to zero.



(b) Free sinkage and trim.

Figure 6.9: Pressure distribution on the hull and the propeller.

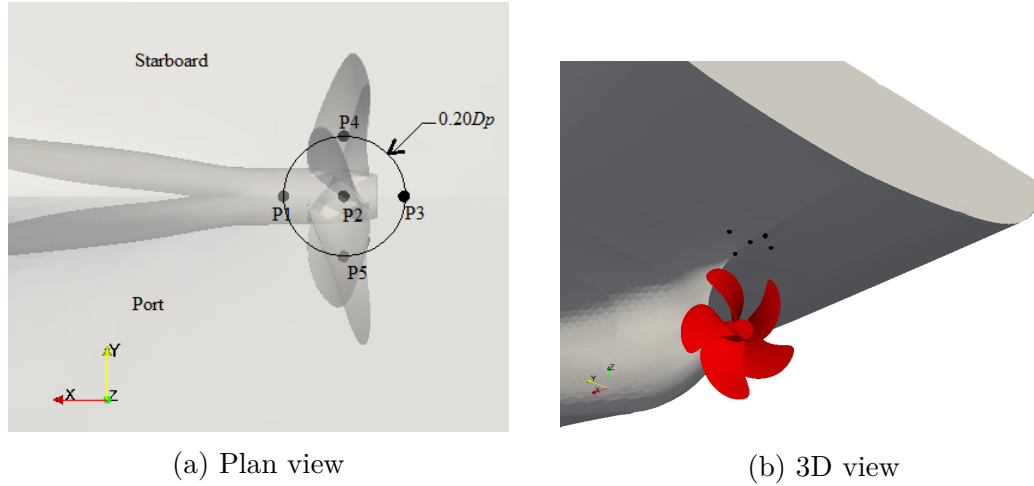


Figure 6.10: Virtual pressure gauge locations.

probes. A larger difference in pressure coefficient is observed in the downstream direction than that for the sideways direction. No difference in pressure coefficient is observed upstream of the propeller due to the ship motion.

6.1.4.2 Flow Velocity

The normalized axial velocities (with respect to the ship velocity) on the center plane are compared in Figure 6.12. The axial velocity distribution above the propeller tip shows larger negative value than the even keel condition due to the ship motions. The vortex core trajectory is also stretched towards the propeller rotational axis due to the ship motions. The axial velocity distribution is also compared at $x/L_{PP} = 0.9910$ looking upstream in Figure 6.13. The axial velocity distribution downstream of the propeller plane shows a small difference.

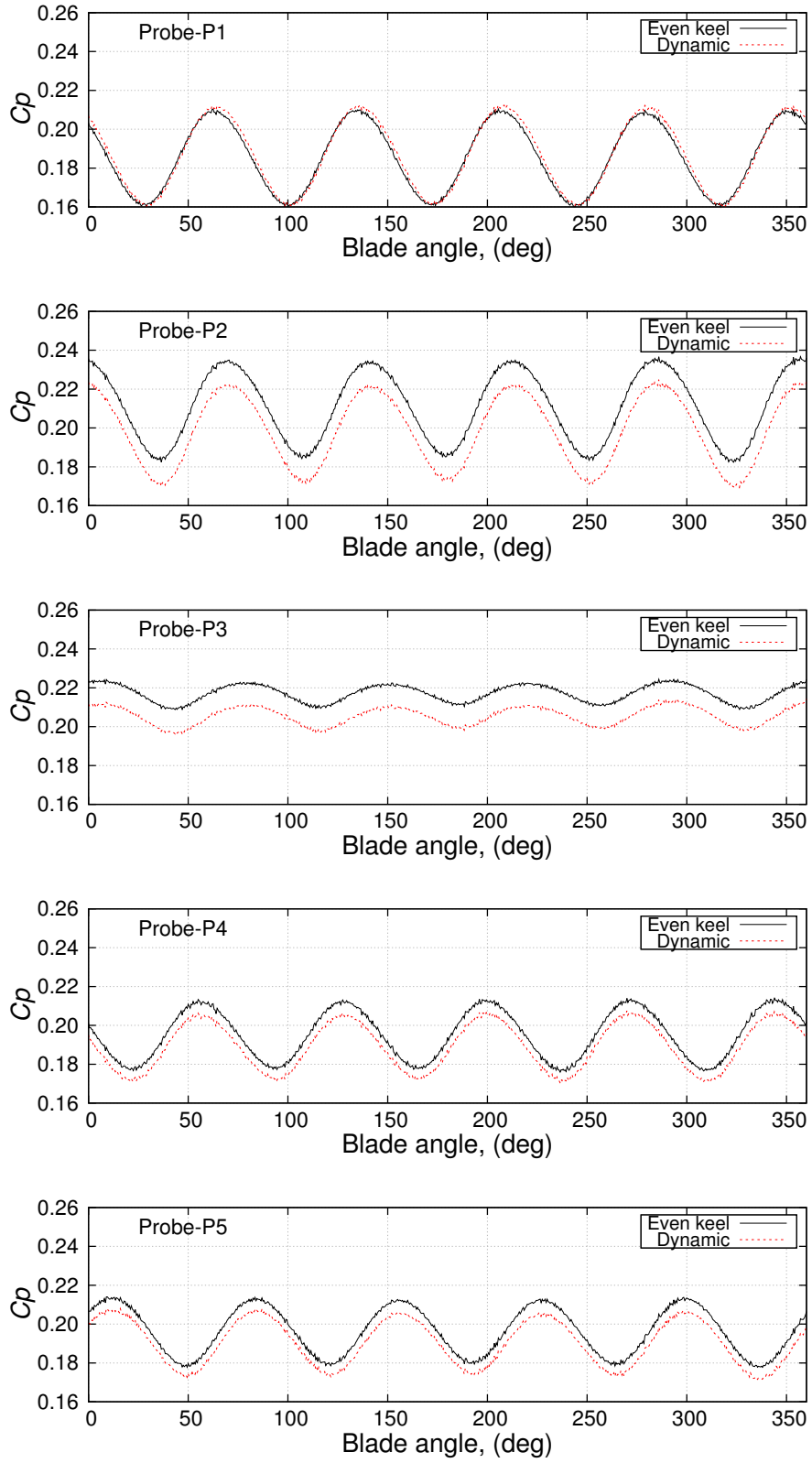
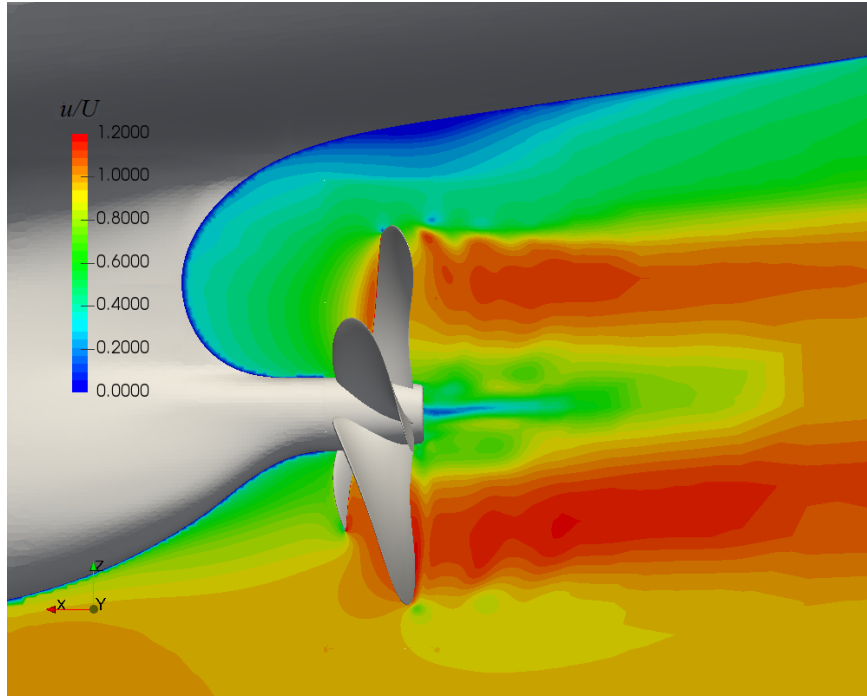
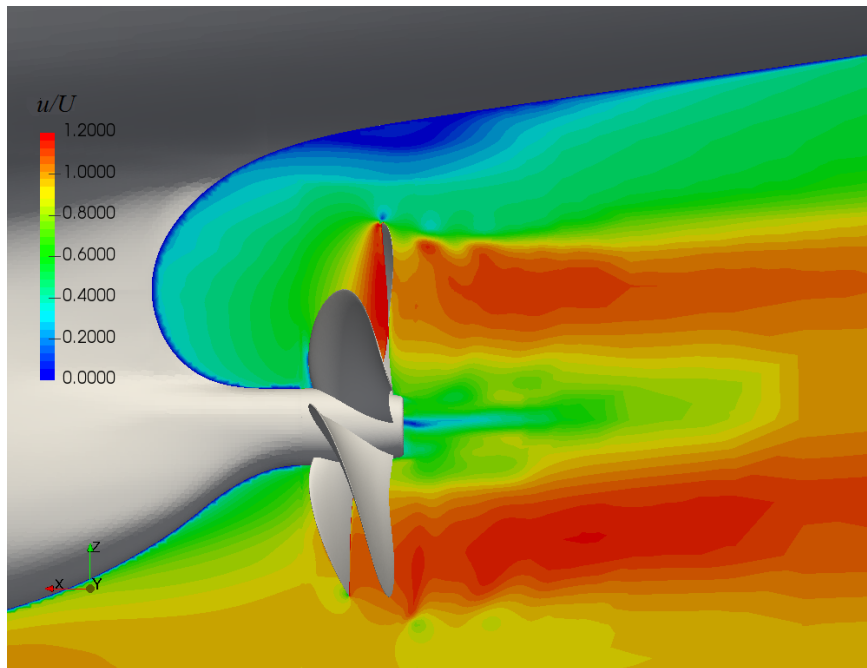


Figure 6.11: Numerical pressure measurement at the pressure gauges.

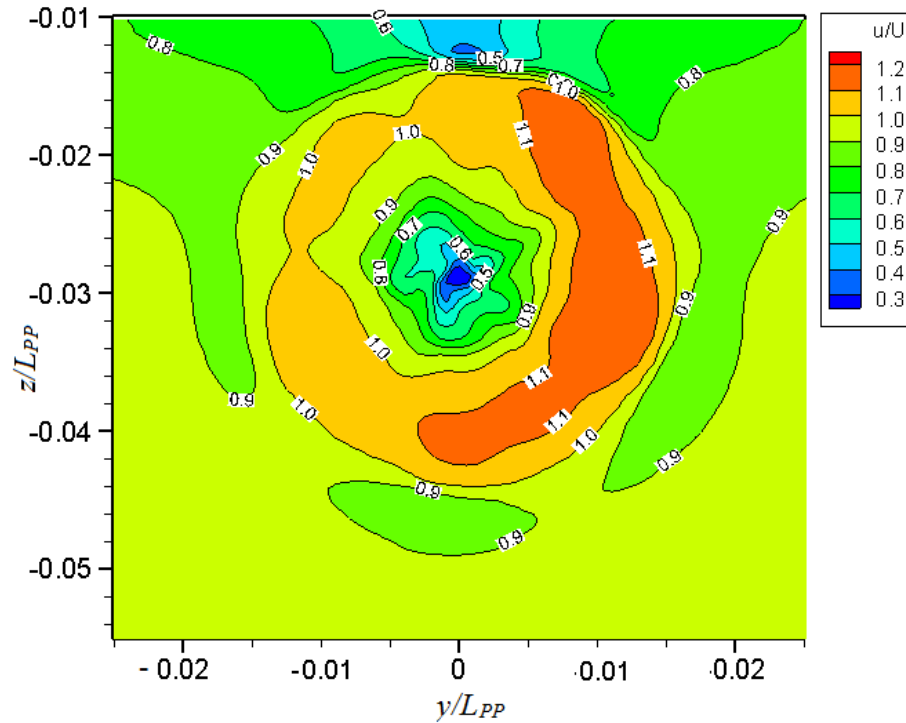


(a) Sinkage and trim constrained to zero.

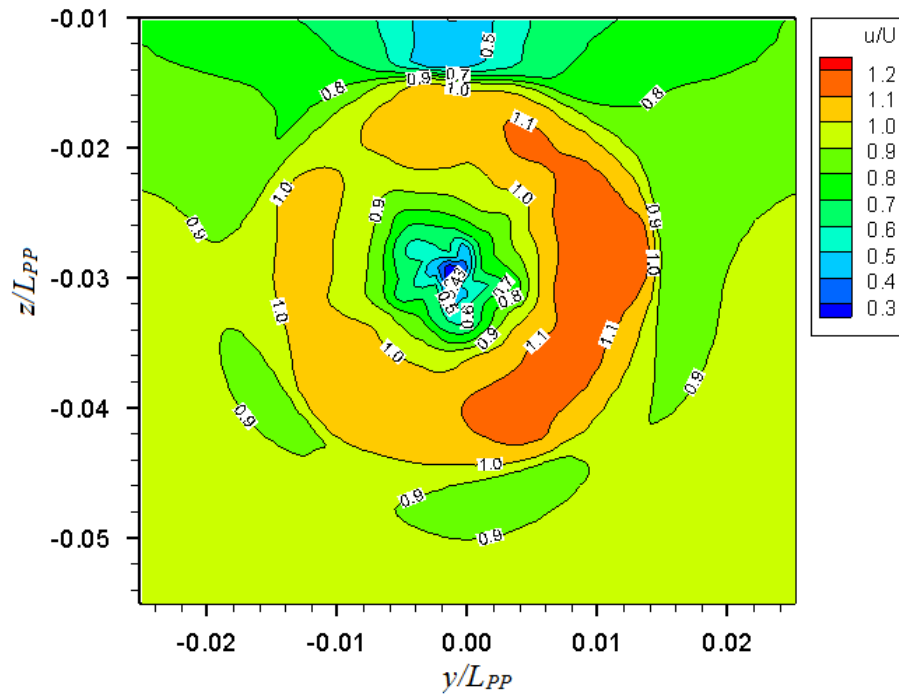


(b) Free sinkage and trim.

Figure 6.12: Axial velocity distribution on the centreplane.



(a) Sinkage and trim constrained to zero.



(b) Free sinkage and trim.

Figure 6.13: Axial velocity distribution at $x/L_{PP} = 0.9910$ (0.25D downstream of the propeller plane).

6.1.5 Seakeeping Simulation

Before proceed to the self-propulsion simulation in wave, the bare hull simulation was carried out in wave with forward speed corresponding to $Fn = 0.26$ for one wave condition. A similar computational domain as the bare hull resistance simulation was used for the seakeeping simulation. The wave generation and and wave absorption conditions were set up for the incoming wave and wave damping. Seakeeping simulation was performed for 10 wave encounter periods for wave $\lambda/L_{pp} = 1.15$. Figure 6.14 shows the comparison of the total resistance comparison in the head sea condition and the even keel condition. In compare to the even keel condition, the total resistance coefficient was increased by about 75 %. The motion response are compared with the experimental data (T2015, 2015) in Figure 6.15. The numerical simulation motion response shows a good agreement with the experimental data.

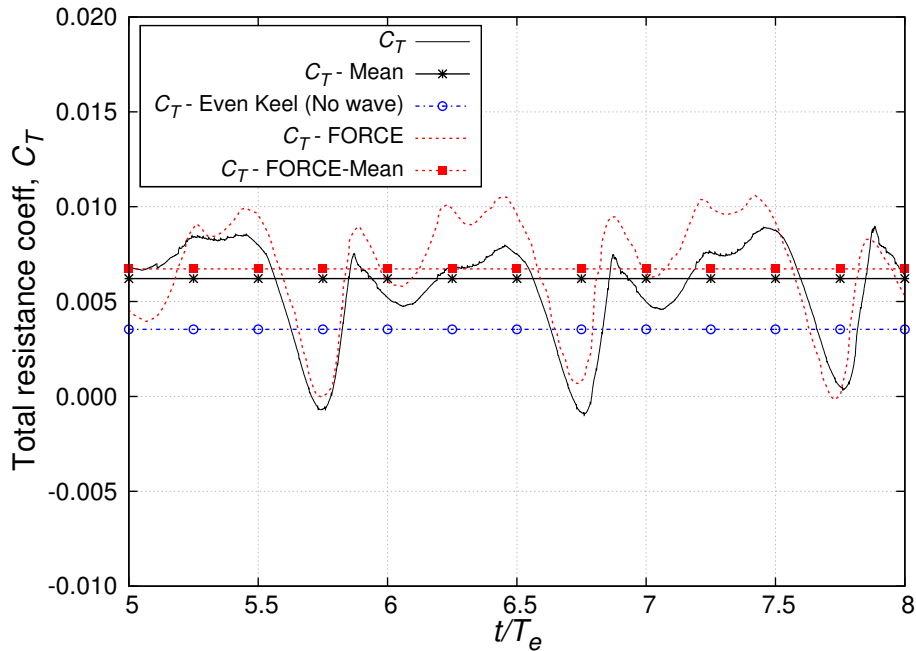
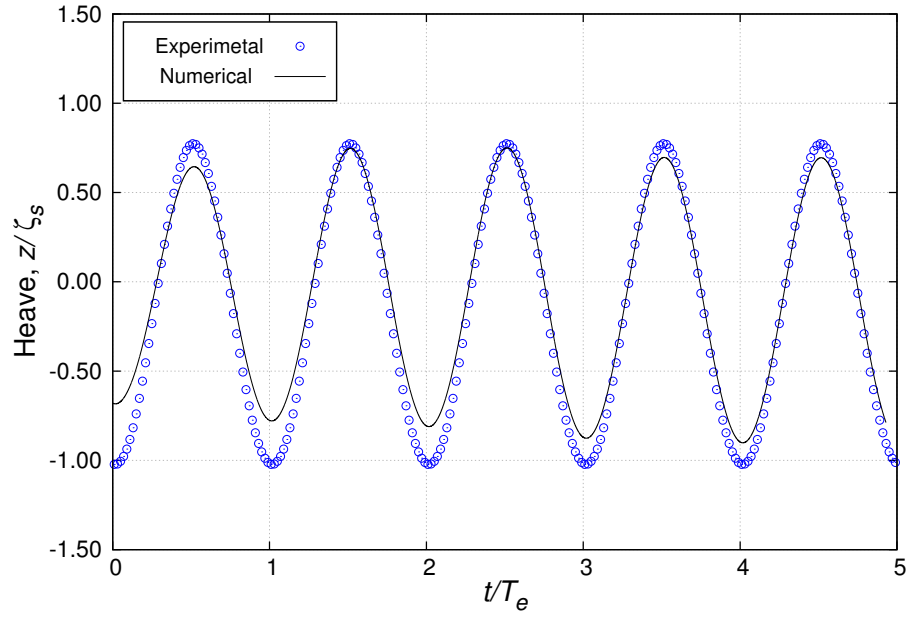
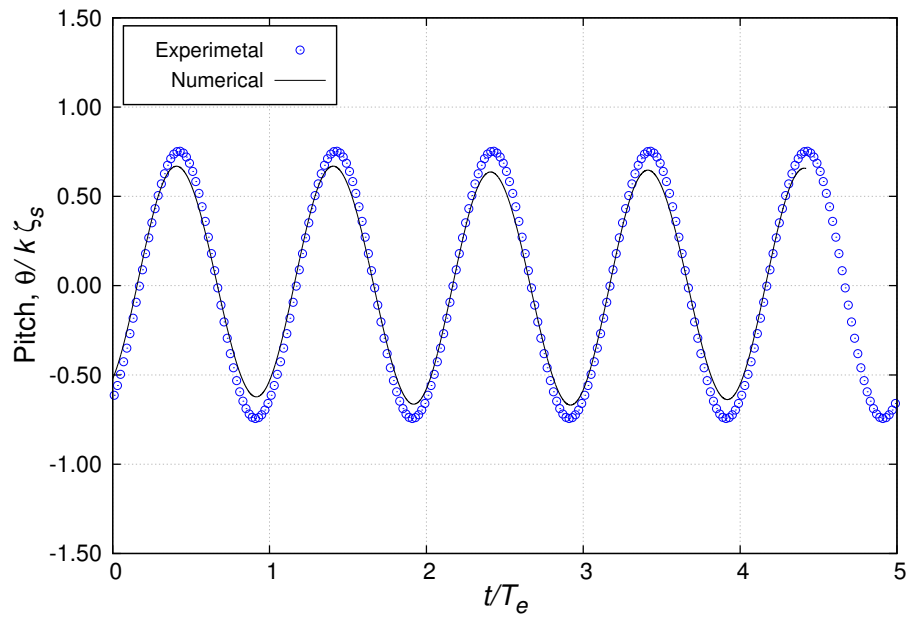


Figure 6.14: Comparison of total resistance coefficient in wave C3.



(a) Heave motion.



(b) Pitch motion.

Figure 6.15: Motion response of KCS bare hull in wave C3.

6.1.6 Self-Propulsion in Waves

The self-propulsion simulation of the KCS model in wave was performed with the detailed propeller geometry. A regular incoming wave of $\lambda/L_{PP} = 1.15$ and $H_S/\lambda = 1/56.74$ with current corresponding to the design speed was imposed on the inlet boundary. The numerical wave tank validation of the selected wave was studied prior to application in the self-propulsion simulation. The effect of the wave on the propeller-hull interaction was investigated using the developed dynamic class based on the sliding mesh approach. The numerical results are presented in Table 6.4. The results show an increase in total resistance coefficient and decrease in wake fraction compared to the even keel condition. The residual convergence history is shown in Figure 6.16. The residuals converged to $10^{-2} \sim 10^{-6}$. Figure 6.17 presents the time history of total resistance coefficient, C_T , for last two wave encounter periods. For the last two wave encounter periods, the resistance curve shows a cyclic pattern, which can be considered as a converged simulation. The variation of thrust coefficient K_T and torque coefficient K_Q over one wave encounter period is shown in Figure 6.18 and 6.19 respectively. The average of K_T and K_Q is lower than the even keel condition for the selected wave condition. The generated thrust from the propeller is reduced by 20%, and the torque is also reduced by 13% which causes reduction of the propulsion efficiency.

Table 6.4: Numerical results of self-propulsion test with ship motion in wave C3.

| Wave crest | R_T (N) | C_T | Thrust, T (N) | Torque, Q (N-m) | $R_T - T$ (N) | V_A (m/s) | w |
|------------|-----------|----------|-----------------|-------------------|---------------|-------------|--------|
| At FP | 166.53 | 7.325E-3 | 45.0574 | 2.3376 | 121.47 | 1.938 | 0.1175 |
| Midship | 158.12 | 6.955E-3 | 54.0788 | 2.4777 | 104.04 | 1.812 | 0.1758 |
| Even keel | 92.88 | 4.08E-03 | 63.4847 | 2.7503 | 28.83 | 1.689 | 0.2309 |

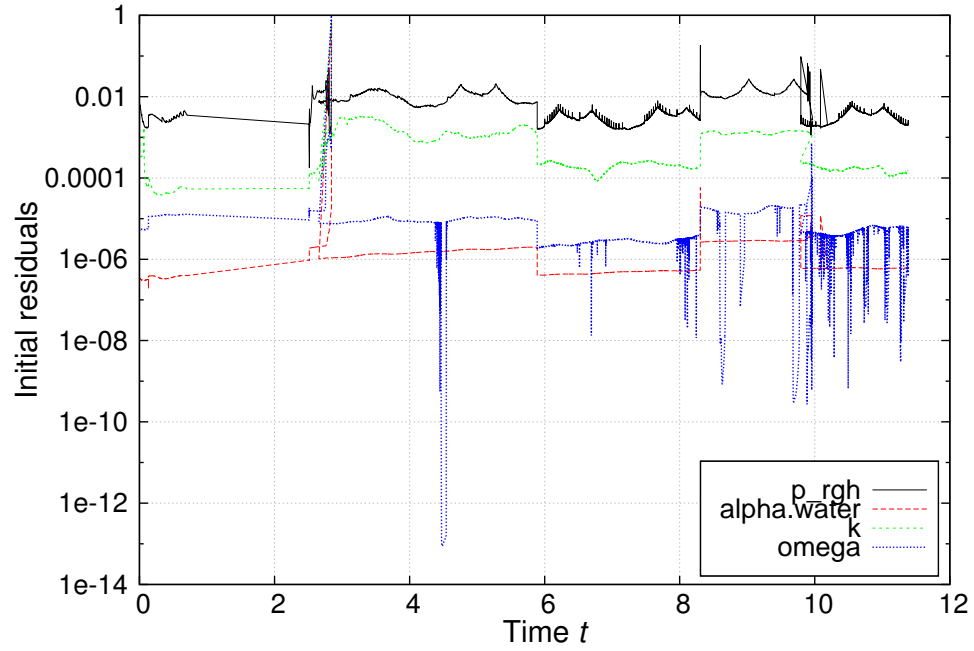


Figure 6.16: Residual convergence for self-propulsion in wave C3.

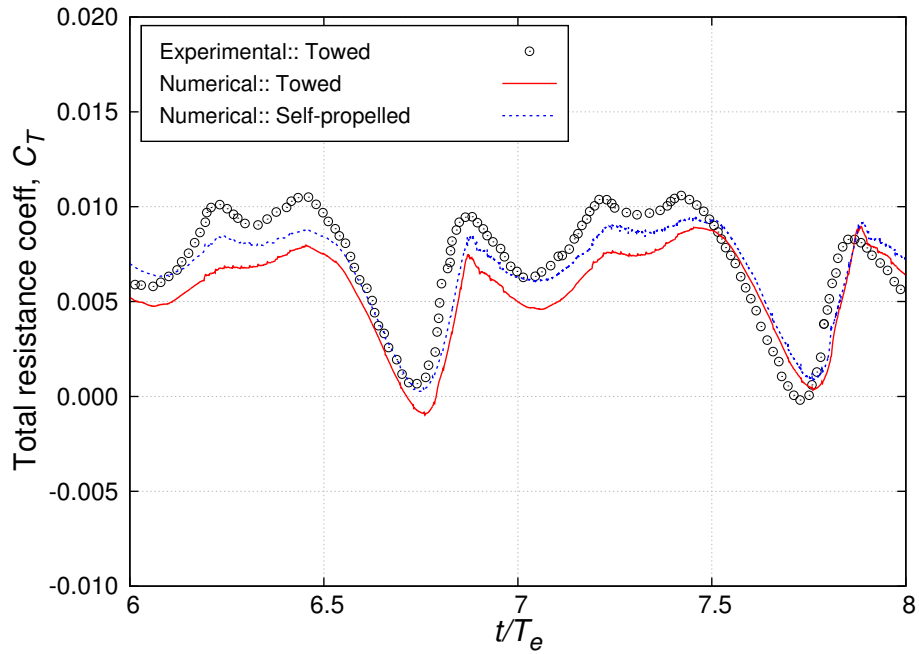


Figure 6.17: Total resistance coefficient for self-propulsion in wave C3.

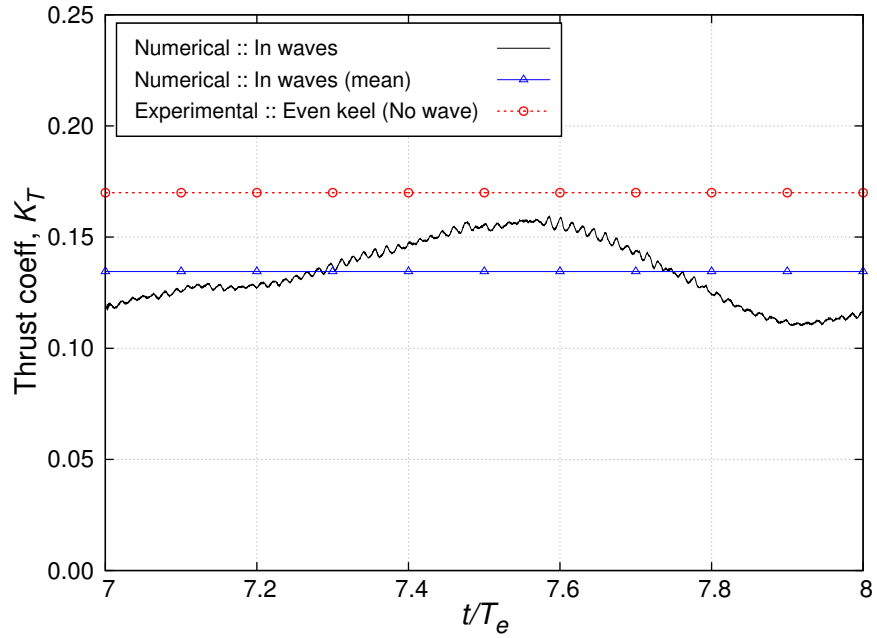


Figure 6.18: Thrust coefficient over one encounter wave period for self-propulsion in wave C3.

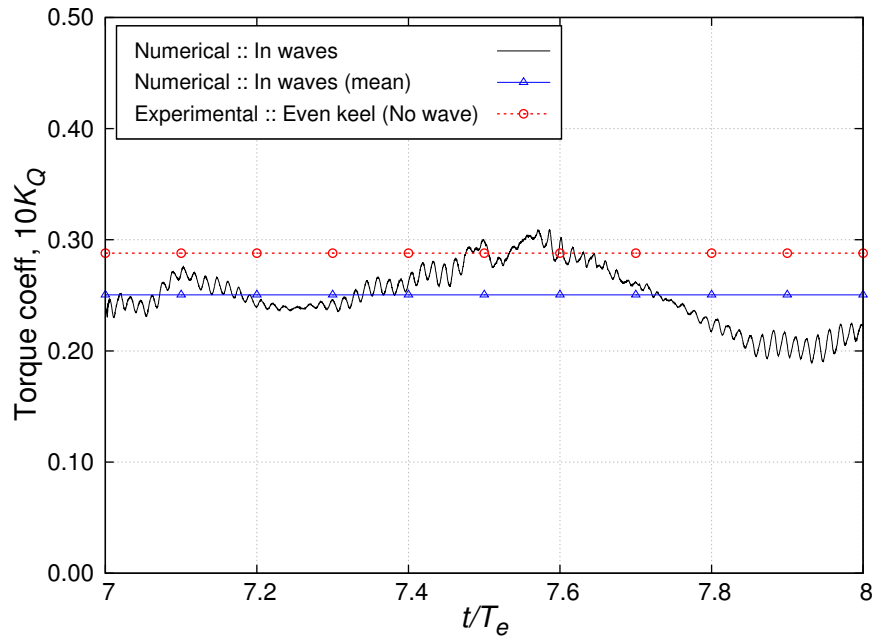


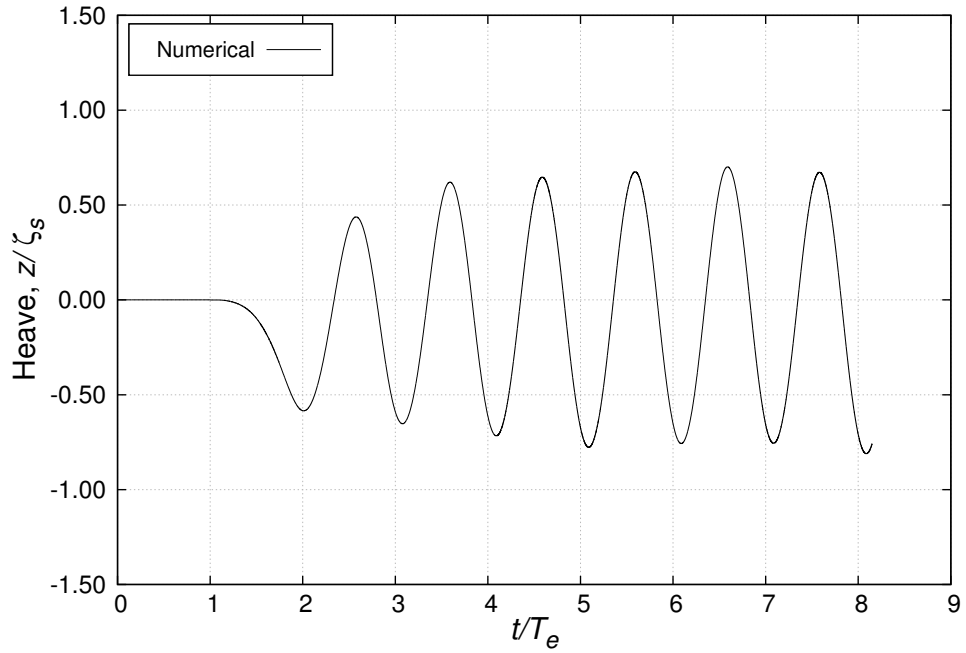
Figure 6.19: Torque coefficient over one encounter wave period for self-propulsion in wave C3.

6.1.6.1 Ship Response

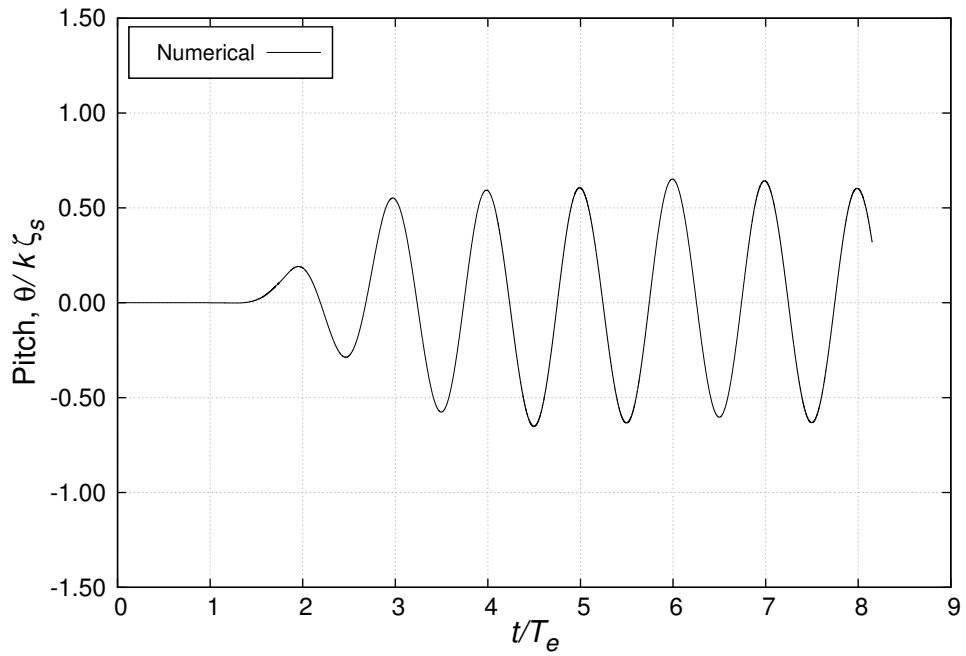
The response of the model with a rotating propeller in a wave with forward speed is shown in Figure 6.20. The simulation was carried out for eight encounter wave periods. A regular response of the model was observed for heave and pitch motion.

6.1.6.2 Free Surface Wave

Figure 6.21 illustrates the generated periodic wave pattern over one encounter wave period which is the combination of an incoming wave and the wave generated by the model. Since $\lambda/L_{PP} = 1.15$, when the bow is in the middle of the wave crest, the stern region is also in a wave crest. At $t/T_e = 0$, the bow is deeply submerged in the wave and the bow flare generates more waves which results in more wave making resistance. As the wave propagates, the bow comes out from the water and generates less wave. At $t/T_e = 1/2$, the model is basically in the hogging condition which means less frictional resistance and less wave making resistance. As the wave propagation continues, the bow again goes into wave crest and generates a similar wave pattern as $t/T_e = 0$.

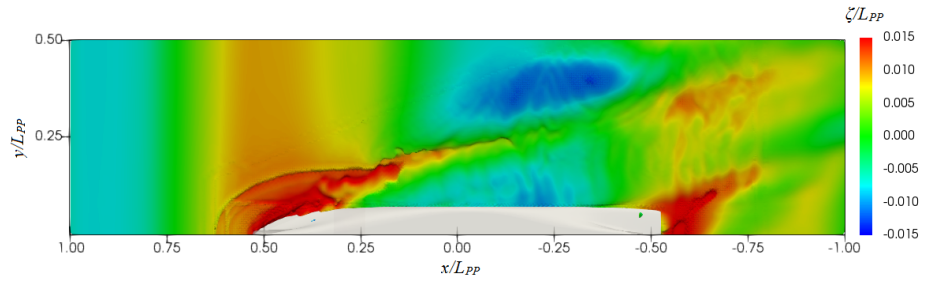


(a) Heave motion.

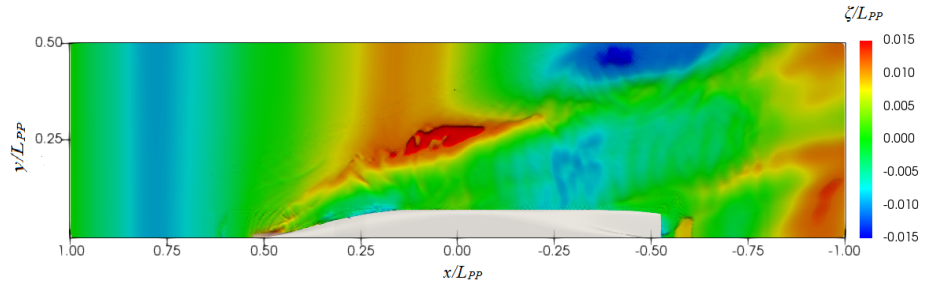


(b) Pitch motion.

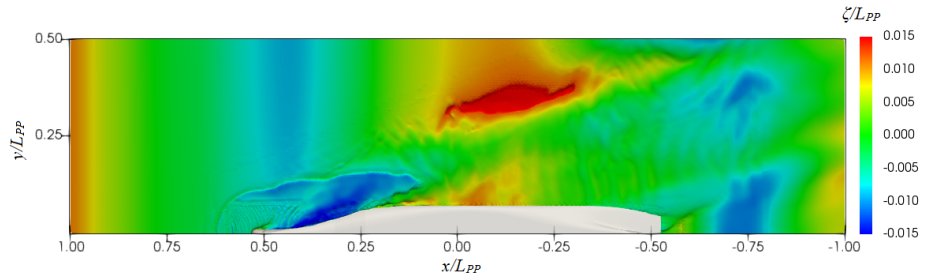
Figure 6.20: Motion response of KCS hull during self-propulsion in wave C3.



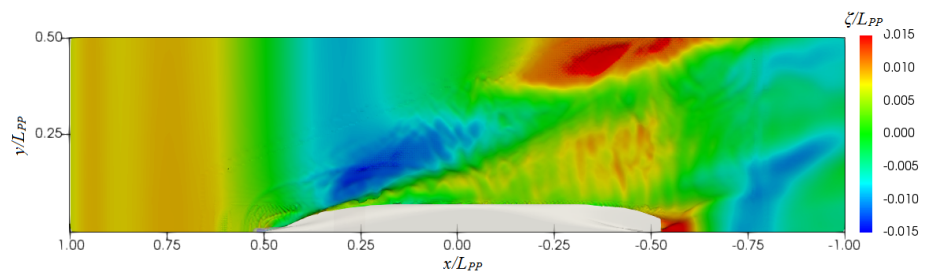
(a) $t/T_e = 0.0$



(b) $t/T_e = 1/4$



(c) $t/T_e = 1/2$



(d) $t/T_e = 3/4$

Figure 6.21: Free surface wave contour over one encounter wave period, T_e for self-propulsion in wave C3.

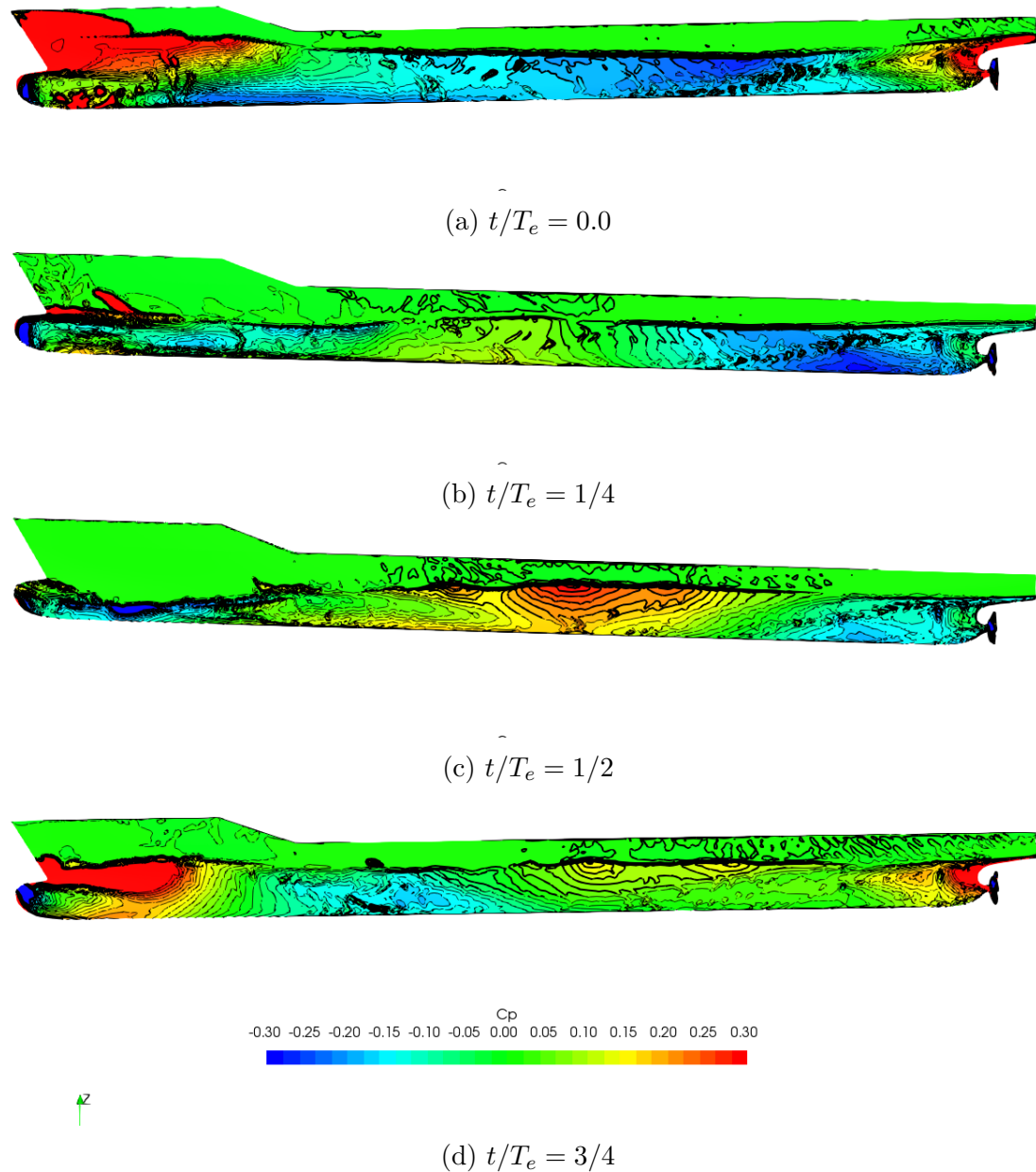


Figure 6.22: Pressure distribution on hull surface over one encounter wave period, T_e for self-propulsion in wave C3.

6.1.6.3 Pressure Distribution

The pressure coefficient, C_P , on the stern part of the model is compared in Figure 6.22 over one encounter wave period. Since the bow is deeply submerged in the wave

crest at $t/T_e = 0.0$, the bow experiences high pressure. The stern part of the model also experiences high pressure due to the wave crest present in the stern region. The bow starts to experience less pressure since it starts to emerge from the wave crest which can be seen at $t/T_e = 1/4$. As the wave crest moves to the midship section, the bow and stern region exerts low pressure at $t/T_e = 1/2$. At $t/T_e = 3/4$, the bow region and stern region start to experience high pressure again due to the incoming wave crest. A similar pressure distribution was observed for the next incoming wave.

6.2 JBC Test Case

The JBC test case allowed comparison between the full numerical self propulsion simulation and a set of experimental data that included measurements of flow velocity and vorticity around the propeller. The test conditions for the self-propulsion of JBC model are listed in Table 6.5. In numerical simulation, fixed rpm was used for propeller rotation.

6.2.1 Geometry

The self-propulsion simulation for the JBC ship model was also performed with a fixed rpm for the propeller. The ship model was equipped with the MP687 propeller as shown in Figure 6.23. The rudder and energy saving device (ESD) were not included with the model during the experiments, and also not included in the numerical simulation.

Table 6.5: Test conditions for JBC self-propulsion simulation

| | |
|----------------------|---|
| Case | 6.4 |
| Wave | Calm |
| Condition | Self-prop (ship) |
| L_{PP} | 7.00 m |
| Fn | 0.142 |
| $Rn \times 10^7$ | 0.746 |
| Rudder | without |
| Propeller | with |
| Attitude | sinkage & trim |
| Validation variables | prop factor, wave elevation mean flow velocity |
| EFD provider | NMRI |

6.2.2 Computational Domain and Grid Generation

As a first step in the self-propulsion simulation, the bare hull resistance and propeller open water tests were validated. Based on the numerical results analysis, the computation grid for the numerical self-propulsion simulation was generated combining the optimum bare hull grid with the propeller grid. Bare hull grid, GRID-C was combined with propeller grid GRID-B for the computational grid in the JBC self-propulsion simulation. Due to the non-symmetric condition of the propeller wake, the whole computational domain was used in the numerical simulation. The grid distribution of the self-propulsion simulation using the actual propeller geometry is shown in Figure 6.24. To reduce the computational time, a steady simulation was carried out initially, and then the steady solution was used as the initial condition for the unsteady simulation.

6.2.3 Results Validation

The model was free to heave and pitch during the model test as well as in the numerical simulations. The numerical simulation was started with the larger time step size. When the ship motion was stable, the time step size was reduced to the corresponding 1.0° rotation of the propeller for every time step. The effect of the change in time step



Figure 6.23: Geometry for JBC model for self-propulsion simulation.

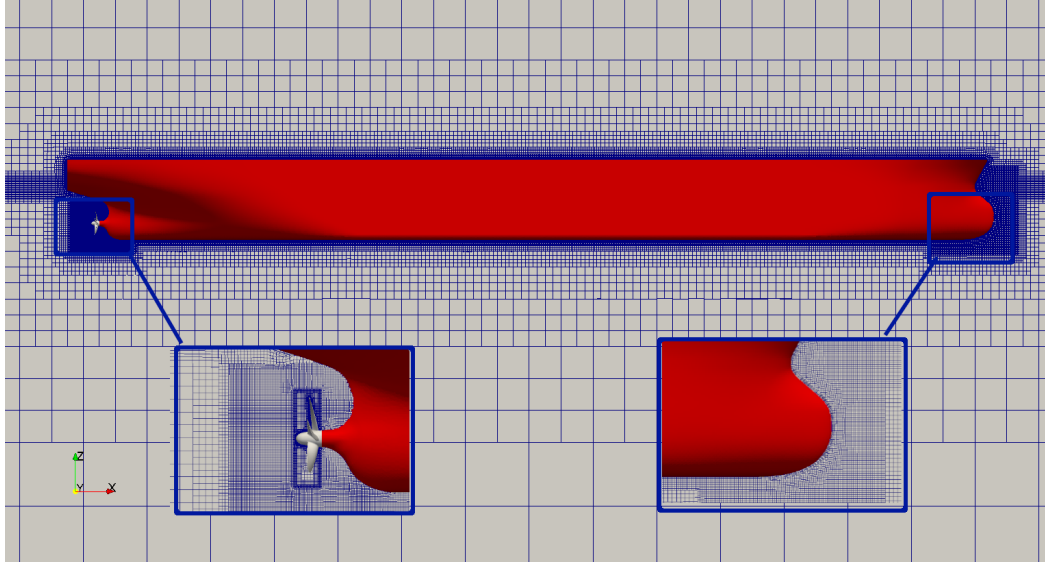


Figure 6.24: Computational grid for self-propulsion of JBC model.

size is clearly seen in the residual convergence which is shown in Figure 6.25. The time step size was changed after about 8.40 sec and the residuals dropped another order of magnitude. The convergence error for total resistance is calculated and presented in Figure 6.26. It was found that the convergence error at the lower time step was much lower than 1.0%. The numerical results for the self-propulsion simulation are compared with the experimental data in Table 6.6. The comparison of C_T against the experimental data shows just above 5.0% error. The error in SFC was about 7.0%. The overall comparison shows good agreement with the experimental results.

Table 6.6: Numerical results of self-propulsion of JBC model.

| | $R_{T(SP)}$ (N) | C_T | Thrust, T (N) | Torque, Q (N-m) | $R_{T(SP)} - T$ (N) | V_A (m/s) | w |
|--------------|-----------------|----------|-----------------|-------------------|---------------------|-------------|--------|
| Numerical | 43.30 | 5.10E-03 | 26.45 | 0.6073 | 16.85 | 0.4909 | 0.5836 |
| Experimental | 40.82 | 4.81E-03 | 22.40 | 0.5846 | 18.20 | 0.5624 | 0.5230 |
| $ E\%D $ | | 6.08 | | | 7.39 | | 11.60 |

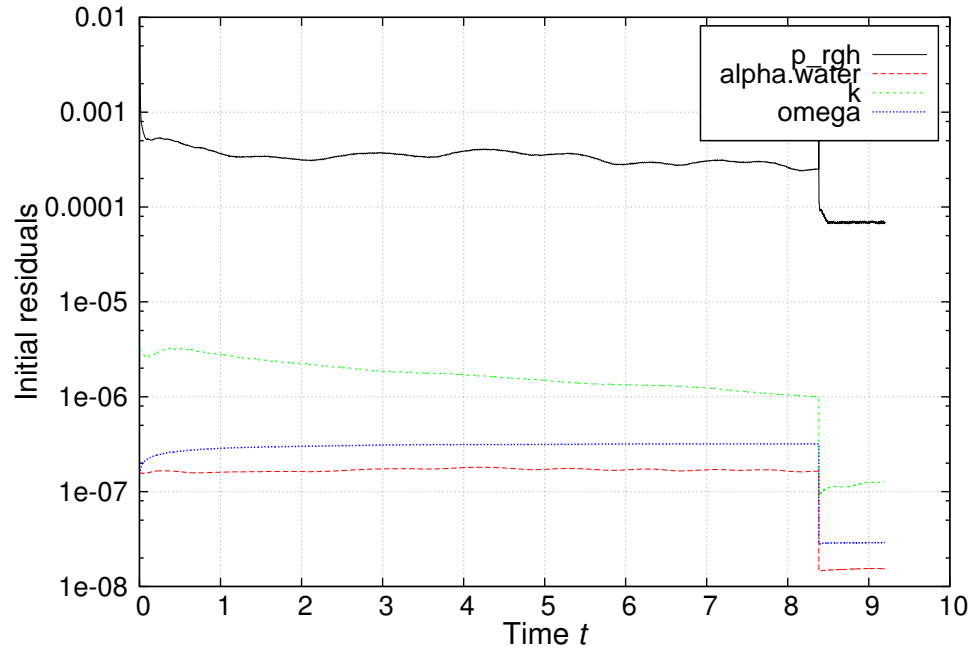


Figure 6.25: Residual convergence of self-propulsion simulation of JBC model.

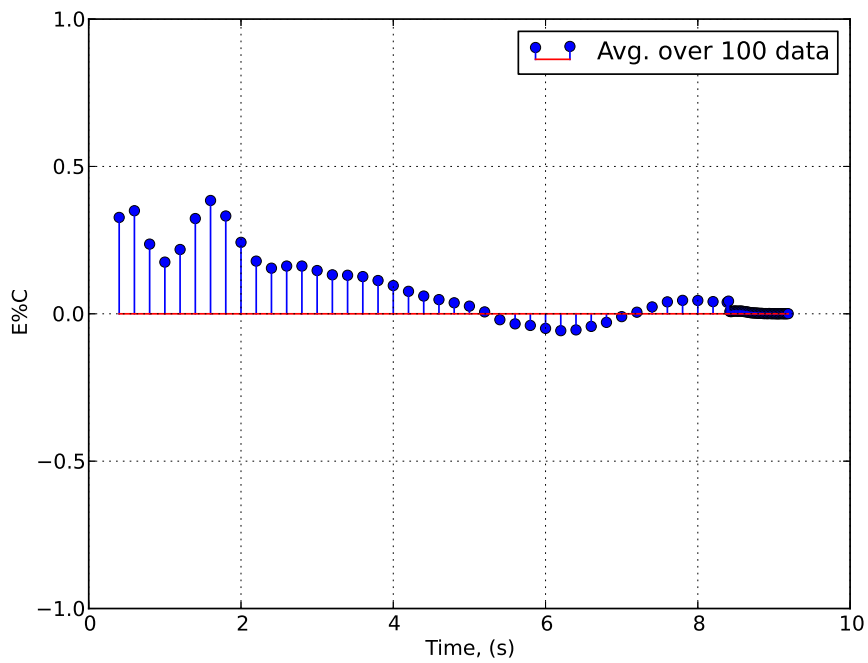


Figure 6.26: Convergence of total resistance of JBC model.

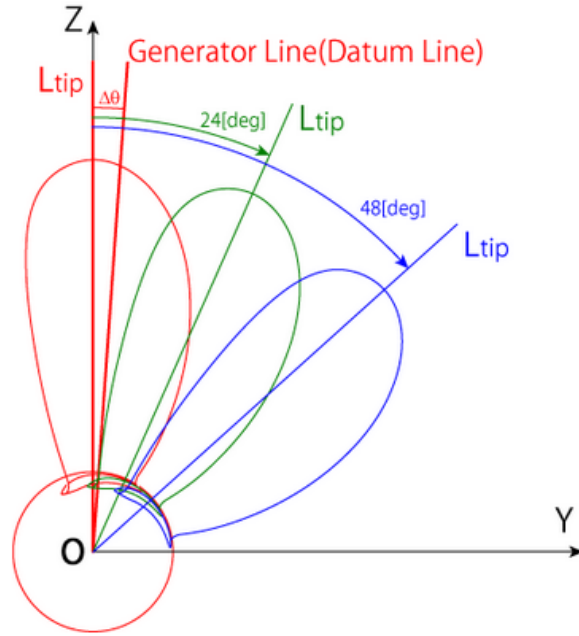
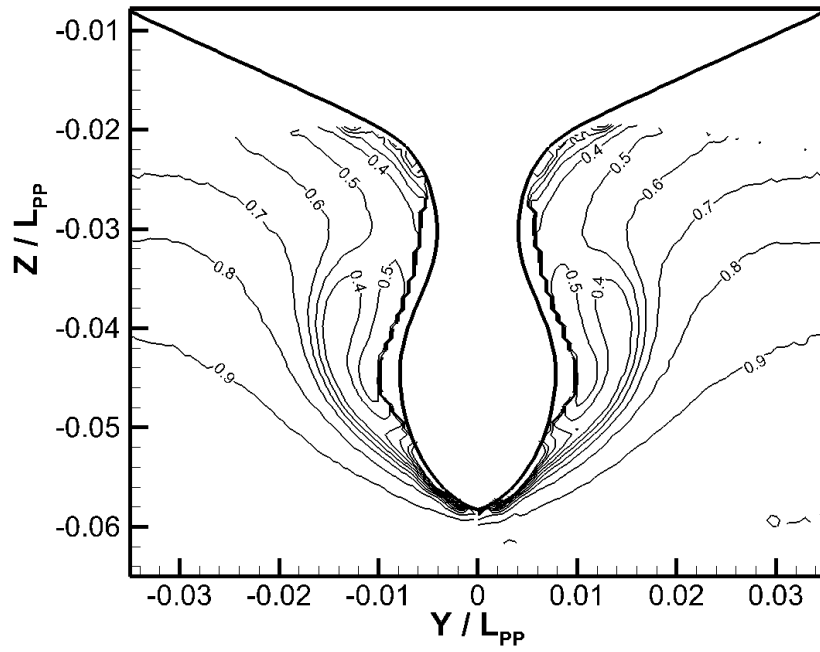


Figure 6.27: Blade angle definition.

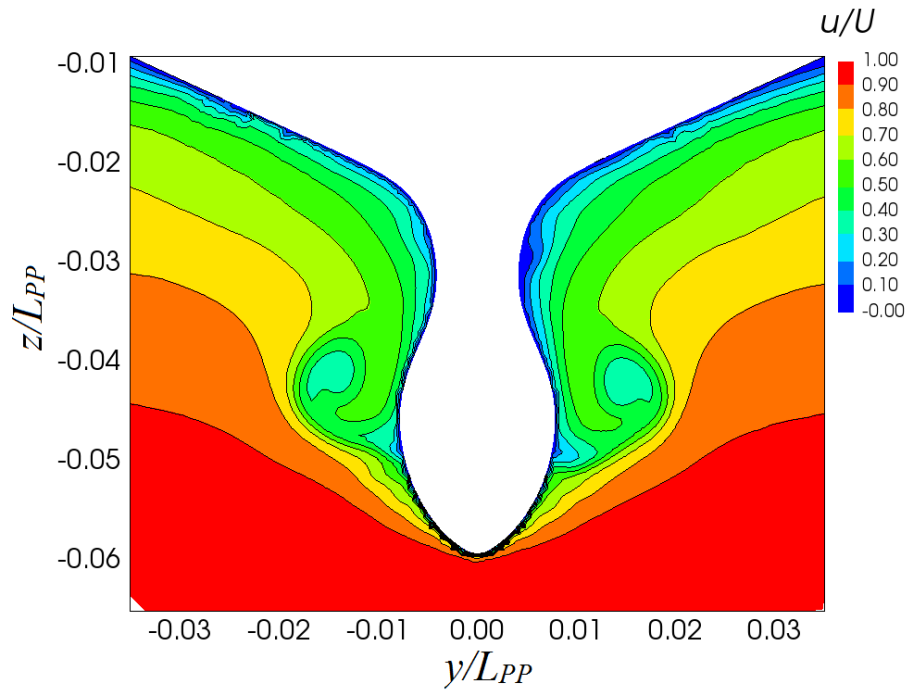
6.2.4 Flow Velocity

The non-dimensional axial velocity distribution is validated with the experimental data for three longitudinal locations at $S2$ ($x/L_{PP} = 0.9625$), $S4$ ($x/L_{PP} = 0.9843$), and $S7$ ($x/L_{PP} = 1.00$). For $S2$ and $S7$ sections, the numerical results are compared for the blade angles 0° and 48° . The definition of blade angle is explained in Figure 6.27. Figure 6.28 shows the axial velocity distribution at $x/L_{PP} = 0.9625$. The bilge vortices in the numerical simulation separated earlier and moved further outwards than the experimental vortices. However, the overall velocity distribution shows good agreement with the experimental results. Figure 6.29 and 6.30 present the comparison of experimental and numerical results at $x/L_{PP} = 0.9843$ for blade angles 0° and 48° . This section is just upstream of the propeller. It was expected to see the suction effect of propeller on the velocity distribution and the numerical simulation was also able to capture the effect. The comparison shows fairly good agreement with the

experimental results. The axial velocity was also compared just downstream of the propeller ($x/L_{PP} = 1.0$). The implemented dynamic motion class turbulence model was able to capture the hub vortex more accurately and shows good agreement with the experimental data for both blade angles.

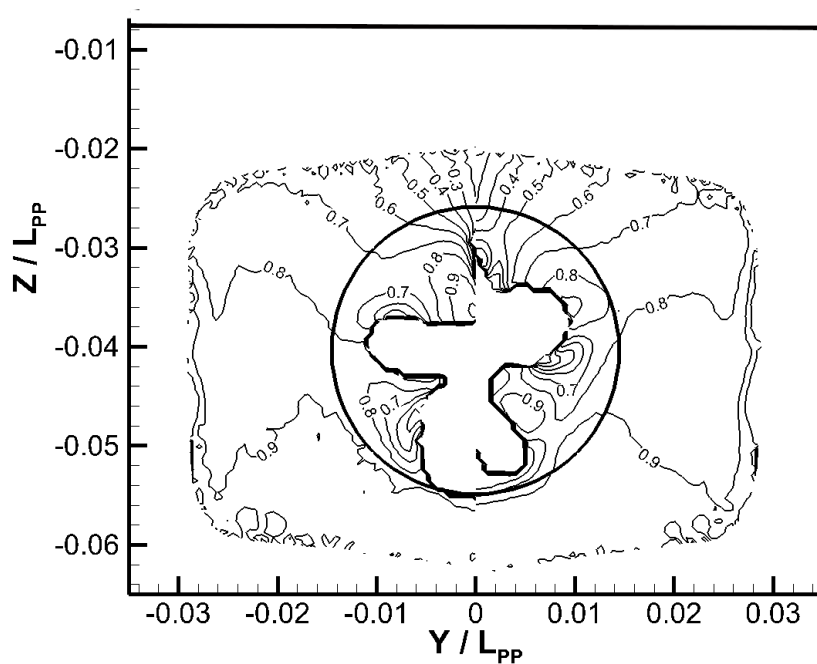


(a) Experimental.

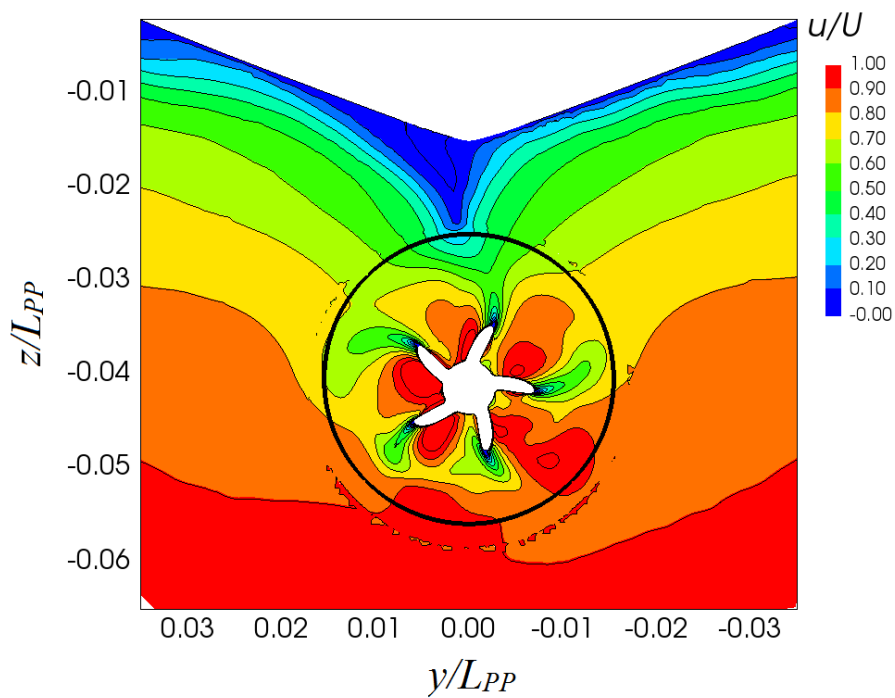


(b) Numerical

Figure 6.28: Axial velocity distribution at $x/L_{PP} = 0.9625$

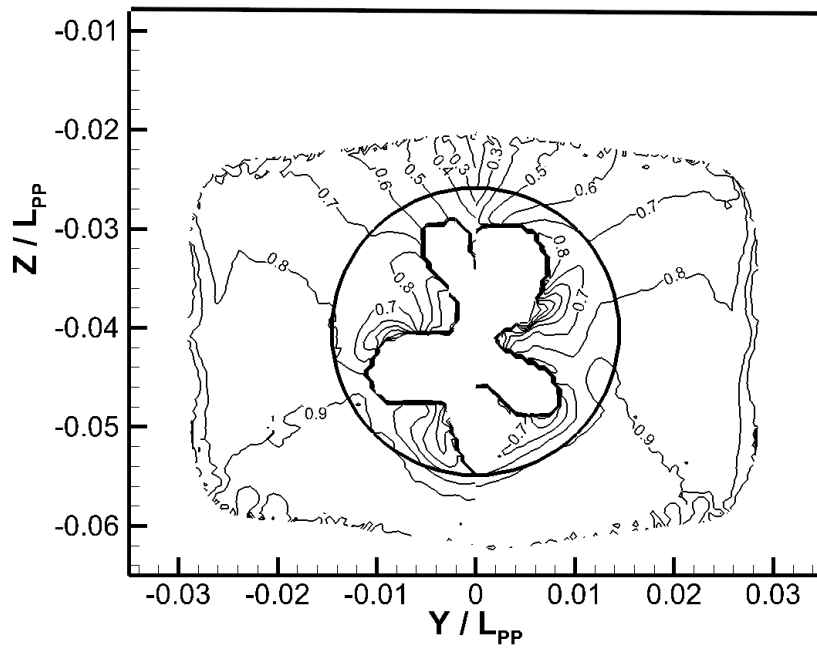


(a) Experimental.

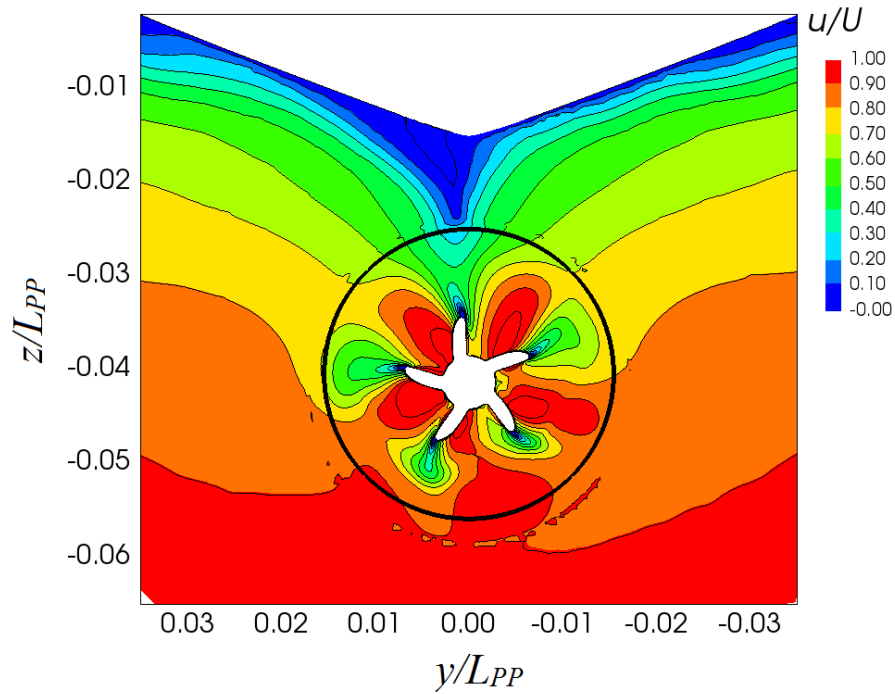


(b) Numerical

Figure 6.29: Axial velocity distribution at $x/L_{PP} = 0.9843$ for blade angle 0°

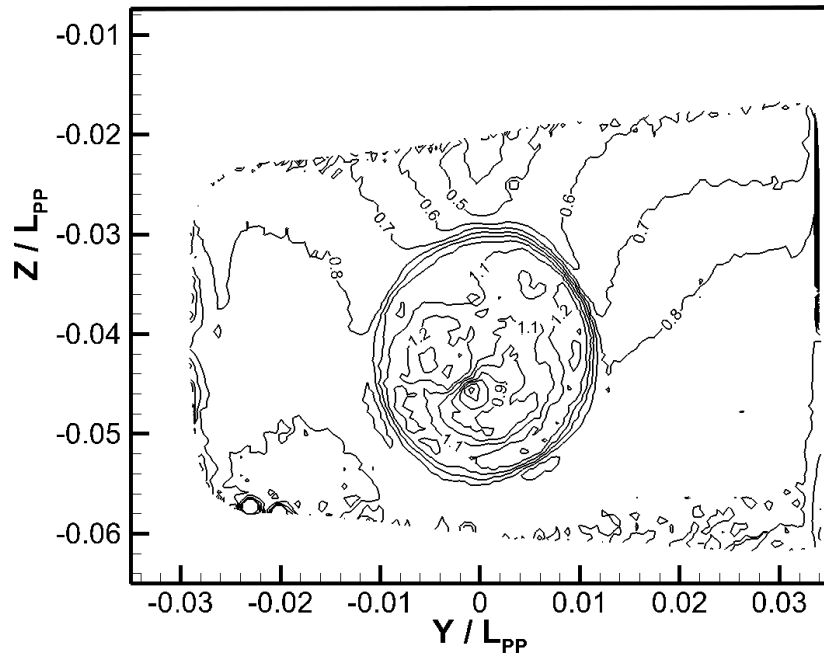


(a) Experimental.

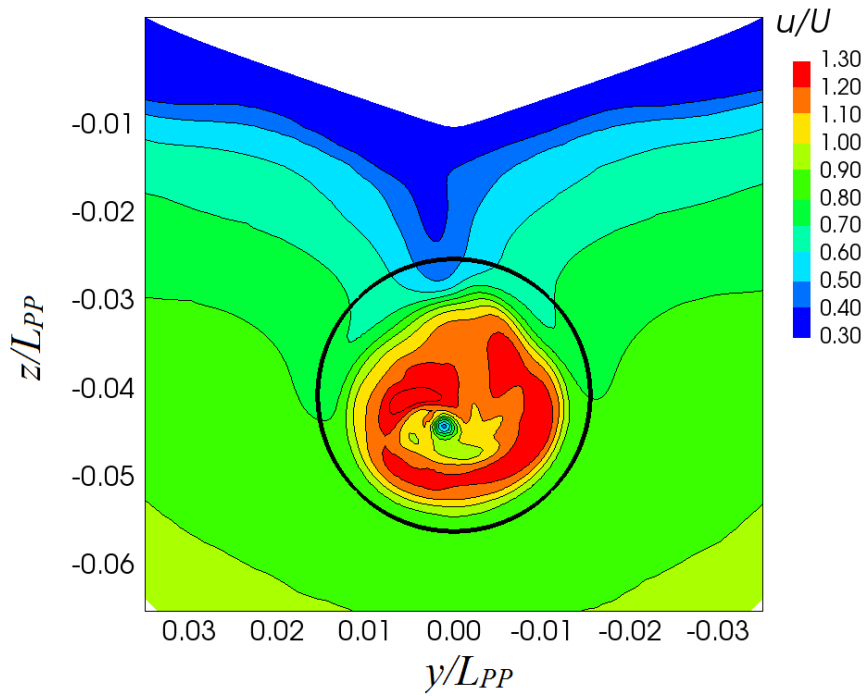


(b) Numerical

Figure 6.30: Axial velocity distribution at $x/L_{PP} = 0.9843$ for blade angle 48°

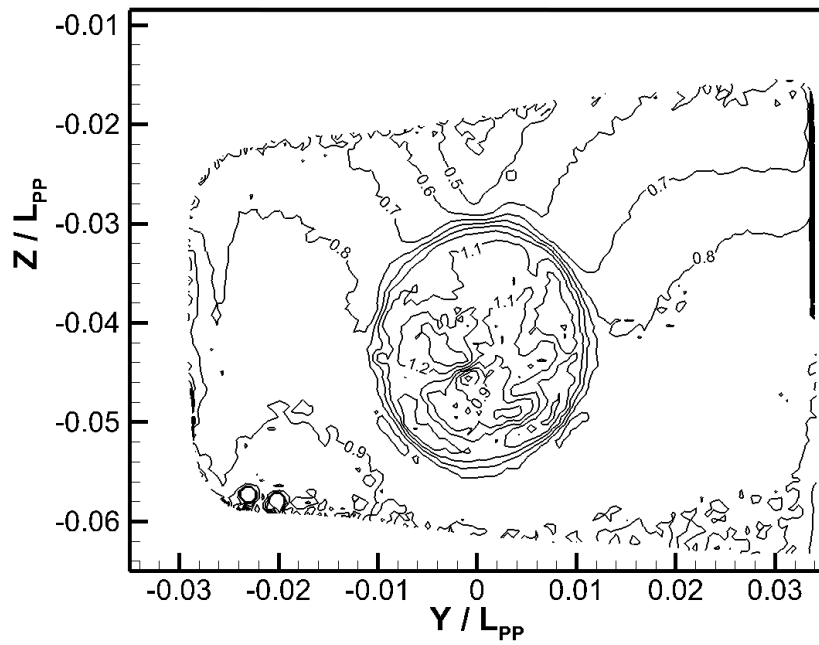


(a) Experimental.

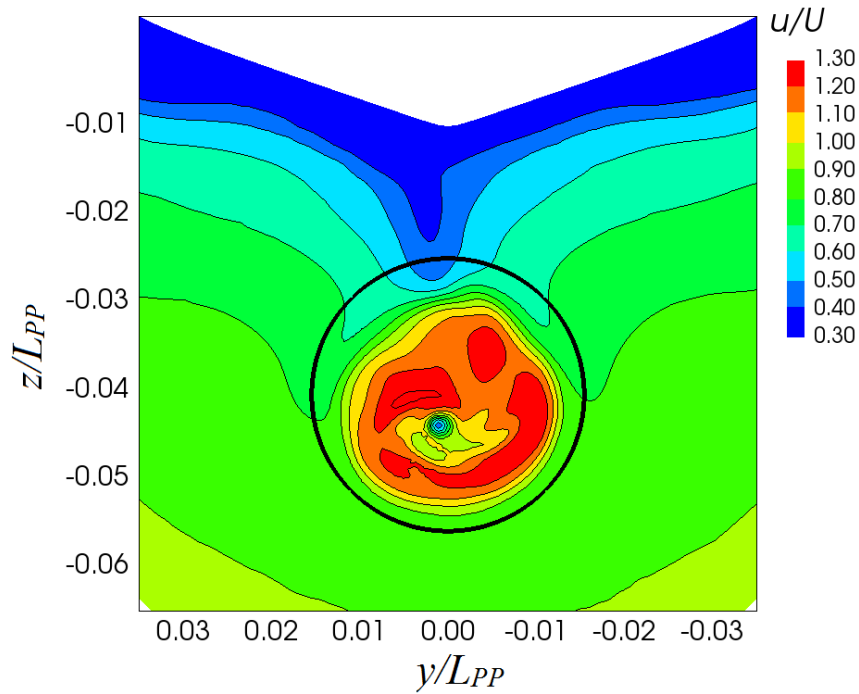


(b) Numerical

Figure 6.31: Axial velocity distribution at $x/L_{PP} = 1.00$ for blade angle 0° .



(a) Experimental.



(b) Numerical

Figure 6.32: Axial velocity distribution at $x/L_{PP} = 1.00$ for blade angle 48° .

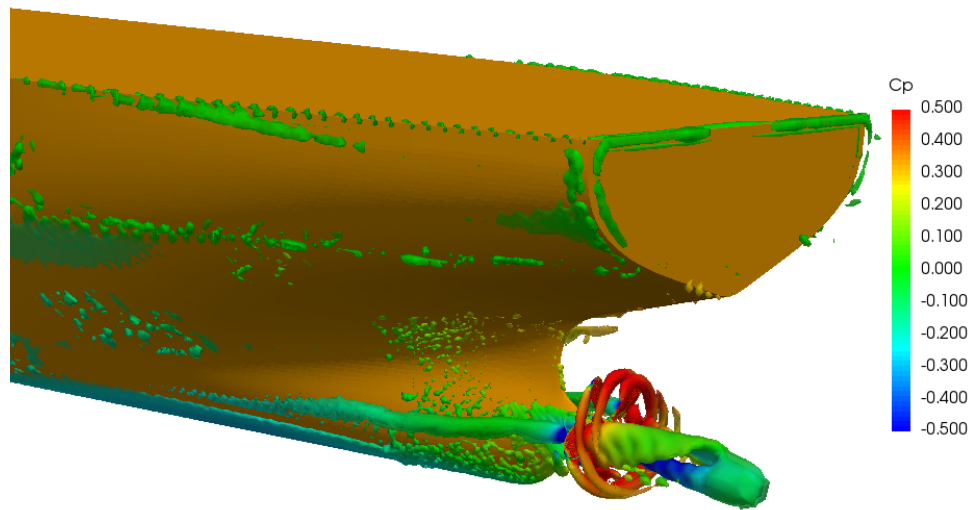


Figure 6.33: Vortex structures based on $Q = 500$ for the self-propulsion simulation with sinage and trim at $Fn = 0.142$.

6.2.5 Vortex Visualization

The Q -*criterion* was used to identify the bilge vortex as well as vortices generated by the propeller and hub. The iso-surface of vortices shown in Figure 6.33 was generated using $Q = 500$. It is clearly seen that the bilge vortex was at the aft-shoulder and it detached from the hull downstream of the propeller plane. In the absence of ESD, the bilge vortices were contracted in the propeller disk. The vortices were generated by the tips of the propeller blades, and the hub were well produced in the numerical simulation. The vortex structures are coloured based on the pressure coefficient.

6.3 Fishing Vessel

The numerical self-propulsion simulations of the fishing vessel were performed using the body-force method. The preliminary study is published by Ali et al. (2019b). A whole computational domain was used for self-propulsion simulation due to the asymmetric propeller force distribution. GRID-C was selected for self-propulsion based on the uncertainty analysis and validation error in the numerical prediction. A cylindrical refined domain was used as a propeller disk, which ensures the required grid resolution based on open water data validation. During the numerical simulation, the ship model was free to heave and pitch. The grid distribution with refined propeller domain is shown in Figure 6.34. The numerical simulations were carried out using the FV-BFM and LV-BFM methods.

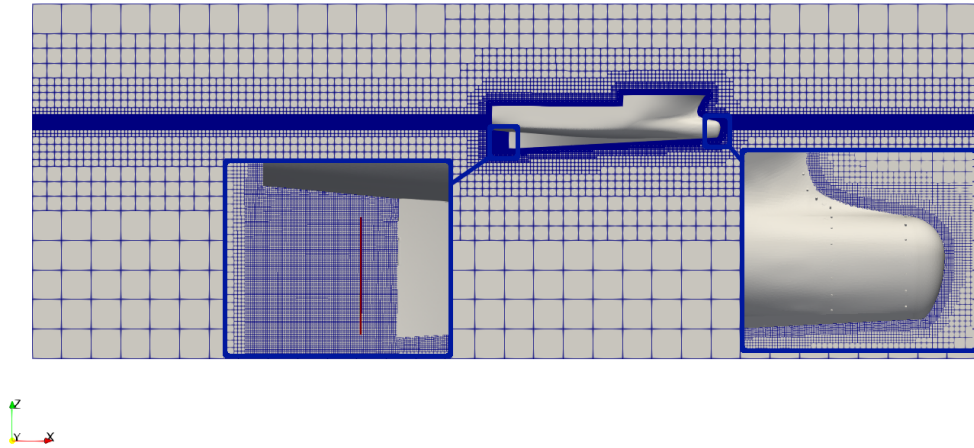
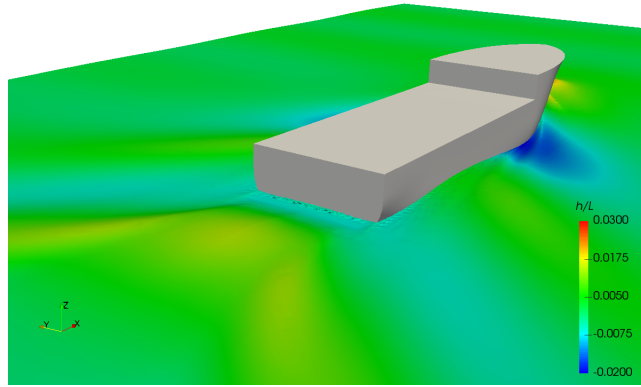
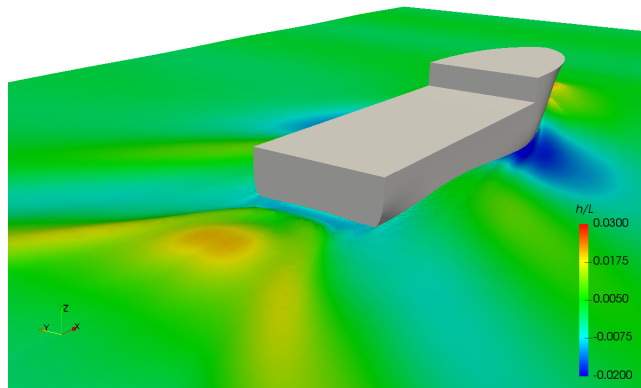


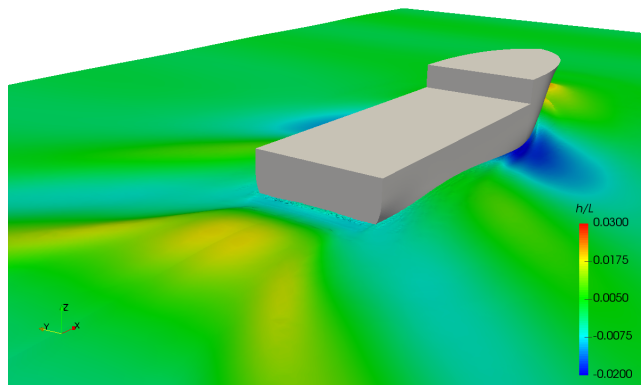
Figure 6.34: Computational grid for self-propulsion of Fishing vessel.



(a) Bare hull



(b) FV-BFM with $n = 15.92$



(c) LV-BFM with $n = 15.82$

Figure 6.35: Comparison of free surface wave contour for GRID-C at $Fn = 0.34$ in calm water.

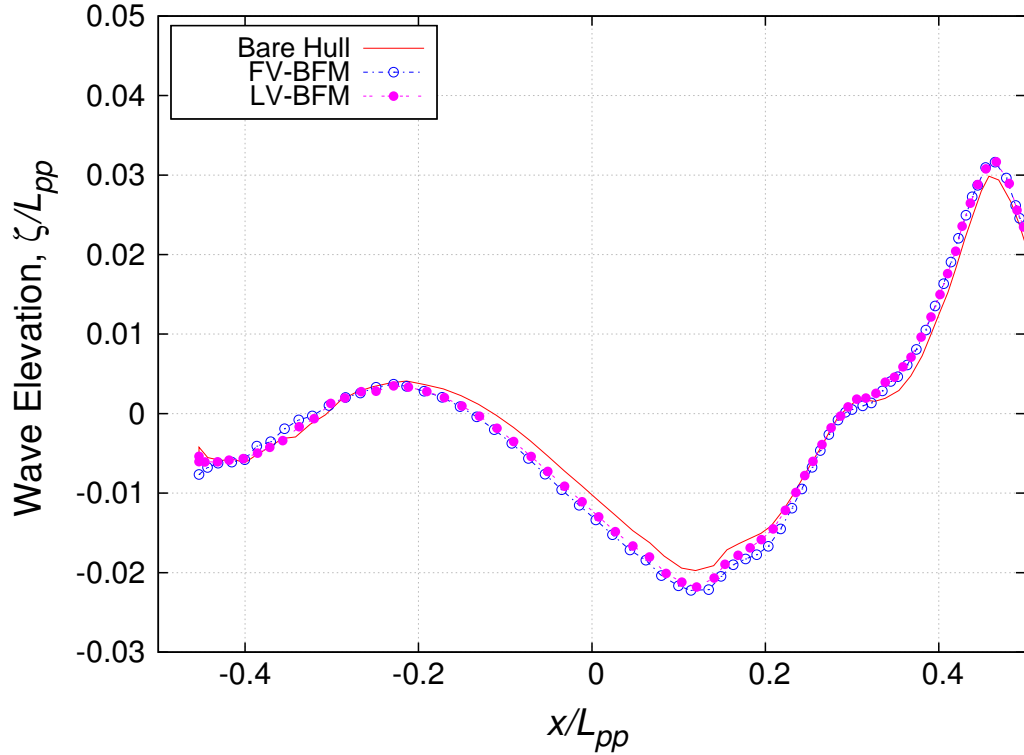


Figure 6.36: Comparison of wave elevation along the hull for GRID-C at $Fn = 0.34$.

6.3.1 Wave Elevations

The free surface wave elevation behind the stern of the fishing vessel for the bare-hull and the self-propulsion simulations are compared in Figure 6.35. It is observed that the flow behind the vessel was accelerated due to the propeller action which increased the wave elevation behind the transom. Differences were also observed in the flow predicted by the two body-force models.

The non-dimensional wave elevations along the hull surface are compared in Figure 6.36 for the bare hull and the self-propulsion cases. The predicted wave elevation for the self-propulsion case is slightly higher than that of the bare hull case near the bow and is lower near the middle of the model. The difference in the wave elevation is due to different sinkage and trim for the bare hull and the self-propelled hull.

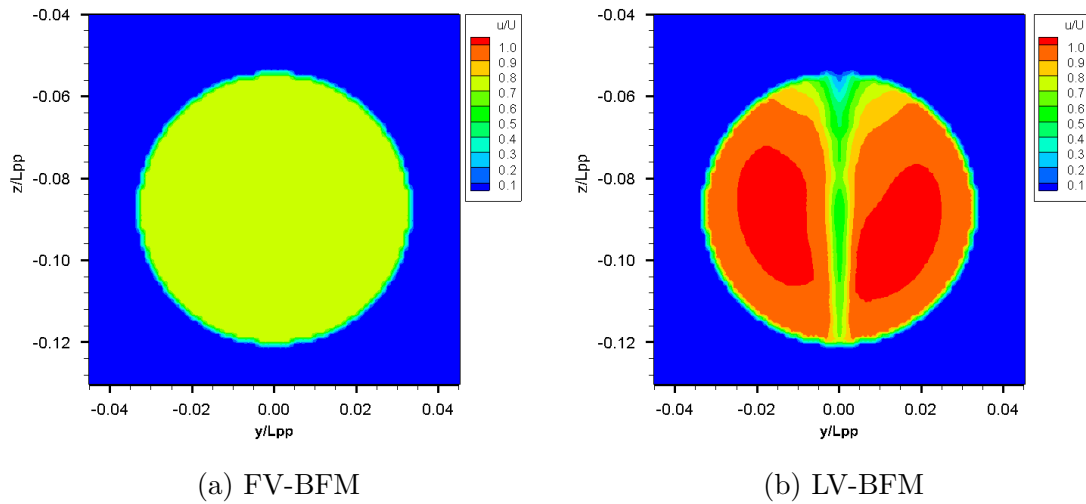
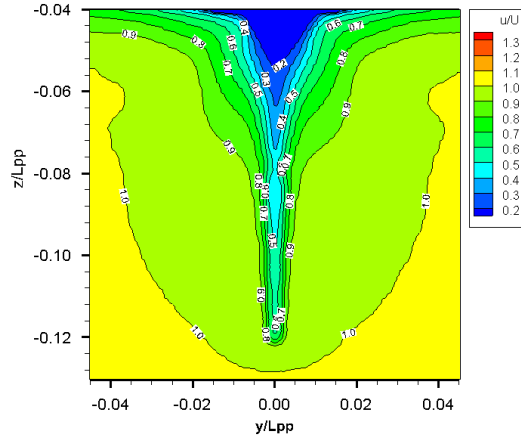


Figure 6.37: Input velocity distribution on the propeller plane at $F_n = 0.34$.

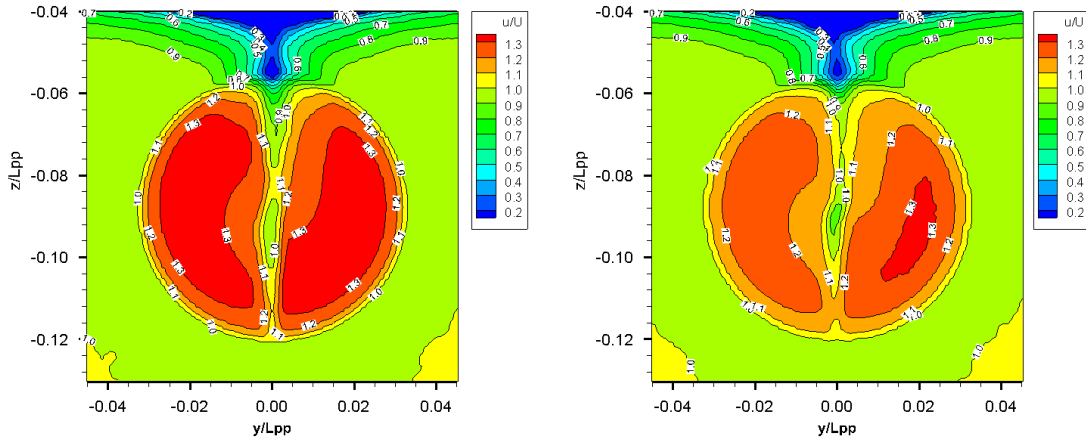
6.3.2 Velocities on Propeller Plane

The difference in the distribution of input velocity for the two body-force models is shown in Figure 6.37 on the propeller plane. In case of FV-BFM, the input velocity is the same as that on the propeller plane, which neglects the local incoming flow. The input velocity for LV-BFM method varies over the propeller disk as it samples the incoming velocity on a plane upstream of the propeller disk.

The axial velocities with and without propeller modelling were computed on the propeller plane using the unsteady solver and compared in Figure 6.38 for $F_n = 0.34$. As shown in the figure, a strong boundary layer effect due to the skeg is visible in the axial velocity distribution. In the case of the axial velocity with the FV-BFM method, the average flow is accelerated due to the propeller action. The axial velocity distribution is almost symmetrical about the center plane. For the axial velocity distribution based on the LV-BFM method, the effect of local flow can be clearly observed. A stronger velocity is seen on one side than the other side. The effect of



(a) Without propeller modeling



(b) FV-BFM

(c) LV-BFM

Figure 6.38: Axial velocity distribution on the propeller plane at $Fn = 0.34$.

Table 6.7: Comparison of $|E\%D|$ for F_{Tow} , sinkage and trim at $Fn = 0.34$

| | $R_{T(SP)}$ (N) | T (N) | Q (N-m) | n (rps) | F_{Tow} (N) | $ E\%D $ | Sinkage (m) | Trim (deg) | $ E\%D $ |
|--------------------|-----------------|---------|-----------|-----------|---------------|----------|-------------|------------|----------|
| $k - \omega$ SST | 14.6048 | 15.9 | 0.438 | 15.9218 | -1.2952 | 61.99 | -0.0156 | 0.2810 | 18.76 |
| $k - \omega$ SSTCC | 14.4751 | 15.9 | 0.438 | 15.9218 | -1.3682 | 59.82 | -0.0156 | 0.2936 | 15.12 |
| Experimental | | 15.902 | 0.464 | 15.8255 | -3.4071 | | - | 0.3459 | - |

rotational flow on the propeller plane can also be observed. Strong vortices are seen in the axial velocity contours due to the propeller action.

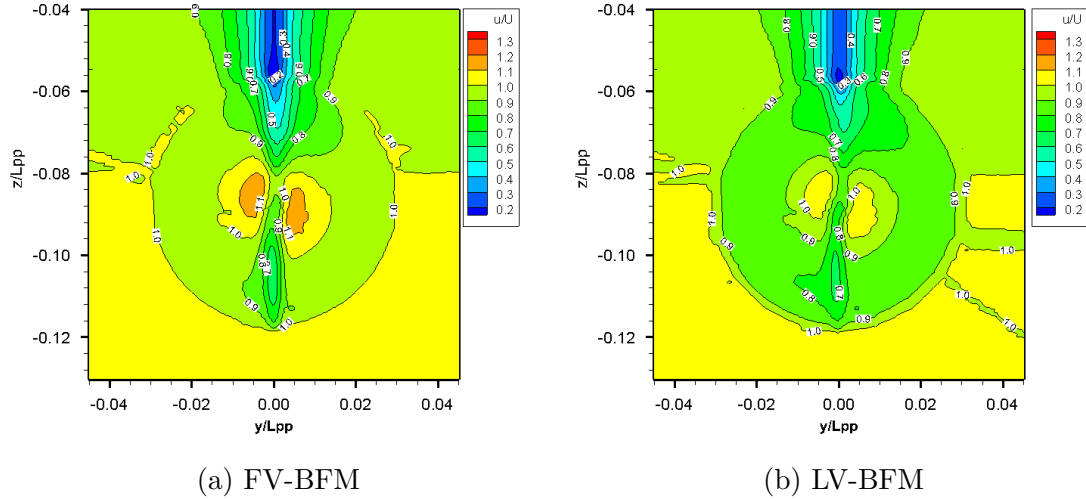


Figure 6.39: Effective wake distribution on the propeller plane at $F_n = 0.34$.

Table 6.8: Self-propulsion simulation results using the load varying method by FV-BFM at $F_n = 0.34$

| | Numerical | | | Experimental | | |
|--------|-----------|---------------|------------|--------------|---------------|------------|
| | n (rps) | F_{Tow} (N) | Trim (deg) | n (rps) | F_{Tow} (N) | Trim (deg) |
| CASE01 | 13.8751 | 4.1924 | 0.4318 | 13.7760 | 2.1189 | 0.4327 |
| CASE02 | 14.7391 | 1.7548 | 0.3635 | 14.6566 | -0.3246 | 0.4095 |
| CASE03 | 15.4899 | -0.2972 | 0.3200 | 15.3975 | -2.4043 | 0.3431 |
| CASE04 | 15.9218 | -1.3682 | 0.2936 | 15.8255 | -3.4072 | 0.3459 |

Table 6.9: Self-propulsion simulation results using the load varying method by LV-BFM at $F_n = 0.34$

| | Numerical | | | Experimental | | |
|--------|-----------|---------------|------------|--------------|---------------|------------|
| | n (rps) | F_{Tow} (N) | Trim (deg) | n (rps) | F_{Tow} (N) | Trim (deg) |
| CASE01 | 13.7760 | 4.4160 | 0.4363 | 13.7760 | 2.1189 | 0.4327 |
| CASE02 | 14.6566 | 1.3620 | 0.4786 | 14.6566 | -0.3246 | 0.4095 |
| CASE03 | 15.3975 | 0.4074 | 0.3854 | 15.3975 | -2.4043 | 0.3431 |
| CASE04 | 15.8255 | -0.1583 | 0.3107 | 15.8255 | -3.4072 | 0.3459 |

The effective axial velocity distributions on the propeller plane by two different body-force models are compared in Figure 6.39. Note that the effective axial velocity, u , is defined as the difference between the induced axial velocities obtained from open

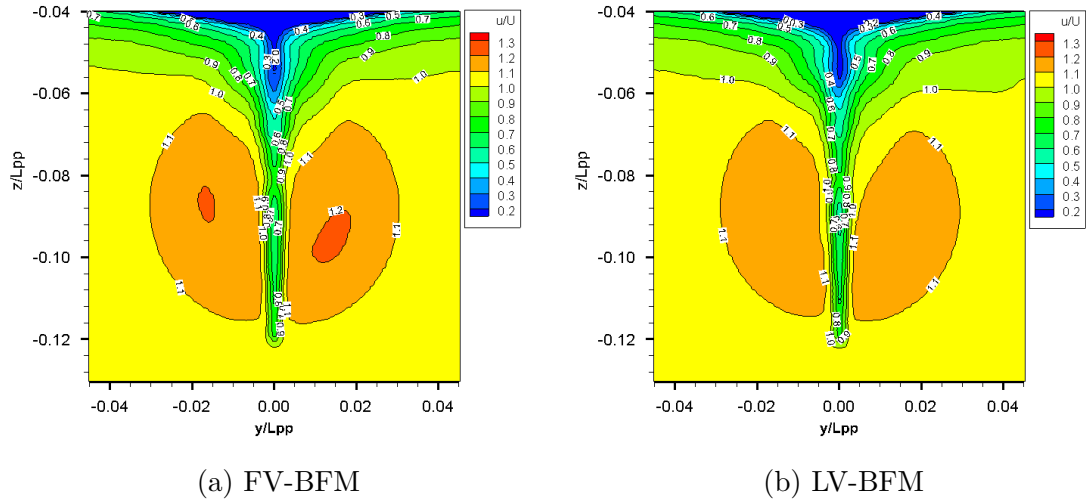


Figure 6.40: Propeller suction effect at $x/L_{pp} = 0.10D$ at $Fn = 0.34$.

water and self-propulsion simulations, and it is normalized using the ship speed. The effective axial velocity by FV-BFM is in general greater than that by LV-BFM method. In other words, the flow was more accelerated in the simulations by the FV-BFM method. The predicted propeller suction effects by the two methods at $d/D = 0.10$ upstream of the propeller plane are compared in Figure 6.40. The predicted suction effect is more asymmetric about the ship center plane by the LV-BFM method.

6.3.3 Thrust, Torque, Tow Force and Self-Propulsion Point

In the self-propulsion simulations, the effect of turbulence model on the numerical solution was investigated using two turbulence models, $k - \omega$ SST, and $k - \omega$ SSTCC for $Fn = 0.34$ with the FV-BFM method. The predicted tow force, F_{Tow} , thrust, T , torque, Q , propeller revolution rate, (n) , and trim and sinkage of the model are presented in Table 6.7. The relative errors, $|E\%D|$, for F_{Tow} and trim, are calculated using the experimental data.

Table 6.10: Self-propulsion parameters of fishing vessel at $Fn = 0.34$

| | n_s | η_R | η_H | η_o | P_E (kws) | P_D (kws) | QPC |
|--------------|--------|----------|----------|----------|-------------|-------------|---------|
| FV-BFM | 3.4134 | 1.0019 | 0.9714 | 0.4954 | 364.90 | 836.68 | 48.22 % |
| LV-BFM | 3.3697 | 0.9968 | 1.0040 | 0.5022 | 364.90 | 775.13 | 50.26 % |
| Experimental | 3.2287 | 0.9004 | 1.0786 | 0.5012 | 377.05 | 759.75 | 48.67 % |

To determine the self-propulsion point, additional cases were simulated using different propeller rates of revolution with the $k - \omega$ SSTCC turbulence model and using FV-BFM and LV-BFM. The numerical results are summarized in Tables 6.8 and 6.9. The tow force, F_{Tow} , K_T , and $10K_Q$ are plotted against the rate of revolution, n , and compared with the experimental data in Figure 6.41. A larger deviation between the numerical results and the experimental data can be observed in the results by both body-force models. At higher n , both FV-BFM and LV-BFM led to a large discrepancy from the experimental data. The ship self-propulsion point obtained from the experiment is at $n = 13.82$ rps, while $n = 14.61$ rps and $n = 14.42$ rps were determined from FV-BFM and LV-BFM, respectively.

6.3.4 Self-Propulsion Results

Results of self-propulsion simulations in full scale for the fishing vessel at 12.28 knots are presented in Table 6.10 in terms of efficiency and power. At this vessel speed, the skin friction correction SFC is 2.0873 N. Note that the results were extrapolated from model scale to full scale. From the table, it can be seen that LV-BFM was able to predict the self-propulsion results with a greater accuracy than FV-BFM although it slightly over-predicted the QPC .

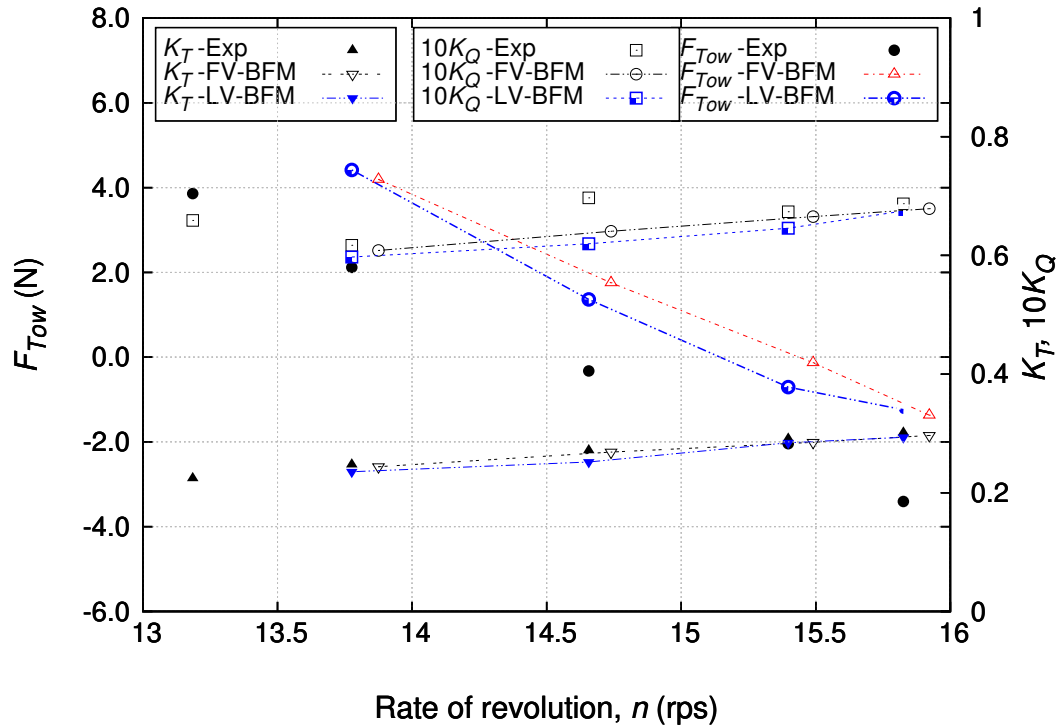
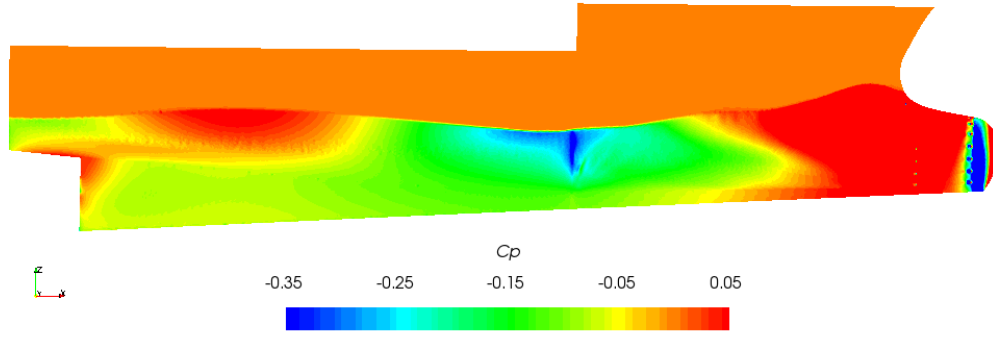


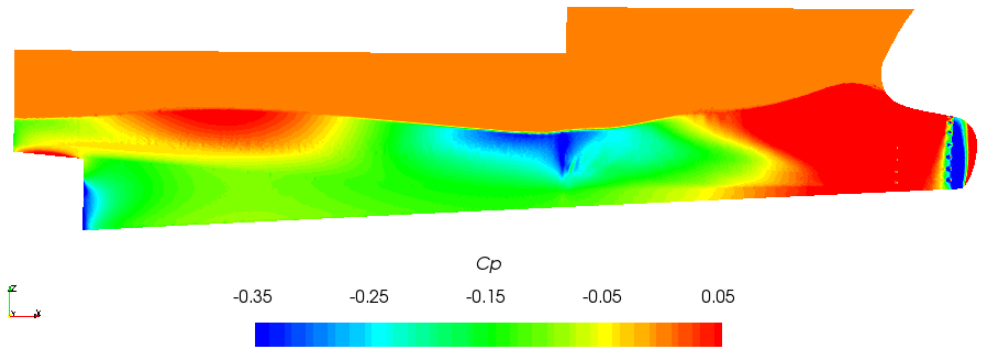
Figure 6.41: Comparison of tow forces at $Fn = 0.34$.

6.3.5 Pressure Distribution

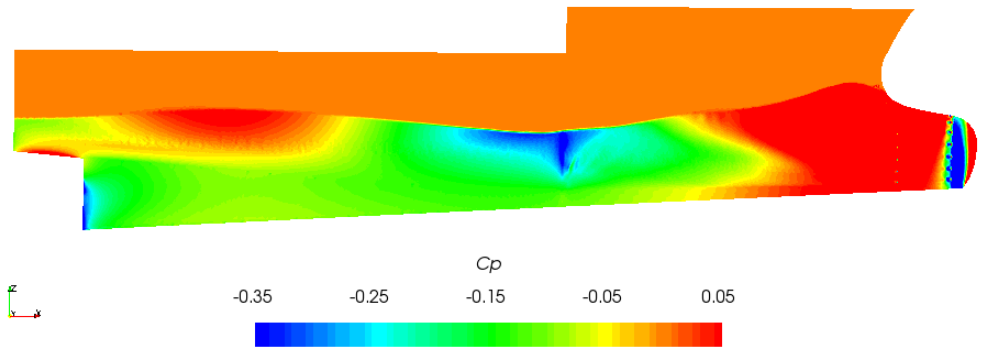
The distributions of dynamic pressure coefficient C_P on the hull are presented in Figure 6.42 for the bare hull and the hull with the propeller. The pressure at the end of skeg for the self-propulsion case is lower than that for the bare hull case due to the flow acceleration in front of the propeller. As expected, the pressure distribution on the other part of the hull generally remains the same in the three cases. The effect of the body-force modelling on the streamlines in the downstream of the propeller plane is shown in Figure 6.43. Slight differences can be observed.



(a) Bare hull

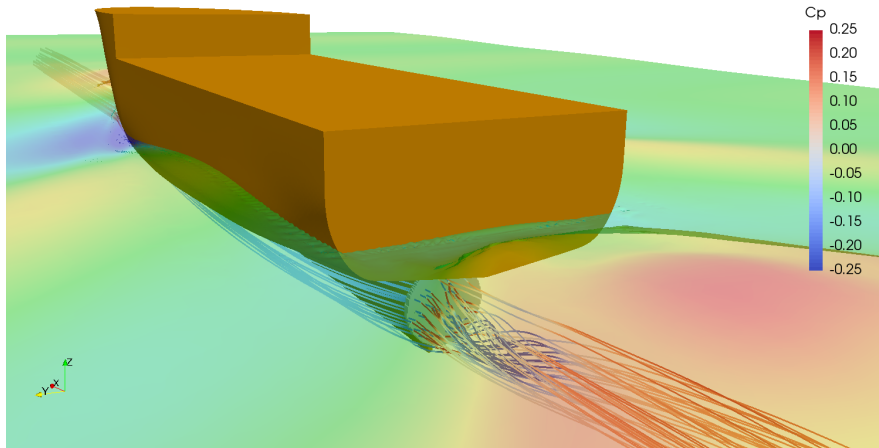


(b) FV-BFM

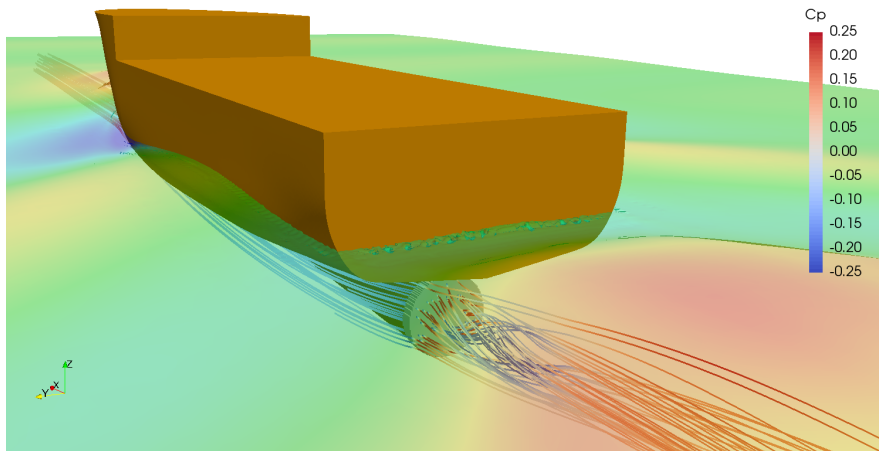


(c) LV-BFM

Figure 6.42: Pressure distribution on the hull at $Fn = 0.34$.



(a) FV-BFM



(b) LV-BFM

Figure 6.43: Streamlines around the propeller plane for $Fn = 0.34$

6.4 HPC and Computational Time

The numerical simulations for this thesis were carried in skipper and openfoam server. Both of the server are located at Memorial University. Most of the time, 120 to 132 computing cores were used on 7 nodes, 196 core cluster. Each of nodes were equipped with two Intel processors at 1.20 GHz. The cluster was running 64-bit Centos 6.5 with Rocks 6.1.1 (Sand Boa) Cluster Management. A single node openfoam server, 56 cores with two Intel(R) Xeon(R) CPU E5-2697 @ 2.60GHz processors was used for small simulations. The openfoam server was running Red Hat Enterprise Linux 7. The number of calculation cores were different for different type of simulations. Table 6.11 presents the computational time for different type of cases.

Table 6.11: Computational time in skipper and openfoam server.

| Cases | Number of cells (millions) | Number of Processors | Computing Time per time step or Iteration | Time Required |
|------------------------------------|----------------------------|----------------------|---|----------------------------------|
| Steady Resistance | 4.22 | 72 | 33 sec | 5,000 |
| Steady Resistance | 8.43 | 144 | 33 sec | 3,000 |
| Unsteady Resistance | 10.31 | 120 | 66 sec | |
| Wave Simulation | 1.32 | 48 | 38 sec | 500 ~ 1000 steps per wave period |
| Self-propulsion (Actual propeller) | 12.00 | 100 | 55 sec | |
| Self-propulsion (body-force) | 8.98 | 72 | 78 sec | |
| Self-propulsion in wave | 12.00 | 96 | 363 sec | 1,000 steps per wave period |

Chapter 7

Conclusions and Recommendations

7.1 Conclusions

Detailed propeller and inflow modelling is an important step for the accurate prediction of the effective wake due to propeller-hull interaction, including the propeller suction effect. The ship's motion affects the incoming flow to the propeller, which affects the loading on the propeller, the propeller performance, and the propeller induced noise and vibration. Consideration of all these effects allows greatly improved predictions of the actual propeller loading, leading to more efficient propulsion system designs that consider realistic operating conditions. In the present research, numerical simulations of propeller-hull interaction including ship motions were performed using a multiphase viscous flow solver in OpenFOAM with the $k-\omega$ SST and the $k-\omega$ SST with curvature correction turbulence models. The propeller-hull interaction was studied using both the propeller detailed geometry and two body-force models.

Due to the complexity of the final numerical model, the simulation models were developed and validated in several steps. The steps in the propeller-hull interaction study include (I) bare hull resistance, wave profile, and flow velocity

model development and validation, (II) propeller open water model development and data validation, (III) numerical wave tank implementation and validation, (IV) self-propulsion simulation implementation at an even keel condition, (V) self-propulsion simulation with sinkage and trim and (VI) final full self-propulsion simulation in waves with ship motions.

In the case of bare hull resistance, wave profile, and flow velocity model validation, the three ship models, KCS, JBC and a Fishing vessel, were used to validate the numerical simulations. An anisotropic meshing capability was developed and implemented in OpenFOAM meshing module snappyHexMesh to overcome the limitation of anisotropic mesh generation. The computational grids for the bare hull simulations were generated using the newly developed meshing module, named navalSnappyHexMesh. Anisotropic meshing in the free surface region greatly reduces the overall grid numbers by providing the required grid resolution in the free surface region, which is essential to capture the generated wave elevation, but allowing for lower grid resolutions in less critical regions. For the KCS and JBC models, a Kelvin wedge shape grid refinement was used on the free surface with further local grid refinement in the bow and stern regions. Wall functions were used for near-wall treatment in the numerical simulations.

Simulations for fixed condition cases were performed using a multiphase steady solver. The steady solver was also used for dynamic cases, but in the dynamic cases, the steady solutions were used as initial conditions to reduce the computational time required for the unsteady simulations. Verification and validation included uncertainty calculations. The resistance validation and verification show that a minimum of about seven hundred cells over the ship's length are necessary for adequate numerical prediction. This conclusion is also supported by the comparison

between predicted and measured wave elevation along the hull surface. Predictions of wave elevation at different longitudinal cuts are also confirmed with good accuracy. Axial velocity distributions at different transverse locations, including the propeller plane, were compared with experimental data using local grid refinement in the same way as for the hull grid refinement. From comparison with experimental measurements, it is concluded that numerical simulation using the anisotropic grid refinement reduces the number of computational grids without compromising the accuracy of the numerical results.

Propeller open water simulations were validated using data for four propeller models; KP505, MP687, DTMB5168, and a stock propeller. The KP505, MP687, and DTMB5168 propellers were used to validate simulation cases that used detailed geometry modelling. The KP505 and the stock propeller were used for the simulation cases that used the body-force models. Due to the poor quality mesh generated by snappyHexMesh for the complex geometries, such as propellers, the propeller meshes were generated using NUMECA Hexpress. Propeller open water simulations were carried out using a single-phase viscous solver. Wall functions were also employed for near-wall treatment of turbulence modelling. The thrust and torque generated by the detailed propeller geometry simulations showed good agreement with the experimental data. However, the numerical results for efficiency showed large deviation at higher advance coefficients. The implemented effective local velocity body-force model agreed well with the experimental data for torque, thrust and propeller efficiency.

For the numerical wave tank validation, different wave steepness was studied with different grid resolutions and different time-step sizes. In case of the high wave steepness, more cells were required per wavelength and wave height. A grid dependency study showed that 160 cells per wavelength and 20 cells per wave height

are required. The required number of time steps per wave period was less for low wave steepness than for high wave steepness. In the case of high wave steepness, a minimum of 1000 time steps per wave period were required with a higher-order divergence scheme for the convective term. If the second-order divergence scheme is used, almost double the number of time steps is required for the same wave. For low wave steepness cases, the required number of time steps was almost half that of the high wave steepness cases. The effect of the turbulence models on numerical wave generation was also investigated using the realizable $k - \epsilon$ and $k - \omega$ SST turbulence models. In all cases 0.10% turbulence intensity was used. It was found that grid resolutions and time step sizes were adequate for numerical wave generation with both turbulence models. The numerical wave tank was validated for low wave steepness for self-propulsion simulation in waves. It was found that less number of cells per wave length and less number of time steps are adequate for low steepness waves than high steepness waves.

For the study of propeller-hull interaction, the self-propulsion simulations were carried out at a fixed even keel condition for the KCS ship model. The optimum grids for the hull and propeller from the bare hull study and the propeller open water study were merged for the case of the rotating propeller behind the hull. The simulations were also carried out using both the nominal average velocity body-force model and the effective local velocity body-force model. Steady simulations were performed until the resistance converged. Then the steady simulation results were used as the initial condition for the unsteady simulations. This approach significantly reduces the computational time. Rotational speed was applied to the propeller at a fixed rate of revolution. The numerical results using the detailed propeller geometry agree well with the available experimental data. Since the flow around the propeller is highly non-linear and rotational, the $k - \omega$ SSTCC turbulence model was used to

better model the rotational effect of the flow. The axial velocity distribution at $0.25D$ downstream of the propeller plane was compared with experimental data. The derived skin friction coefficient was also compared with that calculated as part of the experimental data analysis. The effective local velocity body-force model and nominal average velocity body-force model were also used for self-propulsion simulation. In terms of propeller force coefficient, the effective local velocity body-force model showed better performance than the nominal average velocity body-force model.

Self-propulsion simulations were carried out with ship motion in calm water for the KCS and JBC models using the detailed propeller geometry models. Both body-force models were used for the self-propulsion simulation of the fishing vessel. During these numerical simulations, the ship models were limited to heave and pitch motion only. For self-propulsion simulation with detailed propeller geometry, the developed dynamic class with sliding mesh was used to allow the combination of ship motions and a rotating propeller. The overall comparison of the numerical results for the JBC hull simulation with the experimental data found to show good agreement. In the case of the KCS model, the total resistance was higher than in the even keel condition. The propeller thrust was decreased due to the changes in incoming flow. The motion of the KCS ship model introduced an asymmetric pressure distribution on the hull above the propeller. All these results were as expected based on the numerical modelling that allowed these features to be captured. Ships are known to suffer increased resistance when motions are introduced and propeller thrust is known to decrease. Asymmetric pressure distributions arise from the propeller rotation and this can lead to vibration on the hull. The ability to capture the phenomena shows that the developed dynamic class can be successfully used for self-propulsion simulation with ship motions and a rotating propeller.

A seakeeping simulation was carried out in advance of the self-propulsion simulation in waves. The optimum numerical settings based on the previous validations of the resistance, propeller open water, and wave modelling were used in the seakeeping numerical simulation. Comparison of the simulated motion responses shows reasonable agreement with the available experimental data. As a concluding demonstration of the capability of the developed dynamic class for this research, a self-propulsion simulation with ship forward speed and ship motion was conducted in a regular wave. Due to a lack of experimental data, it was not possible to compare these numerical results. The pitch and heave motion plots show that the self-propulsion simulation can be successfully conducted with the fully assembled numerical model when the ship experiences relatively large motions. This model provides a realistic simulation of propeller performance in operating conditions that fully captures all the effects of a ship operating in a seaway. This allows the variability in flow and propeller performance inherent in realistic operations to be analyzed as part of a complete propulsion system design process.

The step-by-step validation of numerical simulation results against the available experimental data using the developments in this Ph.D. demonstrates the effectiveness and importance of the continuing development of CFD models and modelling techniques for flow conditions that ultimately may be too challenging for experimental measurement. The effective wake and self-propulsion parameters were well predicted for the ship in calm water and ships with motion using detailed propeller geometry modelling. The developed dynamic motion class using the sliding mesh method exhibits good performance without increasing computational time with respect to the overset grid method. Simplified propeller body-force models that can be used to speed up computations or for cases where detailed propeller geometry is not yet known were also developed for self-propulsion simulation and validated with experimental data.

7.2 Best practice for propeller-hull interaction.

The following sections provide guidance for the development of numerical models involving the interaction between propellers and ship hulls. This guidance is intended to speed development of future models and is based on the experiences of the present work. These tips are specific to the OpenFOAM meshing and solver software and to the algorithms developed as part of this study, but it is expected that many items would also be applicable to other viscous flow solver packages.

7.2.1 Selection of computational domain.

1. The inlet boundary should be at 1.0 ~ 2.0 ship lengths in front of the model. For the simulation with incoming wave, the inlet boundary should be placed at least 2.0 ship lengths in front of the model.
2. The outlet boundary should be 3.0 ~ 4.0 ship lengths behind the model to avoid wave reflection from the outlet boundary.
3. The side boundaries should be at least one ship length from the hull.
4. The bottom boundary should be one ship length below the hull to reduce the blockage effect.
5. The top boundary can be set 0.5 ~ 1.0 ship lengths above the calm water surface.
6. The bottom boundary in wave simulation should not be placed less than water depth of the experimental facility. When the experimental facility's water depth is unknown, the water depth should be set according to the deep water wave condition.

7.2.2 Mesh generation.

1. The mesh quality and resolution is crucial in numerical simulations with OpenFOAM.
2. The non-dimensional first layer thickness, $y^+ \geq 30$ allows the use of wall functions to reduce the total number of cells. To solve the detailed flow features, such as tip vortex, y^+ should be less than 5.0.
3. The mesh resolution should be fine enough to capture the geometry accurately.
4. Local refinements are necessary for regions where flow changes. The cell size should be of the same order as that of the cell near the body.
5. For numerical simulation of ship resistance with free surface, 700 to 1000 cells per ship length should be distributed.
6. For numerical simulation of propeller-hull interaction, 160 cells per wave simulation, and 20 cells per wave height is recommended for accurate input wave simulation for high steepness waves. The required cell number can be reduced for low steepness waves.
7. The ratio of near wall thickness to the undistorted cell size along the body surface should not be less than 0.1. Otherwise numerical ventilation will occur in numerical simulation. The mesh quality should be checked in OpenFOAM before running the simulation. Attention should be paid to non-orthogonality and skewness of cells.

7.2.3 Selection of propeller modelling

1. The choice of propeller modelling method depends on the required parameters from the simulation as well as the data availability.
2. Detailed flow features, tip vortex propagation, pressure fluctuation due to the propeller rotational effect and suction effect, and wake distribution can be obtained using the detailed propeller model.
3. Because of two different time scales for the ship hull and propeller, the simulation time is higher for the detailed propeller method than that for the body-force method.
4. For fast self-propulsion simulation, the body-force method can be used, which requires propeller open water curves.

7.2.4 Solver selection

1. The steady solver is adequate to predict the force in steady flow with reasonable accuracy.
2. If the wave making resistance in a low speed region ($0.1 < Fn < 0.2$), the single-phase steady simulation would be a good choice. If not, unsteady simulation with free surface is recommended.
3. The steady simulation is recommended for the initial condition of unsteady simulation, which can reduce the computational time significantly.

7.2.5 Boundary conditions set-up

1. Velocity boundary conditions should be imposed on the inlet boundary.

2. Neumann boundary conditions can be imposed on the outlet boundary since it is far from the body.
3. For deep water simulations, side boundaries and the bottom boundary can be set as symmetry planes. The top boundary can be set as pressure inletOutlet boundary.
4. The body needs to be set as a no-slip wall boundary.
5. Depending on y^+ , the wall functions for turbulence parameters need to be set. If $y^+ \leq 1.0$, fixed value condition is recommended for turbulence parameters. In case of $y^+ \geq 30$, a fully turbulent wall function is recommended for turbulence parameters.

7.2.6 Selection of turbulence model

1. Reynolds stress models predict the vortex more accurately with a greater computing cost.
2. Turbulence models with curvature correction are recommended.
3. realizable $k - \epsilon$ turbulence model is recommended for wave simulation since over-production of the turbulence viscosity in the $k - \omega$ SST turbulence model damps out the wave height as the simulation progresses.

7.2.7 Selection of numerical schemes

1. First-order schemes can be used to start the numerical simulation.
2. To improve accuracy, numerical schemes need to be changed to second order after initial convergence. The change in numerical scheme can be done manually or automatically using `timeActivatedFileUpdate` function.

7.2.8 Time step size selection

1. In OpenFOAM, the PIMPLE algorithm helps to increase the time step size, i.e., a higher Courant number. In this case, the number of outer iterations should be increased. For better accuracy, the Courant number for free surface should be less than 5.0.
2. For self-propulsion simulation, the time scales for the hull and propeller are different. The Courant number should be less than 1.0. A greater Courant number could lead to incorrect results.
3. With the sliding mesh technique, 360 to 720 time steps per revolution of the propeller is recommended.

7.2.9 Setting convergence criteria

1. For convergence of numerical simulation, the physical quantity (such as resistance for ship) should be monitored along with the residuals.
2. The initial residual for pressure should be set to 10^{-2} or less.
3. For other parameters, such as volume fraction, k and ω , the initial residual should be set to 10^{-6} .
4. For resistance convergence, 0.01% in error is suggested as the convergence criterion.

7.3 Recommendations for Future Work

Based on the experience of the present research, the following should be considered for future work. This work can improve some aspects of the methods and codes developed

as part of this research or in some cases build additional capability using the present work as a base.

1. The prism layer generation in snappyHexMesh is inadequate, particularly when the cell has a high aspect ratio. The prism layer generation module can be improved.
2. Only constant rotational speed is implemented for propeller rotation in the present study. Time dependent motion can be developed for propeller rotation and can also be applied for rudder motion.
3. The present simulation is limited to regular waves. Irregular wave trains could be incorporated into the simulation to provide more realistic motion simulations.
4. Because of the different time scale for ship hull and propeller simulations, the detailed propeller numerical simulation requires longer simulation time. When using the time scale for the hull, the propeller force and moment predictions are incorrect. A numerical method might be developed to achieve propeller force and moment convergence at a higher time scale.
5. Ultimately ship maneuvering simulation can be implemented, based on the present code, by adding sway and yaw motions which would allow the effects of horizontal plane ship motions on the propeller inflow and loading to be simulated.

Bibliography

- Ali, M. A., Peng, H., and Qiu, W. 2017a. Benchmark Studies of Wave Run-Up and Forces on a Truncated Square Cylinder. International Conference on Offshore Mechanics and Arctic Engineering, Volume 1: Offshore Technology.
- Ali, M. A., Peng, H., Qiu, W., and Bensow, R. 2017b. Prediction of Propeller Tip Vortex Using OpenFOAM. International Conference on Offshore Mechanics and Arctic Engineering, Volume 7A: Ocean Engineering.
- Ali, M. A., Peng, H., and Qiu, W. 2018. Resistance computation of an optimized fishing vessel. *In: 26th annual conference of the computational fluid dynamics society of canada.*
- Ali, M. A., Peng, H., and Qiu, W. 2019a. Resistance prediction of two fishing vessel models based on RANS solutions. Physics and Chemistry of the Earth, Parts A/B/C, 113, 115–122. Computational Environmental Flow and Transport Phenomena.
- Ali, M. A., Peng, H., and Qiu, W. 2019b. Simulations of self-propulsion model tests of a fishing vessel using a body-force method coupled with a RANS solver. *In: The Joint Canadian Society for Mechanical Engineering and CFD Society of Canada International Congress 2019.*

- ASME. 2009. Standard for verification and validation in computational fluid dynamics and heat transfer-ASME V&V 20-2009. The American Society of Mechanical Engineers (ASME).
- Banks, J., Phillips, A. B., and Turnock, S. R. 2010. Free surface CFD prediction of components of ship resistance for KCS. 13th Numerical Towing Tank Symposium, Germany.
- Bensow, R. E. 2013. Simulation of unsteady propeller blade loads using OpenFOAM. 16th Numerical Towing Tank Symposium, NuTTS'13.
- Bertram, V. 2012. Practical Ship Hydrodynamics. Second edn. Oxford: Butterworth-Heinemann.
- Brackbill, J. U, Kothe, D. B., and Zemach, C. 1992. A continuum method for modeling surface tension. Journal of Computational Physics, 100(2), 335–354.
- Carrica, P. M., Mofidi, A., Eloit, K., and Delefortrie, G. 2016. Direct simulation and experimental study of zigzag maneuver of KCS in shallow water. Ocean Engineering, 112, 117–133.
- Castro, A. M., Carrica, P. M., and Stern, F. 2011. Full scale self-propulsion computations using discretized propeller for the KRISO container ship KCS. Computers & Fluids, 51(1), 35–47.
- Chandar, D. D, and Gopalan, H. 2016. Comparative analysis of the Arbitrary Mesh Interface (AMI) and overset methods for dynamic body motions in OpenFOAM. 46th AIAA Fluid Dynamics Conference.
- Chesnakas, C. J., and Jessup, S. D. 1998. Propeller tip vortex measurements using 3-component LDV. Proc 22nd Symp on Naval Hydrodynamics, 156–170.

- Chong, M. S., Perry, A. E., and Cantwell, B. J. 1990. A General Classification of Three-Dimensional Flow Fields. *Physics of Fluids A: Fluid Dynamics*, 2(5), 765–777.
- Dhinesh, G, Murali, K, and Subramanian, A. V. 2010. Estimation of hull-propeller interaction of a self-propelling model hull using RANSE solver. *Ships and Offshore Structures*, 5(2), 125–139.
- Doormaal, J. P., and Raithby, G. D. 1984. Enhancements of the SIMPLE method for predicting incompressible fluid flows. *Numerical Heat Transfer Part A - Applications*, 7(2), 147–163.
- Eça, L., and Hoekstra, M. 2006. Discretization Uncertainty Estimation based on a Least Squares version of the Grid Convergence Index. *In: 2nd Workshop on CFD Uncertainty Analysis*, Lisbon. International Conference on Offshore Mechanics and Arctic Engineering.
- Eça, L., and Hoekstra, M. 2014. A procedure for the estimation of the numerical uncertainty of CFD calculations based on grid refinement studies. *Journal of Computational Physics*, 262, 104–130.
- Eça, L., Vaz, G., and Hoekstra, M. 2010. Code Verification, Solution Verification and Validation in RANS Solvers. *In: 29th International Conference on Ocean, Offshore and Arctic Engineering: Volume 6*.
- Farrell, P. E., and Maddison, J. R. 2011. Conservative interpolation between volume meshes by local Galerkin projection. *Computer Methods in Applied Mechanics and Engineering*, 200(1), 89–100.
- Felli, M, and Felice, F. D. 2004. Analysis of the propeller-hull interaction by LDV phase sampling techniques. *Journal of Visualization*, 7(1), 77–84.

- Ferziger, J. H., and Peric, M. 2012. Computational methods for fluid dynamics. Springer.
- Friis, D., Bass, D., Gradner, A., and Edward, L. S. 2007. Design of two multi-species fishing vessel. Phase 2. Industrial Outreach Group, Faculty of Engineering and Applied Science. MUN.
- Fujisawa, J., Ukon, Y., Kume, K., and Takeshi, H. 2000. Local velocity field measurements around the KCS model in the SRI 400 m towing tank. Tech. rept. Ship Performance Division Report No. 00-003-02, The Ship Research Institute of Japan.
- G2010. 2010. Gothenburg 2010 A Workshop on CFD in Ship Hydrodynamics, Gothenburg, Sweden.
- Gaggero, S., Gaggero, T., Rizzuto, E., Tani, G., Villa, D., and Viviani, M. 2016. Ship propeller side effects: Pressure pulses and radiated noise. *Noise Mapping*, 3(01).
- Goldstein, S. 1929. On the vortex theory of screw propellers. *Proceedings of the Royal Society of London. Series A, Containing Papers of a Mathematical and Physical Character*, 123(792), 440–465.
- Higuera, P. 2020. Enhancing active wave absorption in RANS models. *Applied Ocean Research*, 94, 102000.
- Higuera, P, Lara, J. V., and Losada, I. J. 2013. Realistic wave generation and active wave absorption for NavierStokes models: Application to OpenFOAM. *Coastal Engineering*, 71, 102–118.
- Hirt, C. W., and Nichols, B. D. 1981. Volume of fluid (VOF) method for the dynamics of free boundaries. *Journal of Computational Physics*, 39(1), 201–225.

- Holmen, V. 2012. Methods for vortex identification. Masters thesis, Lund University.
- Hough, G. R., and Ordway, D. E. 1964. The generalized actuator disk. Tech. rept. Therm Advanced Research, Inc.
- Hsiao, C., and Pauley, L. L. 1999. Numerical computation of the tip vortex flow generated by a marine propeller. *ASME Journal of Fluids Engineering*, 121(3), 638–645.
- Hylarides, S. 1978. Some hydrodynamic consideration of propeller induced ship vibrations. *In: The Ship Vibration Symposium*. Society of Naval Architects and Marine Engineers.
- Inukai, Y., and Ochi, F. 2009. A study on the characteristics of self-propulsion factors for a ship equipped with contra-rotating propeller. First International Symposium on Marine Propulsors, SMP09.
- Issa, R. I. 1986. Solution of the implicitly discretised fluid flow equations by operator-splitting. *Journal of Computational Physics*, 62(1), 40–65.
- ITTC. 1978. ITTC recommended procedures and guidelines. ITTC performance prediction method, 7.5-02-03-01.4.
- ITTC. 2008. ITTC recommended procedures and guidelines. ITTC testing and extrapolation methods propulsion, performance propulsion test, 7.5-02-03-01.1.
- ITTC. 2011. ITTC recommended procedures and guidelines. Practical Guidelines for Ship CFD Applications, 7.5-03-02-03.
- Jacobsen, N., Fuhrman, D. R., and Fredsøe, J. 2012. A wave generation toolbox for the opensource CFD library: OpenFOAM. *International Journal for Numerical Methods in Fluids*.

- Jasak, H. 1996. Error analysis and estimation for the finite volume method with applications to fluid flows. Ph.D. thesis, Imperial College of Science, Technology and Medicine, Department of Mechanical Engineering.
- Juretic, F. 2017. cfMesh: Advanced Meshing Tool.
- Kawamura, T., Miyata, H., and Mashimo, K. 1997. Numerical simulation of the flow about self-propelling tanker models. *Journal of Marine Science and Technology*, 2, 245–256.
- Kerwin, J. E., and Lee, C. S. 1978. Prediction of steady and unsteady marine propeller performance by numerical lifting-surface theory. *The Society of Naval Architects and Marine Engineers, Transaction.*, 86:21853.
- Kim, S., Su, Y., and Kinnas, S. A. 2018. Prediction of the Propeller-induced Hull Pressure Fluctuation via a Potential-based Method: Study of the Influence of Cavitation and Different Wake Alignment Schemes. *In: Proceedings of the 10th International Symposium on Cavitation (CAV2018)*. ASME Press.
- Kim, W. J., Van, S. H., and Kim, D. H. 2001. Measurement of flows around modern commercial ship models. *Experiments in Fluids*, 31(5), 567–578.
- Larsson, L., Stern, F., and Visonneau, M. 2014. *Numerical Ship Hydrodynamics An assessment of the Gothenburg 2010 Workshop*. Springer, Dordrecht.
- Launder, B. E., Reece, G. J., and Rodi, W. 1975. Progress in the development of a Reynolds-stress turbulence closure. *Journal of Fluid Mechanics*, 68(3), 537566.
- Lee, S., and Chen, H. 2005. The influence of propeller/hull interaction on propeller induced cavitating pressure. *In: The Fifteenth International Offshore and Polar*

- Engineering Conference, International Society of Offshore and Polar Engineers ISOPE.
- Lewis, E. V. (ed). 1988. Principles of Naval Architecture: Volume II: Resistance, propulsion and vibration. Society of Naval Architects and Marine Engineers.
- Mayer, S., Garapon, A., and Sørensen, L. S. 1998. A fractional step method for unsteady freesurface flow with applications to nonlinear wave dynamics. International Journal for Numerical Methods in Fluids, 28, 293–315.
- Menter, F. R., Kuntz, M., and Langtry, R. B. 2003. Ten years of industrial experience with the SST turbulence model. Turbulence, Heat and Mass Transfer, 625–632.
- Muzaferija, S., and Peric, M. 1997. Computation of free-surface flows using the finite-volume method and moving grids. Numerical Heat Transfer, Part B: Fundamentals, 32(4), 369–384.
- Nagamatsu, T. Sasajima, T. 1975. Effect of propeller suction on wake. Journal of the Society of Naval Architects of Japan, 1975(137), 58–63.
- Nakatake, K. 1989. On ship hullpropellerrudder interactions (in Japanese). In Proceedings of the 3rd JSPC symposium on flows and forces of ships, 231259.
- Oliveira, P. J., and Issa, R. I. 2001. An improved PISO algorithm for the computation of buoyancy-driven flows. Numerical Heat Transfer, Part B: Fundamentals, 40(12), 473–493.
- OpenFOAM. 2019 (December 23). OpenFOAM Users Guide-1912. OpenFOAM.
- Paik, B. G, Lee, C. M., and Lee, S. J. 2004. PIV analysis of flow around a container ship model with a rotating propeller. Experiments in Fluids, 36, 833–846.

- Paik, B. G., Kim, G. D., Lee, J. Y., and Lee, S. J. 2007. Visualization of the inflow ahead of a rotating propeller attached to a container ship model. *Journal of Visualization*, 10(1), 47–55.
- Paik, K-J, Park, H-G, and Seo, J. 2013. RANS simulation of cavitation and hull pressure fluctuation for marine propeller operating behind-hull condition. *International Journal of Naval Architecture and Ocean Engineering*, 5(4), 502–512.
- Patankar, S. V. 1980. *Numerical heat transfer and fluid flow*. Hemisphere Pub.
- Patankar, S. V., and Spalding, D. B. 1972. A calculation procedure for heat, mass and momentum transfer in three-dimensional parabolic flows. *International Journal of Heat and Mass Transfer*, 15(10), 1787–1806.
- Pecoraro, A., Felice, F. D., Felli, M., Salvatore, F., and Viviani, M. 2013. Propeller-hull interaction in a single-screw vessel. *Third International Symposium on Marine Propulsors*, 10.
- Peng, H., Qiu, W., and Ni, S. 2013. Effect of turbulence models on RANS computation of propeller vortex flow. *Ocean Engineering*, 72, 304–317.
- Pereira, F. S., Eça, L., and Vaz, G. 2017. Verification and validation exercises for the flow around the KVLCC2 tanker at model and full-scale Reynolds numbers. *Ocean Engineering*, 129, 133–148.
- Qiu, W., Peng, H., Ni, S., Liu, L., and Mintu, S. 2013. RANS computation of propeller tip vortex. *International Journal of Offshore and Polar Engineering*, 23(1), 73–79.
- Roache, P. J. 1998. *Verification and validation in computational science and engineering*. Albuquerque, NM: Hermosa.

- Rusche, H. 2002. Computational Fluid Dynamics of dispersed two-phase flows at high phase fractions. Ph.D. thesis, Imperial College of Science, Technology and Medicine.
- Shen, Z., Wan, D., and Carrica, P. M. 2015. Dynamic overset grids in OpenFOAM with application to KCS self-propulsion and maneuvering. *Ocean Engineering*, 108, 287–306.
- Sigmund, S., and el Moctar, O. 2017. Numerical and experimental investigation of propulsion in waves. *Ocean Engineering*, 144, 35–49.
- Smirnov, P. E., and Menter, F. R. 2009. Sensitization of the SST turbulence model to rotation and curvature by applying the Spalart - Shur correction term. *Journal of Turbomachinery*, 4(131).
- Stansberg, C. T., Baarholm, R., Kristiansen, T., Hansen, E. W. M., and Rortveit, G. 2005. Extreme wave amplification and impact loads on offshore structures. *In: Offshore technology conference*.
- Stern, F., Kim, H. T., and Patel, V. C. 1988. A viscous flow approach to the computation of propeller-hull interaction. *Journal of Ship Research*, 32, 246–262.
- Stern, F., V. Wilson, R. V., Coleman, H. W., and Paterson, E. G. 1999. Verification and validation of CFD simulations. Tech. rept. Iowa Institute of Hydraulic Research, The University of Iowa.
- T2005. 2005. CFD Workshop 2005 Tokyo, Japan.
- T2015. 2015. Tokyo 2015 A Workshop on CFD in Ship Hydrodynamics, Japan.
- Tocu, A. M., and Amoraritei, M. 2008. Numerical study of the flow field around a ship hull including propeller effects. *Journal of Maritime Research*, 5(3), 67–78.

- Tryggvason, G., Bunner, B., Esmaeeli, A., Juric, D., Al-Rawahi, N., Tauber, W., Han, J., Nas, S., and Jan, Y.-J. 2001. A front-tracking method for the computations of multiphase flow. *Journal of Computational Physics*, 169(2), 708–759.
- Versteeg, H. K., and Malalasekera, W. 2007. *An introduction to computational fluid dynamics: the finite volume method*. John Wiley.
- Villiers, E. 2006. *The potential of large eddy simulation for the modeling of wall bounded flows*. Ph.D. thesis, Imperial College of Science, Technology and Medicine, Department of Mechanical Engineering.
- Watanabe, O., Masuko, A., and Shiorose, Y. 1994. Numerical simulation of a wave-viscous flow about a ship including propeller effects. *Proceedings 20th Symposium on Naval Hydrodynamics*, 946–958.
- Weller, H. 2008. *A new approach to VOF-based interface capturing methods for incompressible and compressible flow*. Tech. rept. OpenCFD Ltd.
- Win, Y. N., Tokgoz, E., Wu, P. C., Stern, F., and Toda, Y. 2013. Computation of propeller-hull interaction using simple body-force distribution model around Series 60 $C_B = 0.6$. *Journal of the Japan Society of Naval Architects and Ocean Engineers*, 18, 17–27.
- Winden, B., Badoe, C., Turnock, S., Phillips, A., and Hudson, D. 2013. Self propulsion in waves using a coupled RANS-BEMt model and active RPM control. *In: Proceedings of the 16th Numerical Towing Tank Symposium*.
- Xing, T., and Stern, F. 2010. Factors of safety for Richardson extrapolation. *Journal of Fluids Engineering*, 132(9), 691–696.

- Zhang, B., Lou, J., Kang, C-W., Wilson, A., Lundberg, J., Svennberg, U., and Bensow, R. 2014. CFD modeling of propeller tip vortex over large distances. *In: International Journal of Offshore and Polar Engineering*. ISOPE.
- Zhang, D. H., Broberg, L., and Larsson, L. 1992. A method for computing stern flows with an operating propeller. *Transaction of Royal Institute of Naval Architect*, 134, 245–259.
- Zhang, Z. 2010. Verification and validation for RANS simulation of KCS container ship without/with propeller. *Journal of Hydrodynamics, Ser. B*, 22(5, Supplement 1), 932–939.
- Zou, L., and Larsson, L. 2014. CFD verification and validation in practice - A study based on resistance submission to the Gothenburg 2010 Workshop on numerical ship hydrodynamics. *In: 30th Symposium on Naval Hydrodynamics*.

This page intentionally left blank.

Appendices

Appendix A

Propeller Tip Vortex Simulation

A.1 Geometry and Test Conditions

A five blade fixed-pitch propeller model, DTMB5168 was used in the numerical simulation for the propeller tip vortex study. The principal particulars of the DTMB5168 propeller model are given in Table A.1. For geometric simplification, an infinitely long constant radius cylinder was considered as the hub on which the blades were mounted, and the root fillet was ignored.

Table A.1: Propeller particulars

| Parameters | Variable | Value | Unit |
|-----------------------------|------------|-------------------|------|
| Diameter | D | 0.403 | m |
| Inflow Velocity | U_∞ | 10.70 | m/s |
| Chord Length at $0.7R$ | C | 0.175 | m |
| Advance Coefficient | J | 1.1 | |
| Rotation Speed | N | 24.167 | rps |
| Combined Velocity at $0.7R$ | V_∞ | 23.93 | m/s |
| Reynolds Number | Re | 4.2×10^6 | |

A.2 Computational Domain and Grid generation

A spiral-like computational domain was adopted similar to the one in the previous work by Peng et al. (2013) so that the grid concentration can be achieved along the tip vortex core to minimize the flow across the periodic boundaries. The computational domain was created using the blade to blade passage of the suction side and the pressure side of the blades with two periodic boundaries as shown in Figure A.1. According to the domain-dependency study by Qiu et al. (2013), it was found that the outlet boundary from D to $1.5D$ gave almost the same results. In this study, the computational domain was created with the inlet boundary at $0.5D$ upstream, the outlet boundary at $1.0D$ downstream, and the outer boundary at $1.0D$ from the propeller axis. A small modification, extending the inlet and outlet boundary in the axial direction of the computational domain was made to avoid the problematic cells during the grid generation process.

In previous work, the grid was generated based on the work of Hsiao and Pauley (1999). It was found that the grid with lower y^+ value and/or a large number of cells within the tip vortex core led to convergence problems in ANSYS CFX due to the large Jacobian values for the generated grid. Thus the smallest first grid spacing was restricted to $y^+ = 7.5$. The local cell refinement was also at a constant radius from the propeller axis rather than along the tip vortex trajectory, which was not sufficiently accurate to capture the tip vortex in the far field.

In this work, an unstructured hexahedral mesh was generated using NUMECA Hexpress to overcome the shortcoming in the previous grid generation method. At the first step, the computational domain was divided into a number of small blocks and the refinement level on the blade surface was obtained by dividing the small blocks

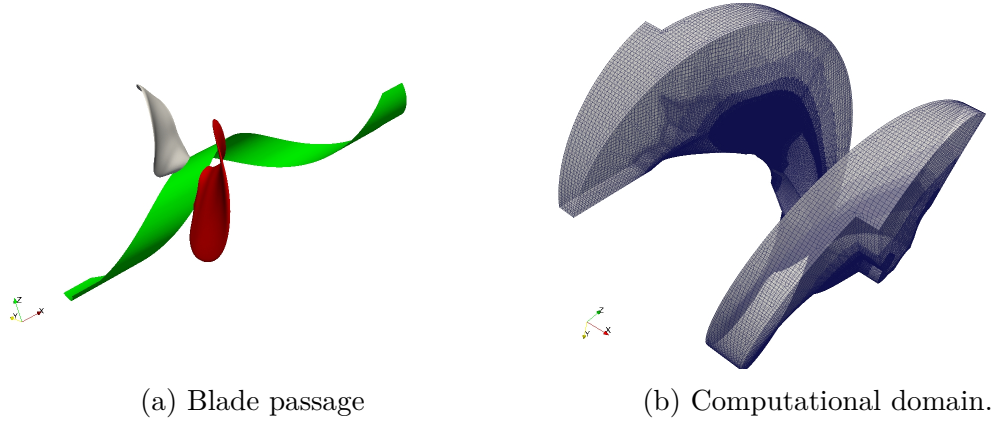


Figure A.1: Geometry and computation domain for grid generation

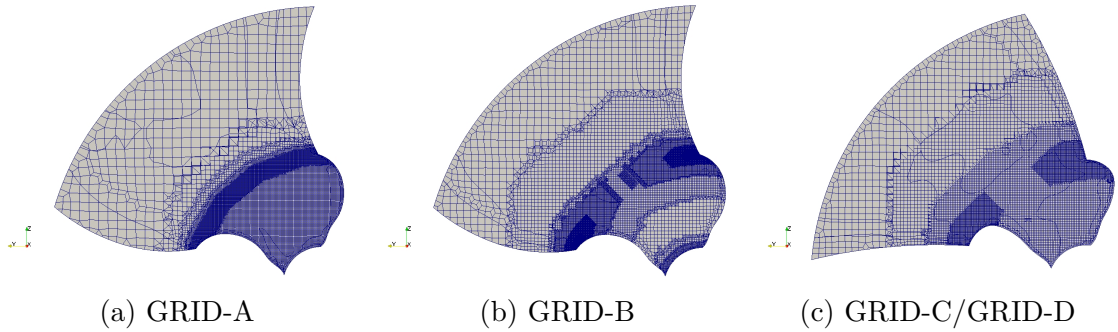


Figure A.2: Type of refinement.

to a certain level. In the second step, the local refinement was applied at the desired location depending on the type of refinement method. Then the boundary vertices were snapped on the boundaries. Finally, the prism layer cells were inserted in the viscous region and the grid was optimized and smoothed. Following the above steps, it is possible to keep the cell quality in terms of the skewness and non-orthogonality in the acceptable range for the solver with a small y^+ .

It is well known that the numerical predictions of the tip vortex are largely dependent on the grid concentration in the vortex core (Zhang et al., 2014). To obtain the grid concentration along the vortex core, three types of grid refinement methods were employed in the grid generation process. An annular cylindrical refinement region

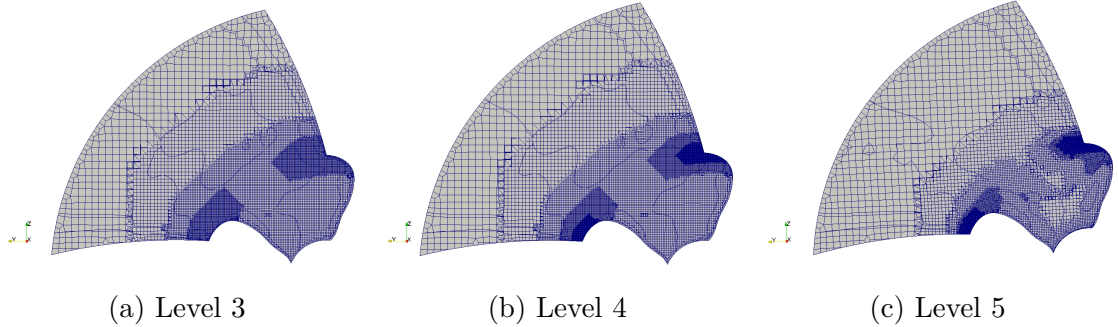


Figure A.3: Refinement level.

was used for GRID-A. The cells within the specified region were refined to a specified refinement level. This refinement type was used to track the initial predicted tip vortex trajectory. In the second approach, the cells around the tip vortex were refined to improve the numerical prediction of the vortex strength which is shown in GRID-B. In the third approach, the cells around the experimental tip vortex trajectory were refined for the better prediction of tip vortex in GRID-C/ GRID-D. Figure A.2 shows the three refinement types. The base cell size was set 0.01 m in grid generation. Then the cells were refined in three directions repeatedly depending on the refinement level. In this study, three refinement levels were used which are shown in Figure A.3. The difference between GRID-C and GRID-D is the y^+ values on the blades surfaces. For GRID-C, the average $y^+ = 5.0$ and for GRID-D the average y^+ on the blade is 2.0. The grid information is summarized Table A.2. In the first-grid spacing dependency study, two y^+ values, 2.0 and 5.0, were used in the grid generation.

A.3 Numerical Results Validation

Validation studies were carried out for the DTMB5168 propeller model at $J = 1.1$. Since the two periodic boundaries are non-conformal, the rotational cyclic Arbitrary

Table A.2: Computational grids for DTM5168 propeller.

| Grid | Number of cells (In million) | y^+ |
|---------|------------------------------|-------|
| GRID-A | 9.47 | 5 |
| GRID-B | 15.56 | 5 |
| GRID-C1 | 10.74 | 5 |
| GRID-C2 | 13.67 | 5 |
| GRID-C3 | 15.84 | 5 |
| GRID-D1 | 18.38 | 2 |
| GRID-D2 | 21.31 | 2 |
| GRID-D3 | 27.19 | 2 |

Mesh Interface (cyclicAMI) was applied. The boundary conditions are summarized in Table A.3.

The computed K_T and K_Q based on different grids are presented and compared with the experimental results by Chesnakas and Jessup (1998) and numerical results by Peng et al. (2013) in Table A.4. Figure A.4 shows the comparison of computed K_T and K_Q using GRID-C3, and GRID-D3 in comparison with the experimental data. It can be seen that the predictions using the two grids are almost the same. Relatively greater discrepancies are shown at the lower advance coefficients. From Table A.4, it can also be seen that the accuracy of the predictions of K_T and K_Q depends on the first-grid spacing. Accuracy increases with the decrease of the first-grid spacing and the increase of the number of grids on the blade surface. However, a greater relative

Table A.3: Boundary conditions for tip vortex simulations.

| Parameters | Inlet | Outlet | Outer | Hub | Blade |
|------------|--------------|--------------|--------------|--------------------------|--------------------------|
| U | fixedValue | inletOutlet | slip | fixedValue | fixedValue |
| P | zeroGradient | fixedValue | zeroGradient | zeroGradient | zeroGradient |
| nut | zeroGradient | zeroGradient | zeroGradient | nutUSpaldingWallFunction | nutUSpaldingWallFunction |
| K | fixedValue | inletOutlet | slip | fixedValue | fixedValue |
| Omega | fixedValue | inletOutlet | slip | fixedValue | fixedValue |

Table A.4: Comparison of K_T and $10K_Q$

| Grid | K_T | $E\%D$ | $10K_Q$ | $E\%D$ |
|--------------------|-------|--------|---------|--------|
| GRID-A | 0.312 | -0.319 | 0.833 | 6.386 |
| GRID-B | 0.310 | -0.958 | 0.824 | 5.236 |
| GRID-C1 | 0.317 | 1.278 | 0.841 | 7.407 |
| GRID-C2 | 0.317 | 1.278 | 0.841 | 7.407 |
| GRID-C3 | 0.312 | -0.319 | 0.826 | 5.492 |
| GRID-D1 | 0.316 | 0.958 | 0.834 | 6.513 |
| GRID-D2 | 0.316 | 0.958 | 0.834 | 6.513 |
| GRID-D3 | 0.316 | 0.958 | 0.834 | 6.513 |
| Peng et al. (2013) | 0.312 | 0.320 | 0.805 | 2.81 |
| Experimental | 0.313 | | 0.783 | |

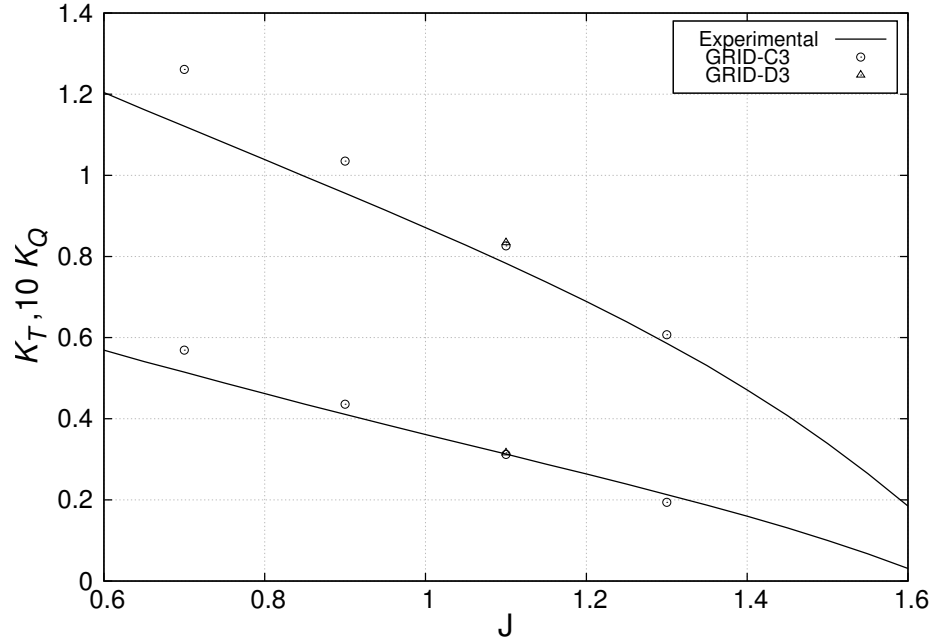
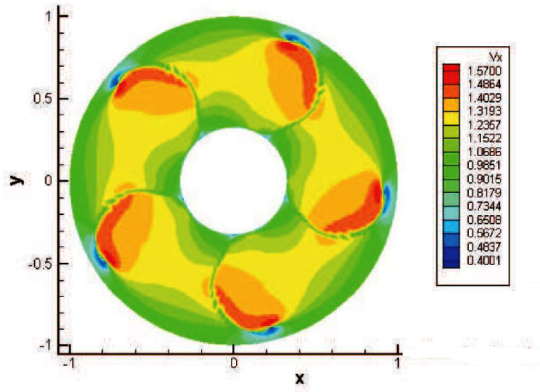


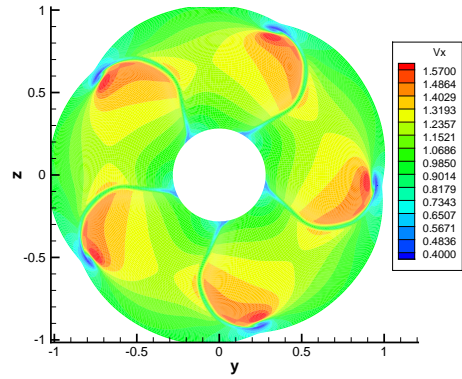
Figure A.4: Comparison of K_T and $10K_Q$ with experimental data (Chesnakas and Jessup (1998))

error was found in comparison with the results of the previous study (Peng et al., 2013).

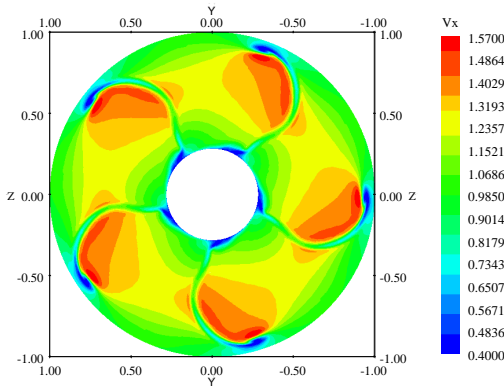
Figures A.5, A.6 and A.7 present the computed velocity contours for V_x , V_t and V_r , respectively at $x/R = 0.2386$ downstream. The numerical results in general show a



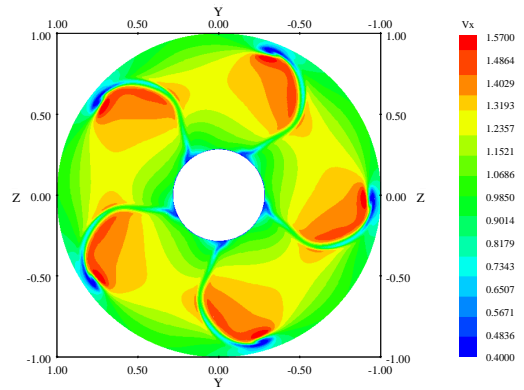
(a) Experimental.



(b) Numerical result by Qiu et al. (2013)



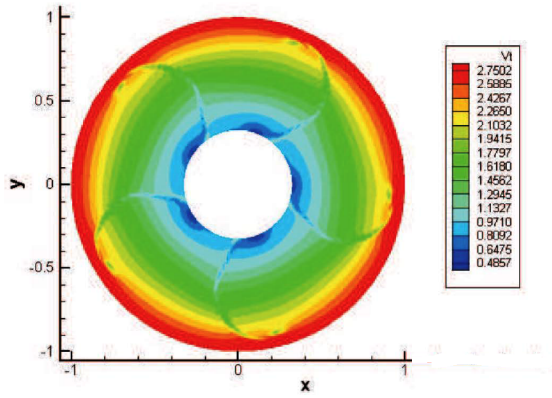
(c) GRID-C3



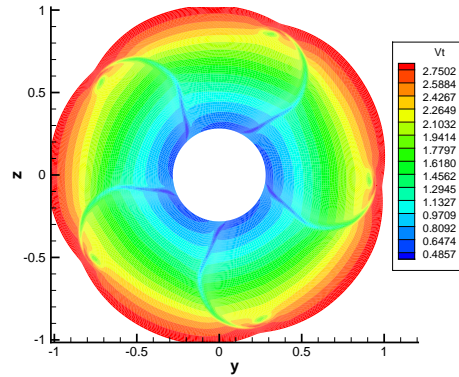
(d) GRID-D3

Figure A.5: Axial velocity V_x contour at $x/R = 0.2386$

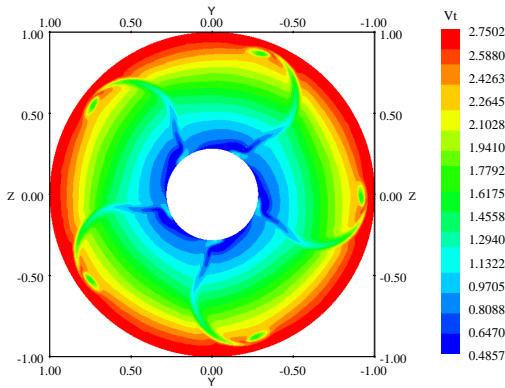
good agreement with the experimental data. To measure the accuracy of the numerical prediction quantitatively, the velocity components, V_x , V_t and V_r across the tip vortex core, based on grids with $y^+ = 2$ and $y^+ = 5$ are compared with the experimental data and the previously computed results by Peng et al. (2013) in Figures A.10 and Figure A.11, respectively. It should be noted that the vortex core was defined as the point on the plane with the minimum pressure and the corresponding value $\theta = 0$. The grid sensitivity is analyzed using root square mean (RMS) error between the experimental and numerical results. Table A.5 and A.6 show the RMS error for V_x , V_t and V_r for $x/R = 0.1756$ and $x/R = 0.2386$. The numerical predictions of the velocity



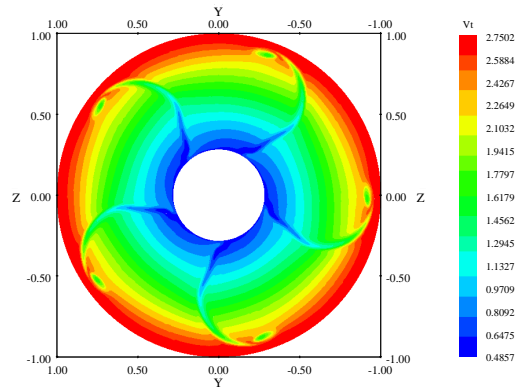
(a) Experimental.



(b) Numerical results by Qiu et al. (2013)



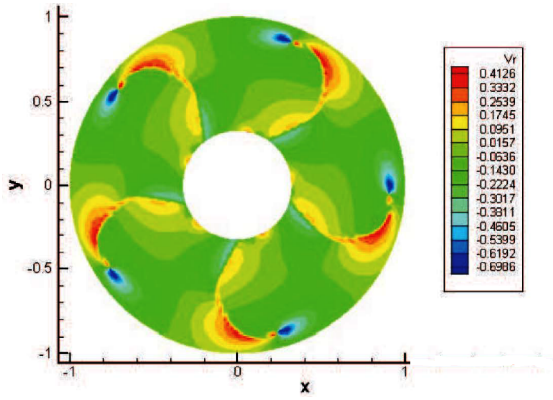
(c) GRID-C3



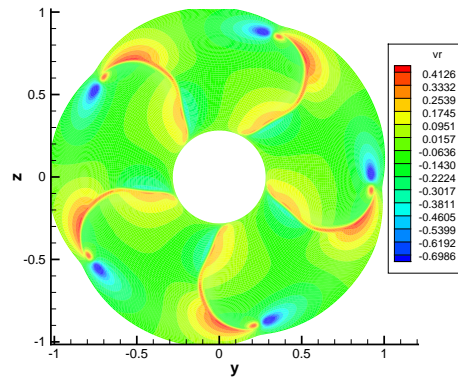
(d) GRID-D3

Figure A.6: Tangential velocity V_t contour at $x/R = 0.2386$

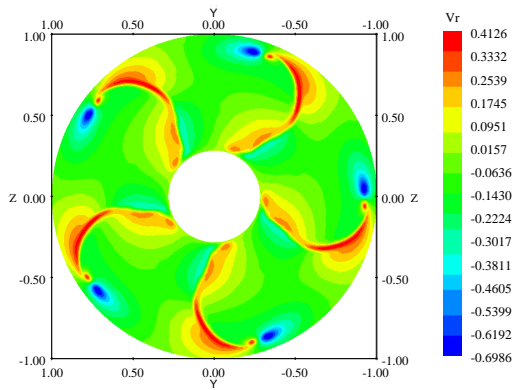
components are improved by using the third grid refinement approach for V_x and V_r . For the tangential velocity components V_t the present approach could not improve the results. However, the numerical prediction of the peak value at the vortex core was improved. The prediction better agrees with the experimental data when the grid refinement around the vortex core is increased and the first-grid spacing, y^+ , is decreased. Similar behaviour is also observed at $x/R = 0.1756$ downstream in Figure A.8 and Figure A.9. The results were improved for V_x , and V_r only. Note that the presented velocity components are normalized using the free stream velocity U_∞ .



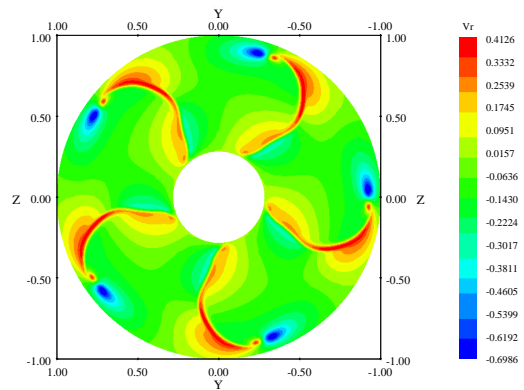
(a) Experimental



(b) Numerical results by Qiu et al. (2013)



(c) GRID-C3



(d) GRID-D3

Figure A.7: Radial velocity V_r contour at $x/R = 0.2386$

The velocity components across the tip vortex core based on different types of grids are compared in Figures A.12 and A.13. From these figures, it can be found that the numerical results based on Grid Type III with refinement level 5 show good agreement with the experimental data.

The pressure coefficients on the suction side and the pressure side of the blade are compared with the numerical results obtained by Hsiao and Pauley (1999) and previously computed results using ANSYS CFX in Figures A.14 and A.15. There are discrepancies in pressure distribution on the suction side in comparison with those by

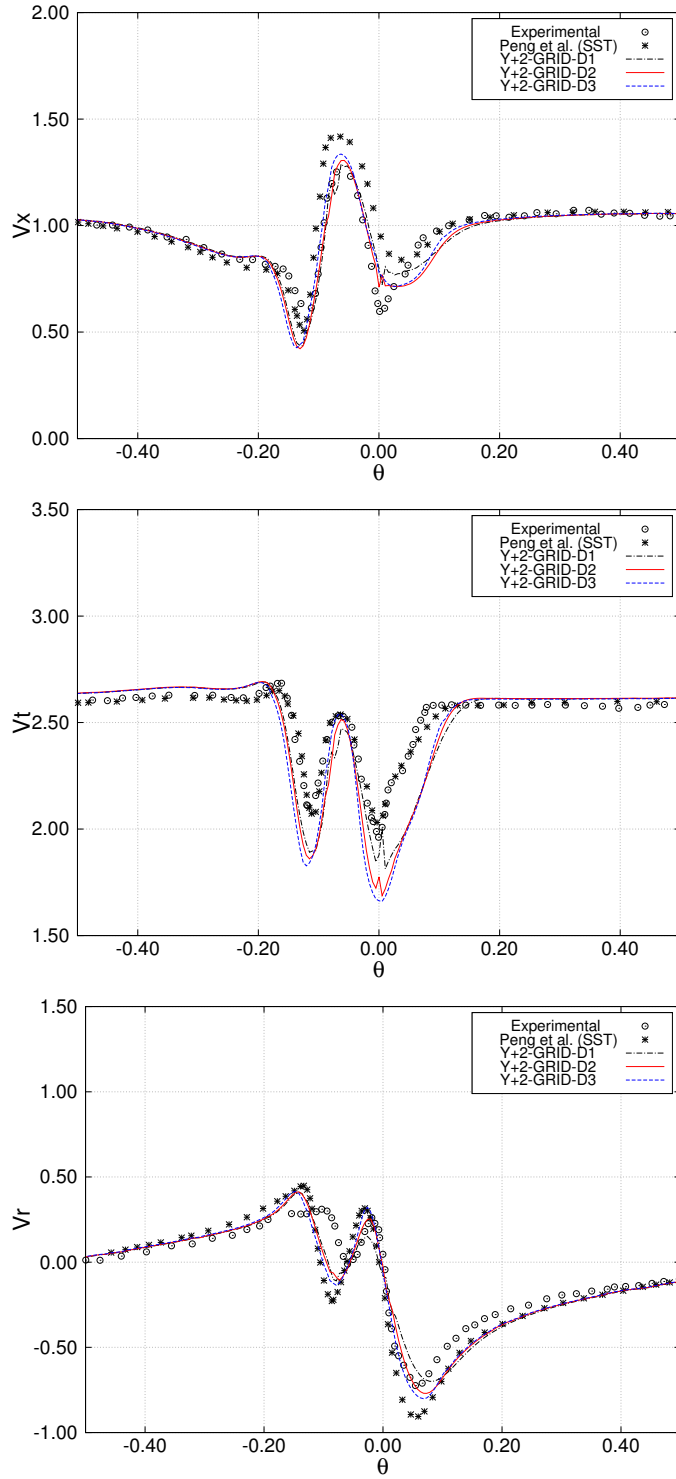


Figure A.8: V_x , V_t and V_r across vortex core at $x/R = 0.1756$

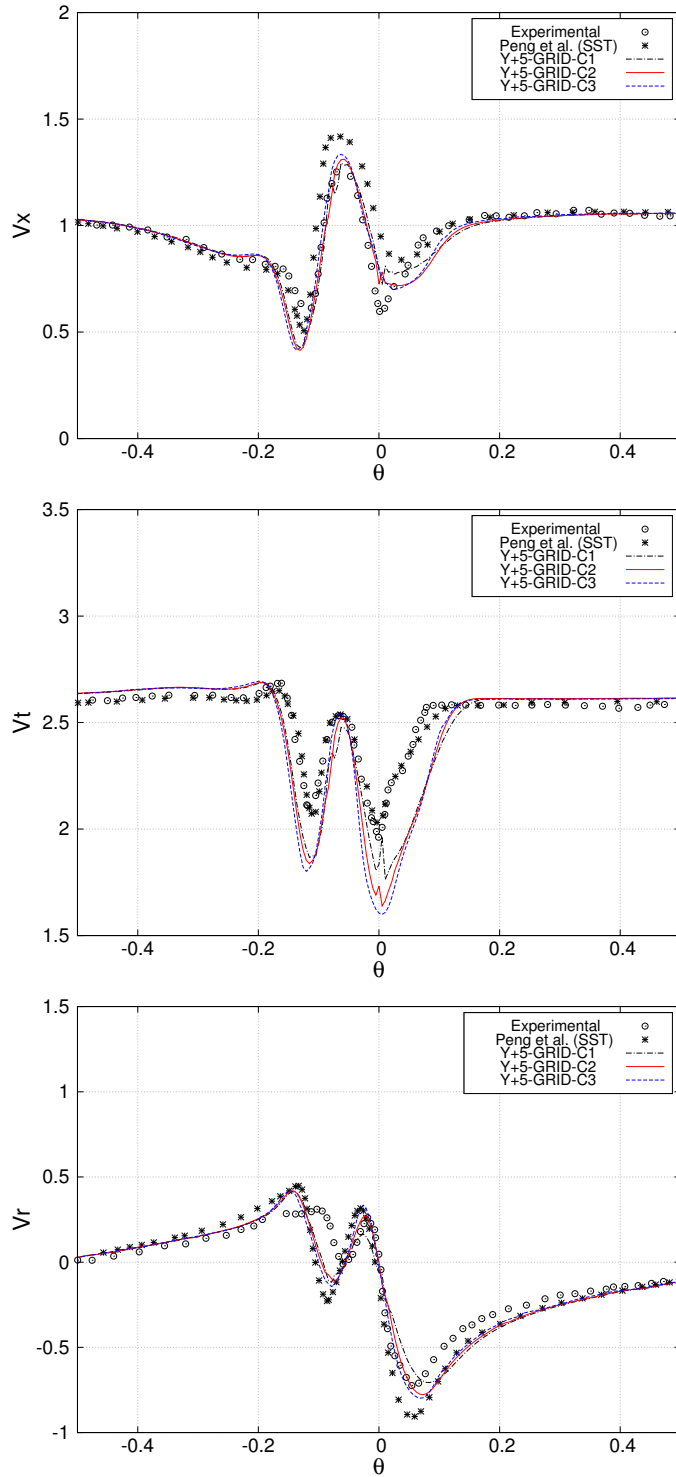


Figure A.9: V_x , V_t and V_r across vortex core at $x/R = 0.1756$

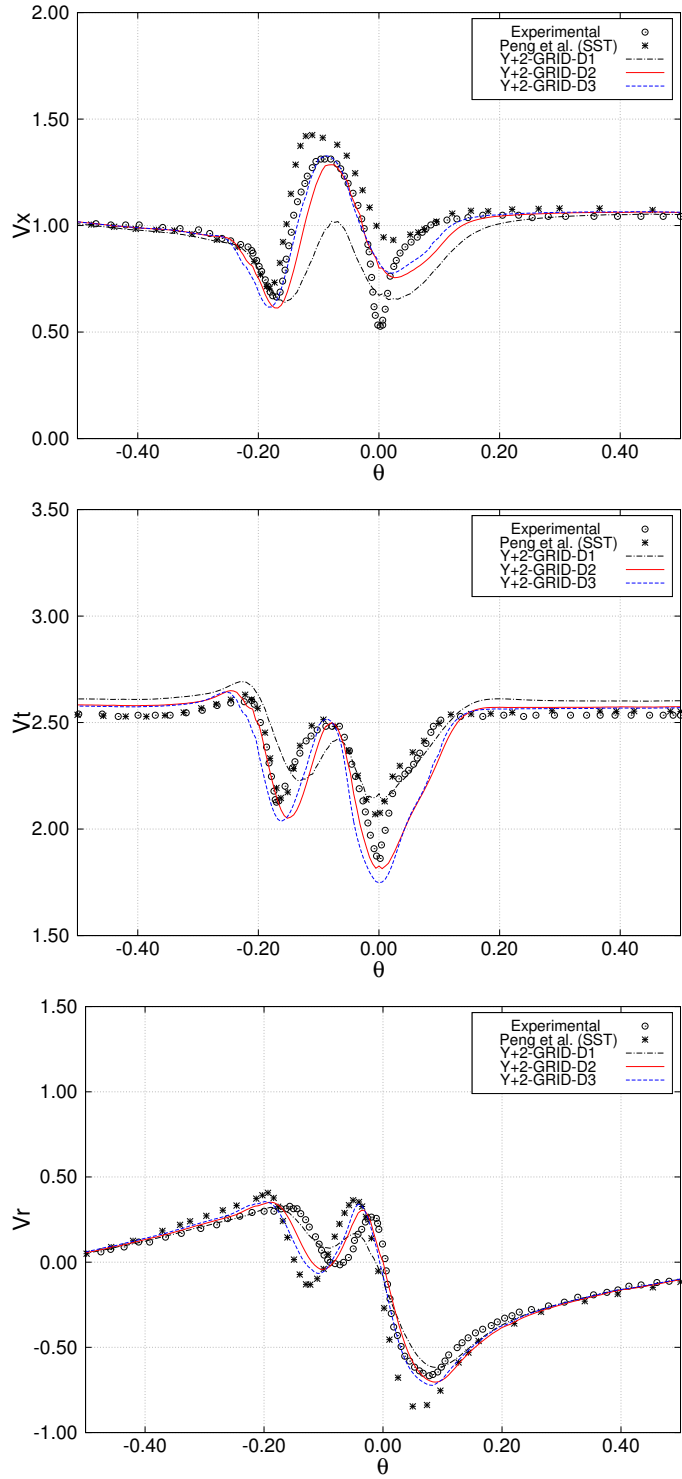


Figure A.10: V_x , V_t and V_r across vortex core at $x/R = 0.2386$

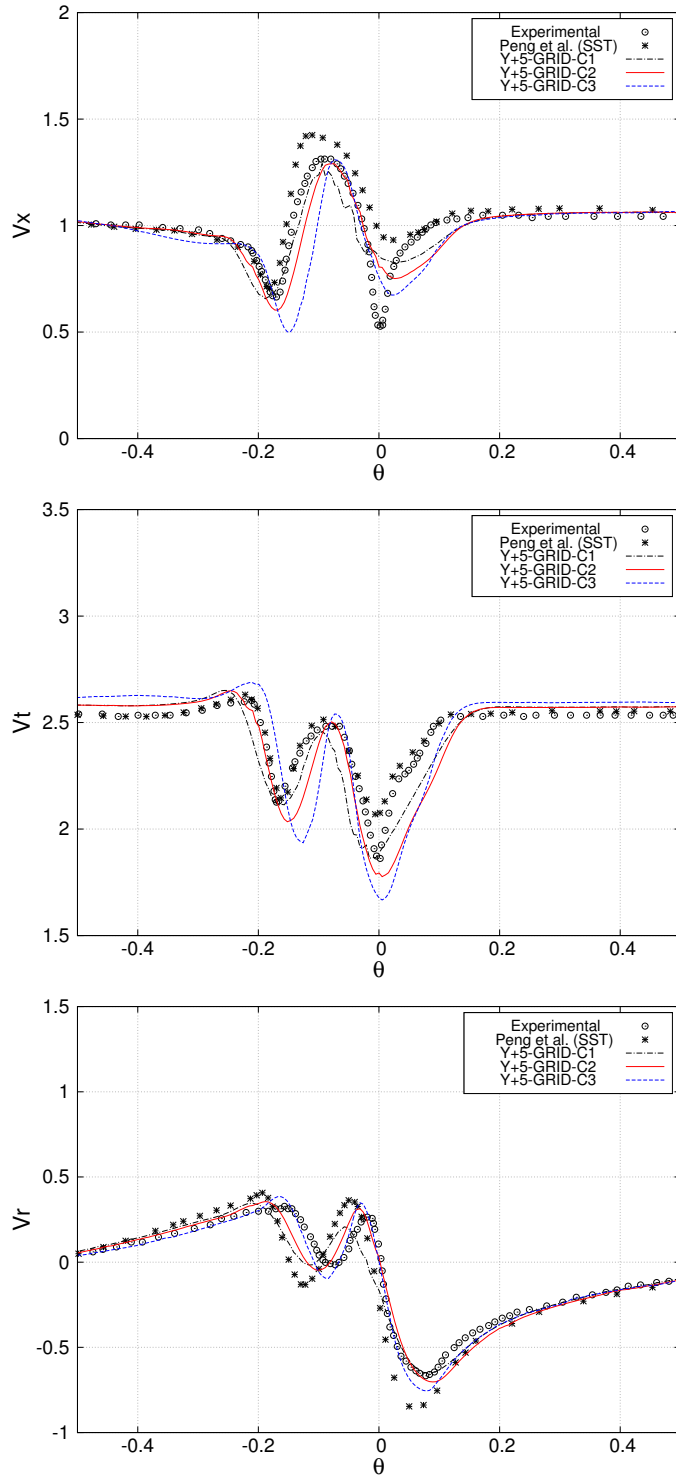


Figure A.11: V_x , V_t and V_r across vortex core at $x/R = 0.2386$

Table A.5: RMS error of V_x , V_t and V_r at $x/R = 0.1756$

| | $V_x(10^{-1})$ | $V_t(10^{-1})$ | $V_r(10^{-1})$ |
|-------------|----------------|----------------|----------------|
| GRID-A | 1.025 | 2.262 | 1.175 |
| GRID-B | 1.210 | 2.519 | 1.393 |
| GRID-C1 | 0.885 | 1.929 | 1.179 |
| GRID-C2 | 0.823 | 2.274 | 1.083 |
| GRID-C3 | 0.889 | 2.584 | 1.163 |
| GRID-D1 | 0.857 | 1.736 | 1.153 |
| GRID-D2 | 0.775 | 2.046 | 1.042 |
| GRID-D3 | 0.877 | 2.277 | 1.165 |
| Peng et al. | 1.574 | 0.403 | 1.592 |

Table A.6: RMS error of V_x , V_t and V_r at $x/R = 0.2386$

| | $V_x(10^{-1})$ | $V_t(10^{-1})$ | $V_r(10^{-1})$ |
|-------------|----------------|----------------|----------------|
| GRID-A | 1.238 | 1.702 | 0.951 |
| GRID-B | 1.135 | 1.496 | 1.018 |
| GRID-C1 | 1.156 | 1.258 | 1.184 |
| GRID-C2 | 1.224 | 1.423 | 0.810 |
| GRID-C3 | 1.876 | 2.055 | 0.589 |
| GRID-D1 | 1.904 | 1.238 | 0.838 |
| GRID-D2 | 1.179 | 1.256 | 0.803 |
| GRID-D3 | 0.994 | 1.484 | 1.022 |
| Peng et al. | 1.652 | 0.619 | 1.747 |

Hsiao and Pauley (1999) and by Qiu et al. (2013). For the pressure side, high pressure on the trailing edge as predicted by the present method and by Qiu et al. (2013) was not shown in the numerical results by Hsiao and Pauley (1999). However the general pressure distributions on the pressure side are similar.

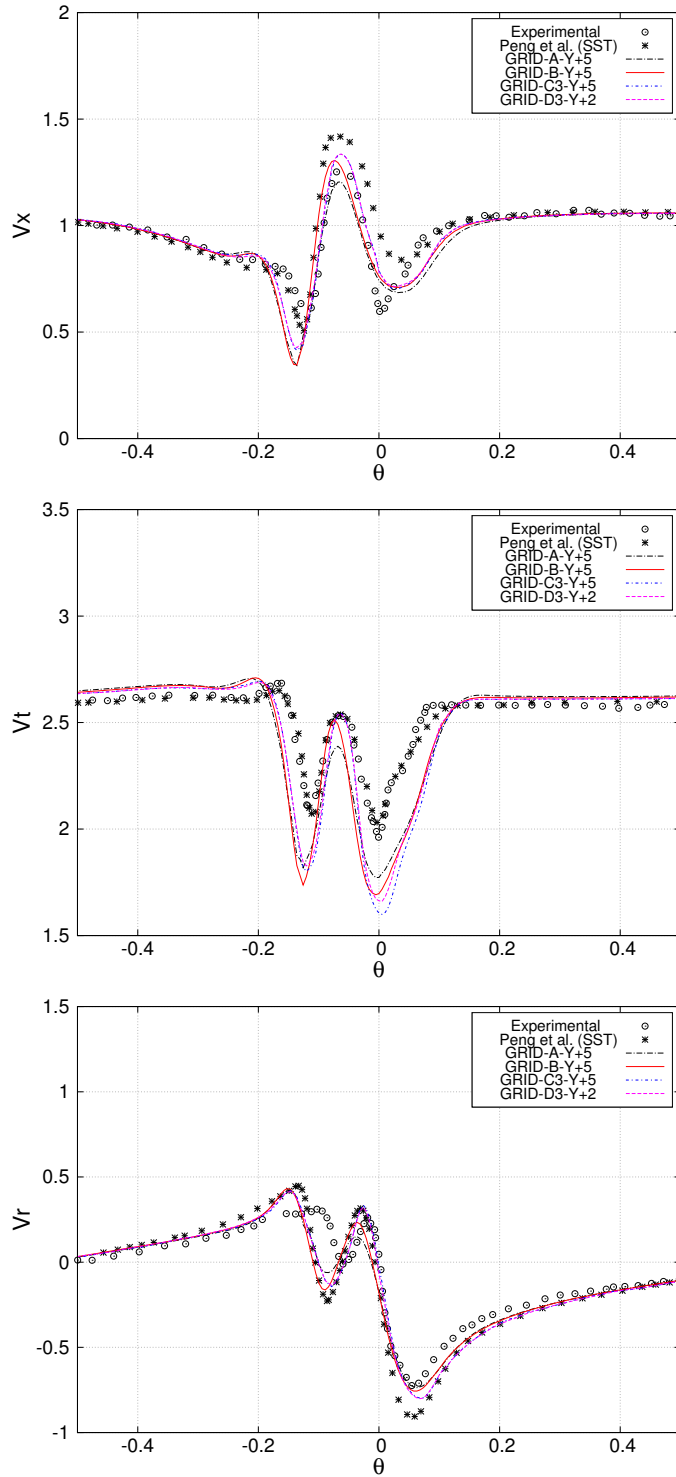


Figure A.12: V_x , V_t and V_r across vortex core at $x/R = 0.1756$

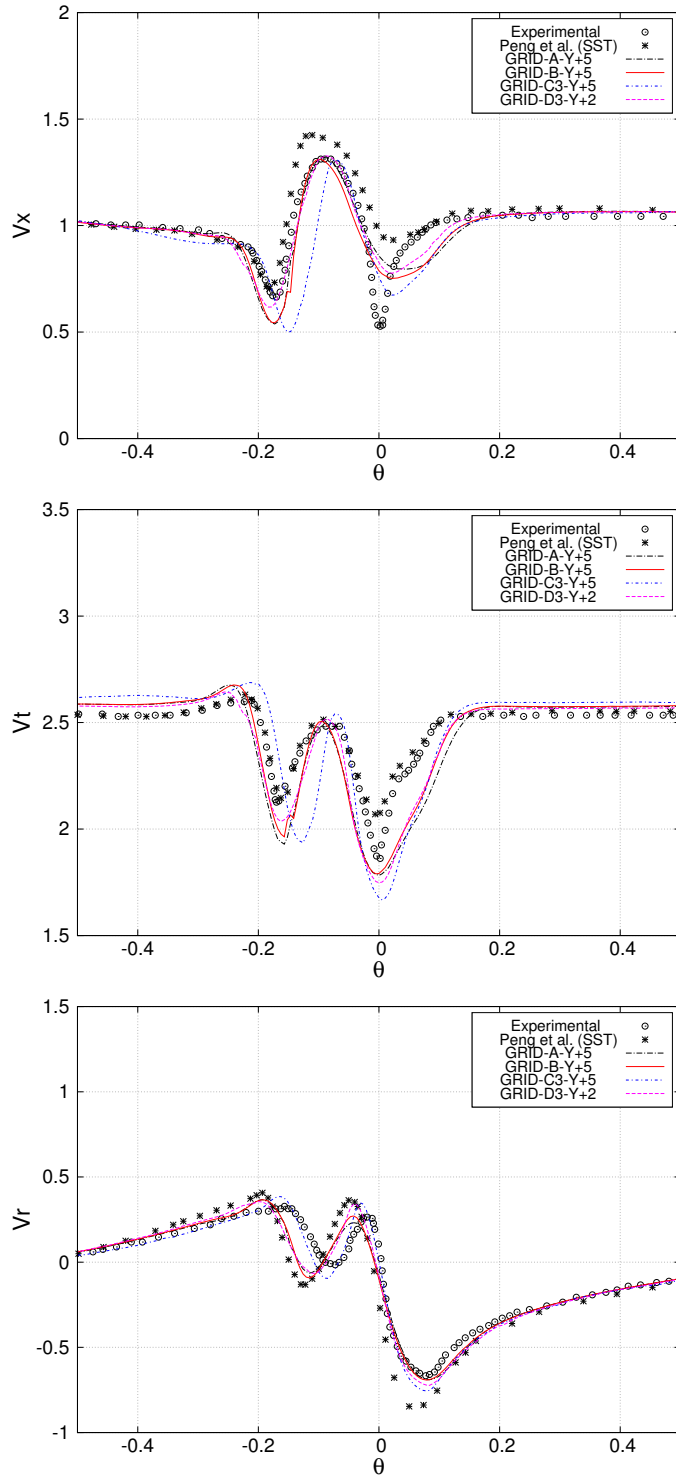
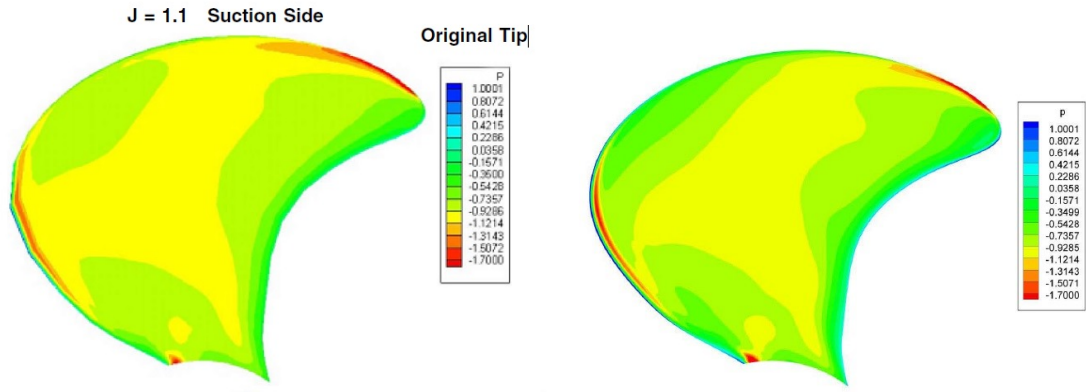
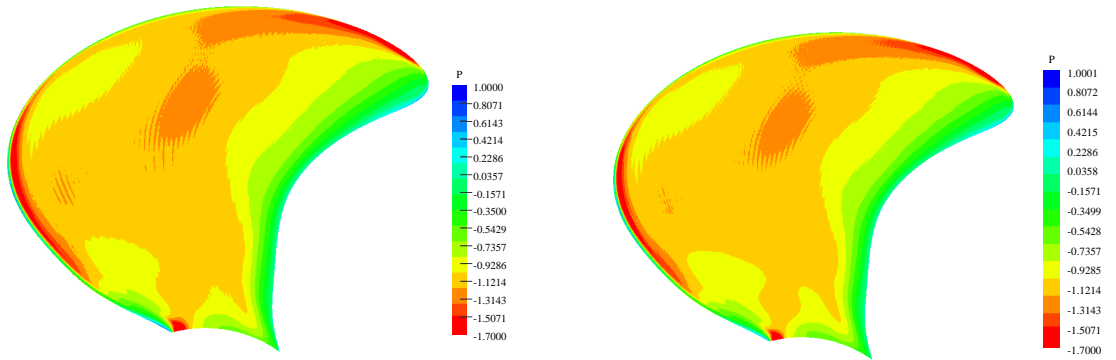


Figure A.13: V_x , V_t and V_r across vortex core at $x/R = 0.2386$



(a) Numerical results by Hsiao and Pauley (1999)

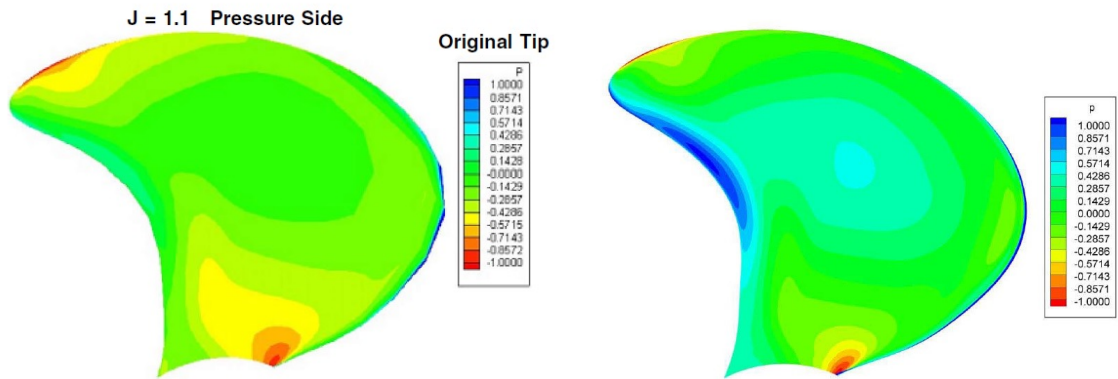
(b) Numerical result by Qiu et al. (2013)



(c) GRID-C3

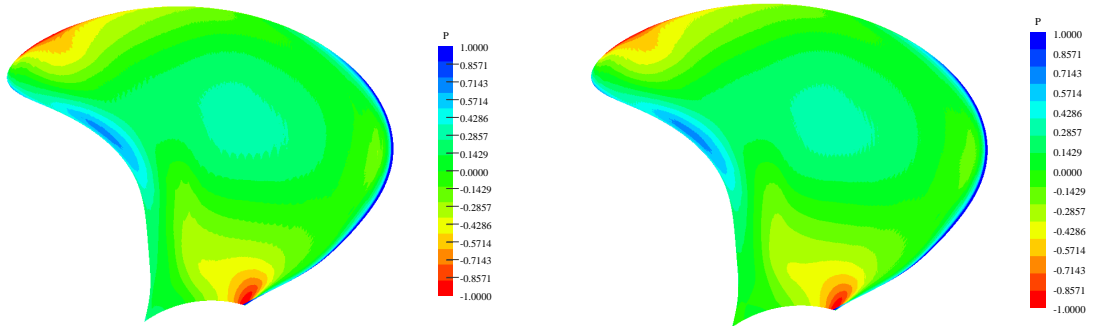
(d) GRID-D3

Figure A.14: Pressure coefficient on suction side.



(a) Numerical results by Hsiao and Pauley (1999)

(b) Numerical results by Qiu et al. (2013)



(c) GRID-C3

(d) GRID-D3

Figure A.15: Pressure coefficient of pressure side.

In Figure A.16, isosurfaces of the vortex structure based on GRID-C3 are plotted using $Q = 100,000$, which is the second invariant of the velocity gradient tensor. The experimental tip vortex trajectory is presented using a black dotted line to show the comparison. The strength of tip vortex core is presented using the normalized axial velocity color label.

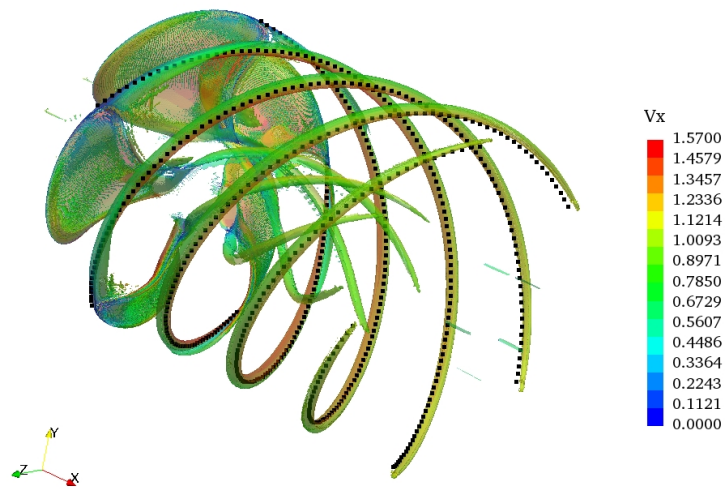


Figure A.16: Vortex trajectory for GRID-C3.

Appendix B

Wave Run-up Simulation

The wave run-up simulations were performed for a single truncated square cylinder using the laminar model. For the simulation with the structure in the domain, a complete computational domain was used.

B.1 Model Experiment

Stansberg et al. (2005) carried out an experimental study of wave run-up around a vertical truncated square cylinder, which was used as an ITTC benchmark study during the 27th Workshop, Nantes, France (2013). In the current work, a similar model set-up was used for validation purposes. In full scale, the diameter of the square cylinder d is 16 m and the draft T_d is 24 m. A scale factor 1:48.93 was used in the experiment for the truncated square cylinder. Wave elevations were measured at twelve locations as shown in Figure B.1. The coordinates of the wave probes are summarized in Table B.1. The wave matrix for this study is given in Table B.2.

Table B.1: Wave probe locations.

| Series | x/d | y/d |
|--------|------------------------------|------------------------------|
| A | (0.000, 0.000, 0.000, 0.000) | (0.503, 0.592, 0.797, 1.000) |
| B | (0.429, 0.492, 0.637, 0.780) | (0.429, 0.492, 0.637, 0.780) |
| C | (0.503, 0.592, 0.797, 1.000) | (0.000, 0.000, 0.000, 0.000) |

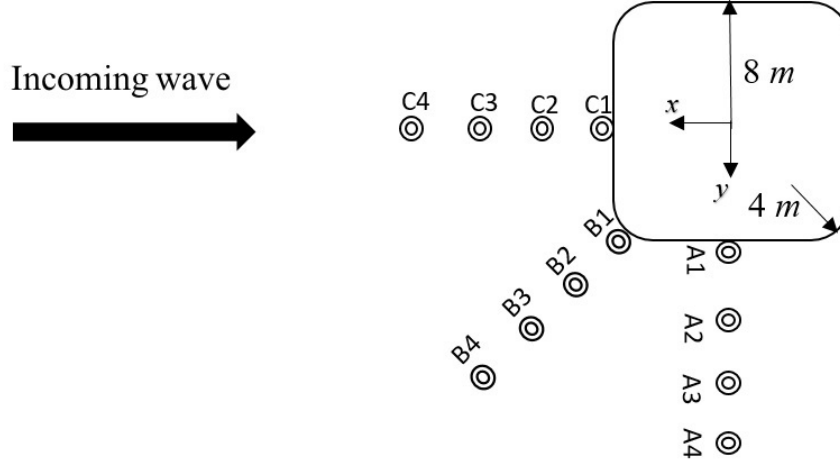


Figure B.1: Wave probes locations

B.2 Computational Domain and Grid Generation

For the wave tank validation, the length of the computational domain was set as $L=6\lambda$, and the width $B = 32d$. Here λ is the wavelength and d is the cylinder diameter. The schematic diagram of the computational domain with wave probes arrangements is shown in Figure B.2. Figure B.3 presents the computational grid for wave tank validation. The grids for the 3D wave tank validation were generated using blockMesh, topoSet, and refineMesh utilities which are available in OpenFOAM. The computational grid for a single truncated square cylinder was generated using navalSnappyHexMesh.

longitudinal distance 2λ in front of the cylinder, the outlet boundary was placed at $x/\lambda = 4$ in the downstream direction, and the side boundaries were placed at distance $16d$ from the center of the structure on both sides in case of the wave structure interaction simulation. The structure was defined as a non-slip wall boundary. The boundary conditions used in the numerical computations are listed in Table B.3. In this work, Stokes second-order wave was used based on the wave theory applicability depending on the wave parameters used during the model test.

B.3 Numerical Set-up

Three computational grids namely GR-01 which has 10 cells per wave height and 80 cells per wave length, GR-02 which has 14 cells per wave height and 120 cells per wavelength, and GR-03 which has 20 cells per wave height and 160 cells per wavelength were used in the numerical computation. Four time step sizes, TS04($T_w/\Delta t = 1000$), TS05($T_w/\Delta t = 2000$), TS06($T_w/\Delta t = 2500$), TS07($T_w/\Delta t = 3000$) were used in the wave tank validation study.

B.4 Wave Generation Modules

The validation studies for the two wave generation modules were performed for the wave T15S110 shown in Table B.2 using time step TS05. For Module-02, the computational domain was extended 2λ in front of the inlet boundary. For the

Table B.3: Boundary conditions for numerical wave generation.

| Parameters | inlet | outlet | bottom | left/right | top | cylinder |
|------------|-------------------|--------------|--------------------------|------------|-----------------------------|--------------------------|
| U | waveInletVelocity | fixedValue | noSlip | slip | pressureInletOutletVelocity | noSlip |
| p_{rgh} | fixedFluxPressure | zeroGradient | zeroGradient | slip | totalPressure | fixedFluxPressure |
| ν_t | fixedValue | zeroGradient | nutUSpaldingWallFunction | slip | zeroGradient | nutUSpaldingWallFunction |
| k | fixedValue | inletOutlet | fixedValue | slip | inletOutlet | fixedValue |
| ω | fixedValue | inletOutlet | fixedValue | slip | inletOutlet | fixedValue |
| α | waveInletAlpha | zeroGradient | zeroGradient | slip | inletOutlet | zeroGradient |

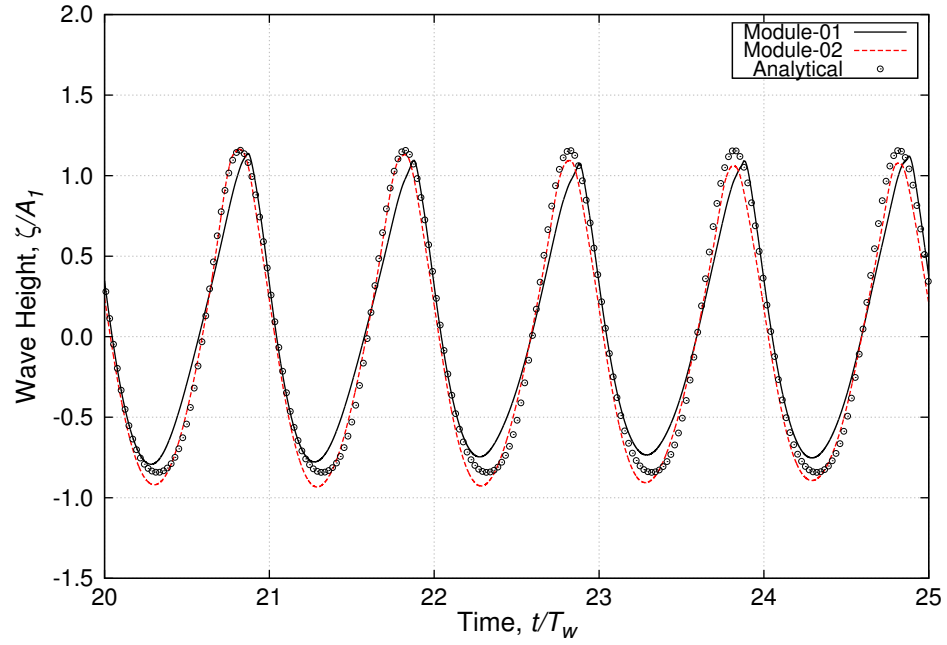


Figure B.4: Comparison of wave elevation at $x/\lambda = 0$ for T15S110 using $T_w/\Delta t = 2000$.

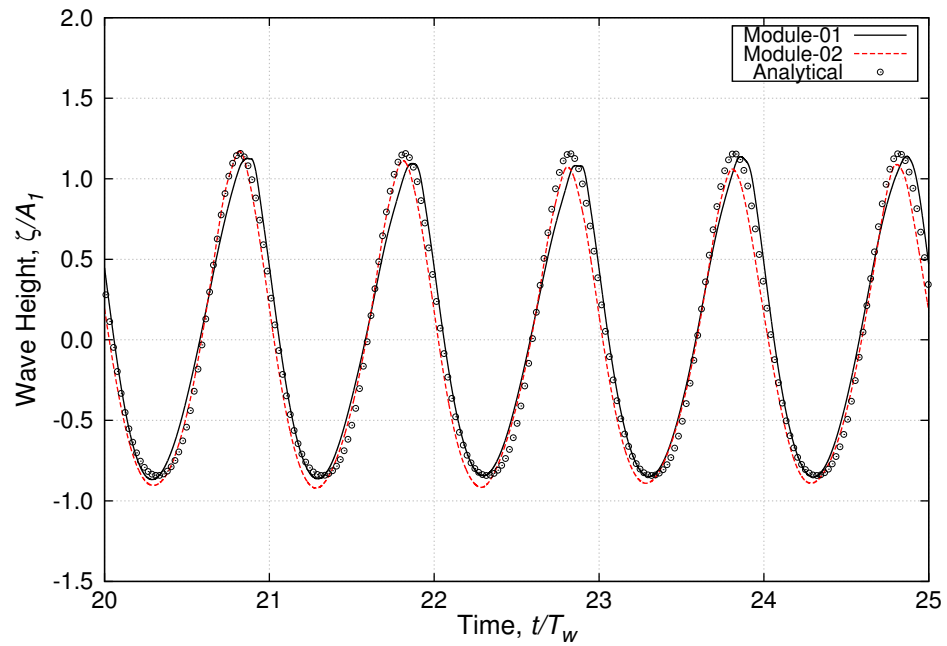


Figure B.5: Comparison of wave elevation at $x/\lambda = 0$ for T15S110 using $T_w/\Delta t = 2000$.

analytical and numerical simulations, the Stokes second order wave was used. The numerical wave elevation for the two modules are compared for wave probe 03 using grid resolution GR-02 and GR-03. The difference in the two modules is not significant, but there is a significant difference in the total computational grid numbers. On this basis, wave generation Module-01 is used for inlet wave generation with the relaxation based wave damping method for the purposes of the self-propulsion simulation.

B.5 Grid Resolution Study

For the grid dependency analysis, the numerical and analytical time history of wave elevation using time step size TS05 for three grid resolutions for wave T15S110 at $x/\lambda = 0.0$ are compared in Figure B.6. From the comparison, it is seen that the numerical time history of wave elevation shows a good agreement using GR-03. Another comparison is made for wave T15S116 using time step TS05 in Figure B.7 at $x/\lambda = 0$. It is observed that a small time step is necessary for the wave T15S116 for better numerical prediction.

B.6 Time Step Dependency

The dependency on time step size was studied using GR-03 for wave T15S116. From Figure B.8, it is seen that time step TS05 gives the numerical time history of wave elevations with reasonable accuracy. However, the wave crest is over predicted. Figure B.9 shows the comparison between numerical and analytical results for wave T15S116. A better agreement was found for both wave crest and trough. The time step dependency was also studied for T12S110 and T12S116 using GR-03 at $x/\lambda = 0$ and the comparisons are presented in Figures B.10 and B.11 respectively. From the grid resolution and time step study, it is seen that GRID-03 with time step TS-05

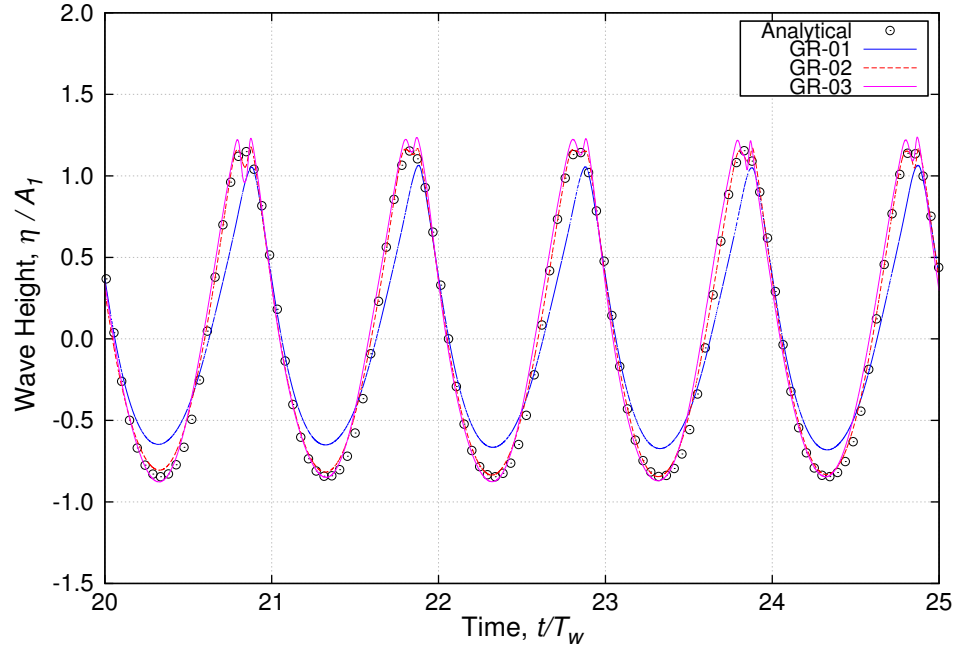


Figure B.6: Comparison of wave elevation at $x/\lambda = 0$ for T15S110 using $T_w/\Delta t = 2000$.

gives acceptable numerical wave height compared to the analytical solution. Please note that the *limitedLinear* (OpenFOAM, 2019) divergence scheme was used in the grid dependency and time step size dependency study.

B.7 Effect of Divergence Scheme

The effect of divergence scheme was investigated for T12S116 using *limitedLinear* and *limitedCubic* (OpenFOAM, 2019) using different time step sizes. The comparison is shown in Figure B.12. The close view of the wave trough on the generated waves shows that the same level of accuracy can be obtained with large time step size using the *limitedCubic* divergence scheme. The difference between the numerical results for TS-04 and TS-05 is not significant compared with the analytical wave elevation.

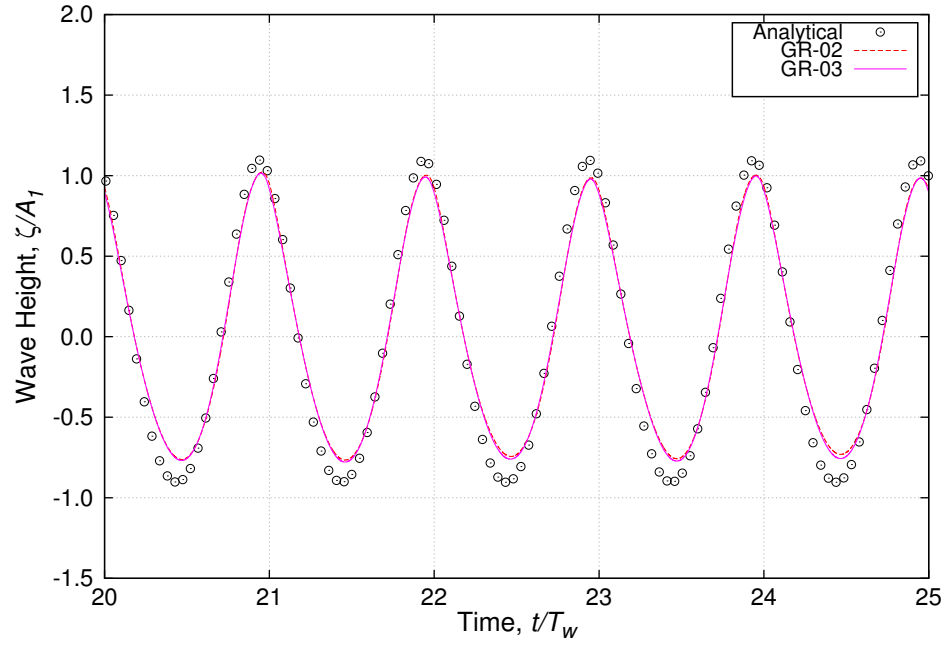


Figure B.7: Comparison of wave elevation $x/\lambda = 0$ for T15S116 using $T_w/\Delta t = 2000$.

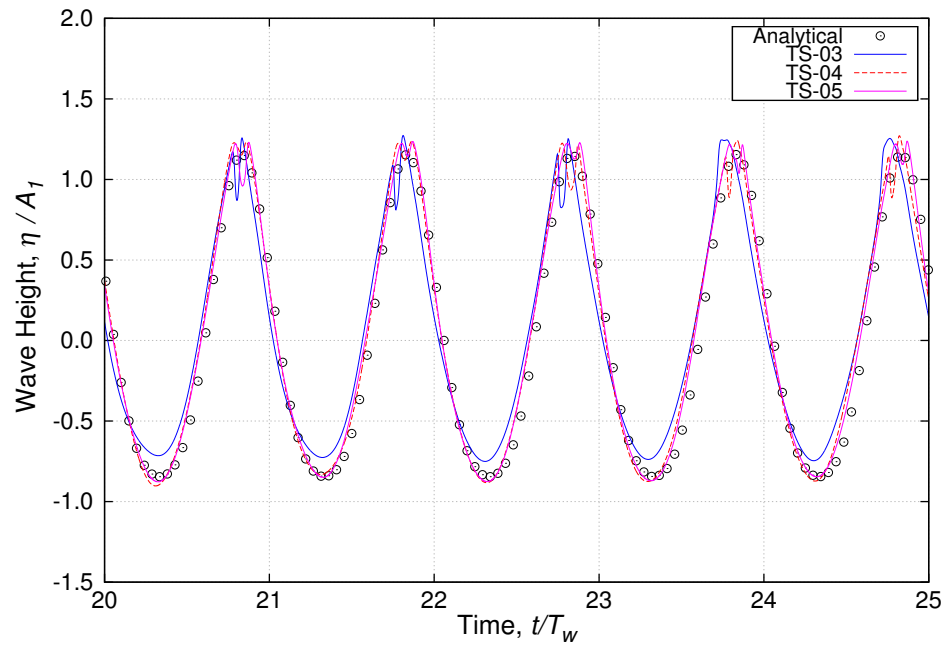


Figure B.8: Comparison of wave elevation at $x/\lambda = 0$ for T15S110 using GR-03.

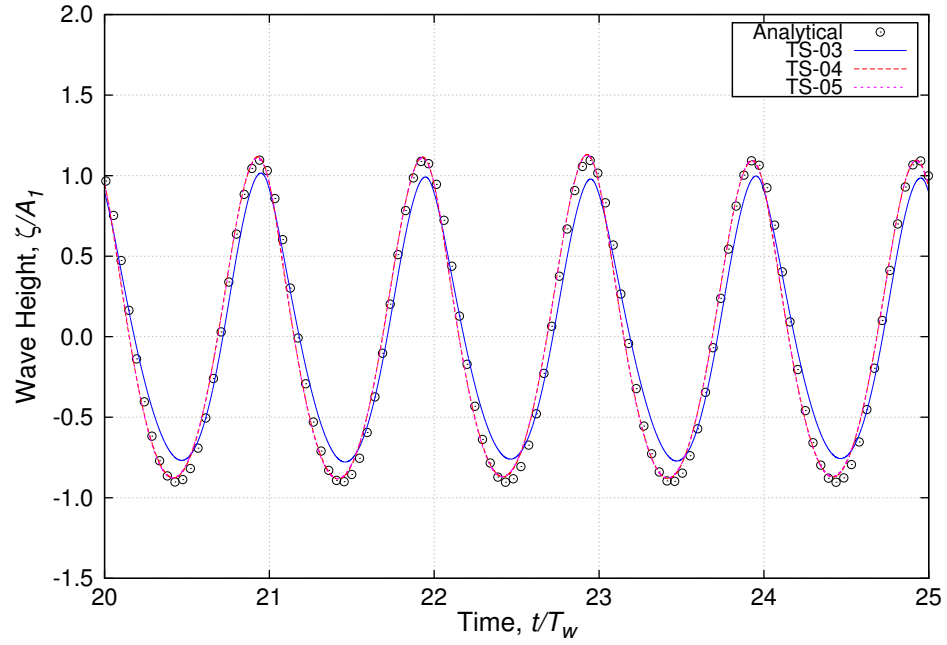


Figure B.9: Comparison of wave elevation at $x/\lambda = 0$ for T15S116 using GR-03.

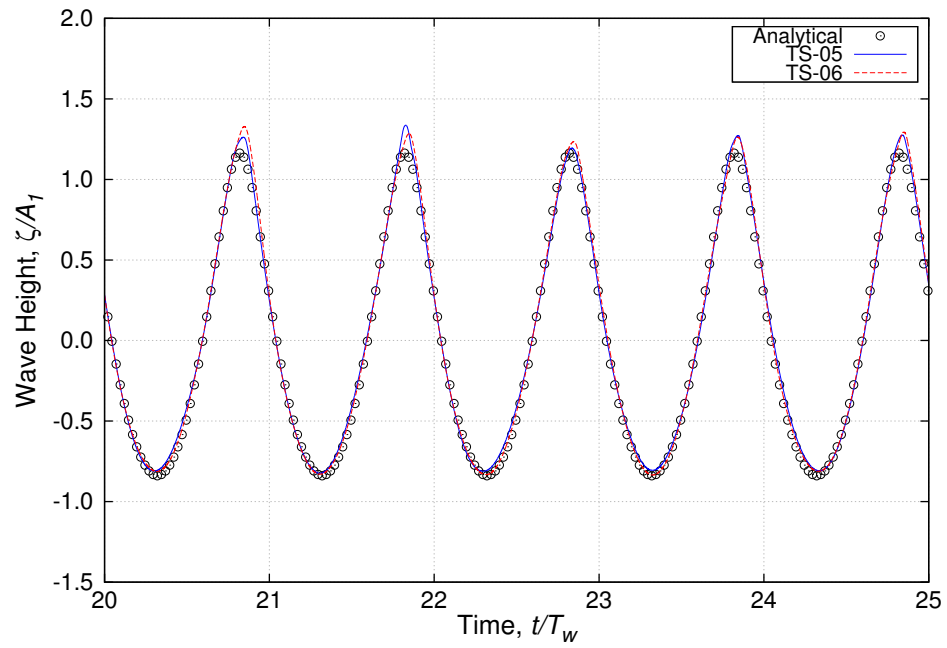


Figure B.10: Comparison of wave elevation at $x/\lambda = 0$ for T12S110 using GR-03.

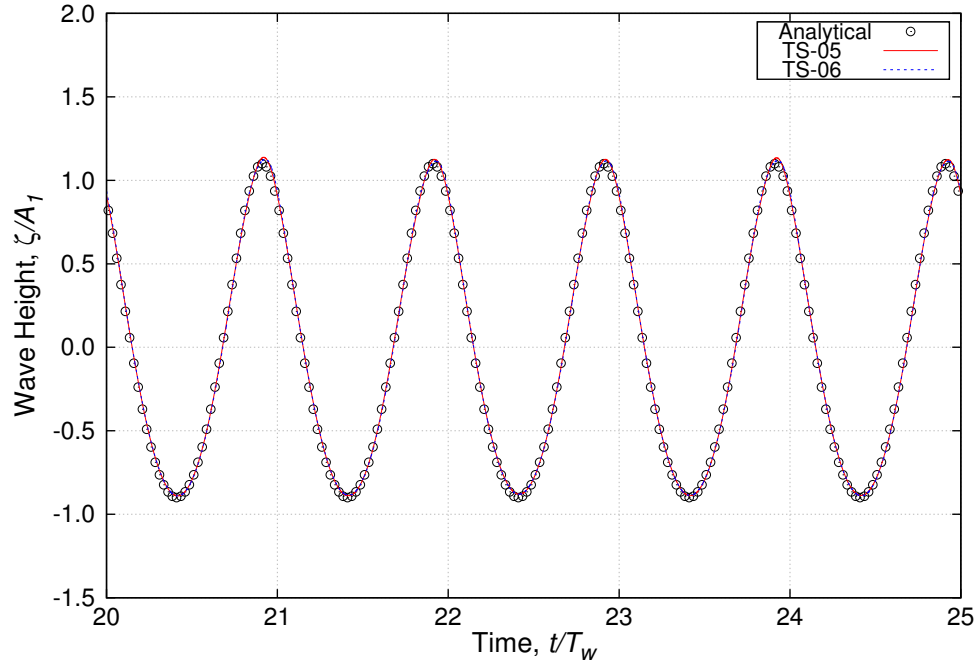


Figure B.11: Comparison of wave elevation at $x/\lambda = 0$ for T12S116 using GR-03.

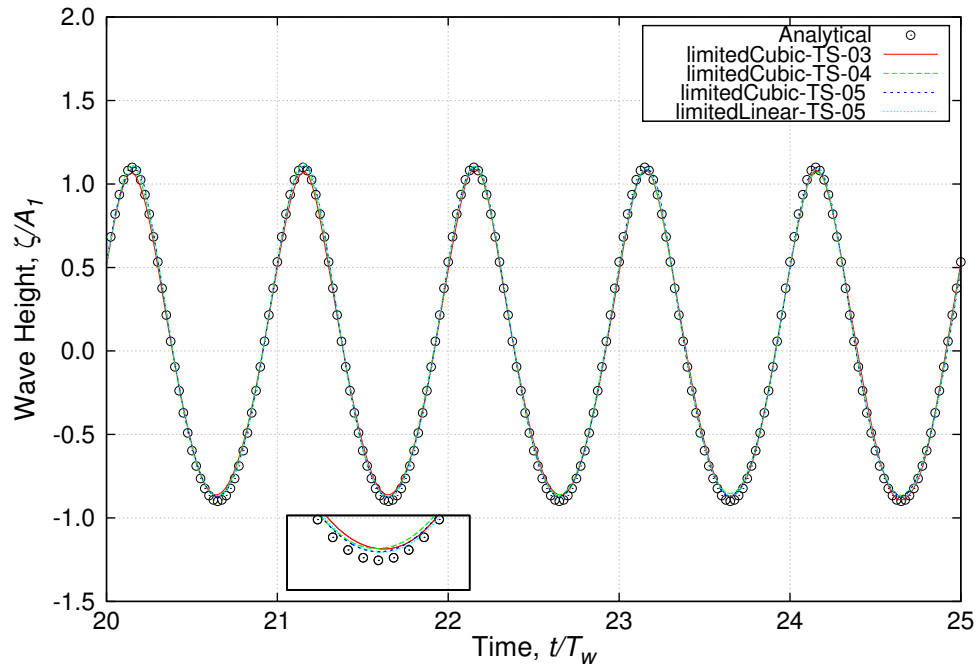


Figure B.12: Effect of divergence scheme on wave generation.

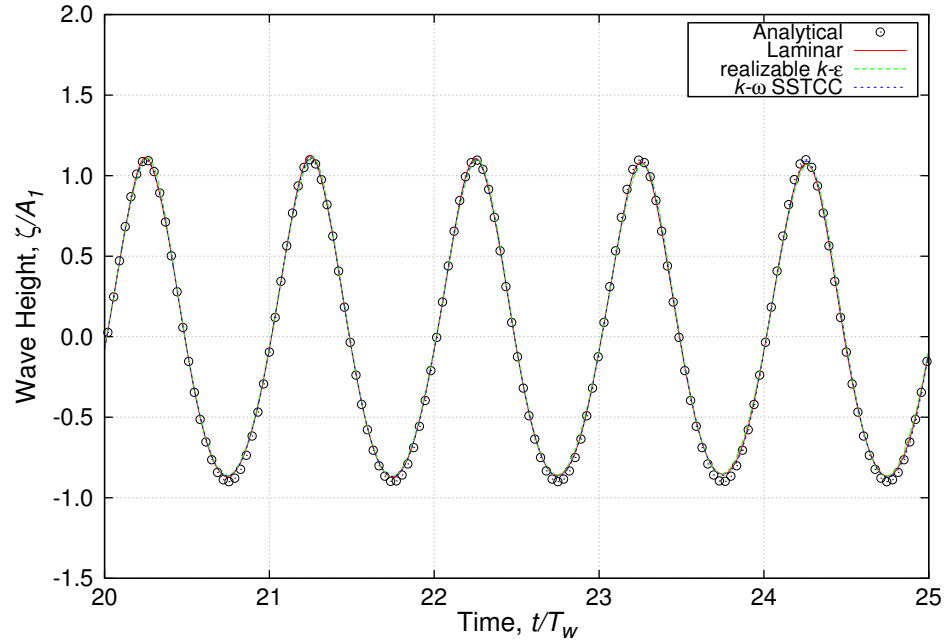


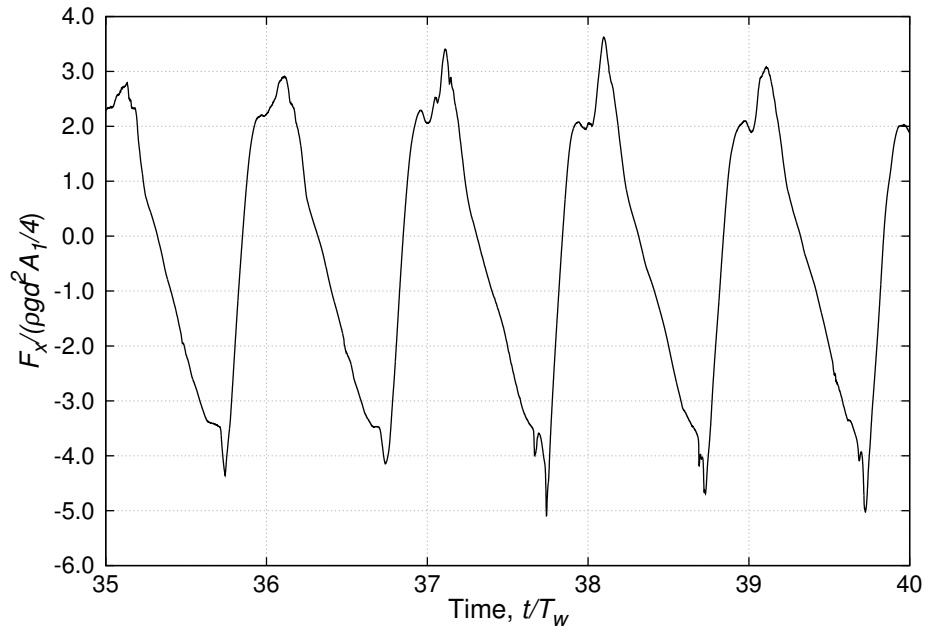
Figure B.13: Effect of turbulence model on wave generation.

B.8 Effect of Turbulence Model

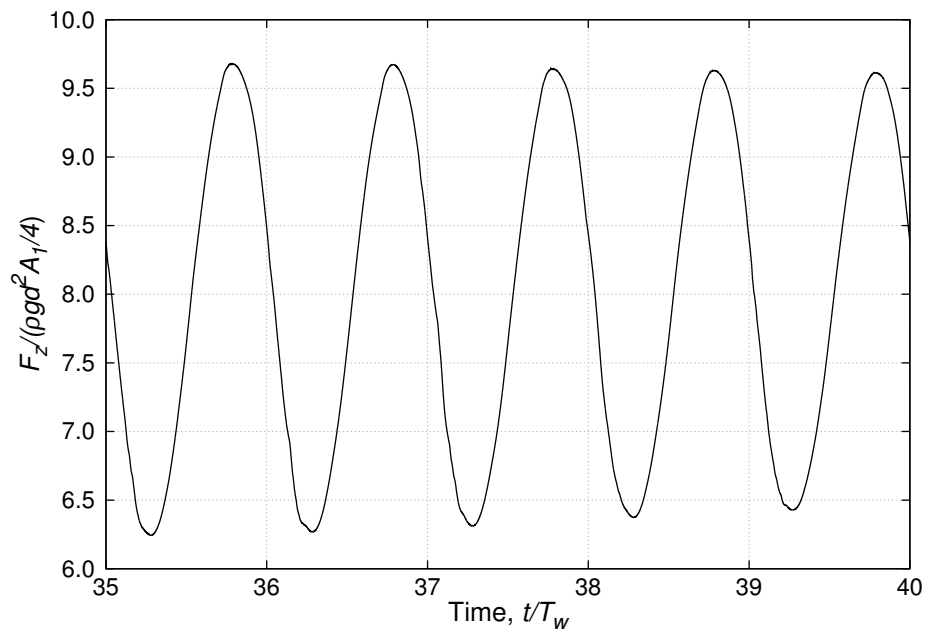
The effect of turbulence model on the numerical wave generation was studied for three conditions, laminar, realizable $k - \epsilon$, and $k - \omega$ SSTCC turbulence model. A 0.10% turbulence with eddy viscosity ratio $\mu_t/\mu = 10$ was used for turbulence parameters calculation. The comparison shown in Figure B.13 between the analytical wave elevation and the numerical wave elevation for the different turbulence model shows almost similar identical results.

B.9 Wave Run-up Results

The non-dimensional horizontal and vertical forces acting on the square cylinder for wave T12S110 are plotted in Figure B.14. Figure B.15 shows the forces acting on the square cylinder for wave T15S110. From these figures, it is seen that the

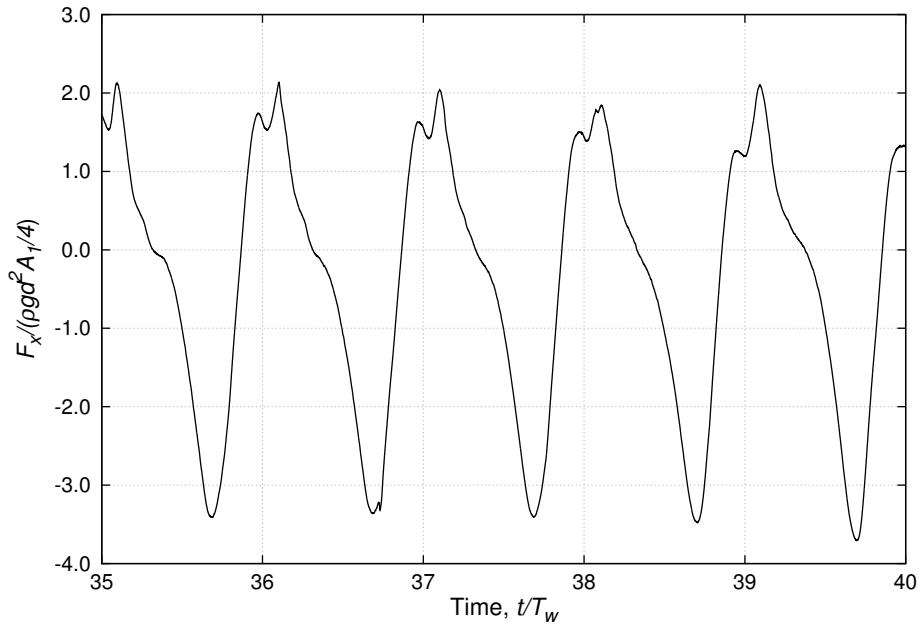


(a) Horizontal force

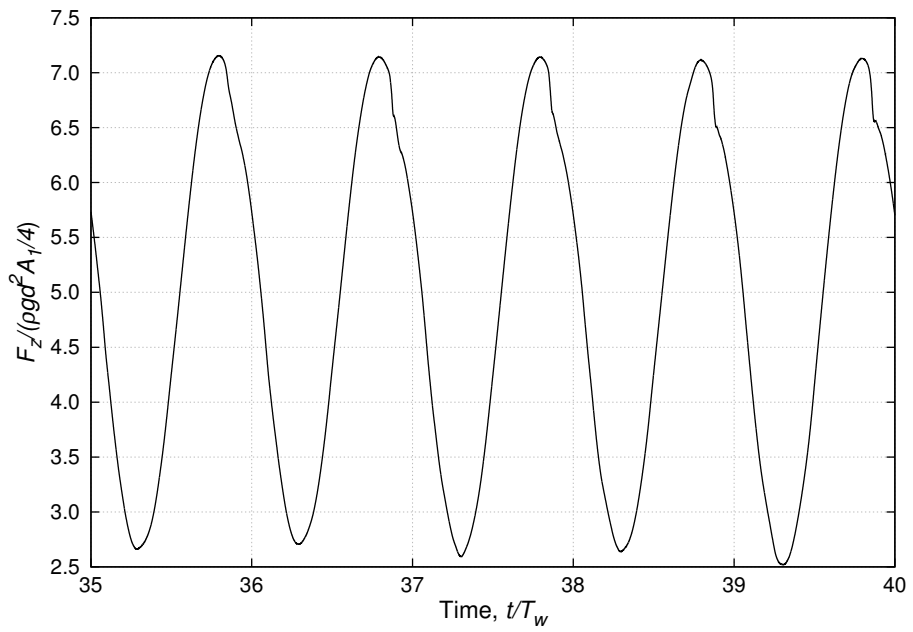


(b) Vertical force

Figure B.14: Time history of wave force on the cylinder for wave T12S110.



(a) Horizontal force



(b) Vertical force

Figure B.15: Time history of wave force on the cylinder for wave T15S110.

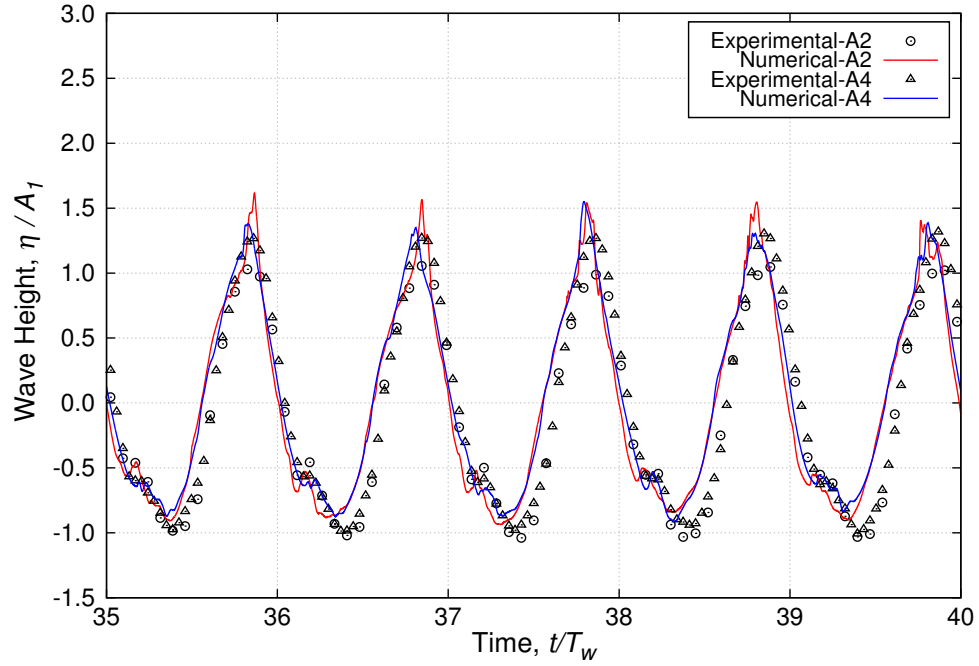


Figure B.16: Wave elevation comparison for wave T12S110 at A2 and A4.

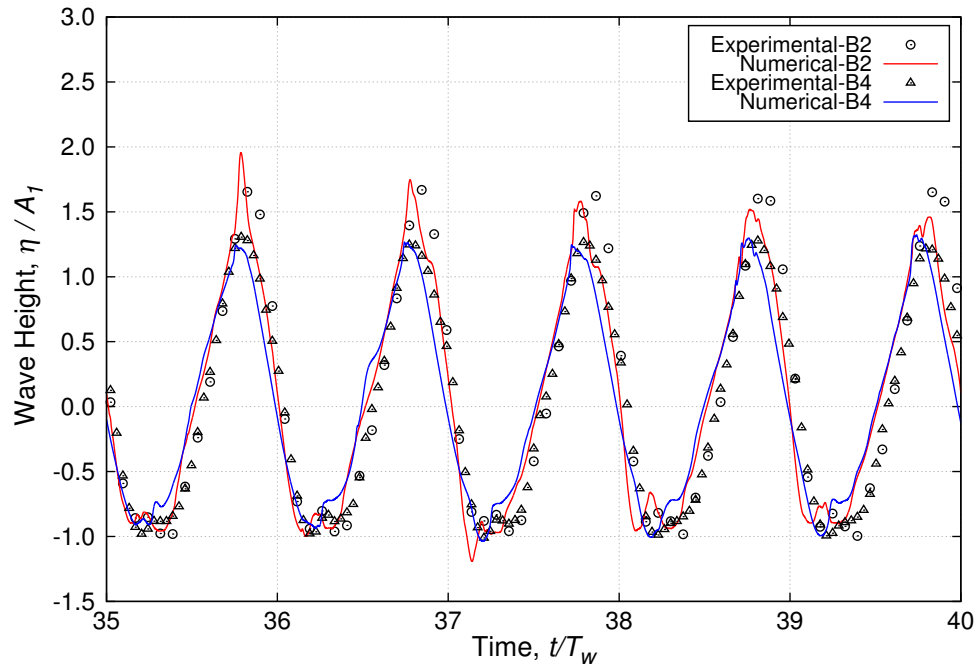


Figure B.17: Wave elevation comparison for wave T12S110 at B2 and B4.

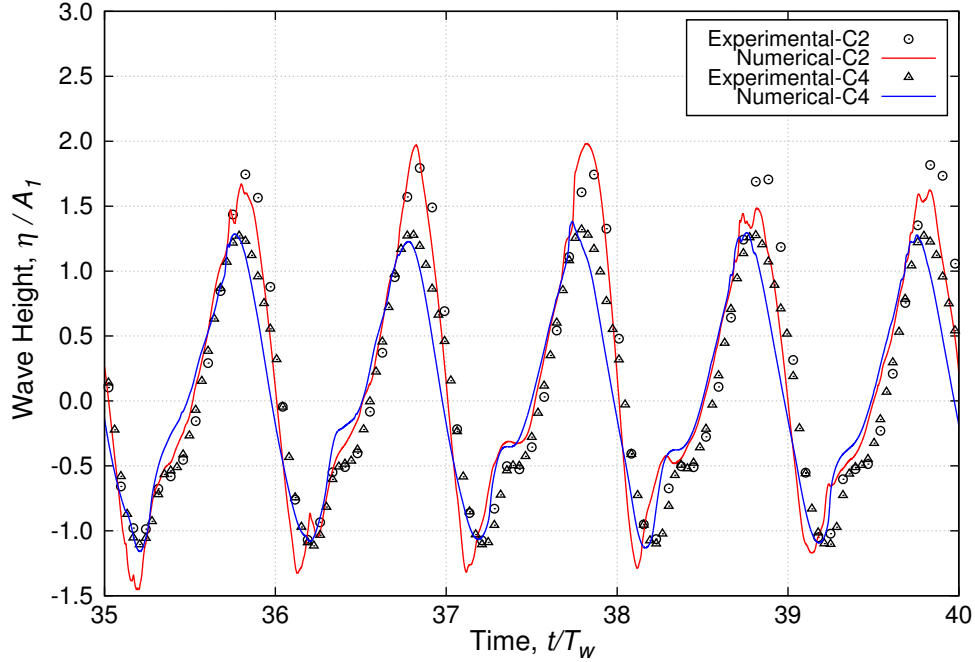
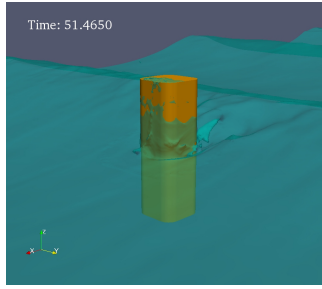


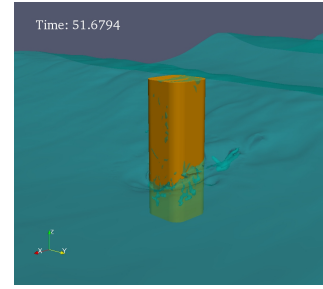
Figure B.18: Wave elevation comparison for wave T12S110 at $C2$ and $C4$.

non-dimensional forces for the short wave are higher than those for the long wave having the same wave steepness. The wave run-up is measured at 12 different locations. The time series of the wave elevations are compared in Figures B.16, B.17, and B.18 for wave T12S110. The predicted wave run-up shows good agreement with the experimental results. The instantaneous free surface for the wave T12S110 with the single truncated square cylinder at different times is presented in Figure B.19.

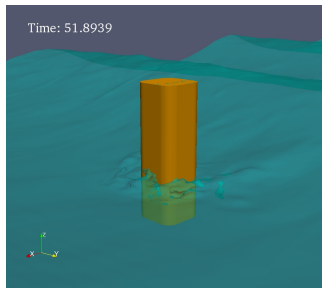
The effect of the turbulence model on wave run-up for a single cylinder is also investigated for wave T12S116. The $k - \omega$ SSTCC, and realizable $k - \epsilon$ turbulence models were used in the numerical simulation. The turbulence parameters were calculated using 0.10 % turbulence intensity. The wave run-up values are compared at probe $A2$, $A4$, $B2$, $B4$, $C2$ and $C4$ in Figures B.20 to B.25. From the comparison, it can be seen that the wave run-up using the $k - \omega$ SSTCC turbulence model is under predicted. The wave run-up is damped out considerably. The turbulence eddy



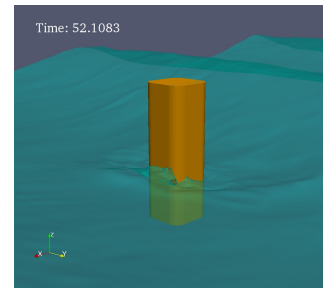
(a) $t = 30T_w + 0T_w$



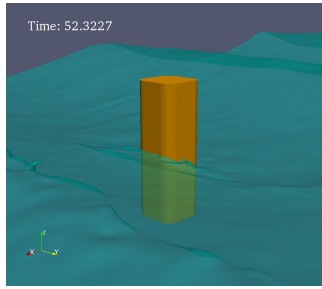
(b) $t = 30T_w + T_w/8$



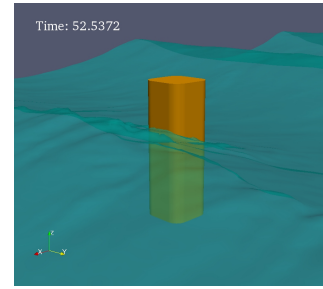
(c) $t = 30T_w + T_w/4$



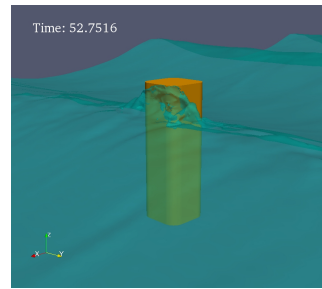
(d) $t = 30T_w + 3T_w/8$



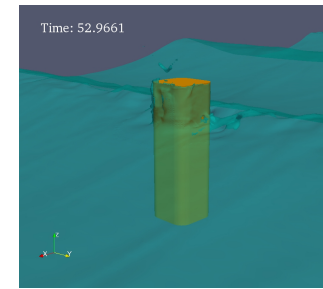
(e) $t = 30T_w + T_w/2$



(f) $t = 30T_w + 5T_w/8$



(g) $t = 30T_w + 3T_w/4$



(h) $t = 30T_w + 7T_w/8$

Figure B.19: Instantaneous free surface for wave T12S110.

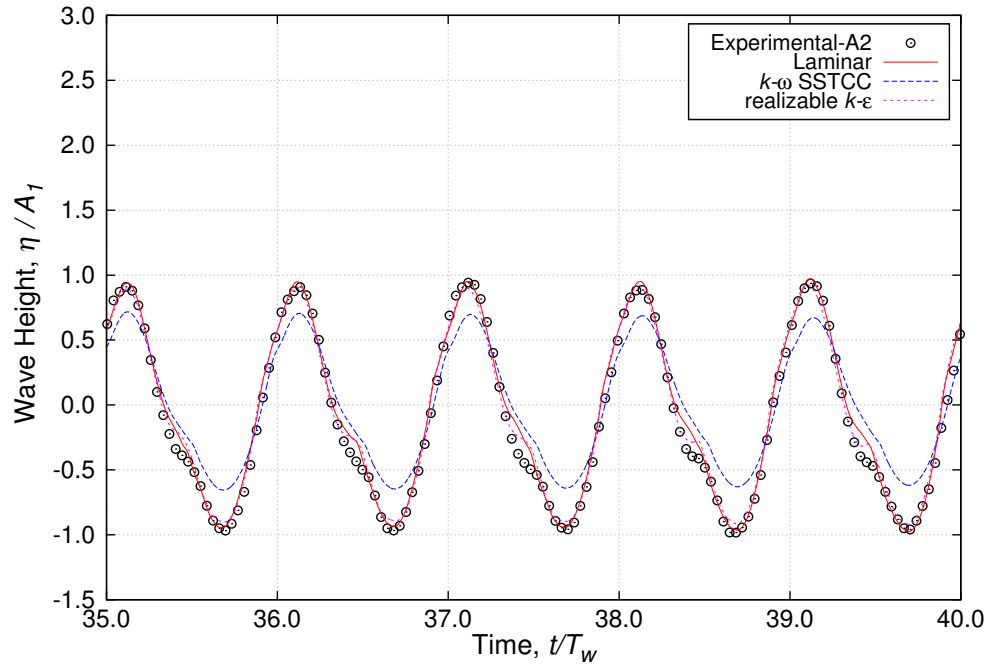


Figure B.20: Wave elevation comparison for wave T12S116 at A2.

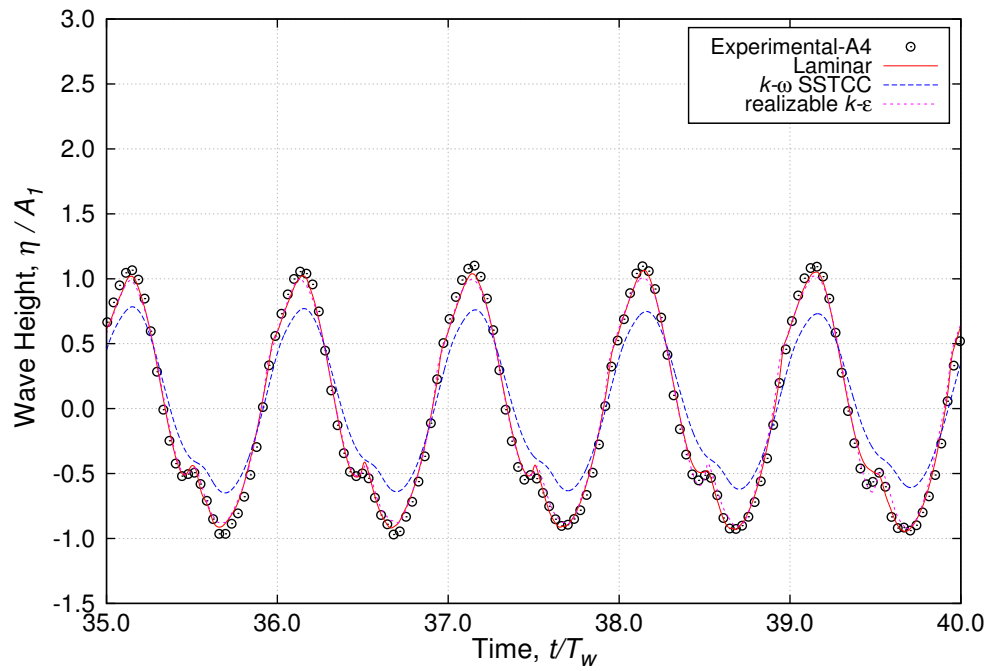


Figure B.21: Wave elevation comparison for wave T12S116 at A4.

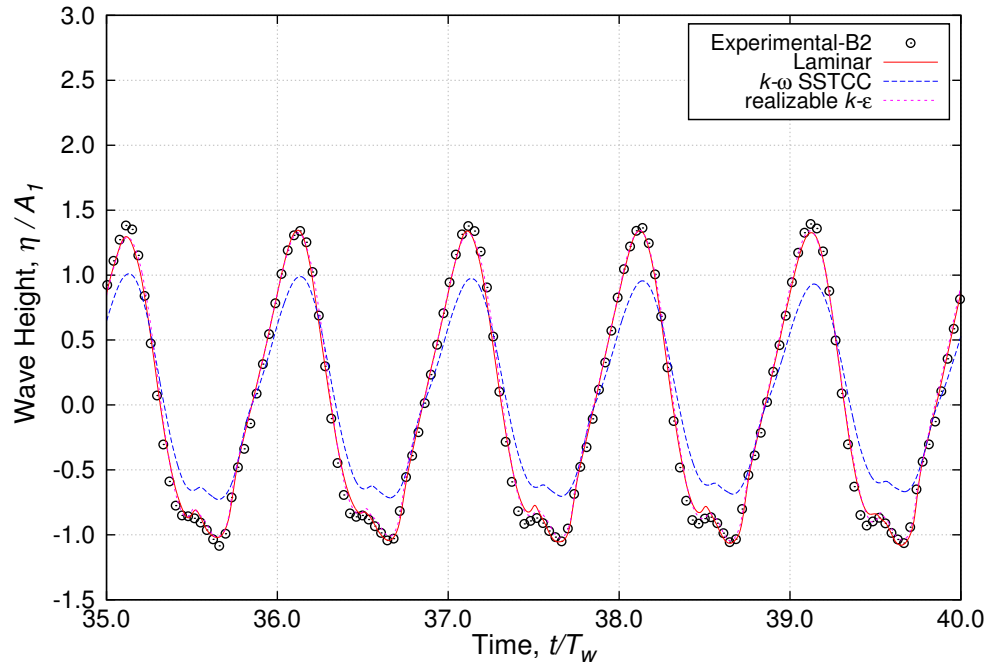


Figure B.22: Wave elevation comparison for wave T12S116 at $B2$.

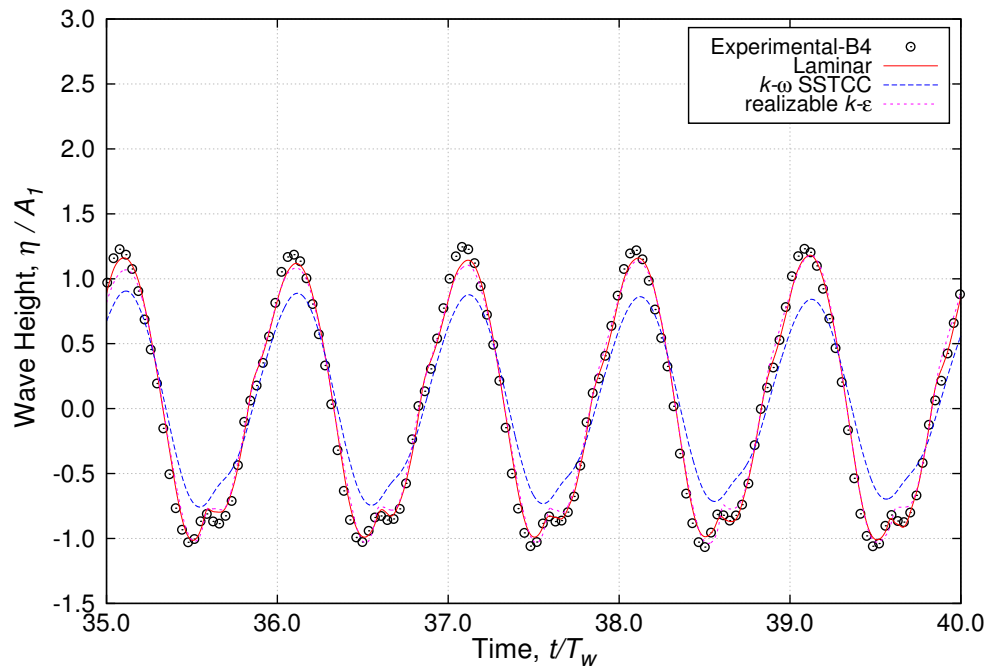


Figure B.23: Wave elevation comparison for wave T12S116 at $B4$.

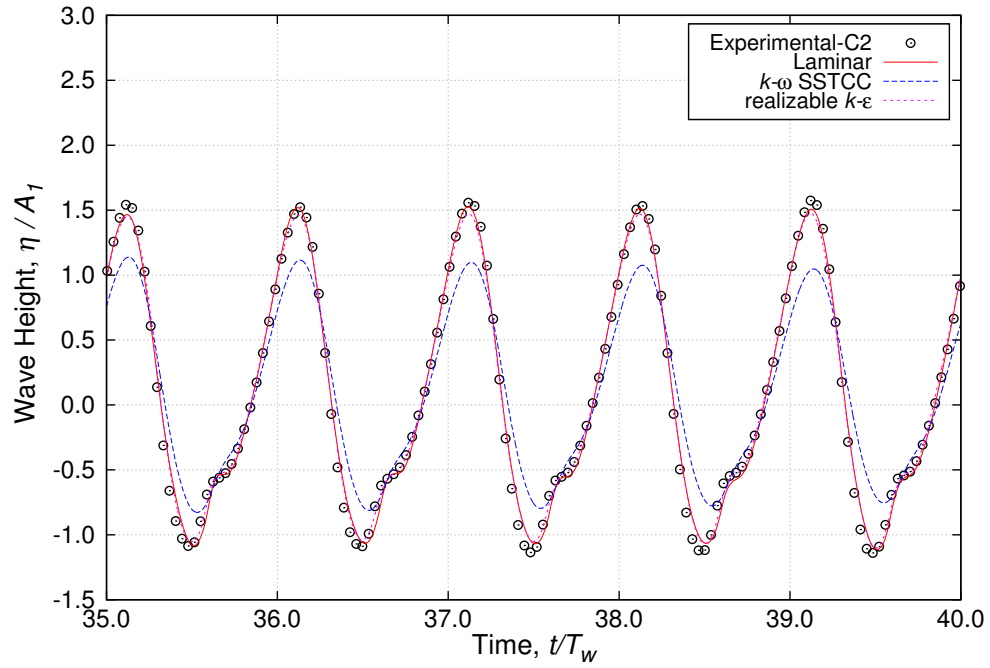


Figure B.24: Wave elevation comparison for wave T12S116 at $C2$.

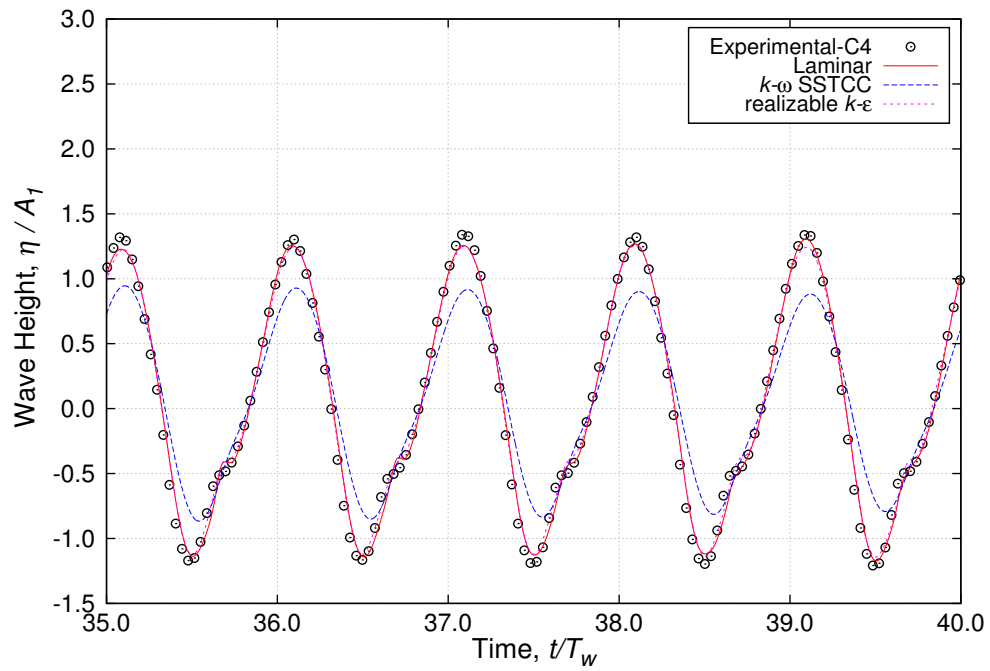
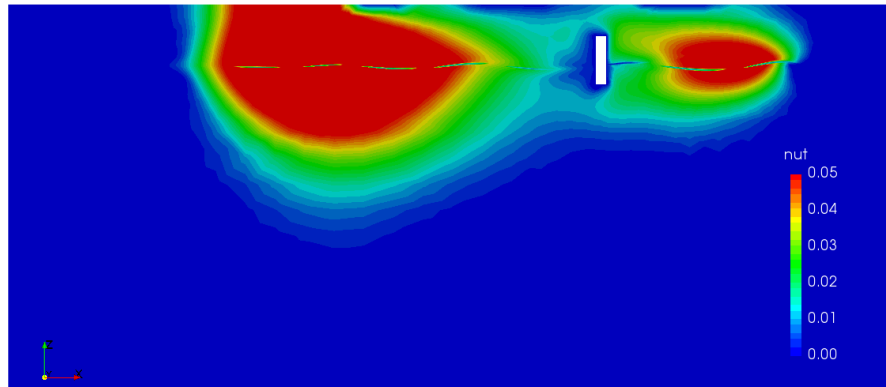


Figure B.25: Wave elevation comparison for wave T12S116 at $C4$.



(a) realizable $k - \epsilon$



(b) $k - \omega$ SSTCC

Figure B.26: Turbulence viscosity distribution on the centre plane.

viscosity distribution on the center plane is shown in Figure B.26. It is seen that for the $k - \omega$ SSTCC turbulence model, the turbulence viscosity is much higher than that for the realizable $k - \epsilon$ model. This is a common problem with eddy-viscosity based turbulence models. A numerical treatment must be applied to limit the turbulence viscosity.